Maryam Askarishahi, M.Sc.

Towards Full-Physics Simulation of Wet Fluidized Beds

DOCTORAL THESIS

to achieve the university degree of

Doktorin der technischen Wissenschaften

submitted to

Graz University of Technology

Supervisor

Ass.Prof. Priv.-Doz. Dr.techn. Dipl.-Ing. Stefan Radl

Institute of Process and Particle Engineering, Graz University of Technology

Graz, Austria, July 2018

Maryam Askarishahi

Towards Full-Physics Simulation of Wet Fluidized Beds

Dissertation

Electronical version including all publications. Page numbers adapted.

First assessor

Ass.Prof. Priv.-Doz. Dr.techn. Dipl.-Ing. Stefan Radl

Institute of Process and Particle Engineering

Graz University of Technology

External assessor

Univ.Prof. Dipl.-Ing. Dr.-Ing. Alfredo Soldati

Institute of Fluid Mechanics and Heat Transfer

Vienna University of Technology

This work was funded through the Austrian COMET Program by the Austrian Federal Ministry of Transport, Innovation and Technology (BMVIT), the Austrian Federal Ministry of Economy, Family and Youth (BMWFJ) and by the State of Styria (Styrian Funding Agency SFG).

AFFIDAVIT

I declare that I have authored this thesis independently, that I have not used other than the declared sources / resources, and that I have explicitly marked all material which has been quoted either literally or by content from the sources used.

(Ich erkläre an Eides statt, dass ich die vorliegende Arbeit selbstständig verfasst, andere als die angegebenen Quellen/Hilfsmittel nicht benutzt, und die den benutzten Quellen wörtlich und inhaltlich entnommene Stellen als solche kenntlich gemacht habe.)

……..

July 2018, Maryam Askarishahi

for whom tries to keep me on the way forward

Acknowledgements

The present PhD is the outcome of my serious endeavor to boost my knowledge and skills in my professional life. Despite the faced difficulties, it was a really enjoyable time. Specifically, I learned how to rise to the challenges independently; I had the opportunity to develop my expertise in the research field which I was really interested in. I would like to express my gratitude to all people trying to help and support me during these years.

I would like to express my special thanks to Prof. Johaness Khinast, who provided me with the opportunity to do my PhD at the Institute of Process and Particle Engineering beside my career at RCPE GmbH. I also would like to thank you for your valuable comments and insights to the pharmaceutical applications.

My sincere appreciation is given to my supervisor, Prof. Stefan Radl, who enormously helped me to broaden my experience in simulation tools and supported me to develop my skills in carrying out a research work independently and in a well-structured way. I would like to appreciate you for your great support and valuable guidance during these years.

I would like to express my gratitude to my husband, and actually my coworker, Mohammad-Sadegh Salehi, who always tries to support me to develop myself in my professional and private life. I would like to thank you for your great ideas and contribution in my PhD. I feel a tremendous change in my life since we work and live together. I sincerely appreciate you for your dedication and patience. Your encouragement is always of significant help for me in difficult situations.

I would like to thank you my family for their support. I also would like to wish the best for my mother's soul in the heaven. I cannot forget your support, dedication, and self-sacrifice in my life.

Finally, I would like to thank my God, who let me complete this work. I deeply feel your support and guidance in every moment of my life. Trusting on you is only thing which I cannot live without, so I ask you to keep me on your way for the rest of my life.

Kurzfassung

Die Entwicklung eines mechanistischen Modells für die Entwicklung und Optimierung von Verfahren zur Handhabung von Partikeln hat in verschiedenen Industriezweigen viel Aufmerksamkeit auf sich gezogen. Insbesondere in Beschichtungs- und Agglomerationsverfahren kann eine zuverlässige Vorhersage der Leistungsfähigkeit von Fließbettbeschichtungs- und Granulationsanlagen – speziell in der pharmazeutischen Industrie - im Hinblick auf die Einsparung von Material, Energie und Geld profitieren. Die Entwicklung eines mechanistischen Modells steht jedoch aufgrund der starken Kopplung zwischen den Phänomenen, die in feuchten Fließbetten (wet fluidized beds; WFBs) involviert sind, vor mehreren Herausforderungen.

In der vorliegenden Arbeit wurden Ansätze basierend auf Computational Fluid Dynamics (CFD) erweitert, um die Partikel-Tropfen-Fluid-Wechselwirkungen in einem WFB zu untersuchen. Dies diente dazu, ein kostengünstiges Werkzeug zu entwickeln, um die Leistung eines feuchten Fließbettes hinsichtlich der Eigenschaften fester Partikel und der Fließeigenschaften vorherzusagen. Der Schwerpunkt wurde auf Beschichtungs- und Trocknungsprozesse gelegt. Genauer gesagt wurde die Euler-Lagrange (EL) Plattform erweitert, um die Phänomene zu berücksichtigen, die bei einem WFB auftreten, d.h. i) Tröpfchenverdampfung, ii) Tröpfchenabscheidung auf der Teilchenoberfläche und iii) Partikeltrocknung. Nach der Überprüfung der neu implementierten Modelle wurde die erweiterte Plattform verwendet, um den Beitrag der Austauschphänomene zur Leistungsfähigkeit des Betts zu untersuchen.

In der nächsten Phase, die darauf abzielte, den mit EL-Ansätzen verbundenen Rechenaufwand zu reduzieren, wurde der Effekt der Gittervergröberung auf die Vorhersage der WFB Leistung untersucht. Die Ergebnisse der Simulationen zeigten, dass die Anwendung von groben Gittern zu einer Verwischung der Hohlraumverteilung führt. Daher wurde ein Algorithmus vorgeschlagen, um die Porositätsverteilung zu korrigieren, um die Vorhersage von Strömungswiderstandskraft und Wärmeaustauschrate in Grobgitter-Simulationen zu verbessern.

Schließlich wurde eine Euler-Euler (EE) Plattform erweitert, um die Zuverlässigkeit der Annahme einer "gut durchmischten" Schüttung für ein WFB quantitativ und qualitativ zu

bewerten. Insbesondere wurde der Grad der Ungleichmäßigkeit der Temperatur- und Feuchtigkeitsverteilung quantifiziert. Basierend auf den Annahmen der EE-Ergebnisse wurde ein Kompartimentmodell zur Vorhersage der Leistung einer WFB entwickelt. Ein Vergleich der Vorhersagen des EE-Ansatzes und des Kompartimentmodells zeigt, dass das Kompartimentmodell die WFB-Leistung erfolgreich vorhersagen kann, wenn bestimmte Kriterien erfüllt sind.

Abstract

Developing a mechanistic model for the design and optimization of particle-handling processes gained significant attention in various industry sectors. Specifically, in coating and agglomeration processes, the reliable prediction of the fluid bed coater/granulator performance can highly benefit pharmaceutical industries in terms of saving material, energy, and money. However, developing such a mechanistic model is connected with several challenges due to the strong coupling between phenomena that dictate wet fluidized bed (WFB) performance.

In the present thesis, approaches based on Computational Fluid Dynamics (CFD) were extended to investigate particle-droplet-fluid interactions in a WFB. This was served by developing an affordable tool to predict the performance of wet fluidized beds in terms of solid particle attributes and flow properties. The focus was on coating and drying processes. Specifically, an Euler-Lagrange (EL) platform was extended to account for the phenomena involved in a WFB, i.e. i) droplet evaporation, ii) droplet deposition on the particle surface, and iii) particle drying. After verifying the newly implemented models, the extended platform was used to investigate the contributions of exchange phenomena on bed performance.

In the next phase, aimed at reducing the computational effort associated with EL approaches, the effect of grid-coarsening on the prediction of the performance was examined. The results of the simulations revealed that the application of coarse grids results in blurring the voidage distribution. Therefore, an algorithm was proposed to correct the voidage distribution to improve the prediction of drag force and heat exchange rate in coarse-grid simulations.

Finally, an Euler-Euler (EE) platform was extended to assess the reliability of the "well-mixed" assumption for a WFB in a quantitative and a qualitative manner. Specifically, the degree of non-uniformity of the temperature and moisture distribution was quantified. Based on the assumptions taken from the results of the EE simulations, a compartment model was developed to predict the performance of a WFB. Comparison of the predicted results between the EE approach and the compartment model proved

that the compartment model can successfully predict the WFB performance if certain criteria are fulfilled.

Table of Contents

1

Goals and Content Overview

This chapter summarizes the core concept of the present thesis, as well as details the goals and the content of the thesis. Furthermore, the contribution of the thesis author (M.A.) to individual publications is declared.

1.1 Wet fluidized beds

Fluidized beds (FBs) are characterized by high rates of heat and mass transfer due to efficient mixing of the particles, and intense solid-fluid contact. Therefore, FBs are usually utilized to realize well-mixed condition with varying particle residence times [1] in the system. Likewise, these striking features make the fluidized bed a promising tool for particle-handling processes, such as granulation, coating, and drying.

In the wet fluidized beds, in addition to the solid particles and fluid phase, liquid droplets are injected to the system for various purposes, such as i) to improve the particle flowability, taste, and appearance; ii) to modify the particle density, particle size distribution; and iii) to protect the particles against humidity, light, oxygen etc.

As in agglomeration and coating processes, it is required to consider wetting, drying, particle shaping and size enlargement, as well as the homogenization of the product. Fluidized bed can be employed as one of the promising tools to integrate all of these features into a single process step, mainly due to the high rate of heat and mass transfer in these devices [1].

For the purpose of particle coating and/or enlarging, usually a binder will be injected to the system in the form of an aqueous solution. This binder is served to coat the particle surface or to aggregate the primary particles after the particle-particle collision to form the granule. Aimed at coating the particles efficiently, and/or increasing the strength of the formed granule, the binder should be solidified, e.g., by means of evaporating the solvent. This can be realized using a hot fluidization gas. It should be added that despite the agglomeration process, in the coating process, the particle agglomeration must be prevented by appropriate operating condition. In fact, the particle agglomeration is successful when the kinetic energy of the colliding particles is dissipated via the binder's ability to form a liquid bridge. This condition can be quantified through a critical Stokes Number as described by Ennis et al. [2]. Therefore, for coating purposes, the spray rate and fluidization velocity should be determined in such a way that the colliding particles can rebound after the impact.

1.1.1 Involved phenomena and striking features

One of the main features of a wet fluidized bed (WFB) is associated with the droplet injection, especially relevant for the agglomeration and the coating purposes. The mechanism of the droplet-particle interaction is so important that the fluid bed granulator/coaters are typically classified based on the position of the nozzle into four categories [3]: top-spray, bottom-spray, Wurster, and rotor with side spray [4].

In the top-spray configuration, the droplets are sprayed over the particle bed surface through a nozzle; particles entering the freeboard, e.g., due to bubble bursting, have the chance to impact the droplets and take up the liquid. This region of the fluid bed where droplet-particle collision occurs is known as spraying/wetting zone. After crossing the spray zone, due to their downward velocity, the particles return to the dense bed and lose part of their liquid content due to the contact with the hot gas. As a matter of fact, the driving force for saturation of the gas results in a partial evaporation of free-flowing droplets in the spray zone as well. This highlights the simultaneous occurrence of various phenomena that are involved in a wet fluidized bed: i) deposition of the droplet on the particle surface; ii) evaporation of the free-flowing droplets; and iii) evaporation of the deposited droplet on the particle surface. The schematic illustration of the these phenomena has been presented in Figure 1. The rates of the droplet deposition and evaporation are driven by droplet concentration, so these phenomena are limited to the spray zone. On the other hand, the rate of particle drying is governed by the particle surface area and the driving force to saturate the interstitial fluid with water vapor. Hence, due to the competition against droplet evaporation, the particle drying mainly occurs in the dense bed. As a matter of fact, the performance of the WFB is significantly influenced by the relative contribution of these exchange phenomena which is described in the next section in more detail.

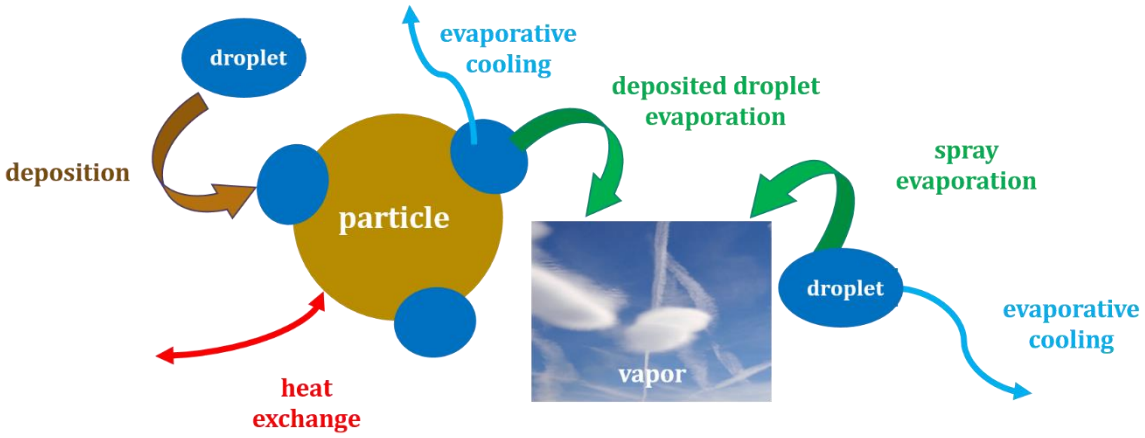

Figure 1- Illustration of the phenomena involved in a wet fluidized bed.

1.1.2 Key parameters

The performance of the fluid bed can be described based on the particle and gas temperature, the bed relative humidity and most importantly the particle size distribution and the liquid content. The latter is known as loss on drying (LoD) in the pharmaceutical context. The term LoD is defined as the fraction of the particles' mass which is evaporable, and can be lost upon drying.

The bed performance depends on the relative contribution of the involved exchange phenomena, which is governed by operating parameters and spray characteristics as follows:

i) Gas temperature: a higher gas temperature increases the driving force for drying, which induces the evaporation from the droplet and the particle surface. Hence, particle LoD will decrease with increasing temperature (and other parameters fixed).

ii) Spray rate: a higher spray rate gives a rise in the particle liquid uptake due to the higher rate of the droplet deposition on the particle surface. As the droplets are injected at a temperature much lower than the temperature of the fluidization gas, an increase in the spray rate reduces the bed temperature. In addition, as the larger droplet surface area is available for the evaporation, the temperature in the spray zone will be even lower due to the droplet evaporation. Consequently, due to the reduction in the drying capacity of the

gas, the particle drying rate is slowed down. Therefore, the effect of the spray rate on the final LoD depends on the relative contribution of these exchange phenomena.

iii) Fluidization velocity: a higher fluidization velocity expands the bed, and hence reduces the time and distance that the droplets need to travel to impact the particles. Therefore, the injected droplets have less chance for the evaporation, and hence the particles are more likely to take up the liquid due to s higher circulation rate. On the other hand, at a higher velocity, the rate of particle drying increases due to the higher mass transfer coefficient.

iv) Atomization air pressure: a higher atomization pressure gives a rise to the droplet velocity, which brings about a shorter droplet travel time, and consequently a higher rate of the droplet deposition. On the other hand, a higher atomization air pressure brings about the generation of smaller droplets [5], which raises the surface area for the droplet evaporation. Therefore, the atomization air pressure influences the particle liquid content in two opposite ways, so the overall effect depends on the contribution of the consequent evaporation and deposition rates.

v) Nozzle position: the nozzle distance from the bed surface plays a vital role in the droplet-particle-fluid interaction in a wet fluid bed. If the nozzle is placed at a higher distance from the bed surface, droplets will spend longer time evaporating. Besides, the droplet penetration into the particle bed will be undermined due to lower droplet-particle relative velocities. Therefore, the rate of droplet deposition on the particle surface will decrease.

In addition to the aforementioned operating parameters, the particles properties, static bed height (i.e. fill level), and the way that droplet are sprayed on the particle surface influence WFB performance.

It is worth noting that the effect of each parameters on the contribution of the exchange phenomena can be quantified based on characteristic times for droplet deposition, droplet evaporation, and particle drying. If it was assumed that the FB is completely well-mixed, and all involved phenomena occur in the same position in the bed, it can

be expected that the larger the characteristic time, the lower the contribution of that specific phenomenon. However, owing to the fact that in the present work a top-sprayed configuration is studied, the analysis of characteristic time becomes more complicated since droplets have time evaporating before depositing on the particle surface (for more information, see chapter 2).

As easily understood from the above discussion, the WFB performance highly depends on the way that fluid, particle, and droplets interact in the bed; as a matter of fact, such interactions are mainly governed by spraying quality and the distribution of the involved exchange phenomena in the bed. Furthermore, the WFB performance is associated with the spatial-fluctuative behaviour of the bed. This reveals that the numerical study of such a system seems indispensable as it will be described in the following section in more details.

1.1.3 The need for numerical simulation

As already mentioned, the phenomena occurring in the WFB are coupled and influenced by both heat and mass transfer. Therefore, the analysis of phenomenon-specific characteristic times is complicated considering the bed configuration. Additionally, the exchange phenomena involved in the WFB compete against each other to consume droplets (i.e. droplet deposition and evaporation) and/or generate vapor (i.e. droplet evaporation and particle drying). Tis shows that, the consequent values for temperature, humidity, and LoD are influenced by the overall exchange rates. Therefore, the contribution of each phenomenon cannot be determined based on the temperature and humidity measurement. This approach has been extensively used for the identification of the well-mixed zones by various studies, such as that of Jiménez et al. [6], Turchiuli et al. [5], and Maronga and Wnukowski [7, 8]. This deficiency of experimental studies highlights the importance of a rigorous CFD approach in demarcating phenomenon-specific zones, which is challenging (and often impossible) via experimental studies.

What is more, as fluidized bed features spatio-temporal fluctuations in flow properties, there is an essential need to obtain point information to acquire a better insight to the bed performance. In fact, the experimental measurement of such a distribution in the

system featuring a bubble-induced particle motion is not readily possible. Therefore, the CFD-based simulations can be a promising tool to achieve this goal.

Design and optimization of the bed requires to deeply understand how operating parameters impact the bed performance. Since running the experiment costs a great deal of material, energy, and time, developing computationally affordable tools can significantly facilitate process design and optimization. This can be realized through linking a CFD-based approach to a compartmental model to establish a more reliable and fast predictive tool. Such a tool can be also extended for industrial application, which is computationally expensive to be simulated using a CFD-based approach alone. Therefore, the reliability of compartment model can be significantly improved by extending the available CFD-based approaches.

1.2 Simulation approach for wet fluidized beds

Simulation of fluid-particle flows is commonly performed based on two approaches: i) Euler-Lagrange (EL); and ii) Euler-Euler (EE) approaches. In the EL approach, the fluid phase is simulated based on the continuum approach by solving Navier-Stokes Equations, while particles are considered as discrete entities and simulated by solving Newton's second law. In the EE approach, both fluid and particle phases are treated as continua. In fact, the solid phase is simulated based on the kinetic theory of granular flow (KTGF), which is an extension of the gas kinetic theory. Therefore, constitutive equations are needed to consider the rheology of the solid phase. In case that only one solid phase is considered, the approach is known as two-fluid model (TFM), while in case having more than one solid phase, the approach is called multi-fluid model (MFM). In the following section, the principle equations for EL and EE approaches will be briefly explained.

1.2.1 Computational fluid dynamics-discrete element method (CFD-DEM)

One of the main categories of EL approach is CFD-DEM in which CFD is used for simulation of the interstitial fluid and DEM for simulation of the particle motion. A brief description of the governing equations for fluid phase and particles are presented below.

For simulation of fluid flow, the momentum equation is solved based on Navier-Stokes Equation as

$$\frac{\partial}{\partial t}\left(\boldsymbol{u}_f \varphi_f \rho_f\right) + \nabla \cdot \left(\boldsymbol{u}_f \boldsymbol{u}_f \varphi_f \rho_f\right) = -\varphi_f \nabla \cdot \tau_f - \varphi_f \nabla P_f + \boldsymbol{\Phi}_d + \varphi_f \rho_f \boldsymbol{g} \tag{1}$$

The first and second terms on left-hand side of the equation denotes the accumulation and convection forces in the same order. The first and second terms on the right-hand side of the equation represents the viscous and pressure forces respectively. The third term stands for the fluid-particle interphase drag force. It is generally accepted that the drag force is the main force contributing in momentum exchange between the fluid and the particle in a gas-solid fluidized bed. Finally, the last term in the right-hand side expresses the gravitational force.

The motion of individual particle is simulated using Newton's second law for the translational and the rotational motion as

$$\rho_{p,i} V_{p,i} \frac{\partial \boldsymbol{u}_{p,i}}{\partial t} = \boldsymbol{f}_{cont,i} + \beta_{sf} V_{p,i}\left(\boldsymbol{u}_f - \boldsymbol{u}_{p,i}\right) - V_{p,i} \nabla P_{f,i} + \boldsymbol{g} \tag{2}$$

$$I_{p,i} \frac{d}{dt} \omega_{p,i} = \boldsymbol{t}_i \tag{3}$$

The right-hand side of Equation 2 represents the forces exerted on the particle surface including the contact force, the fluid-particle drag force, the far field pressure force, and the gravity force in the same order. The particle collision can be described using soft-sphere model based on spring-dashpot model as Tsuji et al. [9] employed for the first time in the fluidized bed.

1.2.2 Two-fluid modeling based on kinetic theory of granular flow (TFM-KTGF)

In TFM approach, the solid and fluid phases are treated as the interpenetrating continua [10]. Therefore, instead of computing the position and velocity of individual particles, the volume fraction and the average velocity of solid phase is predicted by means of solving a Navier-Stokes-like equation. Such an approach offers the advantage of investigating a larger scale gas-particle flow compared to the EL approach. To simulate the solid phase as continuum phase, the kinetic theory of granular flow is employed. In this

theory, in correspondence with the gas temperature, the granular temperature is introduced to represent the particle velocity fluctuation, which strongly influences the solid phase rheology. To close the sets of equations, constitutive equations are required to compute the solid pressure and viscosity (more information can be found in Chapter 4). Eventually, the momentum balance equations for gas and solid phases can be respectively derived as

$$\frac{\partial(u_{fi}\varphi_f\rho_f)}{\partial t}+\frac{\partial}{\partial x_j}(u_{fi}u_{fi}\varphi_f\rho_f)=-\varphi_f\frac{\partial P_g}{\partial x_i}+\frac{\partial\tau_{gij}}{\partial x_j}-\boldsymbol{\Phi}_d+\varphi_f\rho_g g_i \tag{4}$$

$$\frac{\partial(\varphi_s\rho_s u_{si})}{\partial t}+\frac{\partial}{\partial x_j}(\varphi_s\rho_s u_{si}u_{si})=-\varepsilon_s\frac{\partial P_g}{\partial x_i}+\frac{\partial\tau_{sij}}{\partial x_j}+\boldsymbol{\Phi}_d+\varphi_s\rho_s g_i-\frac{\partial P_s}{\partial x_i} \tag{5}$$

The terms presented on the right-hand side of Equation 5 denote i) static pressure force, ii) viscous force, iii) gas-fluid drag force, iv) gravitational force, and v) solid pressure force respectively.

Apart from the hydrodynamics, the performance of the WFB is driven by the heat and mass transfer through the exchange phenomena involved as briefly described in the following section.

1.2.3 Mass transfer in wet fluidized bed

As above mentioned, transport in wet fluidized bed is driven by temperature and humidity gradients, as well as the distribution of droplets. Hence, it is essential to simulate heat and mass transfer. The mass balance equation for vapour can be derived as

$$\frac{\partial}{\partial t}(\mu_{vap}\varphi_f\rho_f)+\nabla\cdot(\boldsymbol{u}_f\mu_{vap}\varphi_f\rho_f)-\nabla\cdot\left(D_{eff}\nabla(\mu_{vap}\varphi_f\rho_f)\right)=\dot{S}_{total} \tag{6}$$

Where is water vapor mass loading and is calculated based on dry mass of gas as $\frac{x_{vap}}{1-x_{vap}}$.

In Eqn. 6, total exchange rate of vapor, $\dot{S}_{total}$, needs to be defined based on the exchange phenomena involved in the WFB. Namely, the vapour is generated due to the evaporation of the freely-flowing droplets, $\dot{S}_{evap,f}$, as well as drying of the deposited droplet from the particle surface, $\dot{S}_{dry}$. Therefore, the total exchange rate for the vapor is given by

$$\dot{S}_{total} = \dot{S}_{evap,f} + \dot{S}_{dry} \quad (7)$$

The derivation of mass balance equation for droplet depends on the way that the droplets are considered in the simulation. Typically, droplets can be simulated in three diverse approaches. In the first approach, droplets are simulated as discrete entities (or parcels, i.e., a group of entities) as adopted by Van Buijtenen et al. [11], Sutkar et al. [12], and Börner et al. [13]. Therefore, to conserve the mass, the droplet must be removed from the simulation domain after the deposition on the particle surface. In case of evaporation, the shrinkage of droplets also needs to be accounted for, e.g., by considering phase change phenomena. In the second approach, droplets are simulated using the population balance equation (PBE) in which droplet deposition and evaporation must be included in the rate of droplet death term. In the third approach, droplets are considered as a component of the gas phase, so two sink terms are required for evaporation and deposition [14]. Each of mentioned approach has its own challenges, which will be explained in detail in the following section.

1.3 Challenges when simulating WFBs

1.3.1 Simulation of spray atomization

Since spraying condition plays a key role in the droplet-particle interaction, droplet characteristics need to be predicted accurately. Aimed at stimulating droplet injection, various approaches have been utilized in the literature.

In the EL approach, the Euler approach such as volume of fluid or level-set model is used to capture the interface and global spreading of the liquid jet [15, 16], and the Lagrange approach is employed to track the generated droplets. As the number of generated droplet becomes too large, this approach is faced with high computation cost. Furthermore, in case of simulating droplets as discrete elements in WFB, defining the physical properties of droplet-particle contact, such as restitution coefficient is required to be determined [12].

In the second approach, with the reduced level of computational expense, a population balance equation is employed to obtain the local droplet size distribution [14]. However, in this approach, the rates of droplet coalescence and breakup needs to be

calculated based on correlations. In the simulation of coating and agglomeration processes, the higher degree of complexity arises due to heat and mass transfer in the FB. Specifically, the temperature distribution can result in shrinking the droplet as well as changing the viscosity of binder solution, followed by a change in the droplet size distribution [4].

In the third approach, aimed at reducing the level of the complexity associated with the simulation of the spray atomization, it is generally accepted to predefine the spray zone with half-angle as well as droplet size and velocity based on numerical and/or experimental studies [17-19]. Since the spray zone is defined based on the measurement of spray half-angle and velocity, such an approach features the advantage of low computational time beside enough accuracy.

Apart from the simulation of the droplet injection, another challenge originated by the droplet injection is simulating the flow of the wet particles due to droplet-particle collision.

1.3.2 Flow of wet particle systems

Due to the deposition of the droplets on the particle surface, wet particle may agglomerate following the formation of the liquid bridges. However, if the kinetic energy of the particles is high enough, the particles will rebound after collision. Therefore, upon adopting the EL approach in simulation of particle-particle contact, it is essential to include a cohesive force in the equation of motion for particle. This force mainly depends on the particle liquid content and thickness, contact angle, and the physical properties of the binder. It should be noted that simulation of the wet particle agglomeration cannot be afforded even in the small-scale fluidized bed utilizing powerful computational resources. This complexity is associated with the fact that the angles of the particle-droplet and particle-particle collision figure prominently in the formation of the liquid bridge and particle agglomeration. Hence, it is necessary to resolve the particle and the formed bridge, which drastically soars the computational cost. Such a resolved simulation is feasible for the bed filled with only few hundred particles. To overcome such a limitation, liquid bridge force can be added to the force balance equation as suggested by various researchers [20-22]. To make the simulation

even more affordable, Girardi et al. [23] used coarse-grid CFD-DEM simulation for simulation of particle agglomeration.

Upon utilizing EE approach, since the particles are considered to form a continuum, the rheology of wet particles will be subjected to change. Therefore, extended closures are required to be established for the kinetic theory-based continuum models. Such an approach was proposed by Liu et al. [24], who utilized DEM and population balance to study the collision of cohesive particles/granules. Numerous studies were also carried out by Roy et al. [25-27] to investigate the rheology of weakly wet granular material just recently.

In addition to the challenges associated with simulation of particle and droplet flow in the WFB, the heat and mass transfer in this system increase the level of complexity of simulating such systems.

1.3.3 Particle drying

Another challenge faced in the study of WFB is associated with the simulation of particle drying. As particles and granules are porous, two mechanisms of drying are involved in the system. In the first mechanism, known as constant-rate period, evaporation occurs from the surface of the particle, so the drying rate is governed by the saturation pressure, the gas relative humidity, the gas-particle relative velocity, and the surface area available for evaporation. Calculation of the latter, known as the surface coverage of particle, is challenging because the fraction of particle surface covered by the droplets depends on the number of the deposited droplets, the angle of contact, the thickness of formed liquid, etc. Based on the coating number, and footprint area of the droplet, Kariuki et al. [28] developed a correlation to calculate the surface coverage of particle and validate it against experimental data.

In the second mechanism, known as falling-rate period, drying occurs inside the particle pores and is driven by the diffusion of the vapour from the pore to the particle surface, so the rate of drying is much smaller than the one in the constant-rate period. The drying rate in falling-rate period is governed by pore size of particles, apparent coefficient of diffusion and particle properties. Owing to the fact that such properties cannot be readily measured, the rate of drying is typically obtained based on the

normalized drying curve, defined as the rate of drying rate in internal regime normalized by the corresponding value at constant-rate regime. As a matter of fact, the transition between these two mechanisms happens at the critical moisture content, x_{cr}. In order to obtain x_{cr} and the normalized drying curve, standard experiments such as microbalance and drying channels [29] can be adopted.

The aforementioned discussion reveals that the performance of the WFB is governed by the fluid-particle-droplet interactions and the involved exchange phenomena which are strongly coupled. Therefore, considering the full-physics of the system seems essential upon studying WFBs.

1.4 The need for full-physics simulation of WFBs

Having considered the aforementioned challenges facing in the simulation of WFBs and the strong coupling between heat and mass transfer in this system, it seems essential to consider all exchange phenomena involved including i) droplet injection; ii) droplet evaporation, iii) deposition of droplet on the particle surface; iv) particle drying. To put in more detail, the interaction between particle and droplet can be attributed to hydrodynamic effect (i.e. the change in the particle flow behavior stemming from atomization air), as well as mass transfer (i.e. the deposition of droplet on the particle surface). On the other hand, the interaction between the particle and the fluid is connected to the fluidization and drying driven by the saturation pressure. Owing to the fact that such interactions influence the WFB performance tremendously, the necessity of considering the involved exchange phenomena needs to be realized for design and optimization purposes using numerical approaches. In this section, the focus is given to the approaches employed for simulation of these phenomena.

1.4.1 Droplet deposition on particles

The deposition of the droplet on the particle surface have been simulated via various approaches in the literature. For instance, Van Buijtenen et al. [11], Sutkar et al. [12], and Börner et al. [13] simulated the particle-droplet interaction using DEM approach in such a way that the particle-droplet collision is considered as a deposition event in their study. Since, in addition to particles, droplets are simulated as discrete entities,

this approach is associated with high computational effort which may be considered as the main drawback of DEM-based simulations.

In the second approach, known as ray-tracing [30], droplets are simulated as a ray in the spray zone; if a particle crosses the spray zone, that particle will take up the droplet. Since the droplets are injected as a ray, no dissipation of droplet kinetic energy is considered, so the droplets have the constant velocity as long as they flow in the bed. Besides, the hydrodynamic interaction between droplet and particle is disregarded in this method. Likewise, the injection velocity cannot influence the motion of the particle, while due to high atomization air flowrate in industrial applications, the particles are pushed downward as proven in the present thesis (more details can be found in Chapter 4). This induces the lower solid volume fraction in the central region of the bed.

In the third approach, Heine et al. [31] considered particle wetting through an analogy to the dust deposition. They calculated the deposition efficiency based on the correlation obtained for the flat surface which may not be applicable for the particles which are few times larger than the droplets in diameter. In fact, this correlation is associated with critical Weber Number which is experimentally defined for a flat surface. In another study, Link and Schlünder [32] determined the droplet deposition efficiency as a function of impact efficiency and adhesion probability through experimental measurement, which limits the application of this approach for numerical simulation. In order to avoid the necessity of experimental measurement, the deposition rate was computed based on the filtration model developed by Kolakaluri [33] through direct numerical simulation.

1.4.2 Droplet injection effect on solid flow pattern

In addition to the heat and mass transfer, the injection of droplets strongly influences the hydrodynamics of FB as demonstrated by experimental and numerical studies conducted by Maronga and Wnukowski [8] and Börner et al. [13] respectively. Particularly, the penetration of droplets to the particle bed affects the particle flow behaviour in the central region of the bed. Therefore, a deeper droplet penetration intensifies the downward motion of the particle in the region far from the walls. Since

the droplets deposit on the particles in the freeboard, less number of droplet have the chance to penetrate to the position close to the distributor surface. This highlights that upon studying (Fluid Bed Coater) FBC hydrodynamic, the deposition of droplet cannot be disregarded as done by Ronsse et al. [34] and Duangkhamchan et al. [35]; they investigated the flow behaviour of solid particles in an FBC while disregarding the droplet deposition and evaporation. This neglection results in the overprediction of the droplet penetration in the bed. This is in contrast with the ray-tracing approach, in which the solid flow behaviour is not influenced by the motion of droplets. This was also supported by the simulation results of Vanderroost et al. [36].

As a consequence, such a strong coupling between heat transfer, mass transfer, and hydrodynamic necessitates considering the full-physics engaged in a wet fluidized bed.

1.4.3 Evaporation from particle surface and suspended droplets

Another reason for the necessity of full-physic simulation is connected to the humidity- and the temperature-driven phenomena involved in the WFB. In other words, as drying and droplet evaporation is driven based on the vapor pressure gradient, they compete against each other. Therefore, neglecting one induces the rate of the other, which may influence the distribution of temperature and humidity in the bed. In case that the evaporation of freely-flowing droplets is neglected, the less amount of water vapor will be generated in the spray zone, followed by less reduction in the bed temperature. Hence, the driving force for drying is higher. Furthermore, in case of neglegting the evaporation, larger number of droplets are available for deposition on the particle surface. Generally speaking, to predict the bed performance more accurately, it is essential to consider the full-physics involved in WFBs, which was marginalized in the most of the studies available in the literature. For instance, Heine et al. [31] and Duangkhamchan et al. [35] disregarded the droplet evaporation in their simulation. Börner et al. [13] also neglected the droplet evaporation and particle drying in the identification of the spray zone. Consequently, such a conclusive study is of higher importance when the travel time of the droplet is comparable with the characteristic time for drying and evaporation.

Another crucial point essential to be respected is the accurate calculation of particle drying rate in the simulation of WFBs. In most of the studies available in the open literature [12, 37, 38], it was assumed that a continuous liquid film is formed on the particle surface, and hence drying occurs from the entire surface of particle. However, the underlying assumptions leads to the overprediction of the rate of drying. In this case, a higher amount of water vapour will be generated, and consequently, the particle LoD and temperature will be underpredicted. This highlights that computation of particle surface coverage seems to be essential. This can be realized by applying the correlation developed by Kariuki et al. [28], as also did in the present work.

Generally speaking, if the contribution of the involved exchange phenomena cannot be reliably computed, the adopted approach fails to predict particle attributes. Therefore, simulating the full-physics of the system sounds essential. Such a numerical approach should realize the communication of exchange phenomena considering reliable assumptions not sacrificing the accuracy.

1.4.4 Goal I: full-physics simulation of droplet-particle-fluid in wet fluid bed

Based on the above discussion, the studies available in the open literature lacks the realization of all phenomena engaged in the WFB and their interaction. Furthermore, the underlying assumptions made in some of these studies make the accuracy of the computed exchange rates questionable. As a result, the first goal of the present study is the ***full-physics simulation of wet fluidized bed realizing particle-droplet-fluid interaction in terms of hydrodynamics, mass and heat transfer (i.e. evaporation, drying, and deposition).***

1.4.5 Goal II: verified CFD-based full-physic simulation platform

In order to achieve the first goal, it is required to develop a reliable tool capable of simulating the exchange phenomena occurring in WFBs. Therefore, the second goal of the present contribution is set the ***development and verification of a CFD-DEM- and TFM-based platform for full-physics simulation of WFBs***.

1.5 The need for an affordable simulation tool

1.5.1 Limitation of CFD-based approaches

In CFD-based approaches, the size of the CFD cell is typically in the order of few particle diameters. Hence, for the simulation of an industrial scale FB filled with at least 10^9 particles, a few hundred micrometers in diameter, the number of CFD cells is too enormous that even the most powerful computational resources can hardly afford simulating such a system for a reasonable flow time. This problem becomes even more severe in case of using the EL approach since the balance equations must be solved for individual particles. Nonetheless, design and optimization of coating and agglomeration processes necessitate investigating the set of operating conditions. Therefore, developing an approach to overcome such a limitation can be of significant help.

As a remedy to this solution, a group of researchers proposed coarse-grid and coarse-graining simulation approaches. In the former, a relatively coarse grid is used for CFD simulation, while in the latter, it is assumed that a given number of particles have identical flow properties and form a grain or a parcel. A large number of research studies [18, 23, 39-43] focus on improving the reliability of coarse-grid and coarse-graining simulations in predicting fluid bed performance.

1.5.2 Limitations of coarse-grid simulations

To improve the prediction of coarse-grid simulation various approaches have been suggested in the literature. For instance, in the filtered approach developed by Sundaresan's research group [23, 40, 44-46], the results of fine-grid simulations are used to adjust the exchange coefficients. However, the model is valid for dilute flow only [41] and needs a sub-grid model to account for unresolved scales. In another approach, so-called Energy Minimization Multi-Scale (EMMS) method [47-50], the local heterogeneity is described through decomposing the flow to the dense and dilute phases. This necessitates the application of a correlation to obtain bubble properties and bed voidage, which can be considered as one of the main drawbacks of this approach besides its validity for the limited type of flows.

Most of the models developed for coarse-grid simulations are based on particle concentration, cell size, and sometimes fluid velocity. Nevertheless, as the results of Fullmer and Hrenya [51] demonstrated, voidage gradient at the interface of cluster plays the main role in the deviation of mean slip velocity in coarse-grid simulations.

1.5.3 Goal III: a voidage correction algorithm to improve coarse-grid CFD-DEM simulation

Having considered the weakness of aforementioned studies on coarse-grid simulations, the third goal of the present contribution is set to the ***development of a straightforward, easy-to-implement voidage correction algorithm to improve the prediction of coarse-gird simulations of gas-particle flow in the wide range of particle volume fractions.*** Consequently, developing an approach which considers the contribution of voidage gradient in blurring the voidage distribution when using coarse grids can improve the prediction of coarse-grid simulations.

1.5.4 The need for compartment model developed based on CFD

As discussed above, the CFD-based approaches suffer from high computational cost, and experts are used to run such simulations. As utilizing these platforms requires the knowledge of CFD and numerical method, developing a verified tool which can be readily used by industry can be of significant help. The simulation of WFB should serve the design and optimization of coating and agglomeration processes, necessitating fast models (i.e., predictions need to be made within a few minutes the most). Hence, a compartment model with high fidelity can be utilized as a promising tool to accomplish this purpose.

In the numerical study of coating and agglomeration processes, the compartment models are typically developed based on the well-mixed assumption. However, based on the experimental observations reported in numerous studies [7, 8], several zones can be identified based on the distribution of temperature and humidity in WFBs. This finding signifies the importance of developing multicompartment models in which the bed is divided into a number of compartments based on the dominant exchange phenomena in each compartment. Nonetheless, this approach is faced with several challenges, including: i) determination of each compartment, and demarcation of

zones' boundaries, ii) the exchange rate of the solid particles between the compartments, governed by fluidization and atomization behaviour of the system, iii) residence time of particles in each compartment, and iv) specification of domain-averaged characteristics for each compartment (e.g. solid volume fraction). Having considered that the identification of well-mixed zone in the FB is too sophisticated to rely on an experimental approach, numerical studies can be of immense value for this purpose. As a matter of fact, the reliability of the well-mixed zones in WFBs can be quantified in terms of degree of non-uniformity of key quantities such as temperature and LoD in the FB. Hence, CFD-based approach can be employed to obtain the point information, to characterize the well-mixed zones, and to compute the variance of key quantities in each zone. Such a study may establish a link between the 0D model and the CFD-based approach in such a way that the prediction of the extended compartment model can be improved via exporting required information from CFD-based simulation to 0D model.

1.5.5 Goal IV: an improved, verified compartment model

Based on the abovementioned discussion, the final goal of the present thesis is set to ***developing and verifying a compartment model base on the well-mixed zones identified by means of TFM simulation and the bed characteristic exported from CFD-based simulation.*** Such a verification of macroscopic model allows us to correlate the deviation of the 0D model from the TFM approach to the degree of non-uniformity of the bed, droplet loss, and solid flow characteristics.

1.6 Concept of the Thesis

The main motivation behind the present thesis was developing CFD-based tools for the full-physics simulation of wet fluidized beds. These tools may pave the way to serve various purposes, and were developed in three steps that are reflected by the three results chapters of the present thesis:

In the first phase of the study, a CFD-DEM code was extended to consider various exchange phenomena, including: i) droplet deposition on the particle surface; ii) droplet evaporation; and iii) particle drying. After verification of the newly implemented models, the contribution of the involved exchange phenomena in the bed

performance was compared and analyzed. These relative contributions were also supported by analyzing the time characteristics of each phenomenon involved. The results of this phase were presented in Chapter 2.

In the second phase, aimed at reducing the computational effort associated with the EL approaches, a comprehensive study was carried out to examine the reliability of coarse-grid simulations in prediction of the exchange rates in dense gas-particle flows. Analyzing the results of this study led to identifying the main root of the failure of coarse-grid simulations. Specifically, an algorithm was proposed to correct the voidage distribution so that the range of voidage gradients can be captured. Afterwards, the reliability of the proposed algorithm (in prediction of drag force and heat exchange rate) was examined for a wider range of voidage gradients. The results of this phase were presented in Chapter 3.

In the third phase, TFM approach is extended and verified to simulate the exchange phenomena involved in WFBs. Subsequently, the degree of non-uniformity of temperature and moisture distributions was quantitatively assessed in the bed so that the reliability of well-mixed assumption can be evaluated for WFBs.

Furthermore, a 0D model was developed based on the output of the TFM simulations. In an extended 0D model, the size of the drying zone in the 0D model was also specified based on the domain-averaged volume fraction of the particle in dense bed computed out of TFM simulation. Finally, aiming at obtaining the range of validity of the developed 0D model, the particle and gas quantities calculated based on the developed 0D model were compared with the corresponding domain-averaged values in the TFM simulation for various sets of operating conditions and spraying properties. In fact, such a comparison enabled us to establish the criteria required to be fulfilled so that the developed 0D model can reliably predict the WFB performance. The results of this phase were presented in Chapter 4.

1.7 Nomenclature

Latin Letters

D_{eff}	m^2/s	Effective diffusivity of vapor in air
D_{vap}	m^2/s	Molecular diffusivity of vapor in air
d_p	m	Particle Diameter
e	$-$	Restitution coefficient
$f_{cont,i}$	N	Contact force exerted on ith particle
g	m/s^2	gravity
h	$kg/s^3/K$	Heat transfer coefficient
$I_{p,i}$	$kg\ m^2$	particles moment of inertia
LoD	$-$	Loss on drying, defined as mass fraction of liquid in the particle
P_f	Pa	Pressure
$\dot{S}_d$	$kg/s/m^3$	Rate of droplet deposition on particle
$\dot{S}_{evap,p}$	$kg/s/m^3$	Rate of evaporation from particle surface
$\dot{S}_{evap,f}$	$kg/s/m^3$	Rate of evaporation from spray
$\dot{S}_{inj}$	$kg/s/m^3$	Rate of liquid (droplet) injection
T	K	Temperature
t	s	Time
$\boldsymbol{u}_d$	m/s	droplet velocity, $\boldsymbol{u}_d = \boldsymbol{u}_f$
$\boldsymbol{u}_f$	m/s	Fluid velocity
x	$-$	mass fraction

Greek Letter

β	m/s	Mass transfer coefficient
β_{sf}	$kg/m^3/s$	Solid-fluid momentum exchange coefficient
μ_{liq}	kg/kg	Mass loading of liquid water in gas phase
μ_{vap}	kg/kg	Mass loading of water vapor in gas phase
ν_f	m^2/s	Kinematic viscosity
ρ_f	kg/m^3	Fluid density
$\rho_{w,Sat}$	kg/m^3	Saturation density of water vapor
τ_f	Pa	fluid stress tensor
ϕ_j	$-$	volume fraction of phase j
$\boldsymbol{\Phi_d}$	N/m^3	Force exerted by particles on fluid phase per unit volume of cell.
ψ_{liq}	m^2/m^2	Particle surface coverage
$\omega_{p,i}$	rad/s	Particle angular velocity

subscripts

d	droplet
f	Fluid
i	i^{th} particle
P	Particle
liq	Liquid (water)
vap	vapor (water)

1.8 Abbreviations

0D	Zero-Dimensional
CFD	Computational Fluid Dynamics
DEM	Discrete Element Method
DNS	Direct Numerical Simulation
EE	Euler-Euler (method)
EL	Euler-Lagrange (method)
FB	Fluidized Bed
FBC	Fluid Bed Coater
FBG	Fluid Bed Granulator
KTGF	Kinetic Theory of Granular Flow
LoD	Loss on Drying
MFM	Multi-Fluid Model
PBE	Population Balance Equation
TFM	Two-Fluid Method
WFB	Wet Fluidized Bed

1.9 The thesis author's contribution to publications

The contributions of the author to the publications that constitute the present habilitation thesis are detailed below. Each publication emerged from original research conducted during the PhD study of thesis author (M.A.).

No.	***Publication***	***Contribution***
1	M. Askarishahi, M.S. Salehi, S. *Radl, Full-physics simulations of spray-particle interaction in a bubbling fluidized bed*, AIChE Journal, 63 (2017) 2569-2587.	M.A. contributed in the code implementation. M.A. verified the implemented models for exchange phenomena, carried out the simulations, analyzed the results, and wrote the manuscript.
2	Askarishahi, M., Salehi, M. S., Radl, S. *Voidage correction algorithm for unresolved Euler–Lagrange simulations*. Computational Particle Mechanics, (2018) 1-19.	M.A. performed the major implementation of the computer code. M.A. developed and implemented the algorithm. M.A. carried out the simulations, analyzed the results, and wrote the manuscripts.
3	Askarishahi, M., Salehi, M. S., Radl, S. *TFM-based Full Physics Simulations of Mixing in Wet Fluidized Beds.* Manuscript in preparation.	M.A. implemented the computer code. M.A. carried out the simulations, analyzed the results, and wrote the manuscripts.

1.10 References

[1] L. Mörl, S. Heinrich, M. Peglow, Fluidized bed spray granulation, Handbook of powder technology, Elsevier2007, pp. 21-188.

[2] B.J. Ennis, G. Tardos, R. Pfeffer, A microlevel-based characterization of granulation phenomena, Powder Technology, 65 (1991) 257-272.

[3] B. Guignon, A. Duquenoy, E.D. Dumoulin, Fluid bed encapsulation of particles: principles and practice, Drying Technology, 20 (2002) 419-447.

[4] P.D. Hede, P. Bach, A.D. Jensen, Two-fluid spray atomisation and pneumatic nozzles for fluid bed coating/agglomeration purposes: A review, Chemical Engineering Science, 63 (2008) 3821-3842.

[5] C. Turchiuli, T. Jimenèz, E. Dumoulin, Identification of thermal zones and population balance modelling of fluidized bed spray granulation, Powder technology, 208 (2011) 542-552.

[6] T. Jiménez, C. Turchiuli, E. Dumoulin, Particles agglomeration in a conical fluidized bed in relation with air temperature profiles, Chemical Engineering Science, 61 (2006) 5954-5961.

[7] S. Maronga, P. Wnukowski, Modelling of the three-domain fluidized-bed particulate coating process, Chemical Engineering Science, 52 (1997) 2915-2925.

[8] S. Maronga, P. Wnukowski, The use of humidity and temperature profiles in optimizing the size of fluidized bed in a coating process, Chemical Engineering and Processing: Process Intensification, 37 (1998) 423-432.

[9] Y. Tsuji, T. Kawaguchi, T. Tanaka, Discrete particle simulation of two-dimensional fluidized bed, Powder technology, 77 (1993) 79-87.

[10] T.B. Anderson, R. Jackson, Fluid mechanical description of fluidized beds. Equations of motion, Industrial & Engineering Chemistry Fundamentals, 6 (1967) 527-539.

[11] M.S. Van Buijtenen, N.G. Deen, S. Heinrich, S. Antonyuk, J. Kuipers, A discrete element study of wet particle–particle interaction during granulation in a spout fluidized bed, The Canadian Journal of Chemical Engineering, 87 (2009) 308-317.

[12] V.S. Sutkar, N.G. Deen, A.V. Patil, V. Salikov, S. Antonyuk, S. Heinrich, J. Kuipers, CFD–DEM model for coupled heat and mass transfer in a spout fluidized bed with liquid injection, Chemical Engineering Journal, 288 (2016) 185-197.

[13] M. Börner, A. Bück, E. Tsotsas, DEM-CFD investigation of particle residence time distribution in top-spray fluidised bed granulation, Chemical Engineering Science, 161 (2017) 187-197.

[14] H.S.M. Aly, Y.A.M.A. Eldrainy, T.M. Lazim, M.N.M. Jaafar, Mathematical Modelling of Droplet Atomization Using the Population Balance Equation, 2009 International Conference on Signal Processing Systems, IEEE, 2009, pp. 955-959.

[15] M. Saeedipour, S. Schneiderbauer, G. Plohl, G. Brenn, S. Pirker, Multiscale simulations and experiments on water jet atomization, International Journal of Multiphase Flow, 95 (2017) 71-83.

[16] L. Zhou, J. Xia, J. Shinjo, A. Cairns, L. Cruff, H. Blaxill, Towards high-fidelity multi-scale simulation of spray atomization, Energy Procedia, 66 (2015) 309-312.

[17] L. Fries, S. Antonyuk, S. Heinrich, S. Palzer, DEM–CFD modeling of a fluidized bed spray granulator, Chemical Engineering Science, 66 (2011) 2340-2355.

[18] J. Link, W. Godlieb, P. Tripp, N. Deen, S. Heinrich, J. Kuipers, M. Schönherr, M. Peglow, Comparison of fibre optical measurements and discrete element simulations for the study of granulation in a spout fluidized bed, Powder technology, 189 (2009) 202-217.

[19] M. Börner, T. Hagemeier, G. Ganzer, M. Peglow, E. Tsotsas, Experimental spray zone characterization in top-spray fluidized bed granulation, Chemical Engineering Science, 116 (2014) 317-330.

[20] T. Mikami, H. Kamiya, M. Horio, Numerical simulation of cohesive powder behavior in a fluidized bed, Chemical Engineering Science, 53 (1998) 1927-1940.

[21] D. Shi, J.J. McCarthy, Numerical simulation of liquid transfer between particles, Powder Technology, 184 (2008) 64-75.

[22] G. Lian, C. Thornton, M.J. Adams, A theoretical study of the liquid bridge forces between two rigid spherical bodies, Journal of colloid and interface science, 161 (1993) 138-147.

[23] M. Girardi, S. Radl, S. Sundaresan, Simulating wet gas–solid fluidized beds using coarse-grid CFD-DEM, Chemical Engineering Science, 144 (2016) 224-238.

[24] P. Liu, K.M. Kellogg, C.Q. LaMarche, C.M. Hrenya, Dynamics of singlet-doublet collisions of cohesive particles, Chemical Engineering Journal, 324 (2017) 380-391.

[25] S. Roy, S. Luding, T. Weinhart, Towards a general (ized) shear thickening rheology of wet granular materials under small pressure, arXiv preprint arXiv:1609.03098, (2016).

[26] S. Roy, S. Luding, T. Weinhart, Towards hydrodynamic simulations of wet particle systems, Procedia Engineering, 102 (2015) 1531-1538.

[27] S. Roy, A. Singh, S. Luding, T. Weinhart, Micro–macro transition and simplified contact models for wet granular materials, Computational particle mechanics, 3 (2016) 449-462.

[28] W.I. Kariuki, B. Freireich, R.M. Smith, M. Rhodes, K.P. Hapgood, Distribution nucleation: quantifying liquid distribution on the particle surface using the dimensionless particle coating number, Chemical Engineering Science, 92 (2013) 134-145.

[29] M. Peglow, T. Metzger, G. Lee, H. Schiffter, R. Hampel, S. Heinrich, E. Tsotsas, Measurement of average moisture content and drying kinetics for single particles, droplets and dryers, Modern drying technology, 2 (2009) 1-70.

[30] G. Toschkoff, S. Just, A. Funke, D. Djuric, K. Knop, P. Kleinebudde, G. Scharrer, J.G. Khinast, Spray models for discrete element simulations of particle coating processes, Chemical Engineering Science, 101 (2013) 603-614.

[31] M. Heine, S. Antonyuk, L. Fries, G. Niederreiter, S. Heinrich, S. Palzer, Modeling of the spray zone for particle wetting in a fluidized bed, Chemie Ingenieur Technik, 85 (2013) 280-289.

[32] K.C. Link, E.-U. Schlünder, Fluidized bed spray granulation: investigation of the coating process on a single sphere, Chemical Engineering and Processing: Process Intensification, 36 (1997) 443-457.

[33] R. Kolakaluri, Direct Numerical Simulations and Analytical Modeling of Granular Filtration, Iowa State University 2013.

[34] F. Ronsse, W. Duangkhamchana, K. Dewettinckb, J.G. Pietersa, Computational Fluid Dynamics (CFD) modelling of the fluidised bed coating process, 7th International conference on Simulation and Modeling in the Food and Bio-industry (Foodsim'2012), Eurosis-ETI, 2012, pp. 34-41.

[35] W. Duangkhamchan, F. Ronsse, F. Depypere, K. Dewettinck, J. Pieters, CFD study of droplet atomisation using a binary nozzle in fluidised bed coating, Chemical Engineering Science, 68 (2012) 555-566.

[36] M. Vanderroost, F. Ronsse, K. Dewettinck, J.G. Pieters, Modelling overall particle motion in fluidised beds for top-spray coating processes, Particuology, 11 (2013) 490-505.

[37] F. Ronsse, J. Pieters, K. Dewettinck, Combined population balance and thermodynamic modelling of the batch top-spray fluidised bed coating process. Part I—model development and validation, Journal of Food Engineering, 78 (2007) 296-307.

[38] F. Ronsse, J. Pieters, K. Dewettinck, Combined population balance and thermodynamic modelling of the batch top-spray fluidised bed coating process. Part II—model and process analysis, Journal of Food Engineering, 78 (2007) 308-322.

[39] M. Sakai, M. Abe, Y. Shigeto, S. Mizutani, H. Takahashi, A. Viré, J.R. Percival, J. Xiang, C.C. Pain, Verification and validation of a coarse grain model of the DEM in a bubbling fluidized bed, Chemical Engineering Journal, 244 (2014) 33-43.

[40] A. Ozel, J. Kolehmainen, S. Radl, S. Sundaresan, Fluid and particle coarsening of drag force for discrete-parcel approach, Chemical Engineering Science, 155 (2016) 258-267.

[41] S. Radl, S. Sundaresan, A drag model for filtered Euler–Lagrange simulations of clustered gas–particle suspensions, Chemical Engineering Science, 117 (2014) 416-425.

[42] J.H. Cloete, S. Cloete, S. Radl, S. Amini, Verification of filtered two fluid models for reactive gas-solid flows, (2017).

[43] S. Schneiderbauer, A spatially-averaged two-fluid model for dense large-scale gas-solid flows, AIChE Journal, (2017).

[44] Y. Igci, A.T. Andrews, S. Sundaresan, S. Pannala, T. O'Brien, Filtered two-fluid models for fluidized gas-particle suspensions, AIChE Journal, 54 (2008) 1431-1448.

[45] S.S. Ozarkar, X. Yan, S. Wang, C.C. Milioli, F.E. Milioli, S. Sundaresan, Validation of filtered two-fluid models for gas–particle flows against experimental data from bubbling fluidized bed, Powder Technology, 284 (2015) 159-169.

[46] C.C. Milioli, F.E. Milioli, W. Holloway, K. Agrawal, S. Sundaresan, Filtered two-fluid models of fluidized gas-particle flows: New constitutive relations, AIChE Journal, 59 (2013) 3265-3275.

[47] J. Li, Particle-fluid two-phase flow: the energy-minimization multi-scale method, Metallurgical Industry Press1994.

[48] J. Wang, W. Ge, J. Li, Eulerian simulation of heterogeneous gas–solid flows in CFB risers: EMMS-based sub-grid scale model with a revised cluster description, Chemical Engineering Science, 63 (2008) 1553-1571.

[49] J. Zhang, W. Ge, J. Li, Simulation of heterogeneous structures and analysis of energy consumption in particle–fluid systems with pseudo-particle modeling, Chemical Engineering Science, 60 (2005) 3091-3099.

[50] J. Wang, M. Van der Hoef, J. Kuipers, Coarse grid simulation of bed expansion characteristics of industrial-scale gas–solid bubbling fluidized beds, Chemical Engineering Science, 65 (2010) 2125-2131.

[51] W.D. Fullmer, C.M. Hrenya, Quantitative assessment of fine-grid kinetic-theory-based predictions of mean-slip in unbounded fluidization, AIChE Journal, 62 (2016) 11-17.

2

Full-physics simulations of spray-particle interaction in a bubbling fluidized bed

This article is published in *AIChE Journal* 63.7 (2017): 2569-2587.
https://doi.org/10.1002/aic.15616

Full-Physics Simulations of Spray-Particle Interaction in a Bubbling Fluidized Bed

Maryam Askarishahi
Research Center Pharmaceutical Engineering GmbH, Inffeldgasse 13/III, Graz, 8010, Austria

Mohammad-Sadegh Salehi and Stefan Radl
Institute of Process and Particle Engineering, Graz University of Technology, Inffeldgasse 13/III, Graz, 8010, Austria

DOI 10.1002/aic.15616
Published online January 31, 2017 in Wiley Online Library (wileyonlinelibrary.com)

Numerical simulations of a gas-particle-droplet system were performed using an Euler-Lagrange approach. Models accounting for (1) the interaction between droplets and particles, (2) evaporation from the droplet spray, as well as (3) evaporation of liquid from the surface of non-porous particles were considered. The implemented models were verified for a packed bed, as well as other standard flow configurations. The developed models were then applied for the simulation of flow, as well as heat and mass transfer in a fluidized bed with droplet injection. The relative importance of droplet evaporation vs. evaporation from the particle surface was quantified. It was proved that spray evaporation competes with droplet deposition and evaporation from the particle surface. Moreover, we show that adopting a suitable surface coverage model is vital when attempting to make accurate predictions of the particle's liquid content. © 2017 American Institute of Chemical Engineers *AIChE J*, 63: 2569–2587, 2017
Keywords: fluidized bed granulation, wet granular matter, CFD-DEM simulation, Euler-Lagrange simulation

Introduction

In various industries such as the petrochemical or the food & pharmaceuticals sector, granulation and agglomeration processes are of key importance. Often, granulation processes are used to stabilize an intermediate of final product, or change product properties, by means of the addition of a liquid binder. Consequently, it is essential to consider wetting, drying, particle shaping, and size enlargement, as well as the homogenization of the product. Fluidized beds are one of the promising tools to integrate all of these features into a single process step, mainly due to the high rate of heat and mass transfer in these devices.[1]

Various phenomena occur in fluidized bed granulators: (1) deposition of droplets on the particle surface due to particle-droplet collisions; (2) evaporation of liquid from the particle surface stemming from the flow of heated gas over the wet particles; and (3) particle agglomeration due to the collision of wet particles. In addition, fluidized beds are characterized by spatio-temporal fluctuations of the flow quantities (e.g., the local particle concentration, the fluid and particle velocity, as well the concentration of vapor or temperature). Since these phenomena are coupled, the overall behavior of a fluidized bed granulator is complex. A variety of approaches for their analysis, of which (1) compartment models, as well as (2) detailed models based on computational fluid dynamics (CFD) are the most important ones.

A comparably large number of researchers use compartment (or zone) models, which strongly simplify the system by utilizing a compartment for each phenomenon. The compartments typically comprise[2]: (1) a spray or wetting zone in which droplets and particles interact[3]; (2) a drying zone in which evaporation from the particles' surface takes place; (3) a non-active zone in which bed temperature and gas humidity fluctuate marginally; and (4) a heat transfer zone, where particles are heated by fluidization gas. These compartment models have been extensively applied for population balance modeling by various researchers, often with good success.[4–9] However, the size of the above mentioned zones are often estimated, and their geometry is based on a number of simplifications: for instance, Link et al.[10] considered the spray zone as a bi-conical region whose size is defined by the injection depth of the jet and spray angle. Fries et al.[11] used a bi-conical zone to estimate the particle residence time distribution in the spray region. Maronga and Wnukowski[2] obtained the temperature and gas humidity distributions experimentally to estimate the above mentioned regions. Börner et al.[12] used a conductivity probe to define the wetting zone and the drying zone in a fluidized bed.

Lower attention was given in previous years to CFD-based models, since the precision of the used model is still fairly low and typical calculation times are in the order of days or even weeks. For example, Sutkar et al.[13] performed CFD-DEM simulations and considered droplets as discrete particles. This previous work used a wet restitution coefficient to account for

Additional Supporting Information may be found in the online version of this article.

Correspondence concerning this article should be addressed to S. Radl at radl@tugraz.at.

droplet-particle interactions. Unfortunately, the evaporation from the spray droplets, as well as particle cooling due to evaporation of the droplets deposited on the particle surface were disregarded in their study. In addition, in the study of wet fluidized bed, the non-uniformity of the droplet distribution on the particle surface was not considered in most studies. However, this non-uniformity plays an important role in the rate of evaporation from the particle surface: Štepánek and Rajniak[14] were one of the first that provided a model for liquid spreading (i.e., a model for "surface coverage") on the particle surface that helps to quantify this effect. While previous modeling approaches were limited, experimental studies presented in the open literature[15–17] are also faced with several constrains in providing local information that could help to clarify the roles of the evaporation phenomena.

Having considered the above studies, it can be concluded that more research seems necessary to better understand the phenomena in a wet fluidized bed. In the current contribution we aim on a purely numerical approach relying on a rigorous CFD-based model. This is motivated by the inability of experimental techniques to provide local information on phase change phenomena (e.g., evaporation). We believe that such a numerical approach, once carefully verified, can be a key tool to probe local phenomena. This is true at least for situations where particles are approximately spherical, have the same size and density, and the system size allows a direct simulation of (primary) particle motion (with primary particles we refer to individual solid bodies in contrast to meso-particles, which can be constituted by multiple primary particles connected by some type of cohesive forces). Exactly this is true for the simulation approach chosen in this work, i.e., the employed CFD-DEM, which has been used with increasing frequency in the recent past by Zhu et al.,[18] Radl et al.,[19] Girardi et al.,[20] Van Buijtenen et al.,[21] and Sutkar et al.[13]. In the present contribution we significantly extend these previous studies by analyzing the distribution of the gas temperature, the liquid content of the particles and the air, as well as the gas humidity. This understanding can be used for a more profound determination of the various zones in the fluidized bed relevant for the widely-used compartment models. Moreover, CFD-DEM simulations allows to extract useful data related to particle-particle (or particle-wall) impact velocities, particles collision angle distribution, or the granular temperature. These data can be utilized in the development of aggregation kernels to be applied in the population balance equation for meso-particle (i.e., agglomerates). Again, this motivates this study which focuses on a quantification of temperature, vapor and liquid distribution in a fluid bed wet granulator.

The overall modeling strategy employed in the present work is as follows: we first implemented all necessary models in the frame of the CFDEM® code to simulate particle-droplet-fluid interaction in a fluidized bed. To keep the model complexity (and hence the number of parameters) low, we focus on non-porous particles. While such particles represent only a small fraction of industrially-relevant systems, this choice allows us to isolate gas-side from intra-particle influence parameters. Furthermore, cohesive inter-particle forces due to liquid bridges were neglected on purpose in the present contribution: we will see that this is justified by the very low liquid content of the particles in our simulations. Second, routines that allows us to perform a local analysis of all relevant phenomena (e.g., droplet deposition, or evaporation) were implemented in CFDEM®. Third, an array of two-dimensional, and explorative (because computationally very expensive) three-dimensional simulations were performed in a bubbling fluidized bed with liquid injection. Interestingly, we find from all of these simulations that particles are wet only in a very small region of the fluidized bed. Thus, cohesive liquid bridge forces will only be relevant in a small fraction of the particle bed, which is in sharp contrast to previous work which often assumed a uniform liquid distribution (e.g., as assumed in Girardi et al.[20] or Sutkar et al.[13]). It is clear that the reason for this is liquid evaporating from the particle surface and the droplet suspended in air—these phase change phenomena obviously play a key role in the overall dynamics of the wet particle bed. Fluid and particle cooling induced by evaporation has been ignored in all relevant previous studies[13,20] we are aware of. This is despite the fact that these cooling effects can affect the distribution of moisture and temperature in the bed, making predictions of, e.g., liquid bridge volume extremely difficult. We will show by an analysis of the rate of evaporation from the droplets, as well as from liquid on the particle surface, the origin of this finding. Furthermore, and to the best of our knowledge, we are the first that quantify in detail the effect of evaporative cooling on the bed behavior. We believe that these pieces of information are of critical importance for the development of simplified models required for a fast estimation of granulation process dynamics, or process control. It should be noted that the present work mainly focuses on gas-particle-droplet interaction in a bubbling fluidized bed. Consequently, the injection velocity was chosen lower than in typical industrial applications to preserve the bubbling characteristics. This leads to longer droplet-in-suspension time scales, and hence droplet evaporation is more pronounced in this study than in a typical industrial application. In addition, the assumption of non-porous particles over-emphasizes evaporation from the particle surface. These facts lead to low LoD, and hence agglomeration would be unlikely to occur in our simulations. Consequently, more research effort would be required to eliminate these constrains so that reasonable LoD values can be predicted, and a real-world fluidized bed granulator can be simulated. This is clearly beyond the current focus, and hence we restrict the current study to systems without agglomeration and low liquid contents.

Our article is structured as follows: in the following section, the governing transport equations, as well as the constitutive equations used for simulation of heat and mass exchange will be described. In the third section, the result of a grid sensitivity study will be presented, followed by an analysis of the effect of model details and operating conditions. Finally, in the last section, the main findings of this study are viewed in the context of available literature, and some thoughts on future research activities are presented.

Mathematical Modeling

In this study, simulations were performed utilizing an extended version of the CFDEM® code.[22] This code is based on an open-source CFD–DEM framework to simulate coupled fluid–particle systems. The motion of the particles is resolved by means of the DEM and simulated using the LIGGGHTS® code.[23] The interstitial fluid flow is resolved through CFD and simulated using the OpenFOAM® code.[24] Key additions to CFDEM® by us include (1) a framework for tracking an arbitrary number of species (and the temperature) in the gas phase, as well as (2) evaporation models. A brief description of the governing equations for the above transport phenomena is presented next.

Fluid phase

Momentum equation for the fluid phase (assumed to consist of air, vapor, and the suspended droplets) is solved based on the well-known Navier-Stokes equation:

$$\frac{\partial}{\partial t}\left(\boldsymbol{u}_f\varphi_f\rho_f\right)+\nabla\cdot\left(\boldsymbol{u}_f\boldsymbol{u}_f\varphi_f\rho_f\right) =-\varphi_f\nabla\cdot\tau_f-\varphi_f\nabla P_f+\Phi_d+\varphi_f\rho_f\boldsymbol{g} \tag{1}$$

Note that the fluid density and viscosity is assumed to be constant and equal to that of air, i.e., we do not consider the effect of suspended droplets and vapor on the fluid's momentum balance. This is justified by the low mass loading (and the very small volume concentration) of droplets and vapor in the system. Specifically, one might want to compute an expected (combined) mass loading of droplet and vapor from the injected amount of liquid and the mass inlet rate of the fluidizing gas $\left(\mu_{liq}+\mu_{vap}\right)_{expected}=\dot{S}_{inj}V_{inj}/uL_{bed}w_{bed}\rho_g$. Here V_{inj} is the volume of the injection region. As long as this expected mass loading is much smaller than unity (one might adopt 0.1 as a threshold), our assumption of negligible effects on the fluid's momentum transport equation will be valid to a first approximation. This is the case for all situations considered in this study.

The term $\Phi_d$is the force exerted by particles on the fluid phase per unit volume, excluding buoyancy effects. In line with previous work and the current understanding in the field, it was assumed that the drag force is the main force contributing to the momentum exchange between gas and particles. These drag forces can be computed using the correlation developed by Beetstra et al.[25] as follows:

$$\Phi_d=-\beta_{sf}\left(\boldsymbol{u}_f-\boldsymbol{u}_p\right) \tag{2}$$

$$\beta_{sf}=18\rho_f\nu_f\varphi_f\left(1-\varphi_f\right)\frac{F\left(\varphi_f,Re\right)}{d_p^2} \tag{3}$$

$$F\left(\varphi_f,Re\right)=10\frac{1-\varphi_f}{\varphi_f^2}+\varphi_f^2\left(1+1.5\sqrt{1-\varphi_f}\right) +\frac{0.413\ Re}{24\varphi_f^2}\frac{\left(\frac{1}{\varphi_f}+3\varphi_f\left(1-\varphi_f\right)+8.4Re^{-0.343}\right)}{\left(1+10^{3\left(1-\varphi_f\right)}Re^{\frac{-1}{2}\left(1+4\left(1-\varphi_f\right)\right)}\right)} \tag{4}$$

Particles

The motion of individual particles is solved using Newtons equation of translational and rotational motion:

$$\rho_{p,i}V_{p,i}\frac{d\boldsymbol{u}_{p,i}}{dt}=\boldsymbol{f}_{cont,i}+\beta_{sf}V_{p,i}\left(\boldsymbol{u}_f-\boldsymbol{u}_{p,i}\right)-V_{p,i}\nabla P_{f,i}+\boldsymbol{g}\rho_{p,i}V_{p,i} \tag{5}$$

$$I_{p,i}\frac{d}{dt}\omega_{p,i}=\boldsymbol{t}_i \tag{6}$$

Where the forces exerted on the particles, as shown on the right hand side of the above equation, include (1) contact, (2) drag, (3) far field pressure, and (4) gravity, respectively. Due to the minute amounts of liquid in the system, we assume that both (1) density and (2) mass of the particles are invariant with time. The contact law is based on a Hertzian interaction model with tangential history tracking. The contact forces in the normal and tangential direction are, respectively, given by

$$\boldsymbol{f}_{cont,i,n}=-k_n\delta_p+\eta_n\Delta u_{i,n} \tag{7}$$

$$\boldsymbol{f}_{cont,i,t}=\min\left\{\left|k_t\int_{t_{c,0}}^{t}\Delta u_{i,t}dt+\eta_t\Delta u_{i,t}\right|,\mu_c\boldsymbol{f}_{cont,i,n}\right\} \tag{8}$$

Here δ_p denotes the particles overlap; k and η represent the stiffness coefficient and damping factor, respectively. These parameters can be calculated as a function of the Youngs modulus Y, the Poisson ratio v, and the coefficient of restitution e. The values of these parameters, as well as of the friction coefficient are reported in Table 2. More details regarding the adopted models can be found in the LIGGGHTS® online documentation[26] (http://www.cfdem.com/media/DEM/docu/Manual.html)

Mass and heat transfer

Due to the temperature difference between the fluid phase, the injected droplets, and the particles, as well as evaporation phenomenon, it is necessary to solve heat and mass transport equations for all relevant species in this system. A key phenomenon is the depletion of the local droplet content due to evaporation. Thus, the transport equation of for the local droplet mass loading needs to be considered, which reads:

$$\frac{\partial}{\partial t}\left(\mu_{liq}\varphi_f\rho_f\right)+\nabla\cdot\left(\boldsymbol{u}_f\mu_{liq}\varphi_f\rho_f\right) -\nabla\cdot\left(D_{eff}\nabla\left(\mu_{liq}\varphi_f\rho_f\right)\right)=-\dot{S}_{evap,f}-\dot{S}_d+\dot{S}_{inj} \tag{9}$$

Here μ_{liq} is the mass loading of the droplets in the gas phase (i.e., the mass of droplets divided by the mass of the gas phase), which equals $\frac{C_{liq}}{\varphi_f\rho_f}$; $\dot{S}_{evap,f}$ is the sink term for evaporation of the spray in the gas phase; $\dot{S}_d$is the rate of droplet deposition on the particle bed, and $\dot{S}_{inj}$ is the source term due to the injection of liquid droplets. The method used for the calculation for these source and sink terms will be described later.

The transport equation for the mass loading of any gas-phase species, in our case water vapor, considering phase change phenomena is given by:

$$\frac{\partial}{\partial t}\left(\mu_{vap}\varphi_f\rho_f\right)+\nabla\cdot\left(\boldsymbol{u}_f\mu_{vap}\varphi_f\rho_f\right) -\nabla\cdot\left(D_{eff}\nabla\left(\mu_{vap}\varphi_f\rho_f\right)\right)=\dot{S}_{evap,f}+\dot{S}_{evap,p} \tag{10}$$

Here the term $\dot{S}_{evap,p}$is the rate of evaporation from the particle surface.

A lumped transport equation for the thermal energy of the fluid phase (i.e., air, vapor, and suspended droplets) can be derived, which is:

$$\varphi_f\rho_fC_{p,f}\frac{\partial T_f}{\partial t}+\nabla\cdot\left(\boldsymbol{u}_f\varphi_f\rho_fC_{p,f}T_f\right)-\nabla \cdot\left(\lambda_{eff}\nabla\left(\varphi_fT_f\right)\right)=-ha_p\left(T_f-T_p\right)-\dot{S}_{evap,f}\Delta H_{evap} \tag{11}$$

The first term on the right hand side of the above equation is the volume-specific rate of heat exchange between the gas phase and the particles. The second term is the sink term due to evaporation of the droplets suspended in the gas phase. Again, we assume that the fluid density and heat capacity is constant and equal to that of air, motivated by the low mass loading of droplets and vapor in the system.

Closure for the Heat Transfer Rate. Parameter h in Eq. 11 is the heat-transfer coefficient, which can be calculated via the Nusselt number correlation developed by Deen et al.[27] for fluidized beds. Thus, we use the following Nusselt number correlation to compute h:

$$Nu=\left(7-10\varphi_f+5{\varphi_f}^2\right)\left(1+0.7Re^{0.2}Pr^{1/3}\right)+\left(1.33-2.4\varphi_f+1.2{\varphi_f}^2\right)Re^{0.7}Pr^{1/3} \quad (12)$$

Here Re is calculated based on the superficial fluid-particle relative velocity; Nu is defined as $\left(hd_p\right)/\lambda_f$. Correspondingly, the equation of heat transfer from or to a single particles is:

$$m_pC_{p,p}\frac{\partial T_p}{\partial t}=hA_p\left(T_f-T_p\right)-\dot{S}_{evap,p}\Delta H_{evap} \quad (13)$$

Note, that the heat of evaporation from the droplets deposited on the particles is taken into account on the particle side only. Thus, evaporation from the particle surface will indirectly affect the fluid's temperature via the coupling of the thermal transport equations of the fluid and particle phase.

Closure for Droplet Evaporation and Liquid Deposited on the Particle Surface. In this study, the rate of droplet evaporation on the particle surface was calculated based on the driving force for transfer of water vapor between the particle and the gas phase. This rate was computed using the saturation density of water vapor at the particle temperature $\rho_{w,Sat}$ as

$$\dot{S}_{evap,p}=|\rho_{w,Sat}-\rho_g\mu_{vap}|a_{dp}\beta \quad (14)$$

Here β is the mass-transfer coefficient which can be calculated based on the Sherwood number defined as $Sh=\left(\beta d_p\right)/D_{vap}$. This coefficient has been calculated in analogy to the heat-transfer coefficient correlation developed by Deen et al.[27] shown in Eq. 12. It should be noted that this correlation condenses to the correct limit (i.e., $Nu = Sh = 2$) for no slip (i.e., $Re = 0$) and an infinitely dilute system (i.e., $\varphi_f = 1$). Hence, we use the same symbol, i.e., β, for denoting the mass-transfer coefficient from the particles and the droplet cloud. Specifically, β is assumed to be constant for all droplets, and $Sh = 2$. This is a realistic assumption, since the droplet volume concentration is very low, and droplets are quickly deposited on particles (i.e., the dependency of Sh and β on φ_f shown in Eq. 12 is assumed to be irrelevant for the droplets; droplets share the same speed as the air).

In Eq. 14, $\rho_{w,Sat}$ can be estimated based on the ideal gas law and the Antoine equation for the vapor pressure of water; a_{dp} is the surface area of the particle that is wetted by the droplets, and hence available for liquid evaporation. Due to the fact that this area is the most difficult parameter to estimate when calculating the particles' evaporation rate, two models were implemented in the code and investigated. The first model assumes that the surface coverage ψ_{liq}, defined as the ratio of the surface area available for evaporation and the surface area of the particle, is linearly related to the dimensionless liquid content as follows:

$$\psi_{liq}=\max\left(0,\ L_p^*-L_{p,noevap}^*\right) \quad (15)$$

Here L_p^* and $L_{p,noevap}^*$ are the volume fraction of liquid on the particle, and a threshold value below which evaporation from the particle surface is impossible, respectively.

The second model considered is that developed by Kariuki et al.,[28] in which the surface coverage is calculated as

$$\psi_{liq}=1-\left[1-f\right]^{\Phi_p/f} \quad (16)$$

Where the parameter f is the fraction of the particle surface coated by a single droplet, and Φ_p is the particle coating number given by

Table 1. Equations for Calculation of Filter Coefficient

$\lambda=\eta_s\frac{3}{2}\frac{\varphi_p}{d_p}$	(T1)
$\eta_s=\frac{St_{eff}^*3.2}{4.3+St_{eff}^*3.2}$	(T2)
$St_{eff}^*=\left[A\left(\varphi_p\right)+1.14Re_m^{\frac{1}{5}}\left(1-\varphi_p\right)^{-3/2}\right]\frac{St}{2}$	(T3)
$A\left(\varphi_p\right)=\frac{6-6\varphi_p^{\frac{5}{3}}}{6-9\varphi_p^{\frac{1}{3}}+9\varphi_p^{\frac{5}{3}}-6{\varphi_p}^2}$	(T4)
$St=\frac{\lvert u_f-u_p\rvert d_d^2\rho_d}{18d_p\nu_f\rho_f}$	(T5)
$Re_m=\frac{\lvert u_f-u_p\rvert\left(1-\varphi_p\right)d_p}{\nu_f}$	(T6)

$$f=\frac{A_{d,projected}}{A_p}=\frac{\frac{\pi}{4}d_d^2}{\pi d_p^2}=\left(\frac{d_d}{2d_p}\right)^2 \quad (17)$$

$$\Phi_p=N_df \quad (18)$$

For the calculation of the rate evaporation of liquid droplets suspended in air the same methodology as for the evaporation from the particle surface was adopted, i.e.,

$$\dot{S}_{evap,f}=|\rho_{w,Sat}-\rho_g\mu_{vap}|\varphi_{liq}a_d\beta \quad (19)$$

Where $\rho_{w,Sat}$ is the saturation density of water vapor in the gas phase at the gas temperature; φ_{liq} is the volume fraction of liquid water in the gas phase; and a_d is the specific surface area of a single droplet given by $a_d=\frac{6}{d_d}$.

Closure for Droplet Deposition. To simulate the deposition of droplets on the particle surface, a clean-bed filter model was adopted from the work of Kolakaluri.[29] Through direct numerical simulation of flow through a packed bed, he developed a correlation for the filtration coefficient as a function of the particle Reynolds Number, the droplet Stokes Number, and the solid volume fraction.[29] In his model, droplet deposition rate can be calculated as

$$\dot{S}_d=-\lambda|\boldsymbol{u}_d-\boldsymbol{u}_p|\mu_{liq}\varphi_f\rho_f \quad (20)$$

Where $|\boldsymbol{u}_d-\boldsymbol{u}_p|$ is the slip velocity between the fluid phase and the particle. The equations required for calculation of the filtration coefficient are summarized in Table 1. It should be noted that the effective droplet Stokes Number St_{eff}^* is calculated based on the true slip velocity, while the mean particle Reynolds Number is calculated using superficial velocity. Thus, we assume that droplets have the same (average) speed as the gas phase. This is justified due to the small droplet diameter, resulting in a very small relaxation time (i.e., ca. 1.2×10^{-3} [s]) of the droplets.

After successful implementation and verification (see Appendix A in Supporting Information) of the above-mentioned models, more than twenty sets of simulations were performed to examine the effect of model details and operation conditions. The results of these simulations will be thoroughly explained in the following section.

Results and Discussion

In wet fluidized beds, due to the interaction among particle, droplet, and fluid, an integral study of such a system appears to be a complex task. Therefore, in this section, the effect and contribution of each phenomenon has been investigated in an isolated manner first. The simulation set up, as well as physical properties and simulation condition for the studied system has been presented in Figure 1 and Table 2. It should be noted

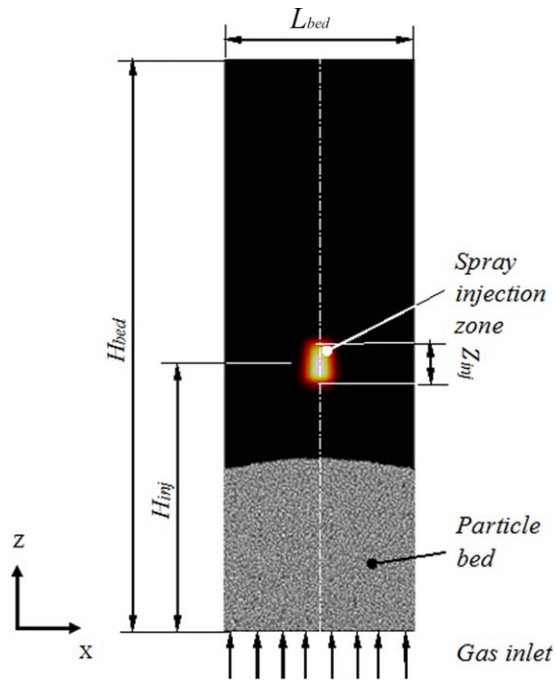

Figure 1. Schematic setup used for the simulation.

[Color figure can be viewed at wileyonlinelibrary.com].

that particles and droplet specifications, as well as operating conditions have been adopted based on a certain industrial application and the experience of our research institute. For instance, the droplet size of 20 μm was chosen, which is a typical size in an industrial application.

Droplets are sprayed on the particles from the top, considering the injection zone. The size of this region was defined such that the relative amount of injected droplets in this region (compared to the particle mass) equals the corresponding value in a typical fluidized bed granulator. Gas and particles are initially considered having the same temperature.

It should be noted that to be able to study the bed behavior in the bubbling regime, the liquid injection velocity was set to ca. two times the fluidization velocity. This is not representative of most industrial applications since in industrial systems the spray injection velocity is chosen often very high, i.e., in the order of 10 (m/s). Such a high injection velocity would destroy the typical fluidization behavior of the particles, and would lead to two large recirculation zones in our simulations. Since our simulation domain only represents a small fraction of a real-world fluidized bed, these recirculation zones are not representative of most industrial applications.

Simulations were performed for 50 s real time for all cases. It took approximately 3 days on six cores of a XEON workstation (Intel® Xeon® CPU "X5680", 3.33 GHz) to complete each 2D case (i.e., approximately 400 CPUhrs/case). For the 3D case we used 32 cores of dcluster.tugraz.at (i.e., a double octo-core cluster relying on Intel® Xeon® "E5-2650" CPUs, 2.0 GHz, InfiniBand Interconnect) for ca. 20 days per case (i.e., approximately 15,000 CPUhrs/case).

Grid sensitivity study

To investigate the independency of the solution on the mesh, several simulations were performed for grid sizes of 1.5 d_p, 2 d_p, and 3 d_p. For the finest grid size, a smoothing model was used to smooth all exchange fields (e.g., the particle volume mapped to the fluid grid) with the smoothing length of 2 d_p. As discerned from Figure 2, refining the computational domain to a value smaller than 2 d_p does not improve the accuracy of results for mass loadings and gas temperature. For the grid size of 3 d_p, small deviations can be observed, especially for the gas temperature and the vapor mass loading near the bed outlet, as well as the spray region. As a result, the grid size of 2 d_p was adopted to achieve high accuracy and low computational cost.

Effect of model details

During the interaction of the three phases (i.e., particles, droplets, and the fluid) in the fluidized bed, a number of phenomena need to be taken into account: for example, the evaporation of the injected liquid will reduce the particles' temperature, which will change the driving force for evaporation. In this section, the role of these phenomena including (1) droplet deposition, (2) the evaporation from the spray's droplet, and (3) from the particle surface in the bed will be studied. This will be done both independently and in connection with other phenomena. In addition, the effect of different models for evaporation from particle surface is evaluated.

Table 2. Physical Properties and Simulation Parameters

	Value/Component	
Parameter	Base Case	Studied range
Bed geometry		
H_{bed} (m)	0.042	–
L_{bed} (m)	0.014	–
w_{bed} (m)	8.4×10^{-4}	$8.4\times10^{-4}-0.014$
H_{nj} (m)	0.021	–
Z_{inj} (m)	0.003	–
L_{inj} (m)	8.4×10^{-4}	–
w_{inj} (m)	8.4×10^{-4}	–
Particle properties		
ρ_s (kg/m^3)	1000	–
d_p (μm)	140	–
N_p	6×10^4	$6\times10^4-10^6$
Contact model	Hertzian, inelastic, with friction and tangential history	
Y (N/m^2)	2×10^5	–
v	0.45	–
$\mu_{c,p}$	1	–
e_{pp}	1	–
$\mu_{c,w}$	0.5	–
e_{wp}	0.3	–
T_{p_0} (K)	335	–
$C_{p,p}$ (J/K)	385	–
LoD_{init}	0.0	0.0–0.334
Spray properties		
ρ_d (kg/m^3)	1000	–
d_d (μm)	20	–
μ_g (Pa.s)	1.79×10^{-5}	–
t_{evap} (s)	1.1×10^{-6}	–
u_{inj} (m/s)	0.06	–
$\dot{m}_{inj}$ (kg/s)	2.14×10^{-9}	1.28×10^{-10} to 1.80×10^{-6}
Gas phase properties		
ρ_g(kg/m^3)	1.188	–
μ_g (Pa.s)	1.79×10^{-5}	–
T_{g_0} (K)	335	–
T_{g_i} (K)	335	305–335
u (m/s)	0.026	–
Wall boundary condition	Slip	–
Simulation parameters		
Δt_{CFD}(s)	1.25×10^{-3}	–
Δt_{DEM}(s)	5×10^{-5}	–
t_{sim}(s)	50	–

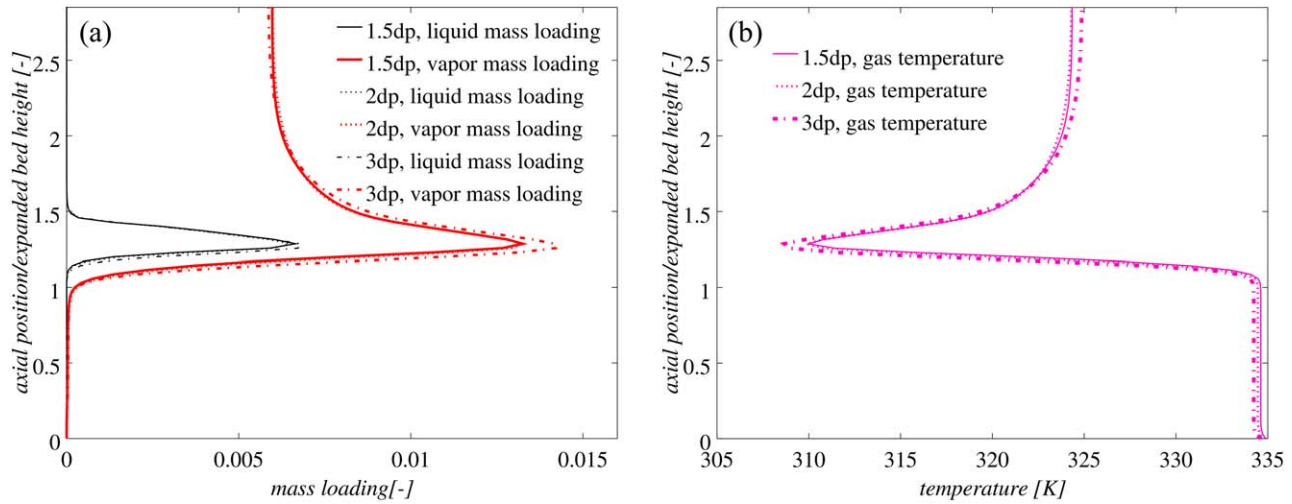

Figure 2. Comparison of time-averaged (a) mass loadings and (b) temperatures along the bed for various grid sizes (data is taken from $x = 7$ [mm], i.e., at the center of the bed).

[Color figure can be viewed at wileyonlinelibrary.com].

The Effect of Involved Phenomena. The contributions of involved phenomena have been investigated through simulation of four cases according to Table 3. It should be mentioned that in Case B, no droplet deposition and zero initial LoD will result in no evaporation of liquid from the particles' surface.

Comparing the exchange rates in Figure 3a–c demonstrates that the rate of spray evaporation is two orders of magnitude larger than the rates of droplet deposition and evaporation from particle surface. Thus, the spray evaporation is hardly affected by particle-related phenomena in Cases A–C. Nonetheless, in the case of no spray evaporation, i.e., Case D, the deposition rate is two orders of magnitude higher in comparison to its rate in the case with spray evaporation. This proves that droplets are consumed due to the deposition since both phenomena depend on droplet concentration. In addition, when neglecting spray evaporation, the rate of evaporation from the particles increases. This is due to a lower vapor mass loading, and consequently the higher driving force for evaporation. It can be concluded that the evaporation from suspended droplets (i.e., the spray) competes against the droplet deposition on one hand, and the evaporation from the particle surface on the other hand.

Regarding the phenomena occurring on the particle surface in Cases A and C, it can be clearly seen that the deposition rate is not influenced by evaporation from the particle surface. This is due to the fact that the main driving force for deposition is the liquid mass loading in the air. Also, it can be seen from Figure 3a that the rate of deposition and evaporation from the particle surface match each other (in a time-average sense) after a few seconds. Thus, the rates of deposition and evaporation adjust rather quickly to their quasi steady state values. At such a quasi steady state, particle deposition and evaporation rates must match each other, since the particles were assumed to be non-porous in this study. Clearly, for Case C (in which we model deposition, but no evaporation from the particle surface) we expect a slow increase of the particles water content, which is confirmed by our data shown in Figure 4c.

Another point discerned from Figure 3 is that the droplet deposition rate fluctuates strongly, i.e., by two orders of magnitude. This is explained by the bubbling nature of the fluid bed granulator, and the fact that the deposition rate strongly depends on the local solid volume fraction.

To compare the exchange rates in a more quantitative way, the integral exchange rates, normalized with the liquid injection rate, have been presented in Table 4. Thereby, normalized quantities are indicated by an asterisk. These rates have been time-averaged over the last 30 s of simulation time, in which the flow was already in the quasi steady state. The mass is conserved in all cases for both liquid and vapor within a maximum error of 1.92% (see rightmost column). As mentioned before, almost matching rates of deposition and evaporation from the particle surface are predicted. However, the droplet evaporation is clearly the dominant phenomenon in the studied cases. In case this phenomenon is not considered, only 11% of the liquid evaporates, and significant mass losses are induced (see the significant increase in the dimensionless liquid mass flow at the outlet).

To gain a deeper insight into the contribution of the investigated phenomena, an analysis via characteristic time scales can be useful. Unfortunately, such an analysis is not straightforward since the involved phenomena occur in different regions of the fluidized bed. However, we have attempted to estimate key time scales by considering ideal compartments in the system, for which we have summarized results in Table 5. A comprehensive description of method to calculate characteristic time scale for each phenomenon has been provided in Appendix B in the Supporting Information. Most importantly, the calculated characteristic time for the droplet deposition is much smaller than the corresponding value for the spray evaporation. Thus, one might argue that droplets are quickly deposited, and hence only little evaporation can occur from air-suspended droplets. The predicted trend using CFD-DEM seems to be opposite, although: clearly, droplet evaporation is the dominating phenomenon. The trend seen in the CFD-DEM

Table 3. Investigated Phenomena in Various Cases

Case	Droplet Deposition	Spray Evaporation	Evaporation from Particle
A	✓	✓	✓
B	×	✓	×
C	✓	✓	×
D	✓	×	✓

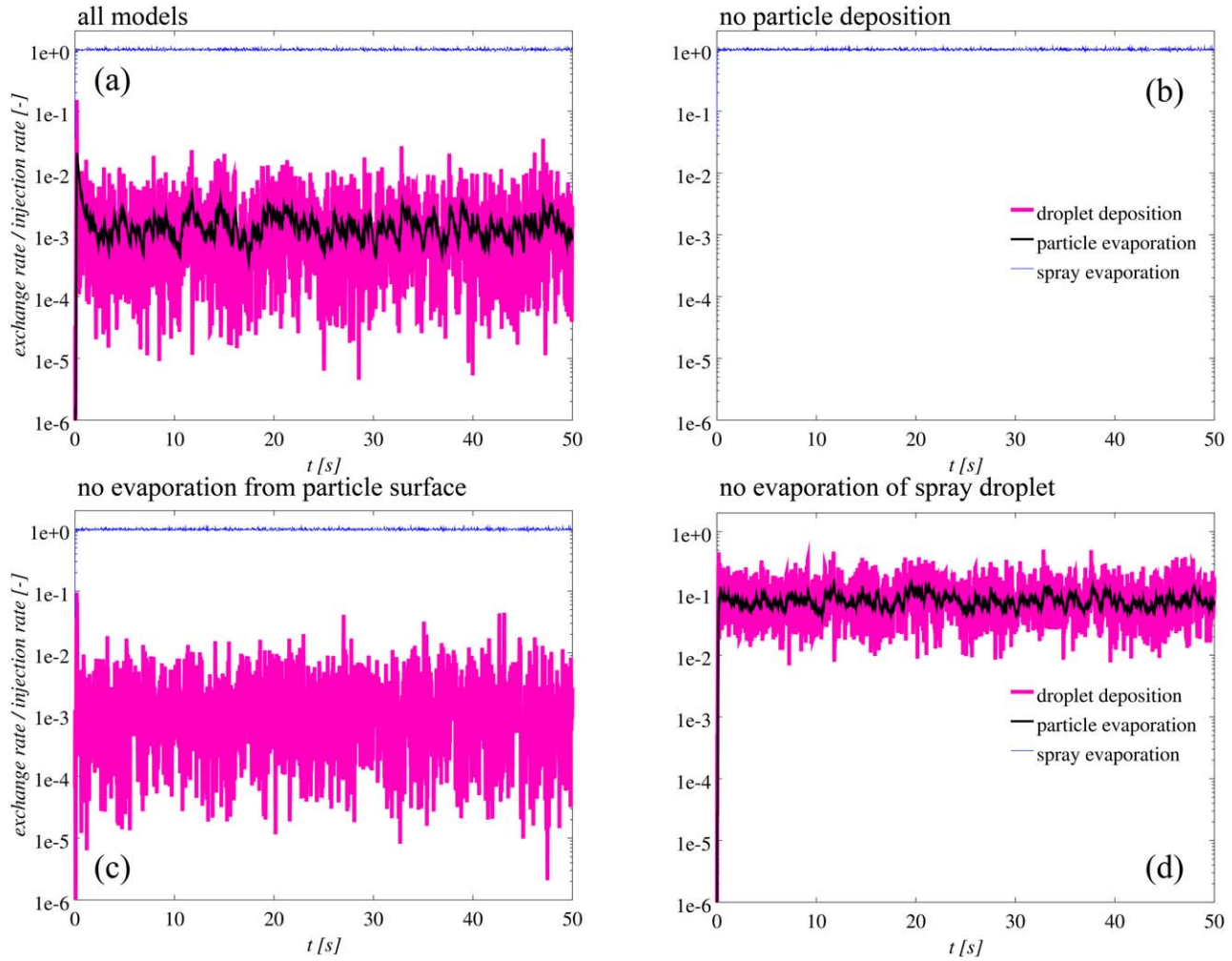

Figure 3. Comparison of exchange rates for cases with (a) all models (case A), (b) no droplet deposition (case B), (c) no particle evaporation (case C), and (d) no evaporation from droplets in the spray (case D).

[Color figure can be viewed at wileyonlinelibrary.com].

simulation can be explained by the fact that the droplets injected in the spray region can evaporate significantly during their downward movement. Hence, there are simply no droplets that can deposit on the particles surface left. We note in passing that the average time that droplets need to collide with the particle bed before deposition is around 7.1×10^{-2} s (we have used the droplet injection speed, as well as the height difference $H_{inj-bed}$ between the injection region and the bed surface to estimate this time scale). This duration is much larger than the characteristic time for spray evaporation, i.e., 1.3×10^{-2} s. Thus, indeed, the droplets seem to have enough time to evaporate before they have a chance to meet particles moving in the system. It is now easy to identify a dimensionless "droplet-in-suspension" time $\tau_{d,susp}$ that governs whether droplet evaporation is relevant or not:

$$\tau_{d,susp}=\frac{H_{inj-bed}/u_{inj}}{t_{d,evap}}=\frac{H_{inj-bed}\ \rho_g}{u_{inj}\ \rho_d}\frac{4\ D_{vap}\ \mu^{eq}}{d_d^2} \qquad (21)$$

It should be noted that the evaporation time has been calculated based on the mass balance for vapor, and hence this characteristic time is independent from nozzle type and arrangement. In contrast, the droplet-in-suspension time is also a function of nozzle distance from the bed surface. Consequently, for nozzle arrangements different from the one studied here (e.g., a bottom-spray configuration) the calculation of this time scale without detailed simulations is not possible. This is because there is not defined distance between the bed surface and the spray region. The droplet-in-suspension time scale is indirectly affected by the nozzle type via the droplet diameter and the droplet injection speed.

To summarize, it is of critical importance to consider the nozzle position relative to the bed, and the speed of the injected droplets. Clearly, the spray should be located closer to the bed surface, or the velocity of droplet injection should be increased, in case one aims on inducing a fast deposition of droplets on the particle surface. Such a situation would be indicated by $\tau_{d,susp} < 1$, i.e., the time droplets are suspended in air is smaller than a characteristic time for their evaporation.

Comparing the characteristic times for mass exchange between the particles and the fluid in Table 5, droplet deposition occurs faster than the evaporation from the particle surface. Of course, the rates have to match in a quasi steady state, as reported in Table 4. The physical meaning of the differences in the above time scales, i.e., that the dynamics of droplet deposition are much faster, is a fact that has been already observed in connection with Figure 3a.

Aiming at investigating the effect of the studied phenomena on the bed performance in terms of heat and mass exchange,

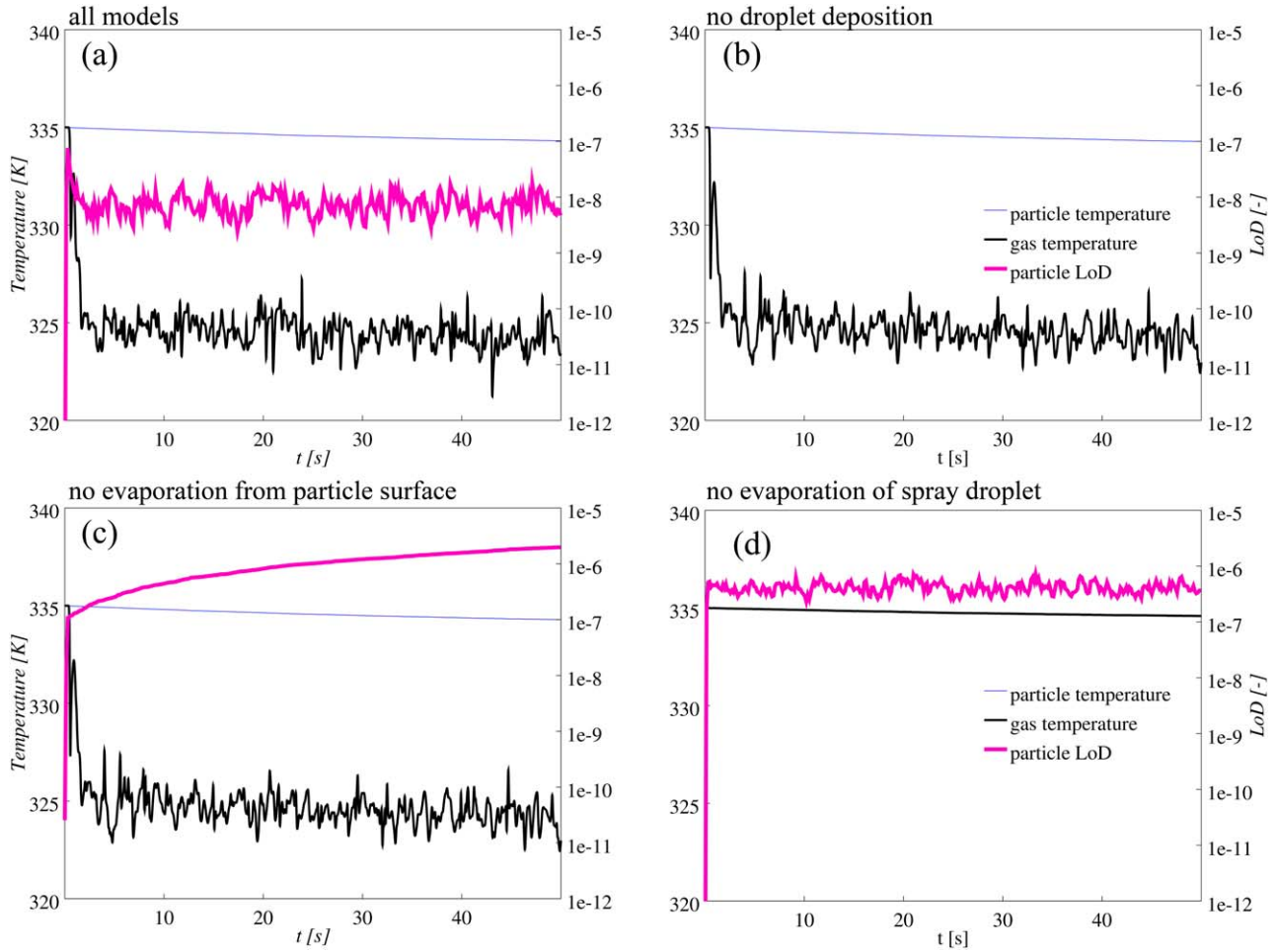

Figure 4. Comparison of mean particle temperature and LoD as well as gas outlet temperature for cases with (a) all models (case A), (b) no droplet deposition (case B), (c) no particle evaporation (case C), and (d) no droplet evaporation (case D).

[Color figure can be viewed at wileyonlinelibrary.com].

the predicted mass loadings, temperatures, and LoD have been plotted in Figures 4 and 5. As seen in Figure 4, in all cases in which the droplet evaporation is considered, the gas temperature drops drastically within a few seconds. In contrast, the particle temperature has a dynamic behavior that differs significantly from that of the gas, and hence the particle temperature decreases very slowly. This can be attributed to two facts: (1) the gas is quickly cooled due to the high rate of evaporation in the spray region (which is located near the bed surface). Thus, the cooled gas leaves the bed without being in intense contact with the particles. (2) The mass (and hence the heat capacity) of gas in the system is much smaller than that of the particles.

Another interesting observation is connected to the predicted temperature profiles along the bed. As shown in Figure 5a, a sharp decrease of the gas temperature occurs near the top of the bed. This temperature jump is absent in case evaporation from air-suspended droplets is not considered (see Figure 5b). In the dense region (i.e., the bubbling bed), however, the gas temperature is approximately constant although a marginal decrease near the bottom of the bed (i.e., the gas inlet) was predicted for both cases (i.e., with or without evaporation from the spray). Therefore, we conclude that the particle temperature is mainly governed by the evaporation of liquid from the particle surface, and not by the evaporation from the air-suspended droplets.

Comparison of the predicted LoD between Cases A and D reveals that spray evaporation results in lower LoD. This is owing to the fact that a lower amount of liquid is available for droplet deposition. However, in the case with no evaporation from the particle surface (i.e., Case C), the particle LoD

Table 4. Comparison of Time-Averaged (Normalized) Integral Exchange Rates, as well as Outlet Mass Loadings for Various Cases at the Quasi Steady State

Case	$\dot{m}_{liq,out}{}^{*}$	$\dot{m}_{Vap,out}{}^{*}$	$\dot{S}_{evap,d}{}^{*}$	$\dot{S}_{dep}{}^{*}$	$\dot{S}_{evap,P}{}^{*}$	$E_{conservation}$ (%)
A	0	1.01	1.00	1.80×10^{-3}	1.5×10^{-3}	1.00
B	0	1.01	1.00	0	0	1.00
C	0	1.01	1.00	1.92×10^{-3}	0	1.92
D	0.92	7.81×10^{-2}	0.00	9.1×10^{-2}	0.11	1.01

Table 5. Comparison of Characteristic Times for Various Phenomena Taking Place in a Wet Fluidized Bed by Considering a Domain-Averaged Deposition Rate ($\psi_{liq}=4.3\times10^{-7}$)

Saturation time scale	$t_{v,evap}=\frac{d_d^2}{12\ D_{vapor}\,{}^{\rho_g}/_{\rho_d\mu_d}}$	3.61×10^{-2}
Droplet evaporation time scale	$t_{d,evap}=\frac{\rho_d}{\rho_g}\frac{1}{4}\frac{d_d^2}{D_{vapor}}\frac{1}{\mu^{eq}}$	1.3×10^{-2}
Liquid-on-Particle evaporation time scale	$t_{evap,p}=\frac{1-\varphi_p}{\varphi_p}\frac{d_p^2}{6\ Sh\ D_{vapor}\psi_{liq}^{eq}}$	3.66×10^{-2}
Droplet deposition time scale	$t_{depos}=\frac{1}{\lambda\lvert u_f-u_p\rvert}$	3.15×10^{-3}

increases approximately linearly over time. This is due to the fact that the droplet evaporation rate is almost constant with rather insignificant fluctuations. Consequently, an approximately constant amount of liquid is available for deposition on the particles.

It should be noted that the predicted LoD is much smaller than its value in typical industrial applications. This difference can be explained by the fact that the rate of evaporation from the particle surface is over-predicted in this simulation: in industrial systems the liquid may be trapped in the particles' pores, where the rate of evaporation is controlled by vapor diffusion. In addition, in this study, the droplet injection velocity is relatively low so that we can observe the system in the bubbling regime. Hence, the spray droplets spend more time evaporating before interacting with the particles, so the deposition rate drops owing to the reduction in the liquid mass loading. Finally, the fluidization gas has been considered completely dry, while in physical systems the air is often humid.

A more detailed examination of the temperature profiles along the bed, as shown in Figure 5 manifests that the gas temperature is approximately constant along the dense bed for both Cases A and D. However, the temperature dramatically decreases up to the spray zone center for the case with droplet evaporation (see Figure 5a), followed by an increase with lower slope due to a locally smaller droplet volume fraction. The latter results in a lower driving force, and also mixing with the hot fluidization gas seems more intense in this region. It should be mentioned that the predicted trend for the temperature and the mass loading in all cases were similar except in Case D with no spray evaporation. As discerned from Figure 5, at $x=3.5$ mm, which is off the center of the fluidized bed and hence outside of the spray region, the gas temperature is higher. Also, the evaporation rate is lower in comparison to the corresponding values at the center position (i.e., $x=7$ mm), even though the outlet gas temperature is eventually the same at both lateral position. As depicted in Figure 5a, virtually no spray loss was predicted, in contrast to the case without droplet evaporation (Figure 5b).

Another point discerned from Figure 5 is that the liquid and vapor mass loadings approach a local maximum in the spray zone center in the case with spray evaporation. Also, the liquid is completely consumed near the bed surface due to the deposition and the evaporation in all cases, as seen from the distribution of the droplet concentration and particles in Figure 6a,c. As observed in Figures 6a, 7, and 8, droplets are rapidly deposited on the particles moving near the bed surface, and droplets are completely consumed in this region due to deposition and evaporation. The droplets' penetration length is very short, especially for the case with spray evaporation, as visible from the distribution of the particles' liquid content shown in Figure 9a (note that we used a logarithmic scale in Figures 9 and 10, and that the ranges of the color-bars for panels a, b, c in Figure 9 are different). This results in the formation of a region with high vapor content near the top of the dense bed surface, as depicted in Figures 5 and 6b (for the latter see the discussion in the next paragraph). Again, it appears that liquid evaporating from the particle surface does not significantly affect the outlet vapor mass loading in most cases: the predicted maps of liquid content shown in Figures 9a and 10a,b indicate that this evaporation rate is not a limiting factor. However, in case particles have initially a high wetness (see Figure 8d, as well as Figure 9c), or the evaporation of air-suspended droplets is not considered (see Figure 8b, as well as Figure 9b), evaporation from the particle surface plays a certain role.

To have a better understanding of phenomena taking place in the bed, contour-plots of source terms for various cases and scalar quantities for Case A have been depicted in Figures 6–9

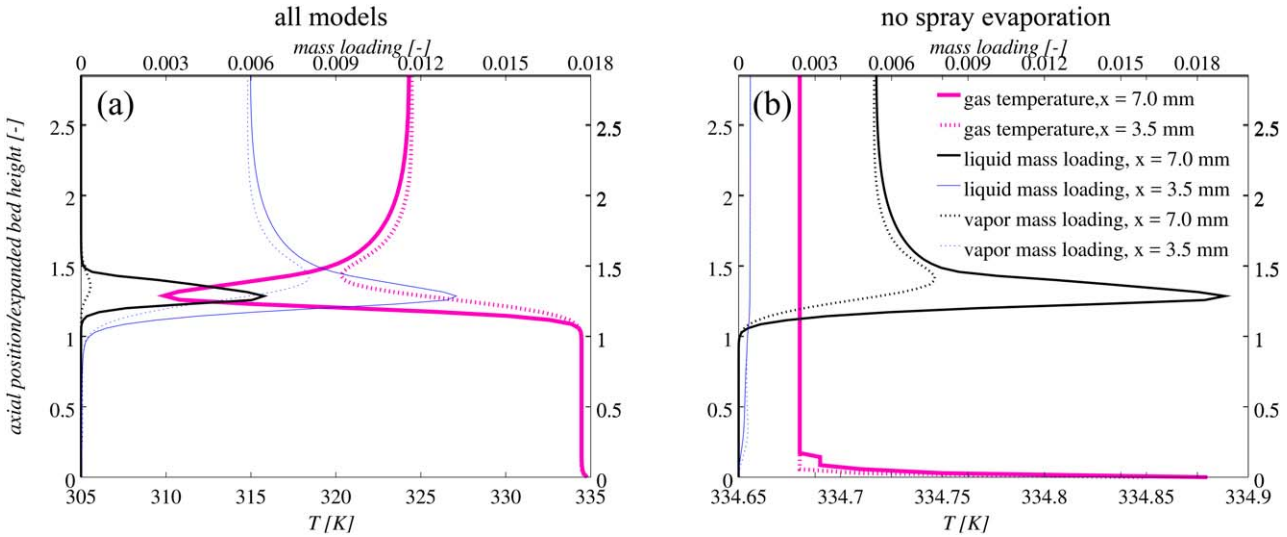

Figure 5. Comparison of time-averaged gas temperatures and mass loadings along the bed for cases with (a) all models and (b) no droplet evaporation.

[Color figure can be viewed at wileyonlinelibrary.com].

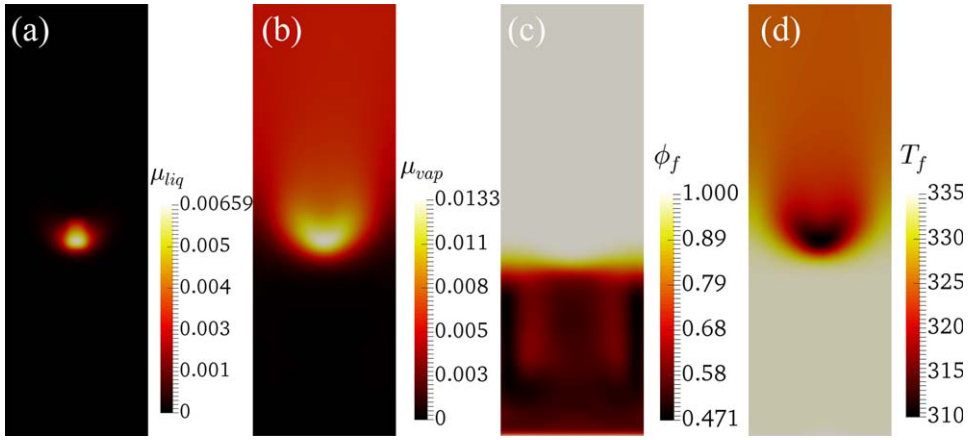

Figure 6. Predicted contour plot at the bed cross section at $Y = 0$ for scalar quantities in case A (i.e., using all models; a: liquid mass loading, b: vapor mass loading, c: voidage, d: gas temperature).

[Color figure can be viewed at wileyonlinelibrary.com].

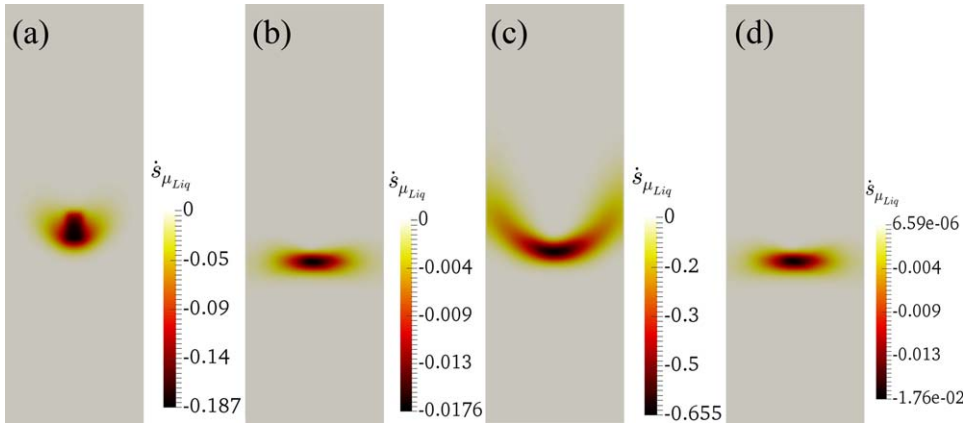

Figure 7. Predicted contour plot at the bed cross section at $Y = 0$ for the liquid exchange rate for cases with (a) all models, (b) no droplet evaporation, (c) highest injection rate, and (d) highest initial LoD (all data shown is time-averaged).

[Color figure can be viewed at wileyonlinelibrary.com].

for the bed cross section at $Y = 0$. Comparing the source terms in Figures 7a and 8a, droplets are mainly consumed due to droplet evaporation, whereas the formation of vapor due to evaporation from the particle surface is negligible. The predicted contour-plots for the vapor mass loading and the bed voidage in Figures 6b,c also support this observation. It can be

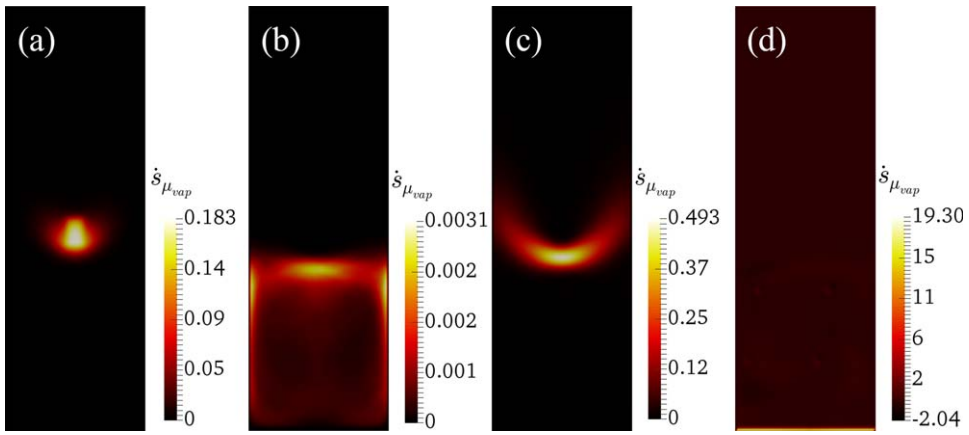

Figure 8. Predicted contour plot at the bed cross section at $Y = 0$ for vapor exchange rates for cases with (a) all models, (b) no droplet evaporation, (c) highest injection rate, and (d) highest initial LoD (all data shown is time-averaged).

[Color figure can be viewed at wileyonlinelibrary.com].

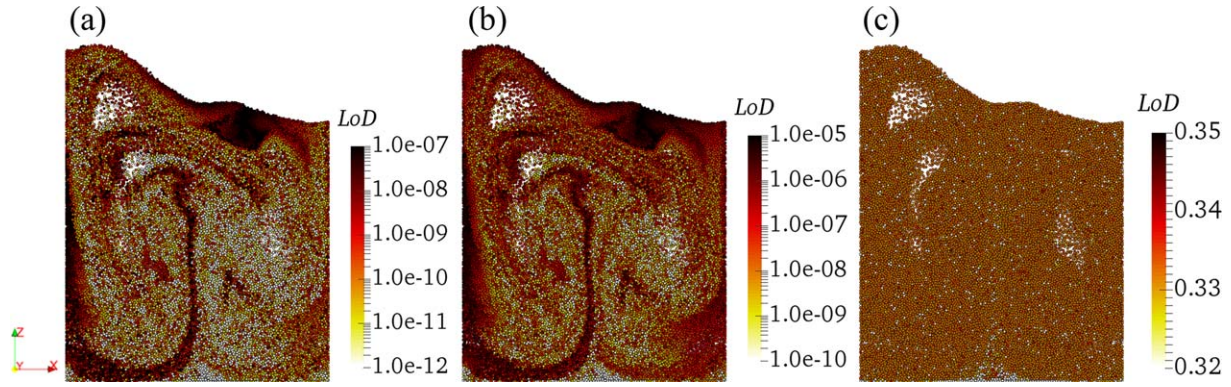

Figure 9. Instantaneous particle liquid content for cases with (a) all models (case A), (b) no droplet evaporation (case D), and (c) initial surface coverage of 0.5.

[Color figure can be viewed at wileyonlinelibrary.com].

also seen in Figure 6d that the temperature decreases significantly in the region between the freeboard and the spray zone, which is associated to spray evaporation.

When neglecting droplet evaporation, i.e., in Case D (see Figures 7b and 8b), the liquid droplets are consumed near the bed surface due to deposition. The distribution of the source term for vapor (Figure 8b) is now significantly different, and indicates a similarity to the circular flow pattern of particles in the bubbling bed. In detail, the particles which manage to reach the freeboard will filtrate the droplets out of the air. After the bubbles carrying these particles burst, the particles will move laterally toward the wall, and then flow downward. After reaching the bottom of the bed, these particles will be again carried upwards due to bubble wake phenomena. This flow can form a circulation pattern for the solid movement in the bed. During the movement of particles in such a way, their

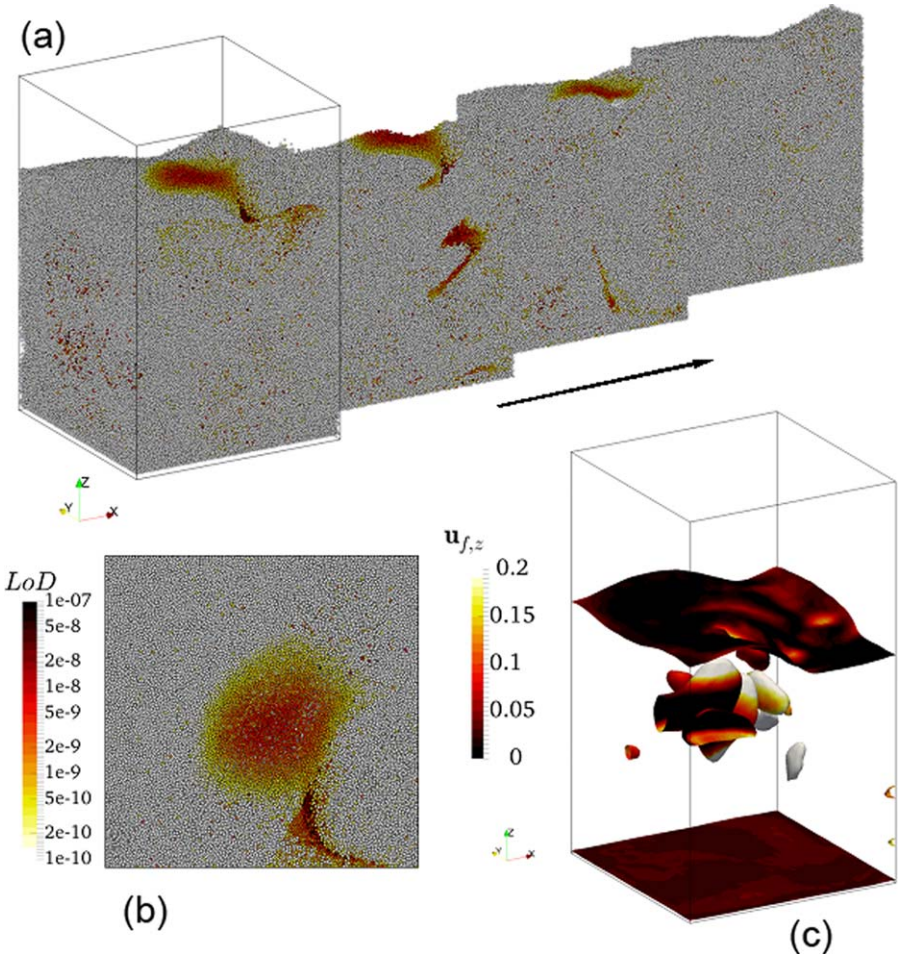

Figure 10. Instantaneous particle liquid content for the 3D case for (a) a sliced-up version of the 3D simulation, (b) a top view, and (c) isocontours of at $\phi_f = 0.8$ colored by the fluid's vertical speed.

[Color figure can be viewed at wileyonlinelibrary.com].

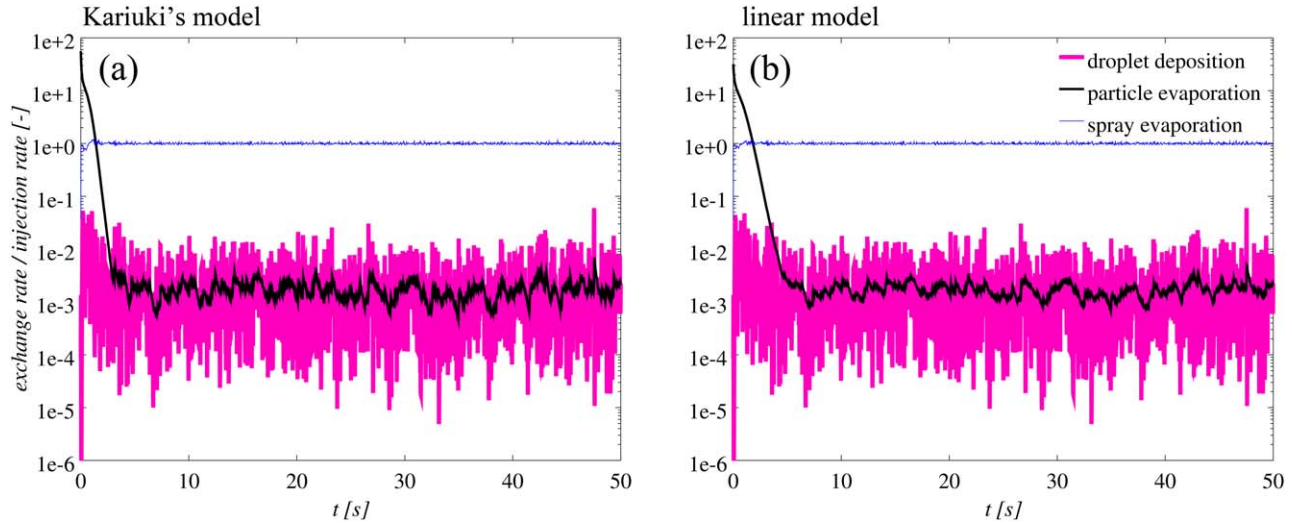

Figure 11. The predicted exchange rates using maximum averaged initial LoD for (a) Kariuki's Model and (b) the linear model.

[Color figure can be viewed at wileyonlinelibrary.com].

LoD gradually decreases due to the evaporation induced by the contact with the hot dry gas entering the fluidized bed.

The Effect of the Surface Coverage Model. The rate of evaporation from particles plays an important role when computing the LoD, and this rate is highly dependent on the area available for the evaporation on the particle surface. Therefore, two surface coverage models were implemented in the CFDEM® code, and their effects were examined. Furthermore, the effects of initial particle liquid content on the equilibrium LoD and the associated exchange rates were evaluated. In detail, the initial LoD was set to the value close to (1) the equilibrium value of LoD calculated based on the droplet mass loading in the injection zone, (obtained as a function of injection rate, gas flow rate, and injection zone volume) i.e., LoD=3.1 $\times 10^{-4}$; (2) the particle-averaged equilibrium value of LoD calculated based on a domain-averaged deposition rate and the number of particles in the bed, i.e., LoD=2.1$\times 10^{-7}$; and (3) the value of LoD calculated based on a given surface coverage of 0.5, i.e., LoD=0.334. More details about the calculation of the initial LoD for each case can be found in Appendix C.

The results of the above described simulations have been depicted in Figures 11–13, respectively. As discerned from these figures, for a specific surface coverage model, i.e., the linear model (right panel) or Kariuki's model (left panel), a higher initial LoD results in a higher rate of droplet deposition. This is due to the fact that higher initial LoD causes larger evaporation rates from the particle surface, such that the driving force for spray droplet evaporation is suppressed. This results in higher droplet mass loading of the air, and consequently a higher deposition rate. In contrast, and as depicted in Figures 14 and 15, the predicted quasi steady state LoD is approximately in the same order of magnitude and is within 25.4% of our results for the base case, i.e., Case A when using Kariuki's model, for different initial LoDs but identical injection rates.

Comparing the deposition rate for the case with different initial LoDs in Figures 11–13, it can be concluded that for an initially higher LoD, the particle evaporation rate exceeds the

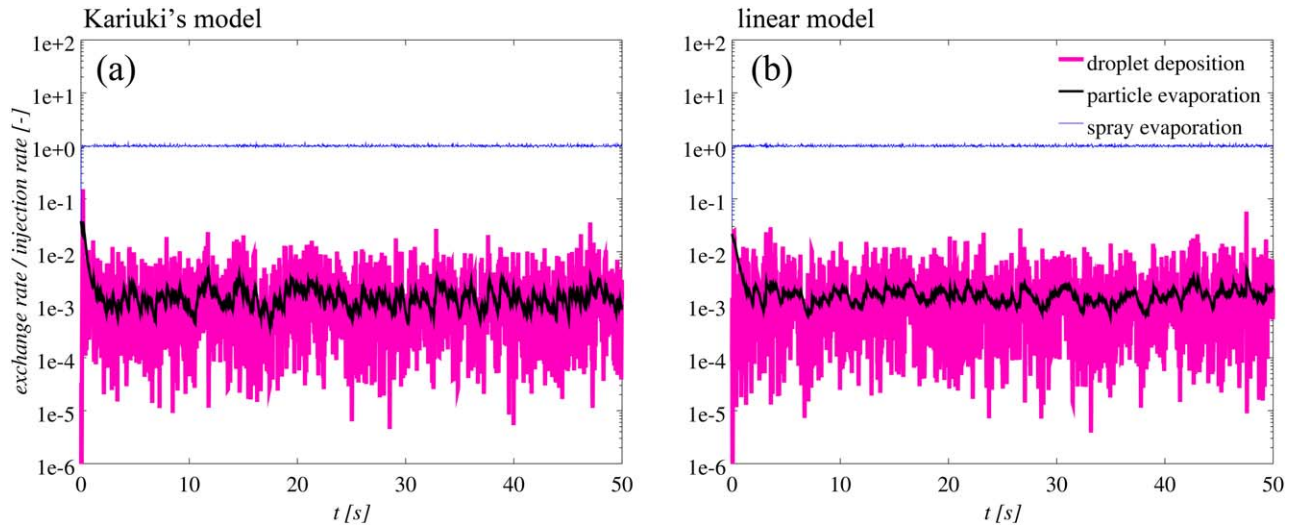

Figure 12. The predicted exchange rates using mean initial LoD for (a) Kariuki's model and (b) the linear model.

[Color figure can be viewed at wileyonlinelibrary.com].

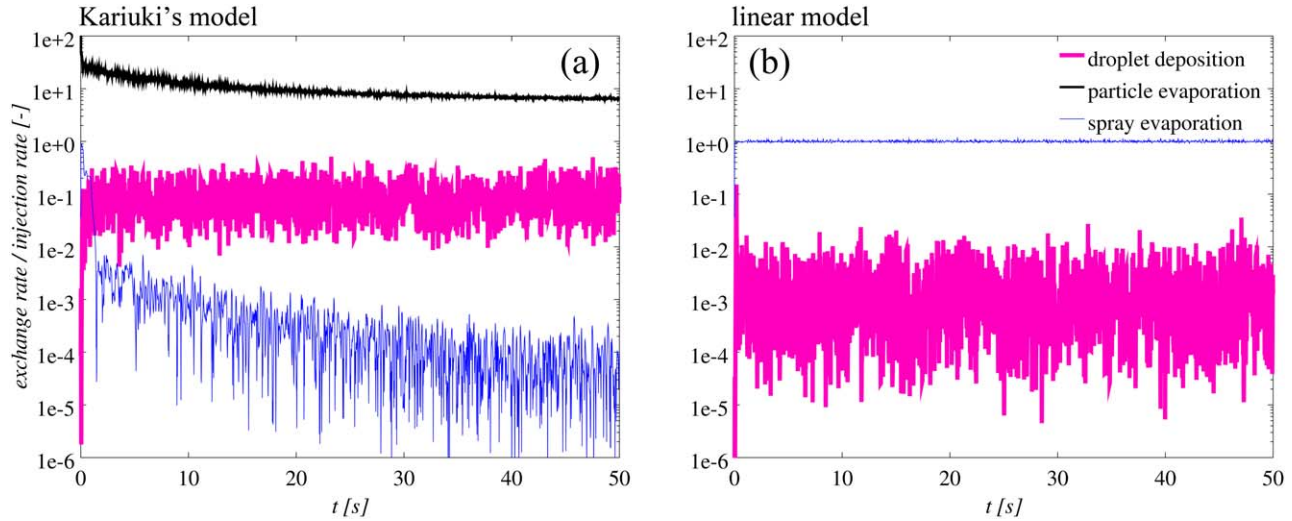

Figure 13. The predicted exchange rates using initial LoD corresponding to surface coverage of 0.5 for (a) Kariuki's model and (b) the linear model.

[Color figure can be viewed at wileyonlinelibrary.com].

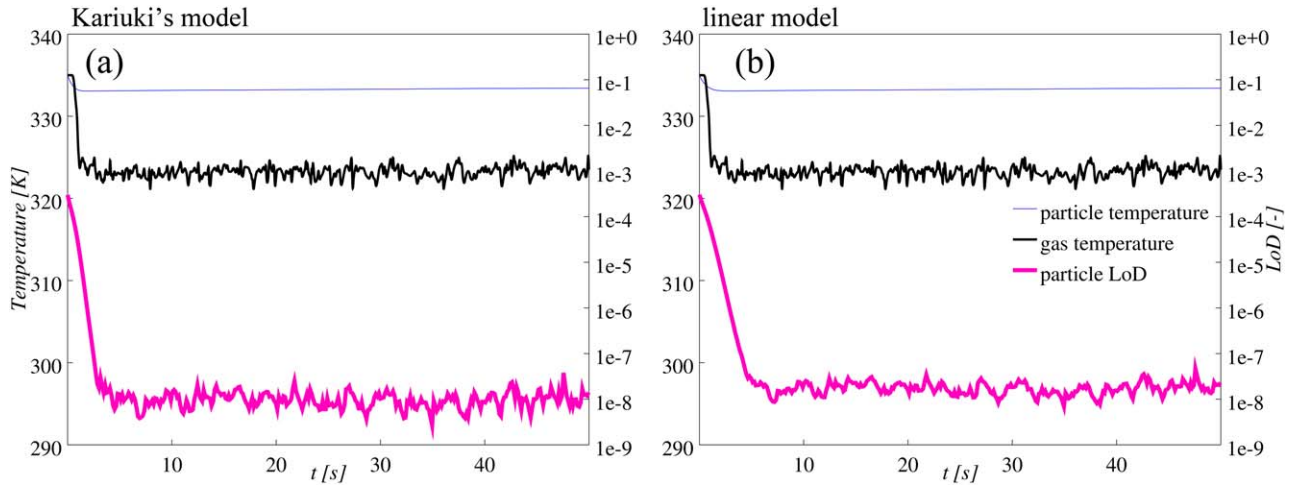

Figure 14. The predicted temperature and LoD using maximum averaged initial LoD for (a) Kariuki's model and (b) the linear model.

[Color figure can be viewed at wileyonlinelibrary.com].

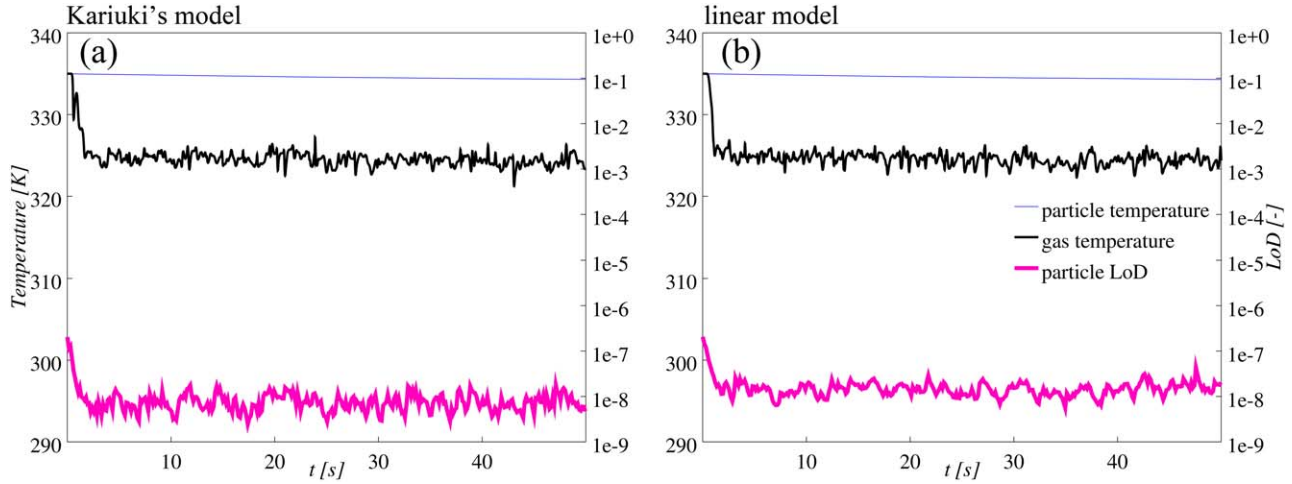

Figure 15. The predicted temperature and LoD using mean initial LoD for (a) Kariuki's model and (b) the linear model.

[Color figure can be viewed at wileyonlinelibrary.com].

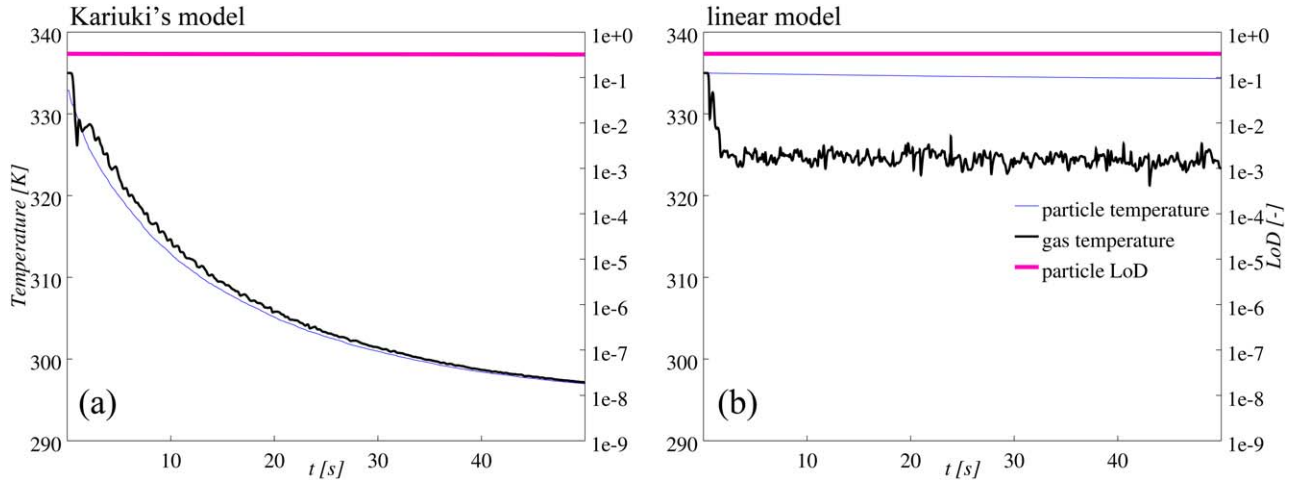

Figure 16. The predicted temperature and LoD using initial LoD corresponding to surface coverage of 0.5 for (a) Kariuki's model and (b) the linear model.

[Color figure can be viewed at wileyonlinelibrary.com].

droplet deposition rate due to the larger wet surface area in the fluidized bed. In this case, the droplet deposition occurs only near the free interface and is limited by the injection rate of droplets. Besides, decreasing the driving force, the evaporation from particle surface discourages spray evaporation, which makes liquid more available for the droplet deposition.

In case of using a very high value for the initial LoD, as shown in Figure 13a, the highest rate for the evaporation from the particles was predicted. This is because of the larger surface coverage and smaller characteristic time (see Table 5: the time scale for evaporating liquid on the particle surface is inversely proportional to the surface coverage). In the case of strong evaporation from the particle surface the rate of the droplet evaporation, as depicted in Figure 7d, is suppressed. This is due to the low gas temperature, and saturated air stemming from the evaporation from the particle surface. In this case, and when considering Figure 16a, the predicted mean particle temperature and the outlet gas temperature decrease with almost the same rate. This is due to the mixing of cool particles with the hot gas in the dense bed. Also, it can be observed that the gas temperature fluctuates marginally due to the fluidized bed nature in this case. In addition, high initial LoDs lead to higher liquid mass loading, and a high rate of evaporation from the particle surface in the bed, as shown in Figure 8d. Consequently, a large amount of water vapor is released in the system. Also, for this situation, the condensation of water vapor near the bed surface was predicted. This means that, in this region, the rate of evaporation from particles is so high that the vapor mass loading can exceed the corresponding saturation value in the gas phase. Consequently, the driving force for the droplet evaporation will be reversed. It should be mentioned that the relative velocity between the gas and the solid enjoys the highest values near the bed surface. Hence, the mass-transfer coefficient, and accordingly the evaporation rate are highest near the bed surface.

Also, it should be noted that a very slow decrease in the LoD was predicted in the case with highest initial LoD, as depicted in Figure 16a,b. Thus, a significantly larger simulation time would be required to understand the full dynamics of the drying process. An appropriate approach to overcome the high computational cost is to use simple 1D or 0D model to capture phenomena with such a long time scale.

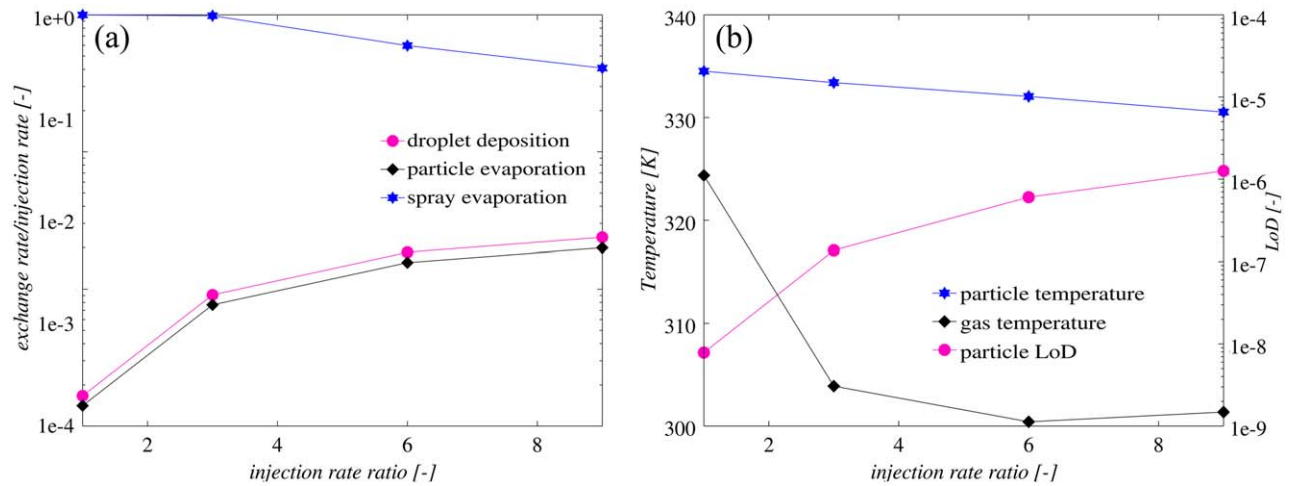

Figure 17. The effect of the liquid injected rate on the normalized exchange rates (panel a), the gas and particle temperatures, as well as the LoD (panel b).

[Color figure can be viewed at wileyonlinelibrary.com].

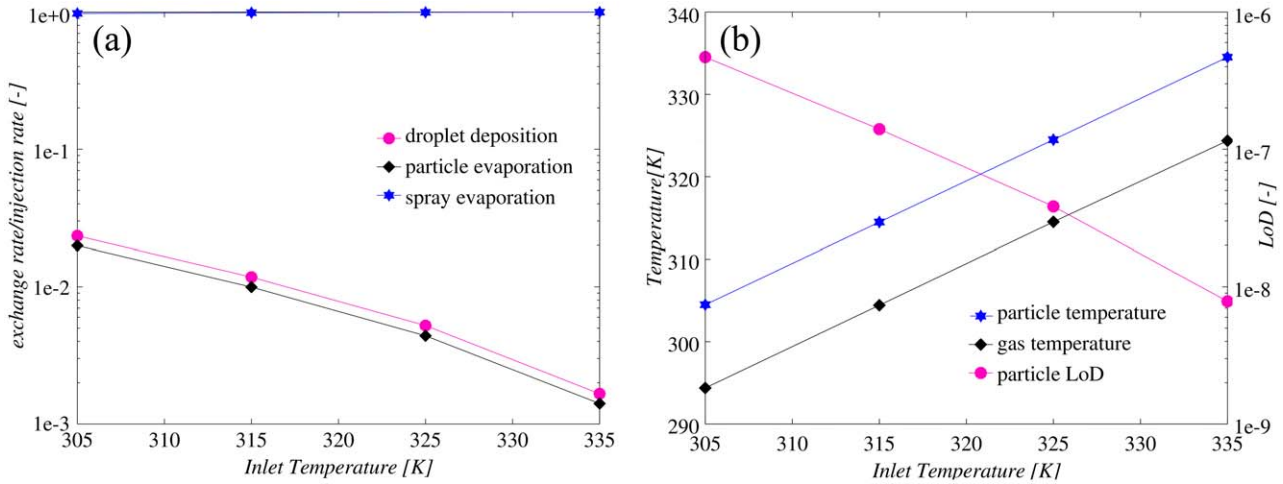

Figure 18. The effect of the inlet temperature on the normalized exchange rates (panel a), the gas and particle temperatures, as well as the LoD (panel b).

[Color figure can be viewed at wileyonlinelibrary.com].

Unfortunately, such a modeling approach was not in the focus of the present contribution, but can be followed in future work. Specifically, one could simplify the expressions presented in our mathematical model for mass and heat transfer, as well as derive a transport equation for the liquid deposited on the particles. Such transport equations would have to include a term accounting for transport due to dispersion by unresolved fluid or particle motion in case a 1D approach is

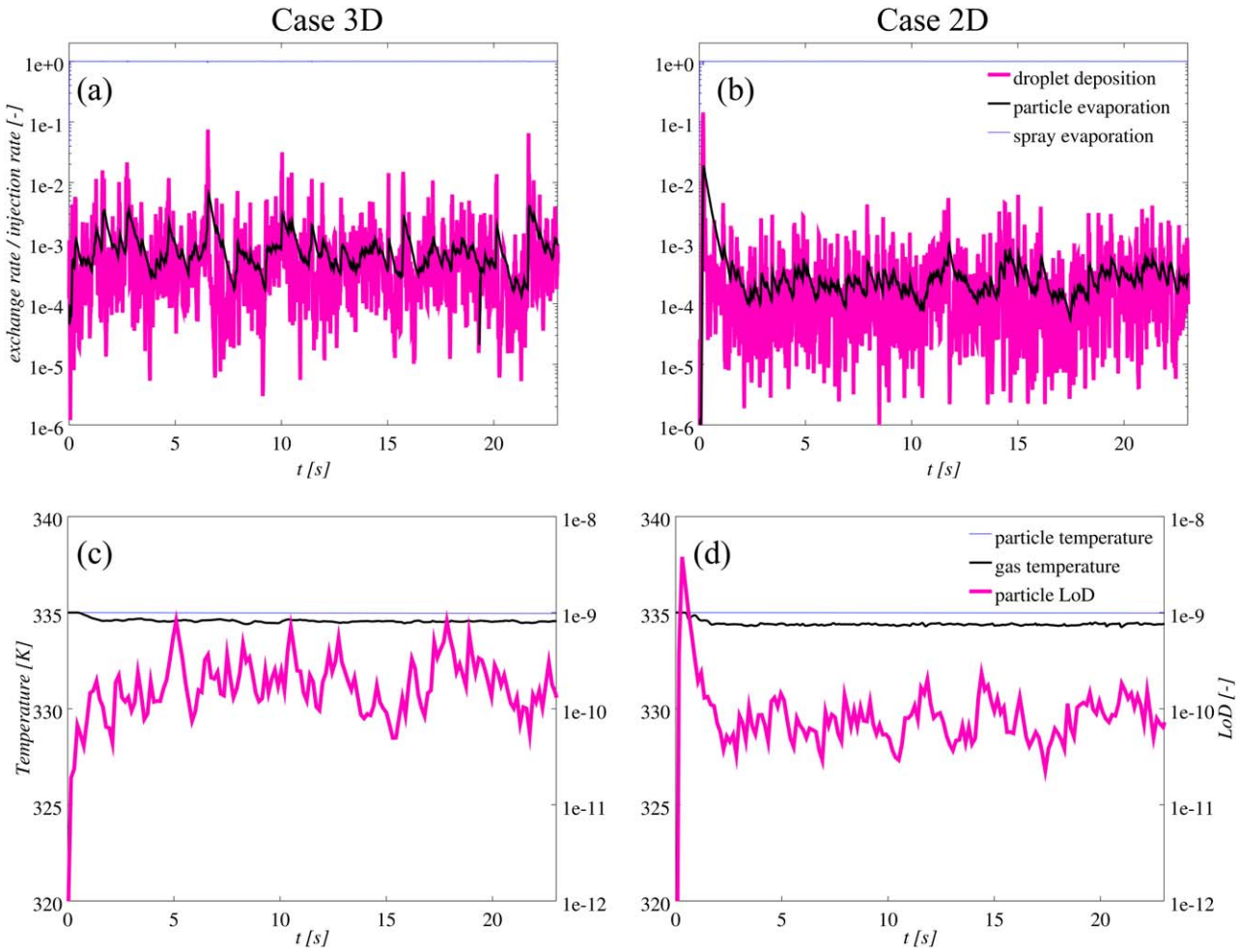

Figure 19. (a) 3D simulation results for the normalized exchange rates (b) 2D simulation results for the normalized exchange rates (c) LoD and temperatures for 3D case (d) LoD and temperatures for 2D case.

[Color figure can be viewed at wileyonlinelibrary.com].

Table 6. Slope of LoD Against Time for Different Models and Initial LoDs

LoD_{init}	2.1×10^{-7}	3.1×10^{-4}
Kariuki model	8.25×10^{-6}	8.25×10^{-6}
Linear model	4.13×10^{-6}	4.13×10^{-6}

chosen. Also, a 1D or 0D approach would require more advanced closures for average heat- and mass-transfer coefficients since these coefficients are significantly altered by bubbling, and cannot be set equal to the local transfer coefficients used in the present work. Thus, while the development of simplified models might appear straight forward on a first view, there are significant hurdles connected to the closures used in future 1D or 0D models.

One important point discerned from Figures 13b to 16b is that due to no evaporation from the particle surface at liquid contents smaller than the critical value, the particle LoD increases linearly over time. Also, the particle temperature decreases very slowly due to the heat exchange with the gas phase. Consequently, the critical value for LoD at which the evaporation starts seems to be crucial to predicting the behavior of the bed. This will come to play on studying porous particles. Therefore, in the case of using a linear model (for modeling surface coverage), and when assuming a high value for $L^*_{p,no\ evap}$, the bed behaves in a distinctly different way. As a result, another simulation was performed using a critical LoD value of zero to compare the bed performance between two surface coverage models in a more straightforward way.

Comparing the different surface coverage models, as discerned from Figures 11 to 12 and Figures 14 to 15, the characteristic time for evaporation from the particle surface for Kariuki's model is shorter than the corresponding time for the linear model. This is based on data for the slope of LoD against time presented in Table 6. This demonstrates that LoD in Kariuki's model reaches a pseudo steady state condition in a shorter time. It should be noted that the slope at different initial LoDs for Kariuki's model is identical. In addition, as computed in Table 7, the linear model over-predicts the quasi steady state LoD by a maximum of 86.9% in comparison to Kariuki's Model. However, the predicted gas and particle temperatures are similar for both models (i.e., they are within 1.33 $\times10^{-2}$ % difference). Therefore, using different models for the surface coverage results in a variation of the predicted LoD by a factor of approximately two. In contrast, the predicted gas and particle temperatures are only insignificantly affected by the surface coverage model in the studied cases. Again, this is due to the dominance of the droplet evaporation rate over the corresponding rate of evaporation from the particle surface at low particle liquid contents.

It can be concluded that the implementation of suitable surface coverage model is of key importance for the correct prediction of the competition between evaporation from the spray and from the particle surface. This is due to their contribution in the amount and position of vapor formation in the bed. This can influence the competition between spray evaporation and droplet deposition. This claim can be proven by considering the exchange rates shown in Figure 13a with high initial surface coverage. Moreover, when assuming the formation of a continuous film on the particle surface, i.e., $\psi_{liq}=1.0$, the characteristic time for particle evaporation is two to three orders of magnitude larger than the corresponding times for the deposition and spray evaporation, see the data in Table 5. These competitions among exchange rates also play a key role in the computation of gas moisture and humidity. What is more, adopting an appropriate surface coverage model is vital in accurate computation of LoD, and consequently the liquid available for liquid bridge formation between wet particles. Those liquid bridges are essential for granulation processes, since they induce granule growth and stabilize existing granules. In detail, the results of the simulations in this study proved that a simplified model, i.e., a linear model can overestimate the particle liquid content in comparison with a more realistic model such as Kariuki's model. The latter has been developed based on Bernoulli's trials, and an assumed uniformly random distribution of droplets on the particle surface. In addition, this model has been validated with experimental data. In short, the choice of the surface coverage model is very important for drying and granulation processes, at least for the case of non-porous particles.

Effect of operation conditions

The Effect of the Injection Rate. Aiming at comparing the dependency of exchange rates on liquid mass loading, the effect of the droplet injection rate was investigated. The results of these simulations have been presented in Figure 17, in which the injection rate ratio is simply the used liquid injection rate divided by the rate used in the base case (see Table 2). It can be readily discerned from Figure 17a that an increase in the injection rate reduces the (relative) spray evaporation contribution. This finding proves that when increasing the injection rate, the fluid flowing in the spray region will be saturated with vapor and consequently higher amount of droplets will be available for deposition on the particles. The predicted spray loss also proves this saturation condition when comparing the sums of the normalized exchange rates shown in Figure 17a.

For the injection rate ratios higher than three, the spray evaporation rate ratio decreases almost linearly with the injection rate ratio. This proves that the rate of evaporation will remain approximately constant and will not change with the injection rate. Also, the trend of the predicted (outlet) gas temperature shown in Figure 17b demonstrates this claim. As seen in this figure, the gas temperature drops significantly for higher injection rates, and then remains constant for injection rate ratios higher than 6. For these very high injection rates, a more intense droplet deposition is observed. Thus, the deposition rate is dependent on the liquid mass loading to a large extent. Since evaporation from particles is in balance with the deposition rate at quasi steady state conditions, the same trend can be observed for the evaporation rate from the particle surface. Therefore, the particle temperature will decrease with increasing liquid injection rates, while the LoD will increase as seen in Figure 17b.

Table 7. Deviation of the Linear Model From the Results Obtained with Kariuki's Model at Various Initial LoDs and Injection Rates

LoD_{init}	2.1×10^{-7}	3.1×10^{-4}	0.334
$\dot{m}_{inj}$ (kg/s)	2.14×10^{-9}	2.14×10^{-9}	1.80×10^{-6}
$E_{\dot{S}_{deposition}}(\%)$	7.91	3.99×10^{-2}	−2.89
$E_{\dot{S}_{evap,p}}(\%)$	6.55	-3.56×10^{-2}	−0.579
$E_{\dot{S}_{evap,d}}(\%)$	-2.1×10^{-2}	0.0	−3.98
E_{LoD} (%)	86.9	75.2	-6.16×10^{-3}
$E_{T_p}(\%)$	-2.99×10^{-3}	-3.00×10^{-3}	-1.33×10^{-2}
$E_{T_g}(\%)$	6.17×10^{-3}	0.0	-2×10^{-2}

The Effect of the Inlet Temperature. Since operating temperature may strongly impact the evaporation in the wet fluidized bed, the effect of inlet temperature was investigated as well. As discerned from Figure 18a, an increase in the inlet temperature decreases the deposition rate and consequently the evaporation rate from the particle surface. This means that the (dimensionless) rate of spray evaporation will gradually approach unity when increasing the gas inlet temperature. Such an increase can be explained considering the fact that the rise in temperature provides the droplets with larger driving force because of higher saturation pressure. Therefore, a lower amount of droplets have the chance to collide with the bed surface, and meet the particles for deposition. As a result, the particle LoD will drop with the same trend as the deposition rate. Conversely, the particle and the (outlet) gas temperature will linearly increase with the inlet gas temperature. This is simple to explain based on the fact of a constant injection rate, and the overall heat balance of the system.

Comparison of 2D and 3D simulation

Since the computational cost for real 3D case is not affordable, the developed models were studied in a pseudo 2D fluidized bed so far. To evaluate the application of the developed model in a 3D bed, a simulation was performed for the bed filled with one million particles. In the 3D simulation, the same ratio of the liquid injection rate and the mass of particles was used. In the 3D simulation, the injection region was positioned in the center of the domain (see Figure 1 and Table 2).

As plotted in Figure 19a,b, the predicted deposition rate is higher in the 3D case since the injection region is more concentrated, which means the ratio of the projected area of injection and the bed's cross sectional is smaller. Hence, the local cooling of the gas is more intense, and a smaller amount of liquid evaporates above the particle bed. Consequently, a larger fraction of the surface of the bed is exposed to droplets, causing higher deposition rates. It can be also discerned form Figure 10a,b that the particles moving on the bed surface below the spray region receive more droplets on their surface. Moreover, as shown in Figure 10c, bubbles mainly move in the central region of the bed. The particles dragged in the bubble wake have somewhat higher velocities after bubble bursting in the freeboard, since the speed of a bubble is in the order of 0.2 (m/s). Hence, the rate of droplet deposition, and consequently their LoD will be higher for these particles. This effect is followed by a higher LoD predicted in the 3D simulations as shown in Figure 19c,d. However, the predicted outlet temperature is identical in both cases.

Conclusion

The exchange of mass and heat between gas, particles, and droplets was simultaneously simulated in a wet fluidized bed using a full-physics CFD-DEM approach. In detail, sub-models in the CFDEM® code were developed that consider (1) droplet deposition on particles, (2) evaporation of freely-flowing droplets, and (3) evaporation of deposited droplets from the particle surface. After successful implementation and verification of these models, the code was used for the simulation of a bubbling fluidized bed with liquid injection. Particularly, the contributions of the involved phenomena in the bed performance were evaluated. Also, we included the cooling effect due to evaporation: this closes an important gap, namely the back-coupling of evaporative cooling on the local evaporation rate of liquid in a wet fluidized bed. Most importantly, our simulations indicate that while the particle temperature is almost homogeneous, the gas temperature fluctuates significantly in the freeboard of the fluidized bed. The results of our simulations indicated that the rate of evaporation from the spray is two orders of magnitude higher than the rates of the evaporation from the particle surface and the droplet deposition. This is due to the fact that the "droplet-in-suspension" time scale is larger than a typical droplet evaporation time. The ratio of these time scales is indirectly affected by the nozzle type via the droplet diameter and the droplet injection speed. The droplet diameter is relatively small in this study due to industry demand, resulting in fast droplet evaporation. However, droplet size can be easily adjusted if necessary for different applications to define a suitable dimensionless "droplet-in-suspension" time. Also, the relative importance of all relevant exchange rates was analyzed through comparison of the characteristic time scales for each phenomenon, i.e., droplet deposition, as well as evaporation from spray and particle surface. While the interpretation of these time scales is non-trivial, they may guide practitioners and modeling experts on developing compartment models. Most importantly, we have identified a dimensionless parameter that helps to decide when evaporation from the droplets should be taken into account or not.

Moreover, it was demonstrated that the gas and particle temperatures are mainly influenced by the rates of evaporation from the droplets and the particle surface, respectively. In the case of no droplet evaporation, due to the efficient particle mixing in the bed, similar temperatures were predicted for both phases. In this case, the particle LoD increases two orders of magnitude, showing that the LoD is highly sensitive to the predicted evaporation from air-suspended droplets.

Furthermore, the effect of surface coverage models was investigated, and a strong influence on the particle LoD was proved. Therefore, implementation of a suitable surface coverage model is crucial when attempting to accurately calculate the particles' LoD, as well as the gas moisture and humidity. This clearly motivates more studies in the area of surface coverage models, and clearly stresses the importance of the work done by Kariuki et al.[28] Apart from this, the effect of injection rate and inlet gas temperature was investigated. Since the particle bed has a fairly uniform temperature, we speculate that it will be easy to calibrate compartment models with the knowledge gained in this study. Also, future work may develop such a compartment model, and lead to an immediate industrial application that allows a prediction of the long-term evolution of the bed dynamics.

In summary, the developed code and understanding may be useful for future studies of granulation processes—both incorporating porous and non-porous particles. However, some extensions that allow full-physics simulations of the latter seem necessary. For example, this could include models for intra-particle transport processes, e.g., of water vapor within the pores. In addition, the future development of appropriate surface coverage model that account for the particles' porosity will be essential. In addition, the newly defined time scale for evaporation from the droplets could help to improve the previous work of Sutkar et al.[13]. Finally, the model of Kolakaluri[29] is of central importance. Clearly, more work in the direction of filtration models for poly-disperse systems would be helpful to improve the fidelity of future full-physics granulation CFD-DEM models.

Notation

Latin letters

a_d = specific surface area of droplet, $6/d_d, 1/\mathrm{m}$
a_{dp} = specific surface area of particle available for droplet evaporation, $1/\mathrm{m}$

a_p = particle specific surface area, $(1-\varphi_f)6/d_p$, 1/m
C_p = thermal capacity, m^2 kg/s^2/K
d_d = droplet diameter, m
D_{eff} = effective diffusivity of vapor in air, m^2/s
D_{vap} = molecular diffusivity of vapor in air, m^2/s
d_p = particle diameter, m
e = restitution coefficient
f = fraction of particle surface coated by droplet, m^2/m^2
$f_{cont,i}$ = contact force exerted on ith particle, N
H_{bed} = bed height in y direction, m
H_{inj} = injection zone height in z direction, m
g = gravity, m/s^2
h = heat-transfer coefficient, kg/s^3/K
$I_{p,i}$ = particles moment of inertia, kg m^2
L_{bed} = bed length in x direction, m
L_{inj} = injection zone length in x direction, m
L_p^* = volume fraction of liquid on particle, m^3/m^3
$L_{p,noevap}^*$ = volume fraction of liquid on particle at which evaporation from particle can start, m^3/m^3
LoD = loss on drying, defined as mass fraction of liquid in the particle
N_p = number of particles in the system
Nu = Nusselt number, hd_p/λ_f
P_f = Pressure, Pa
Pr = Prandtl number, $C_p\nu_f\rho_f/\lambda_f$
Re = Reynolds number
$\dot{S}_d$ = rate of droplet deposition on particle, kg/s/m^3
$\dot{S}_{evap,p}$ = rate of evaporation from particle surface, kg/s/m^3
$\dot{S}_{evap,f}$ = rate of evaporation from spray, kg/s/m^3
$\dot{S}_{inj}$ = rate of liquid (droplet) injection , kg/s/m^3
Sh = Sherwood number, $\beta d_p/D_{vap}$
St = droplet Stokes number
St_{eff}^* = effective droplet Stokes number
T = temperature, K
t = time, s
t_{sim} = simulation time, s
$\boldsymbol{u}_d$ = droplet velocity, $\boldsymbol{u}_d=\boldsymbol{u}_f$, m/s
$\boldsymbol{u}_f$ = fluid velocity, m/s
V_{inj} = injection zone volume, m^3
V_p = particle volume, m^3
w_{bed} = bed width in y direction, m
w_{inj} = injection zone width in y direction, m
Y = distance from the origin in y direction, m
Z_{inj} = injection zone width in z direction, m

Greek letters

β = mass-transfer coefficient, m/s
β_{sf} = solid-fluid momentum exchange coefficient, kg/m^3/s
ΔH_{evap} = heat of evaporation, J/kg
Δt_{CFD} = time step for CFD, s
Δt_{DEM} = time step for DEM, s
η_n = normal viscous damping coefficient, kg/s
η_s = single collector efficiency,
η_t = tangential viscous damping coefficient, kg/s
k_n = normal spring stiffness, kg/s^2
k_t = tangential spring stiffness, kg/s^2
λ = filtration coefficient, 1/m
λ_{eff} = effective Thermal conductivity, m kg/s^3/K
μ_c = Coulomb friction coefficient
μ_{liq} = mass loading of liquid water in gas phase, kg/kg
μ_{vap} = mass loading of water vapor in gas phase, kg/kg
ν_f = kinematic viscosity, m^2/s
ρ_f = fluid density, kg/m^3
$\rho_{w,Sat}$ = saturation density of water vapor, kg/m^3
τ_f = fluid stress tensor, Pa
$\tau_{d,susp}$ = dimensionless "droplet-in-suspension" time scale
ϕ_j = volume fraction of phase j
Φ_d = force exerted by particles on fluid phase per unit volume of cell, N/m^3
Φ_p = particle coating number
ψ_{liq} = particle surface coverage, m^2/m^2
$\omega_{p,i}$ = particle angular velocity, rad/s

Subscripts

d = droplet
f = fluid
i = ith particle
P = particle
liq = liquid (water)
vap = vapor (water)

Literature Cited

1. Mörl L, Heinrich S, Peglow M. Fluidized bed spray granulation. *Handb Powder Technol*. 2007;11:21–188.
2. Maronga S, Wnukowski P. The use of humidity and temperature profiles in optimizing the size of fluidized bed in a coating process. *Chem Eng Process*. 1998;37(5):423–432.
3. Sherony DF. A model of surface renewal with application to fluid bed coating of particles. *Chem Eng Sci*. 1981;36(5):845–848.
4. Li J, Freireich B, Wassgren C, Litster JD. A general compartment-based population balance model for particle coating and layered granulation. *AIChE J*. 2012;58(5):1397–1408.
5. Börner M, Peglow M, Tsotsas E. Derivation of parameters for a two compartment population balance model of Wurster fluidised bed granulation. *Powder Technol*. 2013;238:122–131.
6. Rajniak P, Stepanek F, Dhanasekharan K, Fan R, Mancinelli C, Chern R. A combined experimental and computational study of wet granulation in a Wurster fluid bed granulator. *Powder Technol*. 2009;189(2):190–201.
7. Tan H, Goldschmidt M, Boerefijn R, Hounslow M, Salman A, Kuipers J. Building population balance model for fluidized bed melt granulation: lessons from kinetic theory of granular flow. *Powder Technol*. 2004;142(2):103–109.
8. Vreman A, Van Lare C, Hounslow M. A basic population balance model for fluid bed spray granulation. *Chem Eng Sci*. 2009;64(21):4389–4398.
9. Heinrich S, Peglow M, Ihlow M, Henneberg M, Mörl L. Analysis of the start-up process in continuous fluidized bed spray granulation by population balance modelling. *Chem Eng Sci*. 2002;57(20):4369–4390.
10. Link J, Godlieb W, Deen N, Kuipers J. Discrete element study of granulation in a spout-fluidized bed. *Chem Eng Sci*. 2007;62(1):195–207.
11. Fries L, Antonyuk S, Heinrich S, Palzer S. DEM–CFD modeling of a fluidized bed spray granulator. *Chem Eng Sci*. 2011;66(11):2340–2355.
12. Börner M, Hagemeier T, Ganzer G, Peglow M, Tsotsas E. Experimental spray zone characterization in top-spray fluidized bed granulation. *Chem Eng Sci*. 2014;116:317–330.
13. Sutkar VS, Deen NG, Patil AV, Salikov V, Antonyuk S, Heinrich S, Kuipers JAM. CFD–DEM model for coupled heat and mass transfer in a spout fluidized bed with liquid injection. *Chem Eng J*. 2016;288:185–197.
14. Štepánek F, Rajniak P. Droplet morphologies on particles with macroscopic surface roughness. *Langmuir*. 2006;22(3):917–923.
15. McDougall S, Saberian M, Briens C, Berruti F, Chan E. Using dynamic pressure signals to assess the effects of injected liquid on fluidized bed properties. *Chem Eng Process*. 2005;44(7):701–708.
16. Ariyapadi S, Holdsworth DW, Norley CJ, Berruti F, Briens C. Digital X-ray imaging technique to study the horizontal injection of gas-liquid jets into fluidized beds. *Int J Chem React Eng*. 2003;1(1).
17. Briens C, Dawe M, Berruti F. Effect of a draft tube on gas–liquid jet boundaries in a gas–solid fluidized bed. *Chem Eng Process*. 2009;48(4):871–877.
18. Zhu H, Zhou Z, Yang R, Yu A. Discrete particle simulation of particulate systems: theoretical developments. *Chem Eng Sci*. 2007;62(13):3378–3396.
19. Radl S, Kalvoda E, Glasser BJ, Khinast JG. Mixing characteristics of wet granular matter in a bladed mixer. *Powder Technol*. 2010;200(3):171–189.
20. Girardi M, Radl S, Sundaresan S. Simulating wet gas–solid fluidized beds using coarse-grid CFD-DEM. *Chem Eng Sci*. 2016;144:224–238.
21. Van Buijtenen MS, Deen NG, Heinrich S, Antonyuk S, Kuipers J. A discrete element study of wet particle–particle interaction during granulation in a spout fluidized bed. *Can J Chemi Eng*. 2009;87(2):308–317.
22. Kloss C, Goniva C, Hager A, Amberger S, Pirker S. Models, algorithms and validation for opensource DEM and CFD–DEM. *Prog Comput Fluid Dyn*. 2012;12(2–3):140–152.
23. Kloss C, Goniva C. LIGGGHTS–Open source discrete element simulations of granular materials based on LAMMPS. In: The Minerals, Metals & Materials Society, editors. *Supplemental Proceedings:*

Materials Fabrication, Properties, Characterization, and Modeling. Vol. 2. Hoboken, New Jersey: John Wiley & Sons, 2011;781–788.
24. Jasak H, Jemcov A, Tukovic Z. OpenFOAM: A C++ library for complex physics simulations. In: Terze Z and Lacor C editors. *Proceedings of the International Workshop on Coupled Methods in Numerical Dynamics (CMND2007)*. Dubrovnik, Croatia, 2007.
25. Beetstra R, Van der Hoef M, Kuipers J. Drag force of intermediate Reynolds number flow past mono-and bidisperse arrays of spheres. *AIChE J*. 2007;53(2):489–501.
26. Kloss C. *LIGGGHTS-PUBLIC Documentation, Version 3.X*. Available at https://github.com/CFDEMproject/LIGGGHTS-PUBLIC, Accessed Dec 2016.
27. Deen NG, Kriebitzsch SH, van der Hoef MA, Kuipers J. Direct numerical simulation of flow and heat transfer in dense fluid–particle systems. *Chem Eng Sci*. 2012;81:329–344.
28. Kariuki WI, Freireich B, Smith RM, Rhodes M, Hapgood KP. Distribution nucleation: quantifying liquid distribution on the particle surface using the dimensionless particle coating number. *Chem Eng Sci*. 2013;92:134–145.
29. Kolakaluri R. *Direct Numerical Simulations and Analytical Modeling of Granular Filtration*. PhD Thesis. Ames, Iowa: Iowa State University, 2013.

Manuscript received July 2, 2016, and revision received Oct. 10, 2016.

Appendix A: Model Verification

In order to be assured of the correct implementation of the implemented models, several verification studies were performed. Clearly, such verification studies cannot substitute a thorough validation against experimental results. However, the results presented below document the correct functionality of our models in a number of relevant (but synthetic) flow situations.

A.1. Droplet Deposition on Particle

In order to examine the accuracy of model implementation, assuming an instantaneous interaction between droplets and the particle bed (i.e., the granules), a sink term can be defined in the transport equation for the droplet concentration as follows:

$$\frac{\partial\left(\mu_{liq}\varphi_f\rho_f\right)}{\partial t}+\nabla\cdot\left(u_f\mu_{liq}\varphi_f\rho_f\right)=\dot{S_d} \tag{A1}$$

Aimed at model verification, an analytical solution was obtained for a packed bed with a clean-bed filter (filtration coefficient is assumed to be constant along the bed) as

$$ln\left(\frac{\mu_{liq}}{\mu_{liq,0}}\right)=-\lambda x \tag{A2}$$

Where the filtration coefficient λ is calculated based on volume-averaged voidage and fluid velocity in the packed bed.

The results of CFD-DEM simulation and analytical solution for droplet mass loading along the bed was presented in Figure A.1. As seen in this figure, the predicted non-dimensional droplet mass loading is in good agreement with analytical solution at the positions where voidage is constant. However, small deviation can be observed near the bed inlet and bed surface, which can be attributed to the porosity distribution. In detail, void fraction averaging method results in higher gas volume fraction in the first and last rows of cell in the dense bed. Since filtration coefficient strongly depends on particle volume fraction, small deviation is expected in these regions

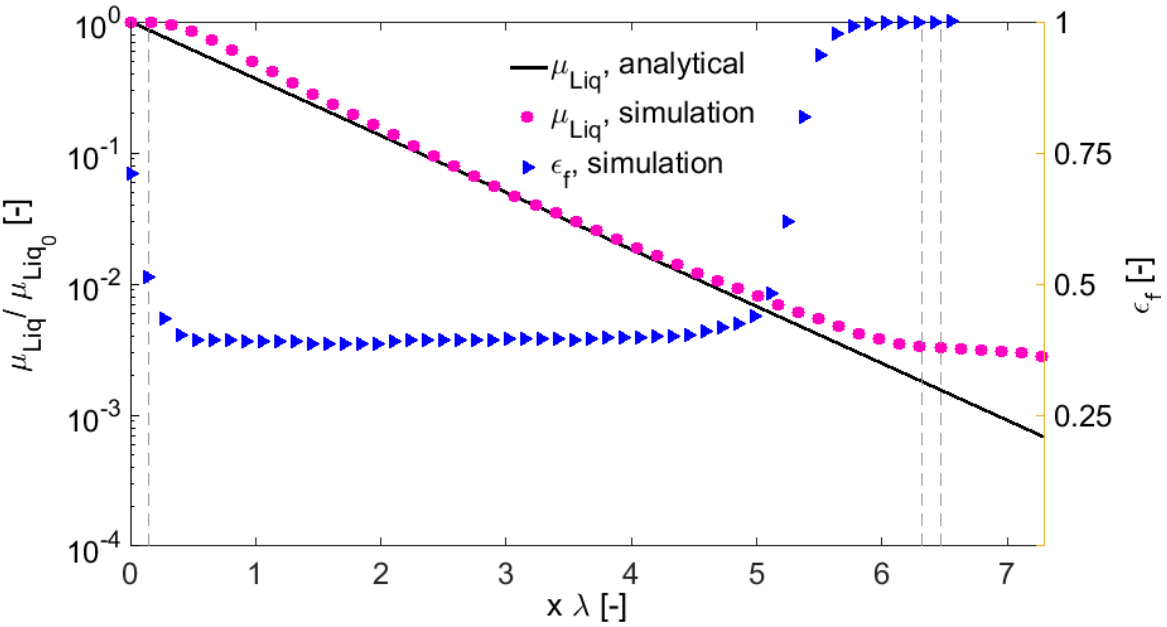

Figure A.1.comparison of the water vapour mass loading predicted by CFD-DEM simulation and the corresponding analytical value

A.2. Droplet Evaporation from the Particle Surface

A.2.1. Deposited Droplet Evaporation in Flowing Fluid

Aimed at verifying the implemented model for heat exchange between particles and fluid phase, initially heat balance equation for both gas and particle phase for 1D packed bed was derived as

$$\varphi_f \rho_f C_{p,g} \frac{\partial T_g}{\partial t} = -\varphi_f \rho_f C_{p,g} u_g \frac{\partial T_g}{\partial z} - ha(T_g - T_p) \quad \text{(A3)}$$

$$(1-\varphi_f)\rho_p C_{p,p} \frac{\partial T_p}{\partial t} = ha(T_g - T_p) - \dot{q}_{evap} \quad \text{(A4)}$$

T_g and $T_p$were theoretically calculated. For verification of model, a pseudo 2D packed bed was simulated in CFDEM. The simulation condition was presented in Table A.1. It should be mentioned that particles were fixed in the DEM simulation so that the bed voidage and relative velocity between gas and particle can remain constant during simulation time.

Table A.1– Simulation Condition for the verification of the heat transfer model.

Catalytic Bed Dimensions			**Solid Phase Properties**		
Height	m	0.6	d_p	m	0.022
Length	m	0.1	λ_p	$W/_{Km}$	0.1
Width	m	0.1	$C_{p,p}$	$J/_{kgK}$	5
			ρ_p	$kg/_{m^3}$	1000
Gas Phase Properties			**Initial Condition**		
$C_{p,f}$	$J/_{kgK}$	1007	T_{g0}	K	300
ρ_f	$kg/_{m^3}$	1.188	T_{p0}	K	300
ν_f	$m^2/_s$	1.5×10^{-5}	**Boundary Condition**		
λ_f	$W/_{Km}$	0.0256	T_{gi}	K	330
Prandtl	-	0.70097	U	m/s	0.1

The results of model verification were depicted in Figure A.2. The temperatures predicted through CFD-DEM simulation is in excellent agreement with corresponding analytical values at different heights.

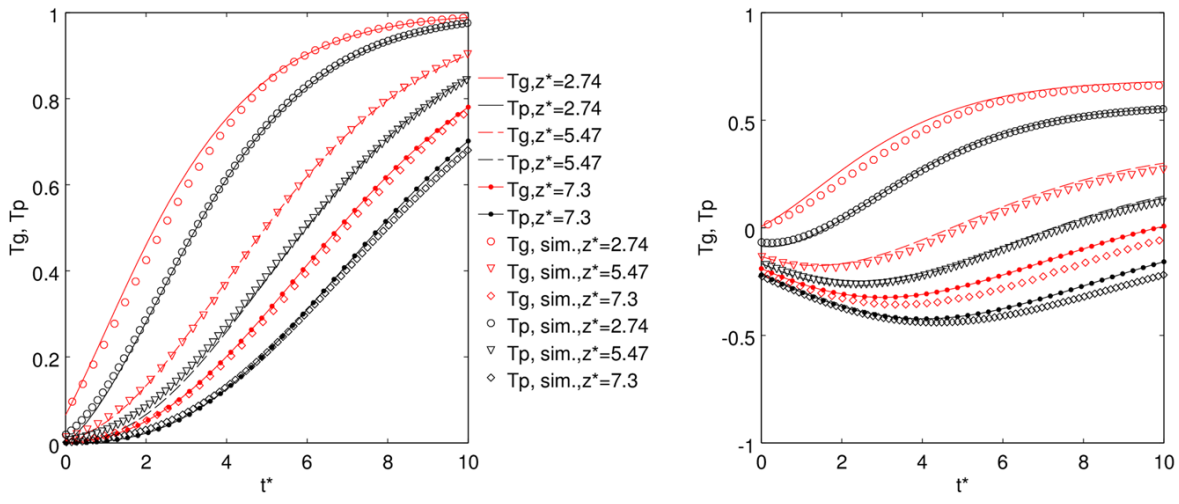

Figure A.2. comparison of the gas and particle temperature predicted by CFD-DEM simulation and the corresponding analytical value

A.2.1. Deposited Droplet Evaporation in Stagnant Fluid

For verification of implemented model for evaporation from particle surface in particle side, a simulation was performed for a bed of particle without gas flow. To do so, particle-fluid heat exchange was not considered. The rate of evaporation was assumed constant in this case. As depicted in Figure A.3, mean particle liquid content and particle temperature as well as vapor mass loading over time were in excellent agreement with the analytical solution

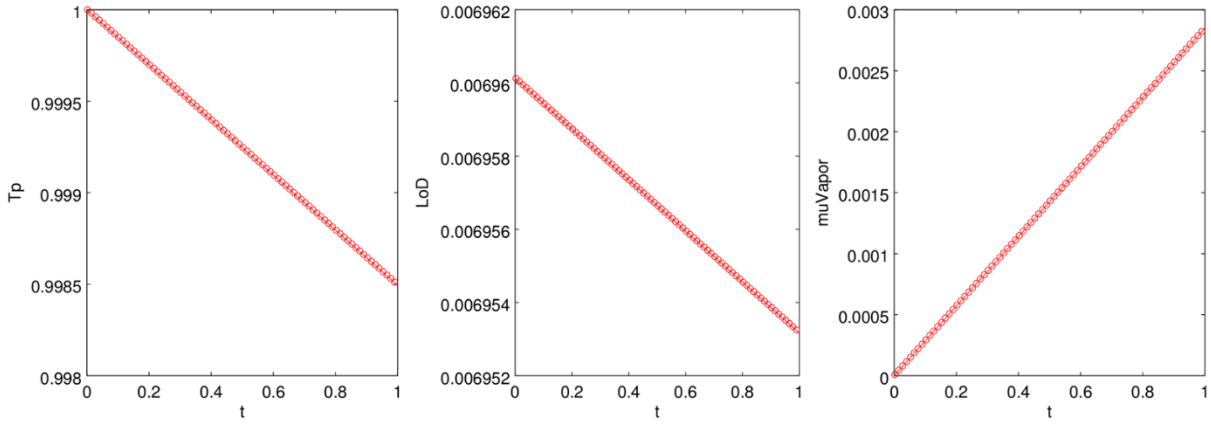

Figure A.3comparison of particle temperature (left panel), LoD (middle panel), and water vapor mass loading (right panel) predicted by CFDEM simulation and the corresponding exact values

A.3. Spray Evaporation

In order to verify the implemented model for spray evaporation, the mass transport equation for vapor mass loading was numerically solved

$$\frac{\partial \mu_{vap} \varphi_f \rho_f}{\partial t} + \nabla \cdot \left(u_f \mu_{vap} \varphi_f \rho_f \right) = \dot{S}_{evap} \tag{A5}$$

The droplet was injected in the bed inlet. For simplification, the characteristic time for droplet evaporation was assumed constant. Besides, the liquid mass loading is high enough to have a constant surface area for evaporation. As shown in Figure A.4, the predicted vapor mass loading is in good agreement with corresponding analytical values at various heights.

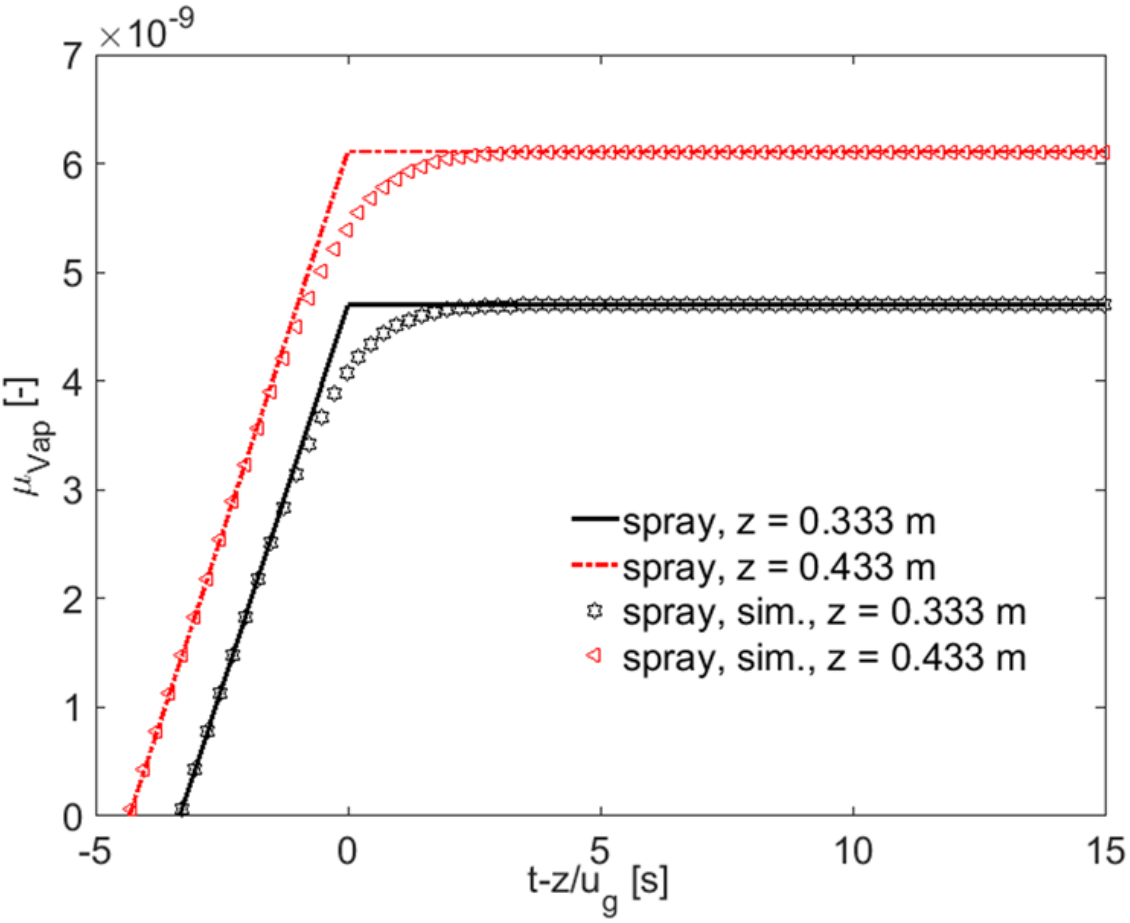

Figure A.4. comparison of the predicted vapor mass loading with corresponding analytical values

Appendix B: Characteristic Time Scales

The average characteristic times for various phenomena taking place in the fluid bed granulator are calculated to compare the relative importance of these phenomena.

B.1. Spray Evaporation (Saturation Time Scale)

The mass balance equation for water vapour in a fixed volume can be derived as:

$$\partial_t m_{vap} = A_d \beta_d (\rho^{eq} - \rho_v), \tag{B1}$$

where ∂_t denotes the time derivative, and

$$A_d = V_{tot} a_d = V_{tot} \varphi_d \frac{6}{d_d} \tag{B2}$$

$$\rho^{eq} = \mu^{eq} \rho_g \tag{B3}$$

$$\rho_v = \mu_v \rho_g \tag{B4}$$

If we assume that droplet volume faction, i.e. φ_d is small, the variation of total volume, V_{tot} , is marginal, such that the Equation B1 can be rewritten as an equation in which all terms are O(1):

$$V_{tot} \rho_g \partial_t \mu_v = V_{tot} \varphi_d \frac{6}{d_d} \beta_d \rho_g (\mu^{eq} - \mu_v) \tag{B5}$$

$$\frac{d_d}{6 \beta_d \varphi_d} \partial_t \frac{\mu_v}{\mu^{eq}} = t_{v,evap} \partial_t \frac{\mu_v}{\mu^{eq}} = 1 - \frac{\mu_v}{\mu^{eq}} \tag{B6}$$

For zero-slip velocity, the Sherwood number equals 2, such that the mass transfer coefficient is given by

$$\beta = \frac{Sh\, D_{vapor}}{d_d} = \frac{2\, D_{vapor}}{d_d} \tag{B7}$$

Droplet volume fraction can be calculated as

$$\varphi_d = \frac{V_d}{V_{tot}} = \frac{{m_d}/{\rho_d}}{{m_d}/{\rho_d} + {m_g}/{\rho_g}} = \frac{{\rho_g}/{\rho_d}\, \mu_d}{{\rho_g}/{\rho_d}\, \mu_d + 1} \cong {\rho_g}/{\rho_d}\, \mu_d \tag{B8}$$

Therefore, droplet evaporation characteristic time is:

$$t_{v,evap} = \frac{d_d^2}{12\, D_{vapor}\, {\rho_g}/{\rho_d}\, \mu_d} \tag{B9}$$

B.2. Spray Evaporation (Droplet Evaporation Time Scale)

The mass balance equation for a single droplet can be derived as

$$\partial_t m_d = A_d \beta_d (\rho^{eq} - \rho_v) \tag{B10}$$

Inserting the definition of droplet mass, surface area, and mass transfer coefficient yields again an equation in which all terms are O(1):

$$\partial_t \left(\rho_d \frac{\pi}{6} d_d^3 \right) = \pi d_d^2 \frac{2\, D_{vapor}}{d_d} \rho_g (\mu^{eq} - \mu_v) \tag{B11}$$

$$\frac{\rho_d}{\rho_g} \frac{d_d^2}{4\, D_{vapor}} \frac{1}{\mu^{eq}} \partial_t d_d^* = t_{d,evap} \partial_t d_d^* = 1 - \frac{\mu_v}{\mu^{eq}} \tag{B12}$$

Here the asterisk refers to a dimensionless quantity, i.e., the droplet diameter. Thus, we arrive at:

$$t_{d,evap} = \frac{\rho_d}{\rho_g} \frac{d_d^2}{4\, D_{vapor}} \frac{1}{\mu^{eq}} \tag{B13}$$

B.3. Evaporation from Particle Surface

The mass balance equation for water vapour upon evaporation from particle can be written as

$$\partial_t m_{vap} = A_d \psi_{liq} \beta_p (\rho^{eq} - \rho_v) \tag{B14}$$

$$(1 - \varphi_p) V_{tot} \rho_g \partial_t \mu_v = V_{tot} \varphi_p \frac{6}{d_p} \beta_p \rho_g \psi_{liq} (\mu^{eq} - \mu_v) \tag{B15}$$

$$\frac{1 - \varphi_p}{\varphi_p} \frac{d_p}{6 \beta_p \psi_{liq}} \partial_t \frac{\mu_v}{\mu^{eq}} = t_{evap,p} \partial_t \frac{\mu_v}{\mu^{eq}} = 1 - \frac{\mu_v}{\mu^{eq}} \tag{B16}$$

Considering the same methodology as above, the characteristic time for evaporation from the particle surface can be expressed as

$$t_{evap,p} = \frac{1 - \varphi_p}{\varphi_p} \frac{d_p^2}{6\, Sh\, D_{vapor} \psi_{liq}} \tag{B17}$$

In which the Sherwood Number must bed calculated using the correlation presented by Deen et al. since mass transfer occurs from a dense gas-particle suspension:

$$\begin{aligned} Sh = {} & \left(7 - 10\varphi_f + 5{\varphi_f}^2\right)\left(1 + 0.7 Re^{0.2} Pr^{1/3}\right) \\ & + \left(1.33 - 2.4\varphi_f + 1.2{\varphi_f}^2\right) Re^{0.7} Pr^{1/3} \end{aligned} \tag{B18}$$

Re is taken as that at the minimum fluidization velocity, same as the value for the voidage.

B.4. Droplet Deposition

The characteristic time for deposition of droplet can be calculated following Kolakaluri:

$$t_{depos} = \frac{1}{\lambda|u_f - u_p|} \tag{B19}$$

Appendix C: Calculation of Equilibrium Surface Coverage

In order to examine the effect of different initial particle wetness levels on the exchange rates and bed behavior, three different scenarios as described below were investigated.

C.1. LoD based on the Droplet Mass Loading in the Injection Zone

We assumed that $\rho_v \approx 0$, a quasi-steady state, and that the particles experience the droplet mass loading given by the injected droplet mass, the induced air velocity (u_{inj}), and a typical cross-sectional area of injection A_{inj}:

$$\frac{d(m_{lp})}{dt} = 0 = \dot{m}_{dep} - \dot{m}_{evap} \tag{C1}$$

$$\dot{m}_{evap} = A_p \, \psi_{liq} \, \beta_p \, \rho^{eq} \tag{C2}$$

$$\dot{m}_{dep} = \lambda \left| u_f - u_p \right| \mu_{liq} \rho_f \frac{\phi_f}{1 - \phi_f} V_p \tag{C3}$$

$$\psi_{liq} = \frac{\lambda \left| u_{inj} - u_p \right| \frac{\dot{m}_{inj}}{u_{inj} A_{inj}} \frac{\phi_f}{1 - \phi_f} \frac{{d_p}^2}{6}}{D_{vap} \, sh \, \rho^{eq}} \tag{C4}$$

Since the rate of deposition is calculated based on the droplet concentration in the spray zone, the corresponding L_p^* represents the maximum expected liquid content of particles. By using Kariuki's surface coverage model (see Section C.4 below) we can now estimate the initial surface coverage, and consequently the initial liquid loading to be

$$\psi_{liq} = 6.32 \times 10^{-4}$$
$$L_{p,max}^* = 0.00036 \tag{C5}$$

C.2. LoD based on a Predefined Domain-Averaged Deposition Rate

Again, we assumed that $\rho_v \approx 0$ and that the system is at a quasi-steady state. We then assumed that $\dot{m}_{dep} = 0.1 \dot{m}_{injection} / N_p$, i.e., 10% of the injected droplets are deposited uniformly-distributed on the particles. This assumption is based on the results of primary simulation we performed. By adopting Kariuki's model, we arrive at:

$$\psi_{liq} = \frac{\dot{m}_{dep}}{A_p\ \beta_p\ \rho^{eq}} = \frac{0.1\ \dot{m}_{inj}/N_p}{\pi d_p\ D_{vap}\ sh\ \rho^{eq}} = 4.3 \times 10^{-7} \tag{C6}$$

$L^*_{p,max} = 2.49 \times 10^{-7}$.

C.3. LoD based on a Predefined Surface Coverage

By using Kariuki's model, it is straight forward to compute the liquid loading level. Thus, for a coverage of 50% we arrive at

$$L^*_{p,max} = 0.395 \tag{C7}$$

C.4. Relationship between of Surface Coverage and Particle Liquid Content for Kariuki's Model

The surface coverage of particle in the model developed by Kariuki et al. [1] is given by

$$\psi_{liq} = 1 - [1 - f]^{\Phi_p/f} \tag{C8}$$

Where parameter f is fraction of particle surface coated by a single droplet, and $\Phi_p$is the particle coating number given by

$$f = \frac{A_{d,projected}}{A_p} = \frac{\frac{\pi}{4} d_d^2}{\pi d_p^2} = \left(\frac{d_d}{2d_p}\right)^2 \tag{C9}$$

$$\Phi_p = N_d f \tag{C10}$$

Here N_d is the number of deposited droplets, which can be calculated as

$$N_d = \frac{V_{d,total}}{V_d} = \frac{V_p L^*_p}{V_d} \tag{C11}$$

By inserting this definition into the original model, we arrive at

$$\psi_{liq} = 1 - \left[1 - f^2\right]^{\frac{V_p}{V_d} L^*_p} = 1 - e^{\left[ln\left(1-f^2\right)\frac{V_p L^*_p}{V_d}\right]} \tag{C12}$$

By rewriting this equation, we now isolate L_p^* as

$$L_p^* = \frac{V_d}{V_p} \frac{ln\left[1 - \psi_{liq}\right]}{ln\left[1 - \left(\frac{d_d}{2d_p}\right)^2\right]} \quad \text{(C13)}$$

References

1. Kariuki WI, Freireich B, Smith RM, Rhodes M, Hapgood KP. Distribution nucleation: quantifying liquid distribution on the particle surface using the dimensionless particle coating number. *Chemical Engineering Science.* 2013;92:134-145.

3

Voidage correction algorithm for unresolved Euler–Lagrange simulations

This article is published in Computational Particle Mechanics (2018): 1-19
https://doi.org/10.1007/s40571-018-0193-8

The open access to this article was funded by Graz University of Technology.

Computational Particle Mechanics
https://doi.org/10.1007/s40571-018-0193-8

Voidage correction algorithm for unresolved Euler–Lagrange simulations

Maryam Askarishahi[1] · **Mohammad-Sadegh Salehi**[2] · **Stefan Radl**[2]

Received: 17 November 2017 / Revised: 6 April 2018 / Accepted: 19 April 2018

Abstract
The effect of grid coarsening on the predicted total drag force and heat exchange rate in dense gas–particle flows is investigated using Euler–Lagrange (EL) approach. We demonstrate that grid coarsening may reduce the predicted total drag force and exchange rate. Surprisingly, exchange coefficients predicted by the EL approach deviate more significantly from the exact value compared to results of Euler–Euler (EE)-based calculations. The voidage gradient is identified as the root cause of this peculiar behavior. Consequently, we propose a correction algorithm based on a sigmoidal function to predict the voidage experienced by *individual* particles. Our correction algorithm can significantly improve the prediction of exchange coefficients in EL models, which is tested for simulations involving Euler grid cell sizes between $2d_p$ and $12d_p$. It is most relevant in simulations of dense polydisperse particle suspensions featuring steep voidage profiles. For these suspensions, classical approaches may result in an error of the total exchange rate of up to 30%.

Keywords Euler-Lagrange approach · Voidage correction · Drag force · Gas-particle flows

1 Introduction

Particle–gas systems are extensively used in various processes such as chemical, petrochemical and pharmaceutical industries. Due to the complexity of such systems, as well as their opaqueness, numerical tools have been widely exploited. This includes simulations to better understanding phenomena originating from (i) particle–particle interactions (e.g., cohesive forces), as well as (ii) particles and the interstitial flow (e.g., elutriation of fines from fluidized beds). This insight can be achieved through detailed local information from two- or three-dimensional simulations, which have become valuable tools for engineers and researchers.

In simulations of particle–gas flow, usually two methodologies can be used to calculate interphase coupling forces: (i) a direct calculation of the coupling force via a particle-resolve (PR) flow simulation or (ii) using a drag closure that relies on average flow information only (i.e., the so-called particle unresolved method, PU). In the first methodology, the boundary between particles and fluid is discretized, and fluid flow is simulated in all detail. The PR method necessitates a comparably fine computational mesh to capture the boundaries and the flow accurately. Consequently, the computation time is high, and the application is typically limited to small particle ensembles in the order of $O(10^3)$ to $O(10^6)$ particles. Studies that have adopted the PR method are, for example, Avci and Wriggers [1], or the early work of Johnson and Tezduyar [2].

For numerical investigations of gas–particle flow using the PU approach, i.e., employing a closure for the drag force, generally two approaches can be employed: (i) the Euler–Euler (EE) approach, in which gas and particles are treated as interpenetrating continua. The kinetic theory of granular flow (KTGF), together with stress closures for enduring particle–particle contacts, is typically applied in order to close the set of equations when using the EE approach; or (ii) the Euler–Lagrange (EL) approach, in which gas phase is considered as continuous phase, while particles are treated individually by solving Newton's equation of motion. Attractive for a number of engineering applications is the so-called particle unresolved EL approach (PU-EL), in which flow details around individual particles are *not* resolved. PU-EL avoids the need for the often prohibitively substantial number of

✉ Stefan Radl
radl@tugraz.at

[1] Research Center Pharmaceutical Engineering GmbH, Inffeldgasse 13/III, 8010 Graz, Austria

[2] Institute of Process and Particle Engineering, Graz University of Technology, Inffeldgasse 13/III, 8010 Graz, Austria

Published online: 30 April 2018

fluid grids and offers comparably fast predictions that can account for, for example, intra-particle effects (e.g., diffusion and chemical reactions within porous particles).

It should be noted that when using a PU-EL approach, the CFD cell size (on which the transport equations for the fluid phase are solved) varies between approximately 2 and 15 times the particle diameter. Most importantly, the CFD cell size typically cannot be strictly enforced, since a complex-shaped unstructured fluid grid has to be used. Nowadays, such grids are built with fully automated gridding techniques and commonly used in many industrial applications of PU-EL. Thus, the voidage (i.e., the relative amount of void space) reconstructed on a typical fluid grid is blurred, with the degree of blurring depending on the local CFD cell size. As we will show, this blurring results in substantial errors when predicting fluid–particle transfer coefficients, and hence it is unwanted.

To obtain accurate distribution of key quantities in such gas–particle systems, both the EE approach and the (PU-)EL approach require a suitable CFD cell size to reduce blurring. Depending on the spatial distribution of the particles, which is dictated by the underlying flow physics, this size is typically in the order of a few particle diameters. The root cause for this need is that the relative void space between the particles can have nonlinear effect on exchange coefficients of momentum, heat and mass. This is especially true for moderately dense to dense gas–particle flows frequently encountered in chemical engineering applications. Hence, EE and EL models that claim to resolve all flow phenomena in this field necessitate so-called fine-grid simulations to resolve the voidage field.

Despite the fast increase in the availability of computational resources, such a fine-grid simulation makes the numerical investigation of industrial scales system computationally very expensive or sometimes impossible. This is especially the case when using the (PU-)EL approach. To overcome such a limitation, a large number of research studies have been devoted to improving the reliability of so-called coarse-grid simulations in predicting the system behavior and performance. To provide a better understanding of such "coarse-grid" simulations, a typical schematic representation of a packed bed with fine and coarse grids is depicted in Fig. 1. It can be easily discerned from this figure that coarsening the CFD (fluid) grid leads the voidage being blurred over a larger region. We note in passing that this blurring is different from numerical diffusion caused by discretization schemes that are employed in solving the governing equations. In contrast, blurring has its origin in the mapping of particle-related information to a finite fluid grid.

1.1 Classical closures for coarse-grid simulations

In a pragmatic approach, as extensively performed by Sundaresan's research group [3–7], the results of fine-grid simulations are filtered considering various grid sizes to obtain so-called filtered models. More precisely, these models are closures that focus on adjusting exchange coefficients (e.g., for the drag), or define a new constitutive model that is needed for coarse-grid simulations (e.g., for the particle-phase stress). For example, via this filtering approach, an average correction factor between zero and unity is developed to establish a "filtered" drag coefficient. This average filtered counterpart is hence predicted to be always *smaller* than the original drag coefficient, i.e., the one would use in a fine-grid simulation (see Schneiderbauer [8]). Note that average here refers to a *particle ensemble average*. This is important since none of the approaches for coarse-grid simulations presented above is currently able to predict the *true distribution* of filtered exchange coefficients.

An alternative concept is that of Parmentier et al. [9], who introduced an (average) subgrid drift velocity to reduce the fluid–particle relative velocity. This drift velocity is defined as the difference between the filtered gas–particle–fluid velocity seen by the particle phase and the resolved filtered gas velocity. In effect, the drift velocity concept leads to a similar modification of the filtered drag coefficient that is smaller than one in fine-grid counterpart. Yet another alternative is to consider the effect of unresolved structures in a more analytical fashion as done by Schneiderbauer [8]. One more example of analytically based coarse-grid corrections uses the energy minimization multi-scale (EMMS) method, originally developed by Li [10]. In this approach, the local heterogeneity is described in terms of decomposed dense and dilute phases. This method was integrated by Wang et al. [11] into an Euler description of gas–solid flow to include subgrid-scale model for drag force. Although the application of such a methodology is rather limited, e.g., by the fact that it is limited to a certain type of fluid–particle systems, it has attracted a significant research [12,13].

1.2 The need to account for coherent structures

Most of the filtered models discussed in the previous paragraph depend on the relative grid size, the filtered particle concentration, as well as sometimes a third marker (e.g., the filtered slip velocity or a subgrid-scale particle agitation [8]). Most importantly, these corrections can only account for a certain phenomenon in an average sense (e.g., the spontaneous clustering of particles [14]) and use a primitive [8] or no information on the heterogeneous structure of the suspension. Consequently, regions featuring large voidage gradients, e.g., structures near the interface of particle clusters, are expected to be a problem for these filtered models. This is simply because these structures are averaged out in the above-discussed approaches, but certainly cause extrema in filtered exchange coefficients. Hence, they are inadequately modeled by currently available models that rely on *average*

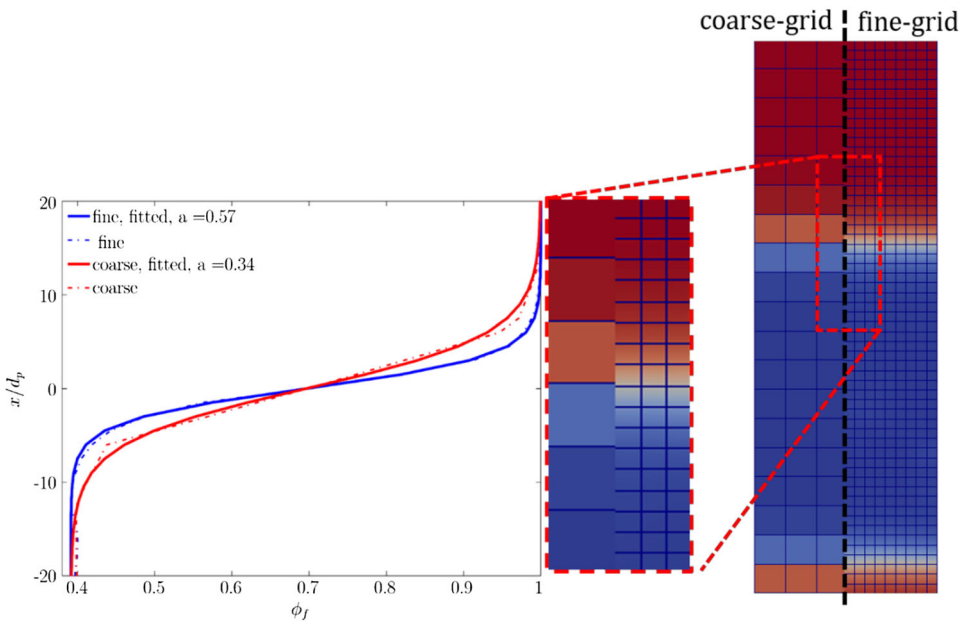

Fig. 1 Schematic representation of fluid coarsening and distribution of the voidage distribution in a packed bed. The bed interface was zoomed in to depict smearing the voidage clearly

exchange coefficients. This is also supported by the study of Fullmer and Hrenya [15] that probed the effect of the local voidage on the mean-slip velocity in a comparably dilute fluidized bed ($\varphi_{p,\max} = 0.25$) using the EE approach. The predicted slip velocity was in a good agreement with the corresponding values from the EL-based simulations of Radl and Sundaresan [16]. However, Fullmer and Hrenya [15] demonstrated that the main reason for the deviation of the slip velocity in coarse-grid simulation of cluster can be associated with the voidage gradient at the boundary of the cluster[17–19]. Specifically, Fullmer and Hrenya [15] conclude that higher (mean) particle concentrations induce sharper voidage gradients, which necessitate a higher spatial grid resolution to capture these gradients.

To include the effect of coherent structures that lead to extrema in filtered exchange coefficients, new parameters, e.g., the gradient of flow variable, are required. The work of ten Cate and Sundaresan [20] followed such a thought and systematically analyzed the effect of voidage gradients on the momentum exchange coefficients. Similarly, corrections to the drag coefficient based on the "structure of the flow" were proposed by Yang et al. [21]. They modified the drag coefficient through correlating the structure parameters with the solids concentration only, though. Only recently their work was followed by Zhou et al. [22] through direct numerical simulation of heterogeneous gas–solid flow. The results of their simulation proved the dependency of the drag force on the local heterogeneity. The latter was quantified in terms of solid concentration and, most importantly, by the magnitude and the angle of the voidage gradient. The latest work following such a chain of thoughts is that of Li et al. [23] who investigated the effect of the local heterogeneity in the particle distribution using an EE approach. They obtained a correction factor for this local heterogeneity with reference to homogenous distribution of particle in a cell as a pre-tabulated correction factor. The local heterogeneity in their study has been defined based on a linear voidage distribution in a computational cell. The model of Li et al. [23] has some limitations, e.g., it is only valid for the Euler–Euler approach and assumes a linear variation of the voidage. Furthermore, it was assumed that the velocity component normal to the flow is zero. This is problematic, since in case that a voidage gradient is present in a computational (Eulerian) cell, the velocity field can deviate from the main direction. The gas prefers to flow in the region with higher voidage, drastically changing the effective drag force in this computational cell.

1.3 Decoupling the effect of nonresolved structures and insufficient grid resolution

The above-mentioned studies focus on the correction of exchange coefficients which lump the effect of (i) nonresolved structures and (ii) numerical parameters (e.g., the grid resolution) into a single correction factor. In our present study, we follow the thought that the correction of the exchange coefficients must be split based on the source of the deviation. For instance, coarsening the grid size artificially introduces a more homogeneous voidage distribution, as depicted in Fig. 1, which drastically reduces the voidage gradient (see the left panel). As it will be explained later, the voidage distribution can be fitted to the sigmoidal function with model parameter a. In fact, as demonstrated by Fullmer and Hrenya [15] as well as Ozel et al. [4], the (Eulerian) grid size mainly influences the exchange coefficient through

its effect on the particle volume fraction calculated in the cell. Thus, even in case one would be able to resolve heterogeneous structures in an EL-based simulation, the *local* particle concentration at each particle's position cannot be probed accurately on a finite-sized Eulerian grid in general.

1.4 Goals

Hence, it is clear that classical (PU-)EL approaches mainly suffer from the inability in the reliable prediction of the *local* voidage as also reported by Lu et al. [24] through direct numerical simulation (DNS) of gas–solid flow. Since the voidage is the most important contributor—next to the fluid–particle relative speed—to predict exchange coefficients, we expect that even minute mispredictions of the local voidage lead to significant errors in the exchange coefficients. It is clear that the effect of a finite grid size on the voidage profile is not related to discretization schemes used for approximating, e.g., convective terms in the governing transport equations. The misprediction of the voidage distribution is associated with the mapping procedure and the subsequent interpolation of the voidage at the particle position. Specifically, when using coarse grids, a larger number of particles reside in a specific fluid cell. Consequently, particles in the same fluid cell will experience a similar voidage, followed by a similar flow speed. Therefore, in the present study, the main effort will be put on the correction of the voidage to eradicate the effect of voidage misprediction due to mapping and interpolation. It is worth mentioning that the corrected voidage will be only used for computing per-particle exchange coefficients (e.g., for drag and heat exchange)—the voidage on the fluid grid will be not modified. Hence, our proposed correction algorithm does not interfere with the conservation of total mass or volume on the fluid grid.

While our correction algorithm is novel in the field of PU-EL simulation models, one may compare it with "interface-sharpening" algorithms [25,26]. The latter are frequently used in the so-called volume of fluid (VoF) method for modeling two phase flows of incompressible fluids and similar in spirit to our algorithm. However, there is a substantial difference between them: In the VoF method blurring of the phase fraction (a quantity that is similar to the voidage in our work) is related to the numerical diffusion introduced via discretization schemes. In contrast, in the gas–particle flows, blurring is connected to mapping the data from particles to fluid grid cells and subsequent interpolation at the particle position. Also, in interface-sharpening algorithms an additional transport equation (i.e., some kind of an anti-diffusion equation) needs to be solved [25,26]. This is computationally expensive and in contrast to our study which relies on a pure algebraic correction approach (i.e., not transport equation needs to be solved).

In the present study, the correction model will be developed specifically for dense gas–particle flows that feature large voidage gradients. Typical examples of such flows include bubbling fluidized beds, packed bed reactors or clustered suspensions (e.g., flows of cohesive powders and granular materials).

One can criticize the approach adopted in our present study by the fact that subfluid cell information (i.e., the arrangement of particles) is ignored. However, using information on the arrangement of particles which would enable, for example, Voronoi tessellation [27] is avoided on purpose in our present study, using such particle-based information typically greatly increases the computational expense for computing the voidage. Thus, the main motivation behind our study is using information available on the fluid grid for the sake of computational efficiency.

The main goals of our present study can be summarized as follows:

1. Examining the influence of fluid coarsening on the total drag force and heat exchange rate in dense gas–particle flows.
2. Improving the prediction of hydrodynamics and heat transfer rates in bubbling fluidized beds, as well as packed beds. Here our focus is on systems that feature large voidage gradients.
3. Developing a straight-forward, easy-to-implement method to correct the voidage (for the calculation of exchange coefficients) and consequently a source of error in PU-EL.

1.5 Outline

The main objective of the present work is developing a voidage correction model based on the local heterogeneity for PU-EL simulations of dense particulate systems. Specifically, we follow a chain of thoughts that is summarized by the following structure of our study: First, the validity of the filtered drag model developed by Radl and Sundaresan [16] is examined in a packed bed (Sect. 3.1). Second, the influence of fluid coarsening on the total predicted drag force, as well as the heat exchange rate, is investigated in a packed and a fluidized bed (Sect. 3.2). In addition, based on an assumed particle distribution the contribution of the voidage distribution on the deviation of drag force in coarse-grid simulation for both the EE approach and EL approach is revealed. An analysis of this deviation is then used to postulate an algorithm that maps the voidage distribution in a coarse-grid PU-EL simulation to the corresponding *local* value that would be obtained in a hypothetical fine-grid simulation (Sect. 3.3). Afterward, the reliability of the developed correction function is examined for the prediction of the total drag force through analytical considerations, as well as CFD-

DEM simulations (see Sect. 3.4). Furthermore, the accuracy of this voidage correction function is assessed for predictions of the fluid–particle heat exchange rate. Afterward, the proposed model is extended to cover different regimes of voidage gradients. Finally, a brief discussion will be performed to take the effect of different angles between the velocity and the voidage gradient field into account for future study.

2 Mathematical modeling

In the present study, simulations were performed utilizing an extended version of the CFDEM® code [28]. This code is based on an open-source CFD–DEM framework to simulate coupled fluid–particle systems. The motion of the particles is resolved by means of the DEM and simulated using the LIGGGHTS® code [29]. The interstitial fluid flow is predicted via a classical (unresolved) CFD approach and simulated using the OpenFOAM® software package [30].

2.1 Flow

The equation of motion for fluid phase and individual particles can be derived based on Navier–Stokes equation and Newton's equation of motion, respectively.

2.1.1 Fluid phase

Momentum equation for the fluid phase is solved based on the well-known Navier–Stokes equation:

$$\frac{\partial}{\partial t}\left(\boldsymbol{u}_f \varphi_f \rho_f\right) + \nabla \cdot \left(\boldsymbol{u}_f \boldsymbol{u}_f \varphi_f \rho_f\right) = -\varphi_f \nabla \cdot \tau_f - \varphi_f \nabla P_f + \boldsymbol{\Phi}_d + \varphi_f \rho_f \boldsymbol{g} \quad (1)$$

The term $\boldsymbol{\Phi}_d$ is the force exerted by particles on fluid phase per unit volume, excluding buoyancy effects. As generally accepted, we assume that the drag force is the main force contributing to the momentum exchange rate between gas and particles. These drag forces can be computed using the correlation developed by Beetstra et al. [31] as follows:

$$\boldsymbol{\Phi}_d = -\beta_{sf}\left(\boldsymbol{u}_f - \boldsymbol{u}_p\right) \quad (2)$$

$$\beta_{sf} = 18\rho_f \nu_f \varphi_f \left(1-\varphi_f\right)\frac{F\left(\varphi_f, Re\right)}{d_p^2} \quad (3)$$

$$F\left(\varphi_f, Re\right) = 10\frac{1-\varphi_f}{\varphi_f^2} + \varphi_f^2\left(1+1.5\sqrt{1-\varphi_f}\right) + \frac{0.413\,Re}{24\varphi_f^2}\frac{\left(\frac{1}{\varphi_f} + 3\varphi_f\left(1-\varphi_f\right) + 8.4Re^{-0.343}\right)}{\left(1+10^{3(1-\varphi_f)}Re^{\frac{-1}{2}(1+4(1-\varphi_f))}\right)} \quad (4)$$

Table 1 Physical properties and simulation parameters

Parameter	Studied range
Bed geometry	
H_{bed} (m)	$72d_p$–$144d_p$
L_{bed} (m)	$24d_p$–$96d_p$
w_{bed} (m)	$24d_p$–$96d_p$
Particle properties	
$\rho_s\left(\text{kg/m}^3\right]$	1000
d_p (m)	$2\times10^{-4}-2\times10^{-2}$
Contact model	*Hertzian*, inelastic, with friction and tangential history
$Y\left(\text{N/m}^2\right)$	2×10^5
ν (–)	0.45
$\mu_{c,p}$ (–)	1
e_{pp} (–)	1
$\mu_{c,w}$ (–)	0.5
e_{wp} (–)	0.3
T_{p_0} (K)	330
$C_{p,p}$(J/K)	385
Gas phase properties	
ρ_g(kg/m^3)	1.188
μ_g (Pa s)	1.79×10^{-5}
T_{g_0} (K)	335
T_{g_i} (K)	335
u (m/s)	0.1–1
Wall boundary condition	*Slip*
Simulation parameters	
Δt_{CFD}(s)	$1.25\times10^{-3}-2\times10^{-2}$
Δt_{DEM}(s)	$5\times10^{-5}-1\times10^{-4}$
$t_\sim$(s)	10
Simulation parameters	
Interpolation scheme	Linear
Discretization scheme	Gauss-limited linear second order

where Re is the particle Reynolds number, which is calculated based on the superficial fluid velocity and the particle individual speed. The equations for the filtered drag model are reported in "Appendix A". The adopted discretization and interpolation schemes are reported in Table 1.

2.1.2 Particles

The motion of individual spherical particles is predicted using Newton's equation of translational and rotational motion:

$$\rho_{p,i} V_{p,i}\frac{\partial \boldsymbol{u}_{p,i}}{\partial t} = \boldsymbol{f}_{cont,i} + \beta_{sf} V_{p,i}\left(\boldsymbol{u}_f - \boldsymbol{u}_{p,i}\right) - V_{p,i}\nabla P_{f,i} + \rho_{p,i} V_{p,i}\boldsymbol{g} \quad (5)$$

$$I_{p,i}\frac{d}{dt}\omega_{p,i} = \boldsymbol{t}_i \tag{6}$$

where the forces exerted on each particle, shown on the right-hand side of Eq. (5), include (i) contact, (ii) drag, (iii) far-field pressure and (iv) gravity contributions, respectively. The contact law is based on a Hertzian interaction model with tangential history tracking to model stick-slip transitions correctly. The contact forces in the normal and tangential direction are given by

$$\boldsymbol{f}_{cont,i,n} = -k_n\delta_p + \eta_n\Delta u_{i,n} \tag{7}$$

$$\boldsymbol{f}_{cont,i,t} = min\left\{\left|k_t\int_{t_{c,0}}^{t}\Delta u_{i,t}dt + \eta_t\Delta u_{i,t}\right|, \mu_c\boldsymbol{f}_{cont,i,n}\right\} \tag{8}$$

Here δ_p denotes the particles overlap; k and η represent the stiffness coefficient and damping factor, respectively. These parameters can be calculated as a function of the Young modulus, the Poisson ratio and the coefficient of restitution. The values of these parameters, as well as of the friction coefficient, are reported in Table 1. The torque on the right-hand side of Eq. (6), t_i, denotes the torques due to (i) particle–particle collisions (i.e., the tangential force component calculated via Eq. (8)) and (ii) fluid–particle interactions. It should be noted that the latter was assumed to be negligible in the present study. This is in line with the common assumption in the literature that only accounts for fluid flow-induced torque in case of nonspherical particles (e.g., the work of Ouchene et al. [32]).

To calculate the voidage in each fluid grid cell, particle data were mapped to the CFD cell via the "divided scheme." This scheme is based on the division of each particle's volume to 14 satellite points. The contribution of a specific particle to the voidage of fluid cells nearby the particle center is then defined based on a weighting factor. The latter is defined as the number fraction of satellite points (for each particle) in the fluid cell. As reported by Radl et al. [33] this algorithm is very robust—even for the case of particles residing near walls, or complex unstructured fluid grids with polyhedral cells. More details regarding the adopted models are available on the LIGGGHTS® online documentation [34] (http://www.cfdem.com/media/DEM/docu/Manual.html)

2.2 Heat transfer

The conservation equation for the thermal energy of the fluid phase can be derived as:

$$\varphi_f\rho_f C_{p,f}\frac{\partial T_f}{\partial t} + \nabla\cdot\left(\boldsymbol{u}_f\varphi_f\rho_f C_{p,f}T_f\right) - \nabla\cdot\left(\lambda_{eff}\nabla\left(\varphi_f T_f\right)\right) = -ha_p\left(T_f - T_p\right) \tag{9}$$

The term on the right-hand side of Eq. (9) is the volume-specific rate of heat exchange between the gas phase and the particles.

2.2.1 Closure for the heat transfer rate

Parameter h in Eq. (9) is the heat transfer coefficient, which can be evaluated from $Nu = \left(h\,d_p\right)/\lambda_f$. Nu is the Nusselt number, which was obtained using the correlation developed by Deen et al. [35] for the fluidized beds:

$$Nu = \left(7 - 10\varphi_f + 5\varphi_f^2\right)\left(1 + 0.7Re^{0.2}Pr^{1/3}\right) + \left(1.33 - 2.4\varphi_f + 1.2\varphi_f^2\right)Re^{0.7}Pr^{1/3} \tag{10}$$

More details about the implementation and verification of heat transfer equations in CFDEM can be found somewhere else [36].

3 Results and discussion

3.1 Assessment of filtered drag model for dense gas–particle flows

The validity of the filtered drag model developed by Radl and Sundaresan [16] was examined for a packed bed setup (see Fig. 2a) having a minimum voidage of 0.5. An array of Eulerian grid resolutions was probed to investigate grid effects. The packed bed setup features two regions characterized by steep voidage profiles and hence is ideally suited to investigate voidage gradient effects.

As shown in Fig. 2b, application of the filtered model deteriorates the prediction of the total drag force. Specifically, enlarging the grid size *reduces* the total drag force in a dense gas–particle flow that features voidage gradients. However, in all classical filtered drag closure models (e.g., that of Radl and Sundaresan [16]) the correction factor for the drag coefficient is smaller than unity. Therefore, employing the filtered model brings about even more reduction of the filtered drag coefficients. We note in passing that the closure of Radl and Sundaresan [16] ensures no correction in the dense packing limit. However, in regions featuring steep voidage profiles, the voidage is somewhat larger than that in the close packing limit. This causes the erroneous reduction of the drag correction in classical filtered drag models if applied to packed beds.

As a consequence, the total drag force is drastically underpredicted by classical filtered models, even though a

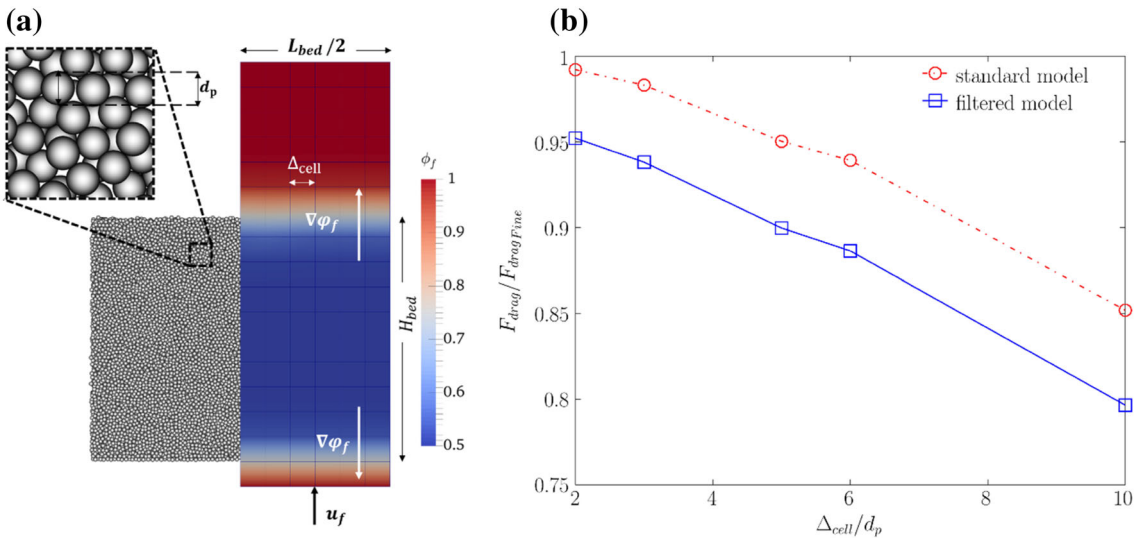

Fig. 2 **a** Schematic view of the packed bed used for simulation and **b** examination of filtered drag model and grid size on predicted total drag force in the packed bed with periodic boundary condition in lateral directions

correction of the exchange coefficients has been considered. Specifically, in the fine-grid simulation of comparably dilute flows, i.e., the ones used to establish classical filtered models, the clusters are sufficiently resolved. Gas prefers to bypass dense particle regions that are *chaotically* oriented for the sake of lower flow resistance. This fact enforces a correction factor smaller than unity for the drag coefficient in comparably dilute flow of *chaotically oriented* particle clusters.

Note that it is difficult to quantify the orientation of clusters in clustered suspensions, and that a significant level of anisotropy might be present. We have adopted the wording "*chaotically*" to reflect that the cluster orientation originates from a fluid mechanical instability that leads to a chaotic system behavior as discussed by Fullmer and Hrenya [37].

Clearly, a correction for *chaotically oriented* particle clusters cannot account for the effect of regions with a well-defined voidage gradient or suspensions with *distinctly oriented* particle clusters. The latter are suspensions that feature a large voidage gradient into one direction, e.g., as this in the packed bed depicted in Fig. 2a. For suspensions with *distinctly oriented* particle clusters a finitely sized Eulerian grid smears out the voidage distribution. Thus, particles are predicted to experience a (on average) higher voidage, and consequently a smaller drag force when using coarse Eulerian grids would be predicted. Hence, a correction factor larger than unity would be required for the exchange coefficients to correct for this error.

An alternative view on the difference between *chaotically* and *distinctly oriented* particle clusters is obtained when considering the angle between the main flow direction and the voidage gradient. Particularly, in a clustered suspension, the main flow direction has in general a certain angle relative to the *local* voidage gradient direction. This necessitates a correction factor of smaller than unity for the drag coefficient, as suggested by Li et al. [23]. However, in a packed bed, i.e., a prototype of a *distinctly oriented* particle suspension, fluid always flows parallel to the voidage gradient. Thus, a correction factor of larger than unity is needed. In short, utilization of a classical filtered model decreases the exchange coefficient even more, which is due to the incorrect assumption of a *chaotically oriented* particle suspension.

3.2 Systematic evaluation of the effect of fluid coarsening

We now aim on proving that smearing out the voidage distribution in a dense gas–particle flow is responsible for the deviation of the total drag force in coarse-grid simulations. Specifically, a calculation of the total drag force was performed for a packed bed considering the three situations depicted in Fig. 3:

(i) A fine grid, in which the grid is aligned with the jump in the voidage profile. This case reflects the "perfect" solution, i.e., the analytically correct drag force (Fig. 3a).
(ii) A "coarse Eulerian grid" with the same particle population as in case (i), but the jump in voidage profile is located at the center of the interface cell (Fig. 3b), as shown as dashed line in Fig. 3a for base case;
(iii) A "coarse Lagrangian grid" with the same particle population and grid as in case (ii), but the voidage is linearly interpolated at each particle position (Fig. 3c). This corresponds to methodology which is typically used in PU-EL simulations.

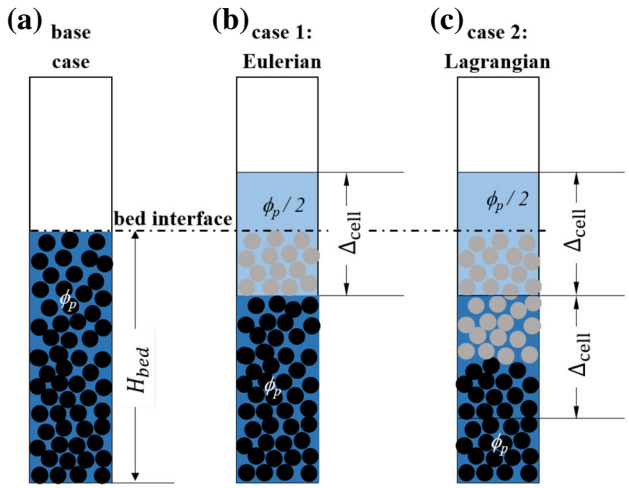

Fig. 3 Schematic representation of voidage distribution in the packed bed for **a** an extremely fine grid and for which the grid cell is aligned with the voidage jump, **b** a coarse Euler grid and **c** coarse Lagrangian grid. Gray circles indicate particles that are influenced by the voidage gradient in the interface cell

The profiles for the voidage and the drag force corresponding to these three situations are presented in Fig. 4. As shown in Fig. 4a, the drag force follows the same qualitative trend of the voidage distribution along the bed. Hence, the prediction of the total drag force can be improved if the voidage is corrected to the corresponding value in the fine-grid one. Upon increasing the cell size/bed length ratio, i.e., decreasing the mesh resolution or considering thinner packed beds, the total drag force calculated in Euler and Lagrangian grid drops. Surprisingly, for the latter the deviation from fine-grid results is higher (see Fig. 4b). This is since the sharp gradient of voidage cannot be accurately captured due to interpolation at the particle position. As discerned from Fig. 4b, the deviation of the total drag force will be drastically increased in case the maximum packing limit increases from 0.5 to 0.8 due to particle concentration effect on the drag force. Thus, the maximum particle volume fraction has a significant effect on the error in the predicted drag force. Such extremely dense beds are observed for strongly polydisperse granular materials, for which the calculated error can, in extreme cases, be as high as 60%.

As mentioned before, coarsening the grid size reduces the voidage experienced by individual particles on average. This is followed by a reduction of the drag coefficient, which is especially pronounced for densely packed systems. This effect is strong when using a PU-EL approach due to the linear interpolation of the voidage at particle position. In contrast, in the EE approach the porosity is lower, but the region that is used for the calculation of drag force is larger than that when using a fine grid. As shown in Fig. 3c, in the PU-EL approach a larger number of particles (shown in gray color) are influenced by the blurred voidage profile that occurs near the interface cell. Hence, the deviation of the total drag force when using the EE approach is lower than the one for a PU-EL approach.

In summary, it can be concluded that unreliable prediction of voidage distribution and its gradient is responsible for the failure of coarse-grid simulation in accurately predicting the drag force. Therefore, it is clear that a correction of the voidage can eradicate the main source of such deviations to some extent.

To generalize this finding to heat transfer and more complex flow situations, a set of simulations was performed to examine the effect of fluid coarsening on the total heat exchange rate in a bubbling fluidized bed. The corresponding results are summarized in Fig. 5, which illustrate the effect of CFD cell coarsening on the predicted thermal performance of the fluidized bed. As shown in this figure, coarsening the grid underpredicts the total heat exchange rate. Therefore, the time evolution of temperature is slowed down in the fluidized bed.

3.3 Voidage correction model

As demonstrated in the previous section, to improve the prediction of the drag force, a correction of the voidage before computing the exchange coefficients is required. To do so, the typical flowchart for CFD-DEM coupling was slightly modified to take the correction of the voidage for the calculation of drag force into account, as depicted in Fig. 6. It should be highlighted that in the modified approach (i.e., when using the voidage correction), the voidage experienced by each particle is *only* corrected for calculation of the drag force. This means that the voidage distribution in the fluid grid cells is not corrected. Therefore, the conservation of the voidage is not problematic. This can be also supported by the fact that the voidage experienced by each particle is *individually* calculated and corrected.

3.3.1 Simple algorithm for voidage jumps

We next aim on correcting for grid size effects in a situation in which the voidage changes within one computational (Eulerian) cell from unity to some minimum values. Thus, we consider a situation near the front row of particles in a packed bed or near the interface of a dense particle cluster. Specifically, we seek a correction function that has the interpolated voidage φ_f from a coarse grid as input and yields the correct voidage jump once a particle is outside of the dense region (i.e., the packed bed or the cluster). The latter is denoted as the corrected voidage $\varphi_{f,\mathrm{corr}}$ in what follows. In such a way, regions with voidage jumps can be correctly handled, even when using comparably coarse grids.

It is clear from geometrical arguments that the correction function must be a step function at $\varphi_f = 1-\varphi_{p,\max}/2$ in case

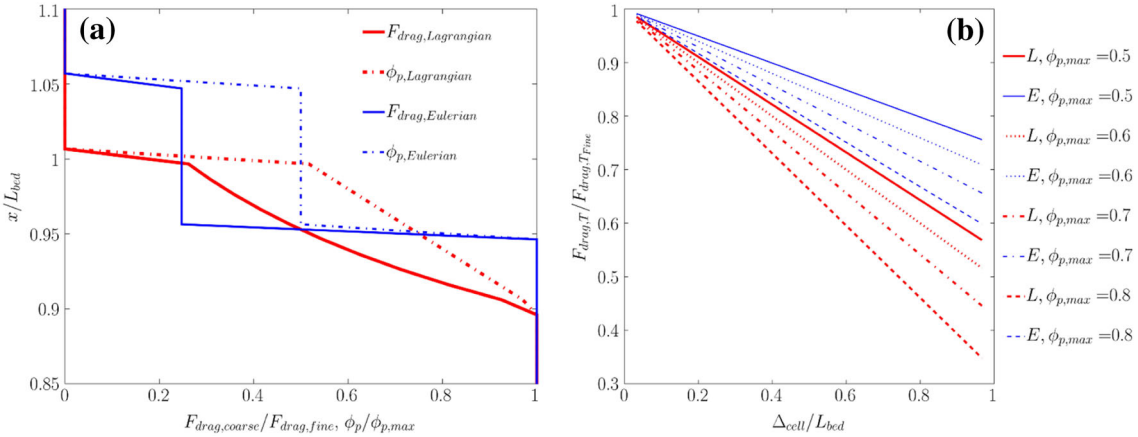

Fig. 4 **a** Distribution of particle volume fraction and drag force for Lagrangian and Euler cases (the forces have been normalized with the corresponding values in infinitely fine-grid one), **b** effect of grid size on normalized total drag for Lagrangian and Euler cases

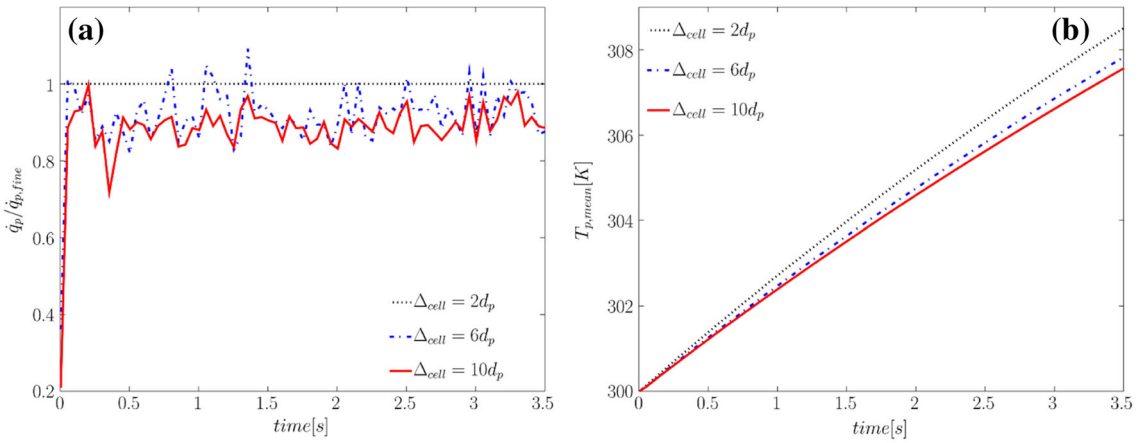

Fig. 5 Effect of the grid size on the variation of **a** the total particle heat exchange rate (the time-averaged deviation for a cell size of Δ_{cell}/d_p of 6 and 10 is -7.8% and -10.8%, respectively), as well as **b** the mean particle temperature versus time in the fluidized bed

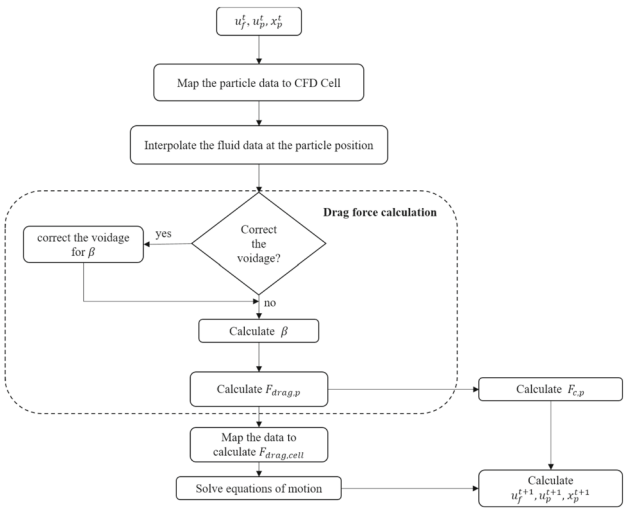

Fig. 6 CFD-DEM coupling flowchart including the correction of the voidage for the calculation of drag force (the section has been shown in dash line)

a linear interpolation of the voidage to the particle location is used (see Fig. 4 for an illustration). Unfortunately, the stability of the overall numerical algorithm is deteriorated in case a step function is used. Similarly, relying on cell-based values of the voidage, i.e., not using a linear interpolation to the particle position, is problematic when using the PU-EL approach due to stability reasons. As a compromise, we find that a piecewise function, such as the one shown in Fig. 7a, improves the prediction of the voidage jump without leading to a significant loss in stability.

$$\varphi_{f,\text{corr}} = \begin{cases} 1-\varphi_{p,\max} & \varphi_f \le \varphi_{f,l} \\ \varphi_{p,\max}\left(\frac{\varphi_f-\varphi_{f,u}}{\varphi_{f,u}-\varphi_{f,l}}\right)+1 & \varphi_{f,l} < \varphi_f < \varphi_{f,u} \\ 1 & \varphi_{f,u} \le \varphi_f \end{cases} \tag{11}$$

As shown in Fig. 7b, employing this correction function can improve the prediction of the total drag force by 15%

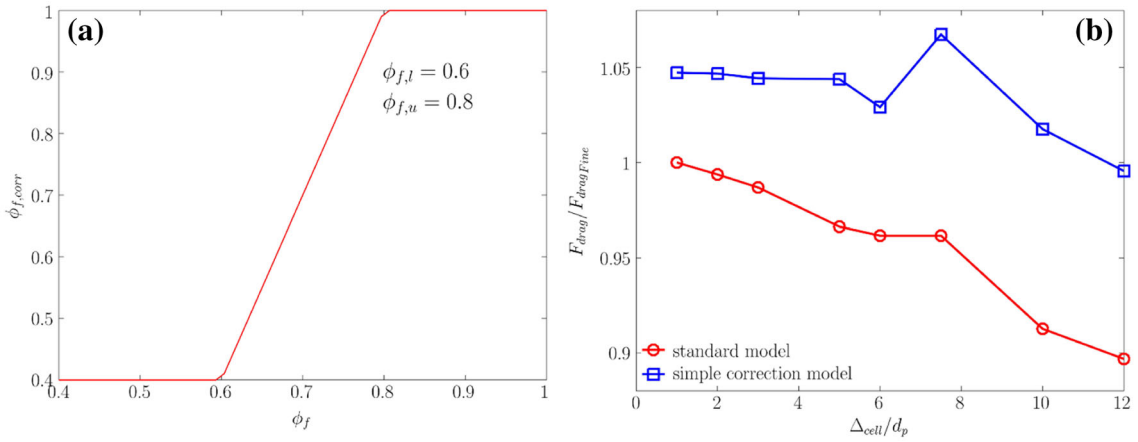

Fig. 7 **a** Correction function for gas volume fraction, as well as **b** the effect of the correction function on the total drag force in a packed bed ("standard model" refers to using no correction, i.e., setting $\varphi_{f,\mathrm{corr}} = \varphi_f$)

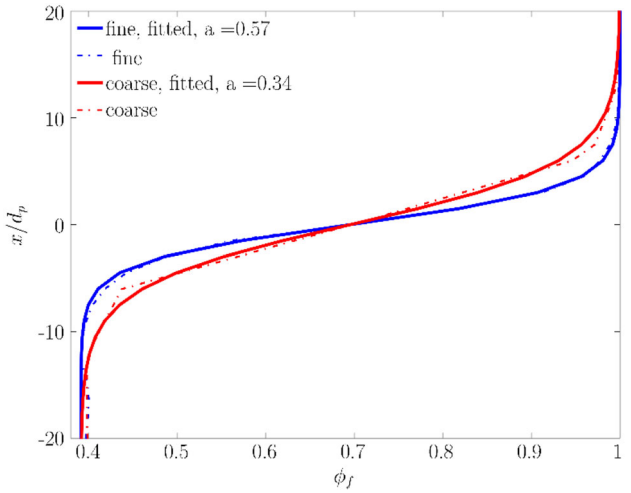

Fig. 8 Voidage profile and fitted sigmoidal distribution in a packed bed with **a** $\Delta_{\mathrm{cell,fine}} = 2d_p$, $\Delta_{\mathrm{cell,coarse}} = 6d_p$, **b** $d_p = 20\,\mathrm{mm}$, $\Delta_{\mathrm{cell,fine}} = 2d_p$

for $\Delta_{\mathrm{cell}}/d_p = 12$. Another point discerned from this figure is a 5% overprediction observed for a fine-grid simulation when using the simple correction model detailed in Eq. (11). This is due to the way that voidage has been corrected in the range $0.4 < \varphi_f < 0.6$. In detail, based on the correction function, particles experience a lower corrected voidage (see Fig. 7a) and consequently a higher drag force, in this range. However, the particle volume fraction should remain unchanged for highly resolved simulation even after correction. This deficiency proves that the correction function should be developed in such a way that the voidage distribution does not change upon using fine grids. Clearly, grid size must be accounted for in the correction function, which is not the case in the simply algorithm detailed in the previous paragraph. Furthermore, the overprediction observed in Fig. 7b can be partially attributed to the inability to obtain the correct superficial fluid speed in CFDEM®. This is due to the fact that in the underlying CFD tool (i.e., OpenFOAM®) the voidage is discretized at the cell centroid, while the fluid velocity is discretized at the face center. While the error associated with this problem of obtaining consistent superficial speeds appears to be fundamental, it is small and hence not discussed in greater detail.

It can be concluded that the robustness of the above simple algorithm depends on the lower and upper threshold value chosen for voidage. In addition, the implemented correction model can overpredict the total drag force in fine-grid simulation that may resolve a finite voidage gradient. Consequently, we next seek a more systematic development that can be applied for wide range of grid sizes.

3.3.2 Generalized algorithm for high voidage gradients

The voidage distribution in the packed bed, as well as near the bubble interphase in a bubbling fluidized bed, was investigated next. Therefore, different cases with a wide range of particle sizes, grid resolutions and bed geometries were considered. It should be noted that near the bubble interphase, the voidage profile was probed in the direction aligned with the voidage gradient. As shown in Fig. 8, our preliminary results for the voidage distribution prove that in the regions with a high voidage gradient, the voidage distribution can be approximated using a sigmoidal function. This is true for both packed and fluidized beds, as shown in Figs. 8 and 9. Therefore, a scaled voidage can be introduced, which is most naturally represented by

$$\varphi'_f = \frac{\varphi_f - \varphi_{f,\min}}{\varphi_{f,\max} - \varphi_{f,\min}} = \frac{1}{1 + e^{-a(x/d_p)}} \tag{12}$$

where x represents the distance from the interface position x_0.

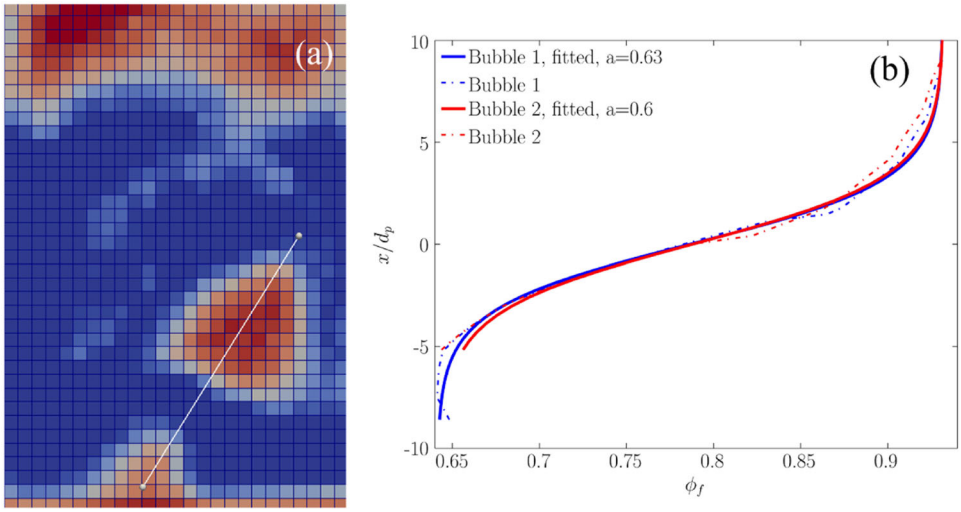

Fig. 9 **a** Voidage profile and **b** fitted sigmoidal distribution in the fluidized bed for different bubbles at the line plotted aligned with the voidage gradient in the bubble

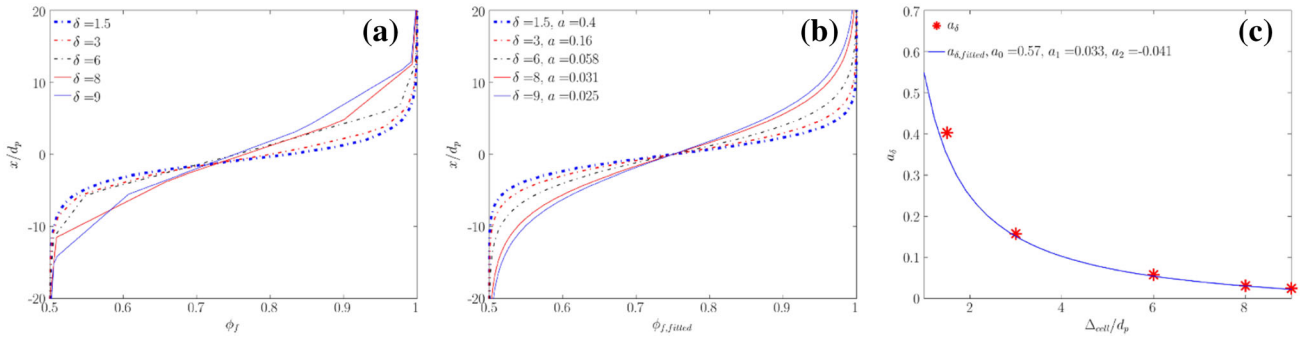

Fig. 10 Comparison of **a** the voidage distribution and **b** the fitted sigmoidal distribution in a packed bed with dimension of $54d_p \times 54d_p \times 96d_p$ for various grid sizes and **c** dependency of the scaled exponent a_δ on grid size $\left(a_\delta = \frac{a}{\Delta_{\text{cell}}/d_p}\right)$

To generalize the function fitted to the voidage distribution, a set of simulations was performed for a wide range of particle diameters, cell sizes and bed dimensions for the packed bed. As shown in Fig. 10a, b, the voidage distribution can be well approximated with a sigmoidal function for various cell sizes. As shown in Fig. 10c, the scaled model parameter a_δ, i.e., $\frac{a}{\Delta_{\text{cell}}/d_p}$, can be fitted using a harmonic function with the three parameters $a_0 = 0.57$, $a_1 = 0.033$ and $a_2 = -0.041$.

$$a_\delta = \frac{a}{\Delta_{\text{cell}}/d_p} = \frac{a_0}{\Delta_{\text{cell}}/d_p - a_1} + a_2 \tag{13}$$

Consequently, the scaled voidage distribution in a coarse-grid simulation can be mapped to the corresponding distribution in a fine-grid simulation. The corresponding mapping function is shown in Fig. 11 and is given by

$$\varphi'_{f,f} = \left[\left(\frac{1}{\varphi'_{f,c}} - 1\right)^{\left(\delta_f a_{\delta_f}\right)/\left(\delta_c a_{\delta_c}\right)} + 1\right]^{-1} \tag{14}$$

where a_{δ_f} and a_{δ_c} are the *scaled* model parameters for the fine- and coarse-grid simulations, respectively, which can be evaluated from Eq. (13). Note, in most practical situations, it is reasonable to use $\delta_f = 1$, i.e., correct the voidage to a fluid grid with a cell spacing that equals the particle diameter. Also, it will be necessary to limit a_{δ_c} to some positive nonzero value for very large cell sizes Δ_{cell}/d_p to avoid division by zero in Eq. (14).

After finding the correlation for the model parameters, the remaining challenge is calculating the minimum and maximum value of the voidage in the neighboring grid cells. This is necessary to calculate the voidage from the scaled voidage via Eq. (12). A straight-forward, but not necessarily the most efficient, algorithm would simply loop over the neighboring cells and calculate these limiting values for the voidage. Such a loop is generally computationally expensive, especially in case of multi-processor simulations where mesh information is residing on a distributed memory. Therefore, we propose an alternative approach in which we compute the minima as follows (more details about the method of calculation of these quantities can be found in "Appendix B"):

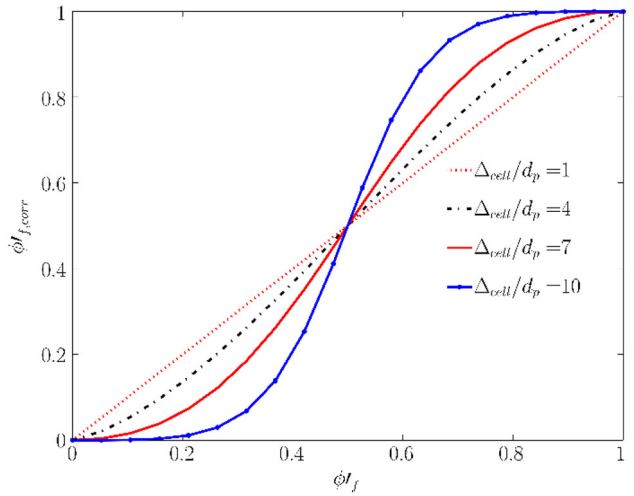

Fig. 11 Correction function for the scaled voidage for different normalized grid sizes Δ_{cell}/d_p

$$\varphi_{f,\min} = \varphi_f - \frac{|\nabla\varphi_f|}{a_\delta \delta/d_p}(\gamma+1) \tag{15}$$

$$\varphi_{f,\max} = \left(1+\frac{1}{\gamma}\right)\left[\varphi_f - \varphi_{f,\min}\right] + \varphi_{f,\min} \tag{16}$$

where γ is given by

$$\gamma = \frac{\frac{a_\delta \delta}{d_p} - \frac{|\nabla^2\varphi_f|}{|\nabla\varphi_f|}}{\frac{a_\delta \delta}{d_p} + \frac{|\nabla^2\varphi_f|}{|\nabla\varphi_f|}} \tag{17}$$

These equations necessitate a calculation of the voidage gradient when correcting the voidage at the particle position, which is typically computationally more affordable. Furthermore, we note that the curvature of the voidage field can be considered when calculating γ, meaning that the proposed correction is valid even on coarse grids for which the voidage profile is no longer linear.

3.3.3 Weighted generalized algorithm for arbitrary voidage gradients

The generalized sigmoidal correction function discussed in the previous section is strictly valid only for situations that feature high voidage gradients. Our preliminary work showed that utilizing such a correction for voidage fields that are characterized by relatively low gradients yields an artificial increase in the total drag force. For such fields, the scaling shown in Eq. (12) is no longer meaningful, since $\varphi_{f,\max} - \varphi_{f,\min}$ approaches zero. Consequently, our assumption of a *distinctly oriented* particle cluster, which forms the basis of our correction, is no longer valid.

To enable our generalized algorithm to also handle low voidage gradients, we next propose a *weighted* correction algorithm. This algorithm is based on a degree of heterogeneity factor D_h that quantifies whether a *distinctly oriented* particle cluster is present or not in a computational cell. In case the voidage gradient is close to the maximum value possible in a computational cell, the contribution of the sigmoidal correction function outweighs. In contrast, in case the distribution of particles is almost uniform, no correction is needed and the sigmoidal distribution has a marginal contribution. The postulated weighted correction function is

$$\varphi'_{f,fi} = \varphi'_{f,\text{sigm}}\, D_h + \varphi'_{f,c}\,(1 - D_h) \tag{18}$$

Here the value for $\varphi'_{f,\text{sigm}}$ is determined via the generalized sigmoidal correction function shown in Eq. (14). We will show in the section that the simple expression in Eq. (18) is indeed suitable to account for situations with low to high voidage gradients. The degree of heterogeneity is calculated based on the ratio of the local voidage gradient to the corresponding maximum possible value $\left(\frac{\varphi_{p,\max}}{\Delta_{\text{cell}}}\right)$ in the cell. It is hence defined by

$$D_{\text{h}} = \frac{|\nabla\varphi_f|}{\frac{\varphi_{p,\max}}{\Delta_{\text{cell}}}}. \tag{19}$$

3.4 Benchmarking the voidage correction algorithms

3.4.1 Drag force in case of voidage jumps

The fidelity of the proposed correction algorithms for predicting the total drag force is examined next. To do so, after successful implementation of the proposed voidage correction model in CFDEM®, a set of simulations was performed for various grid sizes, i.e., $2d_p$–$10d_p$, for the generalized algorithm (denoted as "generalized algorithm," see Sect. 3.3.2). In a fluidized bed the angle between the flow field and voidage gradient contributes to the exchange coefficients [23]. As discussed in Sect. 3.4.4, our correction algorithm will be evaluated for packed beds in the present work—the evaluation for fluidized bed (and hence arbitrary angles between flow field and the voidage gradient) will be left for future work. The benchmark case is a packed bed with a length of $72d_p$ that features two voidage jumps at the inlet and outlet of the particle packing. (More details can be found in Table 1.)

The main criterion for the reliability of the simulation results was that the total drag force in a coarse-grid simulation compared favorably with that in a highly resolved simulation. As shown in Fig. 12a, upon employing the correction model, the voidage distribution can be more accurately predicted in the packed bed at the studied range of cell size and for the region with a sharp gradient of the voidage. As discerned in

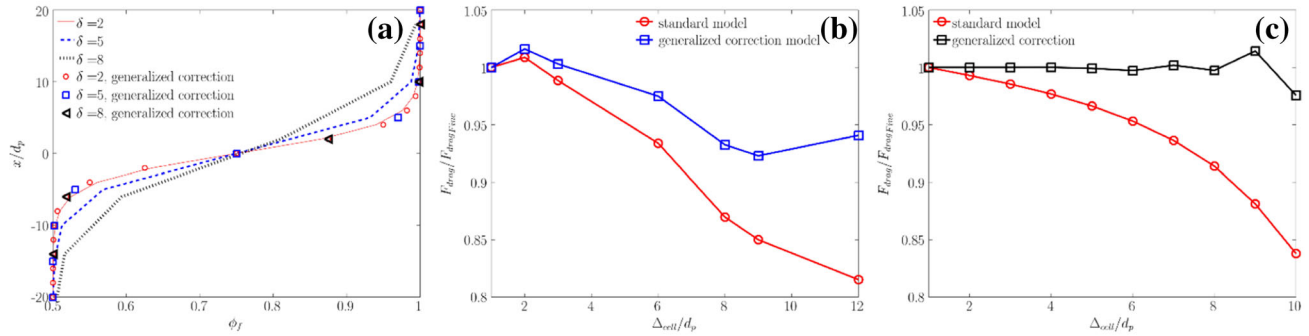

Fig. 12 Effect of employing the correction algorithm for a packed bed with a length of $72d_p$ **a** voidage distribution versus bed height for the uncorrected case, as we as the case with generalized voidage correction; **b** total drag for different mesh resolutions; **c** total drag force analytically calculated for the voidage distribution predicted by CFDEM®; "standard model" refers to using no correction

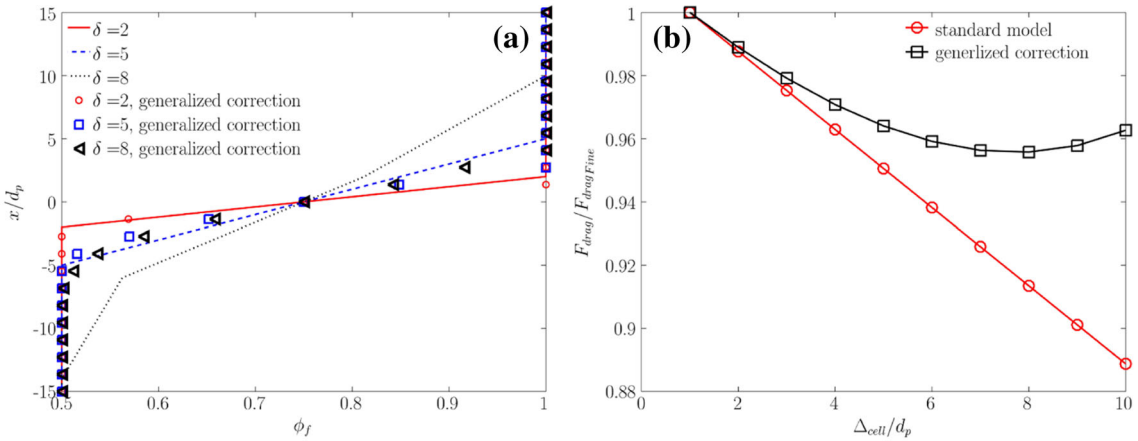

Fig. 13 Effect of employing the correction algorithm for the system shown in Fig. 2c **a** voidage distribution versus bed height for the uncorrected case, as we as the case with generalized voidage correction; **b** total drag for different mesh resolutions

Fig. 12b, the improved prediction of the voidage distribution through the proposed correction function reduces the effect of a coarse computational grid on the total predicted drag force. However, due to the interpolation of the velocity field at the particle positions (note that the fluid velocity is evaluated at the cell faces), there is still a remaining error when using the generalized algorithm. Unfortunately, this amount of deviation (typically up to 7%) is inevitable since the used interpolation scheme cannot guarantee a correct superficial fluid speed at the particle location. To quantify the effect of this incorrect superficial speed, the total drag force was analytically calculated based on a corrected velocity field and the generalized sigmoidal voidage distribution. As depicted in Fig. 12c, when using a correct velocity field, the total drag force can be accurately predicted with less than 2 % relative error when using the generalized algorithm.

The proposed voidage correction function was also examined for situations with a linear decrease in the voidage in the interface cell as schematically illustrated in Lagrangian case of Fig. 3. The results are depicted in Fig. 13a and show that the voidage correction improves the predicted value for the voidage in the bed to a great extent. However, small deviations from the corresponding value in the fine-grid simulation can be still observed. Therefore, it is expected that the predicted total drag force shows some deviations even after the voidage correction. As shown in Fig. 13b, by correction of the voidage, the total drag force in the bed will be improved by 7.7% for an Eulerian cell size of $10\,d_p$. The maximum error in case the corrected voidage is used is below 5% for all grid resolutions studied.

3.4.2 Drag force in case of finite voidage gradients

In order to check the generality of the proposed voidage correction model to situations with different voidage gradients $\nabla\varphi_f$, an additional array of simulations was performed. To generate a defined voidage gradient, and as proposed by ten Cate and Sundaresan [20], an original particle bed (indicated with the subscript 0) having a uniform volume fraction $\varphi_{p,0}$

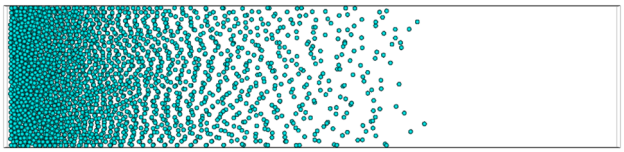

Fig. 14 Schematic distribution of particle with constant voidage gradient in the packed bed

was stretched. Thus, the original particle positions $x_{p,0}$ were stretched to new particle position $x_{p,\text{new}}$ as follows:

$$\frac{\Delta x_{p,\text{new}}}{\Delta x_{p,0}} = \frac{\varphi_{p,0}}{\varphi_{p,\text{new}}} \tag{20}$$

Here we require $\varphi_{p,new} = C_\varphi x + b$, i.e., we realize a linear voidage distribution. Consequently, $\nabla\varphi_{p,\text{new}} = C_\varphi$. Particles were initialized in LIGGGHTS®, compacted to form a random bed, and then the position of each particle was modified based on Eq. (20). An illustration of the resulting particle bed is shown in Fig. 14.

As shown in Fig. 15a, application of the sigmoidal correction model (i.e., the generalized correction algorithm) for a constant voidage gradient of $0.3\frac{\varphi_{p,\max}}{\Delta_{\text{cell}}}$ *worsens* the prediction of total drag force. This is due to the artificial underprediction of the voidage as already discussed in "Sect. 3.3.3."

However, as shown in Fig. 15a, b, using the weighted generalized correction algorithm significantly improves the prediction of the total drag force. This is true for various values of the voidage gradient and cell sizes up to $10d_p$. While the need for a correction is not justified for low values of the voidage gradient (see Fig. 15a), the weighted generalized algorithm greatly improves the predictions for the larger value of $0.5\varphi_{p,\max}/\Delta_{\text{cell}}$ as shown in Fig. 15b.

3.4.3 Validity of the algorithm for heat transfer predictions

The rate of heat transfer in the gas–particle flow is mainly influenced by the particle volume fraction via the heat transfer coefficient and the slip velocity. Hence, unreliable prediction of voidage can influence the accuracy of heat transfer rate and temperature distribution as well. Consequently, the application of the voidage correction, as suggested in the present work for particle–fluid momentum exchange, can be extended to PU-EL simulation of heat and/or mass transfer in gas–solid flows. To assess the fidelity of the proposed voidage correction algorithms for prediction of heat transfer, a set of simulations of gas–solid system with fixed particles and sharp voidage gradient was performed considering various cell sizes. It should be noted that the simulation setup is the same as one used for Fig. 12. To compare the total rate of heat transfer in a steady-state condition, the particles' temperature was kept constant, and the length of the bed chosen in such a way that the gas experiences insignificant heating when flowing through the bed.

The results of simulation for standard (i.e., no correction) and the generalized sigmoidal model are depicted in Fig. 16. As discerned from this figure, increasing the grid size reduces the total heat transfer rate in the system. Similar to its effect on the drag force, coarsening the grid smears out the voidage and consequently decreases the average heat transfer coefficient. This trend demonstrates the role of the voidage in prediction of system thermal performance. However, as depicted in Fig. 16, employing the voidage correction model can only partially improve the prediction of the total heat transfer rate in coarse-grid simulations. This is surprising, since the correction factor for the Nusselt number, $\frac{Nu_{p,\text{corr}}}{Nu_{\text{p}}}$, at a cell/particle size ratio of 8 falls into the range of 0.86–1.28 (see Fig. 16c). This is a lower degree of correction in comparison with the drag coefficient ($0.71 < \frac{\beta_{\text{corr}}}{\beta} < 1.4$, see Fig. 17a in the following paragraph). The observed more significant deviation for the heat transfer rate can hence be related to the interpolation of fluid quantities in the CFD cell. In other words, the fluid–particle heat exchange rate is influenced not only by the interpolation of the voidage and the fluid velocity field, but also by the fluid temperature interpolation. The predicted deviation can be associated with the weak sensitivity of the Nusselt number to the particle volume fraction and the strong influence of the fluid–particle relative speed which is analyzed. Indeed, the used drag law [31] features a more significant dependency on the voidage, but a lower sensitivity to the relative speed when compared to the used Nusselt number correlation [35]. Therefore, the fidelity of the proposed voidage correction function is eroded by the interpolated fluid velocity and temperature. This is since fluid velocity and temperature affect the heat transfer coefficient and the heat transfer rate. To isolate the effect of these two sources of error (i.e., interpolation of velocity and temperature), two sets of simulation were performed with constant values of: (i) gas–particle relative velocity and (ii) gas and particle temperatures + relative velocity. Comparing Fig. 16a, b demonstrated that upon using constant relative velocity, the deviation of total exchange rate in the standard model decreases to around six percent. The prediction of the corrected model improves to approximately five percent. When using a constant gas–particle temperature difference the deviation decreases especially for the generalized correction model. Therefore, it can be concluded that the fidelity of the proposed voidage correction function is mainly governed by the relative contribution of flow quantities, such as temperature and velocity field compared to that of the solid volume fraction on the predicted exchange rate. In short, the closure law employed for the computation of exchange coefficients must be considered. For instance, when applying the correlation of Deen et al. [35], the dependency of exchange

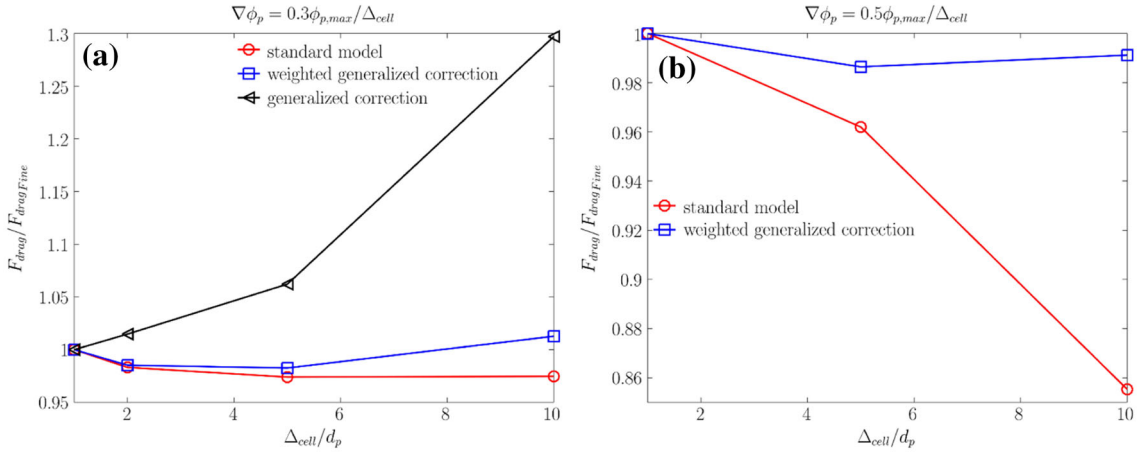

Fig. 15 Assessment of developed correction model for situations with a voidage gradient of **a** $0.3\varphi_{p,\max}/\Delta_{\text{cell}}$ and **b** $0.5\varphi_{p,\max}/\Delta_{\text{cell}}$

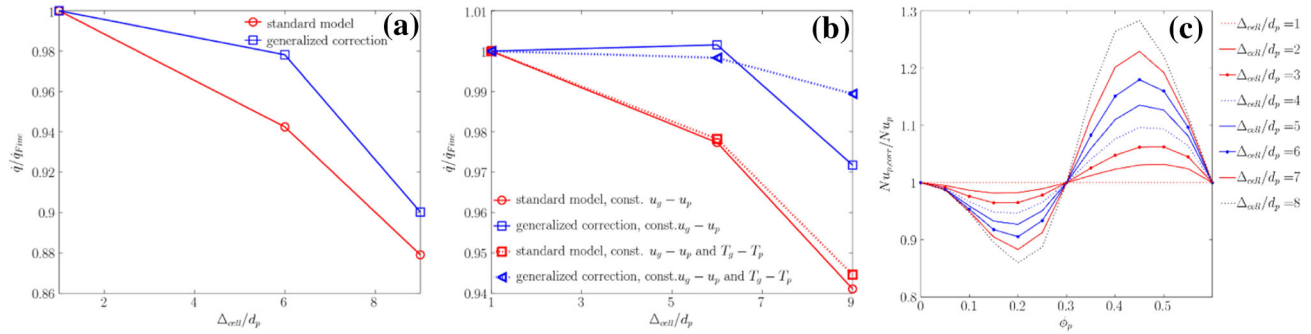

Fig. 16 Assessment of developed voidage correction algorithm for predicting heat transfer rates in a packed bed for **a** generalized correction model and **b** enforcing constant relative velocity and/or temperature difference and **c** dependency of correction factor for the Nusselt number on solid particle volume fraction

coefficient is dominated by the flow speed rather than the solid concentration.

As it can be concluded from this section, the correction model presented in this study is not limited to the hydrodynamics and can be used for heat and mass transfer without modification.

3.4.4 Discussion on the future extension of the algorithm to consider the relative voidage gradient angle

The proposed algorithms have been tested for situations in which the voidage gradient is aligned with the flow field. Also, our algorithm can be potentially useful for more complex situations in which the angle θ between the voidage gradient and the main flow direction is nonzero, e.g., as encountered in fluidized beds. With "main flow" we hereby refer to the fluid–particle relative speed. To do so, the following approach was adopted

(i) The correction function proposed in the current work was used for situations in which the fluid–particle relative speed is aligned with the voidage gradient (see Fig. 17a). Thus, based on the corrected voidage a corrected drag coefficient β_{corr} can be calculated, and one can define:

$$\frac{\beta_{\text{corr}}}{\beta}(\theta = 0) = C_\varepsilon \tag{21}$$

(ii) The filtered drag model proposed by Radl and Sundaresan [16] for clustered flows, i.e., chaotically oriented particle clusters, was used for situations in which the voidage gradient is perpendicular to the fluid–particle relative speed (see Fig. 17b):

$$\frac{\beta_{\text{corr}}}{\beta}\left(\theta = \frac{\pi}{2}\right) = C_f \tag{22}$$

(iii) Following the work of Li et al. [23], and as shown in Fig. 17c, a cosine function was fitted to calculate the correction factor for the drag coefficient for intermediate angles:

$$\frac{\beta_{\text{corr}}}{\beta} = \frac{C_\varepsilon + C_f}{2} + \frac{C_\varepsilon - C_f}{2}\cos(2\theta) \tag{23}$$

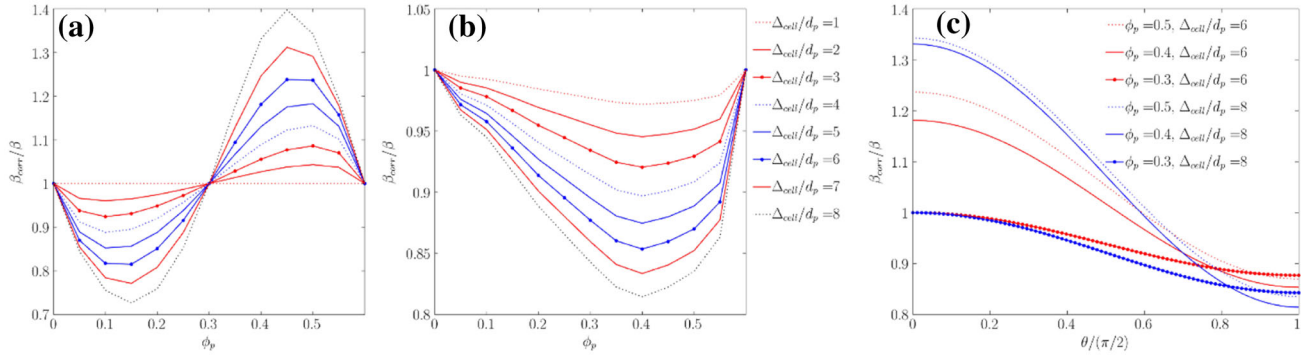

Fig. 17 Dependency of the drag correction factor $\left(\frac{\beta_{\text{corr}}}{\beta}\right)$ versus the coarse-grid voidage for **a** the generalized correction algorithm, **b** the filtered drag model proposed by Radl and Sundaresan 14 and **c** for different values of the voidage gradient angle

As shown in Fig. 17c, the proposed algorithm will hence account for the voidage, the Eulerian grid cell size, as well as the orientation of the voidage gradient when correcting for the drag coefficient. While the magnitude of the voidage gradient is accounted for in the limit of $\theta = 0$, it is not considered when blending between distinctly and chaotically oriented particle clusters. Most importantly, for particle volume fractions φ_p near the close-packing limit, the proposed algorithm would suggest a much stronger positive drag correction compared to the negative correction proposed by Radl and Sundaresan [16]. This remarkable finding may explain the nonmonotonic behavior of the data for $\varphi_p > 0.5$ in Fig. 3 of Radl and Sundaresan [16], i.e., the strong increase in the drag correction near the close-packing limit.

4 Conclusion

In the present work, the effect of grid coarsening and hence that of unresolved property profiles on the predicted flow and thermal behavior of dense fluid–particle systems were investigated. Initially, the validity of filtered drag models developed for dilute flow was evaluated; it was shown that these filtered models cannot be reliably used for dense particulate flows with a coherent particle ordering. Specifically, we presented that available filtered models worsen the prediction for such systems on comparably coarse computational grids. In fact, while *chaotically oriented* particle clusters result in a reduction of the effective drag coefficient, the opposite is true for *distinctly oriented* particle clusters: Due to the nonlinear dependency of the drag coefficient on the voidage, *distinctly oriented* particle clusters necessitate a positive drag correction when performing coarse-grid simulations.

To systematically evaluate the influence of unresolved voidage fluctuations in dense flows, a set of simulations was performed considering packed and fluidized beds using the software CFDEM®. The result of PU-EL simulations demonstrated that coarsening the CFD grid size reduces not only the total drag force, but also the total heat exchange rate in these flows. Therefore, in contrast to comparably dilute flows, a correction factor of larger than unity is required for all exchange coefficients, i.e., the drag and heat or mass transfer coefficients. Another interesting finding is that the deviation of the total drag force when using the EE approach is *lower* than the one when using a PU-EL approach. This is in contradiction with the results of simulations presented by Cloete et al. [38]. Specifically, these authors claimed that a discrete phase method (similar to the PU-EL approach considered in our present work) provides a better prediction of solid fluxes in coarse-grid simulation of a circulating fluidized bed. This disagreement can be explained by the comparison of the fluidization regime and the criterion chosen for judging the reliability of the simulation approach. In detail, in the case simulated by Cloete et al. [38], i.e., risers, the particles flow in form of clusters. Thus, the flow is comparably dilute, and as mentioned before, the effect of the grid size on the drag force arises due to unresolved voidage fluctuations and *chaotically oriented* particle clusters. In addition, Cloete et al. [38] used macroscopic bed characteristics as the measure for judging the reliability of the simulation. Particularly, they compared solid fluxes, while—as reported in their publication—the granular temperature could not be held constant. Since the latter has a fundamental effect on the voidage distribution, the peculiar behavior of the discrete simulation could not be fully revealed. The latter was the case in our present study, and hence we were able to identify this important shortcoming of the PU-EL approach.

We ultimately demonstrate that when adopting an algorithm to map the voidage in a coarse-grid simulation to the corresponding value in a fine-grid simulation, one can improve the prediction of exchange coefficients. Specifically, the voidage distribution in a particle system with voidage jumps was approximated using a sigmoidal function for different grid sizes. This allowed us constructing a voidage correction function that yields stable and accurate results. This correction of the voidage is of high importance to exclude the numerical artifacts from CFD-DEM predictions

as reported by Lu et al. [24]. Considering DNS results as a reference, they proved that the coarse-grid simulation of gas–particle flow using EE and EL approach fails to predict the voidage distribution accurately. After successful implementation of the voidage correction function in CFDEM®, a grid resolution study considering a packed bed proved the fidelity of the proposed correction function. To generalize the proposed correction function for various voidage gradients, the correction model was extended through a weighting function. Our simulation results prove the validity of such an approach for various values of the voidage gradient. Finally, the proposed correction function was applied for the prediction of heat transfer rates in a packed bed. An improvement of the total predicted heat transfer rate could be demonstrated for coarse-grid simulations. However, we show that this improvement is small compared to that for the drag force. This indicates that the functional form of the closure employed, specifically the relevance of the fluid–particle relative speed compared to that of the voidage, affects the overall fidelity of the proposed correction concept. Thus, while a voidage correction helps to improve the prediction of heat and mass transfer rates, more work is needed to account for grid effects on the fluid speed and temperature (or concentration) seen by individual particles.

Ultimately, an algorithm was proposed that blends the correction developed in this study with classical filtered drag models for chaotically oriented particle clusters. The remaining challenge is to systematically investigate whether the proposed blending function, inspired by the work of Li et al. [23], is indeed suitable for a wide range of applications. Along the same line of thoughts, the magnitude of the voidage gradient may be a suitable candidate to further improve the proposed blending between distinctly and chaotically oriented particle clusters. However, such an improvement first necessitates a more profound understanding of the role of voidage gradients on the drag in chaotically oriented particle clusters.

Acknowledgements Open access funding provided by University of Graz University of Technology.

Funding Funding was provided by Die Österreichische Forschungsförderungsgesellschaft FFG.

Compliance with ethical standards

Conflict of interest On behalf of all authors, the corresponding author states that there is no conflict of interest.

Appendix A

Filtered drag model equations

$$\frac{\beta_{sf,\text{filtered}}}{\beta_{sf}} = 1 - f\left(\frac{\Delta_{\text{filter}}}{L_c}, \varphi_{p,c}\right) h\left(\varphi_{p,c}\right) \tag{A.1}$$

$$f\left(\frac{\Delta_{\text{filter}}}{L_c}, \varphi_{p,c}\right) = \frac{1}{a\left(\varphi_{p,c}\right)\left(\frac{\Delta_{\text{filter}}}{L_c}\right) + 1} \tag{A.2}$$

$$L_c = \frac{u_t^2}{g} Fr_p^{-2/3} \tag{A.3}$$

Functions a and f in Eq. (A.1) are piece continuous algebraic functions having the form in Eq. (A.4) and can be obtained through filtering the data from highly resolved CFD-DEM simulation. More details about the model can be found in Ref. [16]

$$a\left(\varphi_{p,c}\right) = \sum_{n=0}^{3} a_n \left(\varphi_{p,c} - \varphi_{p,m}\right)^n \quad for\ \varphi_{p,m-1} < \varphi_{p,c} < \varphi_{p,m} \tag{A.4}$$

Appendix B

The scaled voidage distribution can be approximated by calculation of minimum and maximum voidage in neighboring cells

$$\varphi'_f = \frac{\varphi_f - \varphi_{f,\min}}{\varphi_{f,\max} - \varphi_{f,\min}} = \frac{1}{1 + e^{-a(x/d_p)}} \tag{B.1}$$

The first and second derivative of this function with respect to the position x can be obtained as follows:

$$\frac{\left|\nabla\varphi_f\right|}{\varphi_{f,\max} - \varphi_{f,\min}} = \frac{a}{d_p} \frac{e^{-a(x/d_p)}}{\left(1 + e^{-a(x/d_p)}\right)^2} \tag{B.2}$$

$$\frac{\left|\nabla^2\varphi_f\right|}{\varphi_{f,\max} - \varphi_{f,\min}} = -\left(\frac{a}{d_p}\right)^2 \frac{e^{a(x/d_p)}\left[e^{a(x/d_p)} - 1\right]}{\left[1 + e^{a(x/d_p)}\right]^3} \tag{B.3}$$

After dividing Eq. (B.3) by Eq. (B.2), we arrive at

$$\frac{\left|\nabla^2\varphi_f\right|}{\left|\nabla\varphi_f\right|} = -\frac{a}{d_p}\frac{\gamma - 1}{1 + \gamma} \tag{B.4}$$

where $\gamma = e^{a(x/d_p)}$. Rearranging Eq. (B.4) leads to the expression for the parameter γ that reads:

$$\gamma = \frac{\frac{a}{d_p} - \frac{|\nabla^2 \varphi_f|}{|\nabla \varphi_f|}}{\frac{a}{d_p} + \frac{|\nabla^2 \varphi_f|}{|\nabla \varphi_f|}} \tag{B.5}$$

By dividing Eq. (B.1) with (B.2) an expression for $\varphi_{f,\min}$ is obtained:

$$\varphi_{f,\min} = \varphi_f - \frac{|\nabla \varphi_f|}{a/d_p}(\gamma + 1) \tag{B.6}$$

Finally, after substitution of Eq. (B.6) in Eq. (B.1), the parameter $\varphi_{f,\max}$ can be calculated:

$$\varphi_{f,\max} = \left(1 + \frac{1}{\gamma}\right)\left[\varphi_f - \varphi_{f,\min}\right] + \varphi_{f,\min}. \tag{B.7}$$

References

1. Avci B, Wriggers P (2012) A DEM–FEM coupling approach for the direct numerical simulation of 3D particulate flows. J Appl Mech 79:010901
2. Johnson AA, Tezduyar TE (1997) 3D simulation of fluid-particle interactions with the number of particles reaching 100. Comput Method Appl Mech Eng 145:301–321
3. Igci Y, Andrews AT, Sundaresan S, Pannala S, O'Brien T (2008) Filtered two-fluid models for fluidized gas-particle suspensions. AIChE J 54:1431–1448
4. Ozel A, Kolehmainen J, Radl S, Sundaresan S (2016) Fluid and particle coarsening of drag force for discrete-parcel approach. Chem Eng Sci 155:258–267
5. Ozarkar SS, Yan X, Wang S, Milioli CC, Milioli FE, Sundaresan S (2015) Validation of filtered two-fluid models for gas-particle flows against experimental data from bubbling fluidized bed. Powder Technol 284:159–169
6. Milioli CC, Milioli FE, Holloway W, Agrawal K, Sundaresan S (2013) Filtered two-fluid models of fluidized gas-particle flows: New constitutive relations. AIChE J 59:3265–3275
7. Girardi M, Radl S, Sundaresan S (2016) Simulating wet gas-solid fluidized beds using coarse-grid CFD-DEM. Chem Eng Sci 144:224–238
8. Schneiderbauer S (2017) A spatially-averaged two-fluid model for dense large-scale gas-solid flows. AIChE J 63:3544–3562
9. Parmentier JF, Simonin O, Delsart O (2012) A functional subgrid drift velocity model for filtered drag prediction in dense fluidized bed. AIChE J 58:1084–1098
10. Li J (1994) Particle-fluid two-phase flow: the energy-minimization multi-scale method. Metallurgical Industry Press, Beijing
11. Wang J, Ge W, Li J (2008) Eulerian simulation of heterogeneous gas-solid flows in CFB risers: EMMS-based sub-grid scale model with a revised cluster description. Chem Eng Sci 63:1553–1571
12. Zhang J, Ge W, Li J (2005) Simulation of heterogeneous structures and analysis of energy consumption in particle-fluid systems with pseudo-particle modeling. Chem Eng Sci 60:3091–3099
13. Wang J, Van der Hoef M, Kuipers J (2010) Coarse grid simulation of bed expansion characteristics of industrial-scale gas-solid bubbling fluidized beds. Chem Eng Sci 65:2125–2131
14. Sundaresan S (2003) Instabilities in fluidized beds. Ann Rev Fluid Mech 35:63–88
15. Fullmer WD, Hrenya CM (2016) Quantitative assessment of fine-grid kinetic-theory-based predictions of mean-slip in unbounded fluidization. AIChE J 62:11–17
16. Radl S, Sundaresan S (2014) A drag model for filtered Euler–Lagrange simulations of clustered gas-particle suspensions. Chem Eng Sci 117:416–425
17. Agrawal K, Loezos PN, Syamlal M, Sundaresan S (2001) The role of meso-scale structures in rapid gas-solid flows. J Fluid Mech 445:151–185
18. Wang J (2009) A review of Eulerian simulation of Geldart A particles in gas-fluidized beds. Ind Eng Chem Res 48:5567–5577
19. Andrews AT IV, Loezos PN, Sundaresan S (2005) Coarse-grid simulation of gas-particle flows in vertical risers. Ind Eng Chem Res 44:6022–6037
20. ten Cate A, Sundaresan S (2006) Analysis of the flow in inhomogeneous particle beds using the spatially averaged two-fluid equations. Int J Multiph Flow 32:106–131
21. Yang N, Wang W, Ge W, Li J (2003) CFD simulation of concurrent-up gas-solid flow in circulating fluidized beds with structure-dependent drag coefficient. Chem Eng J 96:71–80
22. Zhou G, Xiong Q, Wang L, Wang X, Ren X, Ge W (2014) Structure-dependent drag in gas-solid flows studied with direct numerical simulation. Chem Eng Sci 116:9–22
23. Li T, Wang L, Rogers W, Zhou G, Ge W (2017) An approach for drag correction based on the local heterogeneity for gas-solid flows. AIChE J 63:1203–1212
24. Lu L, Liu X, Li T, Wang L, Ge W, Benyahia S (2017) Assessing the capability of continuum and discrete particle methods to simulate gas-solids flow using DNS predictions as a benchmark. Powder Technol 321:301–309
25. Cassidy DA, Edwards JR, Tian M (2009) An investigation of interface-sharpening schemes for multi-phase mixture flows. J Comput Phys 228:5628–5649
26. So K, Hu X, Adams N (2011) Anti-diffusion method for interface steepening in two-phase incompressible flow. J Comput Phys 230:5155–5177
27. Rycroft C (2009) "Voro++: A three-dimensional Voronoi cell library in C++."
28. Kloss C, Goniva C, Hager A, Amberger S, Pirker S (2012) Models, algorithms and validation for opensource DEM and CFD-DEM. Progress Comput Fluid Dyn Int J 12:140–152
29. Kloss C, Goniva C (2011) LIGGGHTS-open source discrete element simulations of granular materials based on Lammps. Suppl Proc Mater Fabr Prop Charact Model 2:781–788
30. Jasak H, Jemcov A, Tukovic Z (2007) OpenFOAM: A C++ library for complex physics simulations. International workshop on coupled methods in numerical dynamics. Croatia, IUC Dubrovnik, pp 1–20
31. Beetstra R, Van der Hoef M, Kuipers J (2007) Drag force of intermediate Reynolds number flow past mono-and bidisperse arrays of spheres. AIChE J 53:489–501
32. Ouchene R, Khalij M, Arcen B, Tanière A (2016) A new set of correlations of drag, lift and torque coefficients for non-spherical particles and large Reynolds numbers. Powder Technol 303:33–43
33. Radl S, Gonzalez B, Goniva C, Pirker S (2014) State of the art in mapping schemes for dilute and dense Euler-Lagrange simulations. In: Johansen ST, Olsen JE (eds) Proceedings of 10th international conference on CFD in oil & gas, metallurgical and process industries. SINTEF, Norway, Trondheim, Norway, pp 1–9
34. Kloss C LIGGGHTS-PUBLIC Documentation, Version 3.X
35. Deen NG, Kriebitzsch SH, van der Hoef MA, Kuipers J (2012) Direct numerical simulation of flow and heat transfer in dense fluid-particle systems. Chem Eng Sci 81:329–344
36. Salehi M-S, Askarishahi M, Radl S (2017) Analytical solution for thermal transport in packed beds with volumetric heat source. Chem Eng J 316:131–136

37. Fullmer WD, Hrenya CM (2017) Are continuum predictions of clustering chaotic? Chaos: An Interdisciplinary. J Nonlin Sci 27:031101

38. Cloete S, Johansen S, Braun M, Popoff B, Amini S (2010) Evaluation of a Lagrangian discrete phase modeling approach for resolving cluster formation in CFB risers, In: 7th International Conference on Multiphase Flow

4

TFM-based Full Physics Simulations of Mixing in Wet Fluidized Beds

This chapter will be submitted to a leading international journal in the field of powder technology in summer 2018.

TFM-based Full Physics Simulations of Mixing in Wet Fluidized Beds

Maryam Askarishahi[a], Mohammad-Sadegh Salehi[b], Stefan Radl[b*]

[a]Research Center Pharmaceutical Engineering GmbH, Inffeldgasse 13/III, 8010 Graz, Austria

[b]Institute of Process and Particle Engineering, Graz University of Technology, Inffeldgasse 13/III, 8010 Graz, Austria

*Corresponding author: E-mail: radl@tugraz.at; Tel.: +43 316 873 30412

Abstract

Mixing in a wet fluidized bed was studied using the Two-Fluid Model (TFM) and a zero-Dimensional (0D) approach. The employed TFM was extended to simulate all involved exchange phenomena, including i) droplet deposition on the particles, ii) droplet evaporation, and iii) particle drying. The TFM simulation results suggest the formation of two well-mixed zones: i) a wetting zone dominated by droplet deposition and in which droplet evaporation happens; and ii) a drying zone where particle mixing and drying occurs. To quantify the uniformity in the bed, we computed the variance of the temperature and the particles' Loss on Drying (LoD) field. Subsequently, our TFM simulation data is used to support assumptions used in the calculation of exchange rates and macroscopic bed characteristic in our 0D model.

Comparison of the bed performance predicted by the two developed approaches demonstrates that the 0D model can accurately predict the gas and particle temperatures, as well as the moisture content with a maximum error of 4.3%. However, this good agreement can only be achieved in case the following criteria are met: i) low enough temperature and LoD variance (i.e., less than 5%); ii) deep penetration of the droplets into the bed in such a way that particles flow downward in the central region; and iii) no droplet loss at the top of the bed. In contrast, in case of low bed aspect ratio, large deviations of 9.5%, 14% and 20.2% between the 0-TFM and D model were predicted for particle LoD, gas vapor content and temperature, respectively.

These deviations can be attributed to the highly anisotropic velocity profile, and the resulting inefficient mixing in the bed.

1. Introduction

Fluidized beds (FBs) are characterized by high rates of heat and mass transfer, and are often used to produce coated particles [1]. These FB processes for particle coating utilize a hot gas to supply the necessary momentum for mixing and the heat for drying. In addition, a spray is used to inject a liquid to coat the particles' surface.

Various phenomena occur in wet fluidized beds (WFBs) that need to be considered in addition to that in dry FBs: i) deposition of droplets on the particle surface due to particle-droplet collisions; ii) evaporation of free-flowing droplets; and iii) evaporation of liquid from the particle surface stemming from the flow of heated gas over the wet particles (i.e., drying). Clearly, modelling of WFBs is significantly more involved compared to dry FBs. Consequently, developing the simplified models for WFBs is strongly needed to gain a better quantitative understanding of the above phenomena.

The most striking characteristic of WFBs, i.e., high rates of heat and mass transfer and intense agitation of the particles, as well as the position of the spray lead to the formation of distinct zones in the bed, which can be approximated to be well mixed. The size of these well-mixed zones (see Chapter 1.1.1); gas, droplet and particle exchange between zones (i.e., inter-zone exchange, see Chapter 1.1.2), as well as the residence time of the particles in each zone (see Chapter 1.1.3) are the three key factors that influence the performance of WFBs (with performance we refer to the mass and heat exchange rate within the bed). These three factors are closely linked such that they must be analyzed together, e.g., when performing simulations of WFB performance. This is in contrast to most of the previous detailed flow studies on WFBs, e.g., that of Suzzi et al. [2] and Fries et al. [3]: these studies assumed zones with a pre-defined size that was not affected by particle and/or droplet flow. There is now ample evidence in literature that suggests that such assumptions are weak, and hence should not be used in detailed flow studies. This is also of critical importance for the development of compartment models, since such models are often based on more detailed flow studies.

In the following section we will briefly summarize literature that focused on the above mentioned three key factors, and how they depend on the operating parameters of an FB.

1.1. Factors influencing wet fluidized bed performance

1.1.1 Identification of zones and their size in wet FBs

Identifying well-mixed zones in WFBs is of high importance since it helps to formulate simplified models (e.g., compartment models) for coating processes on the industrial scale. Various approaches have been adopted in the literature for such an identification, which will be reviewed next.

Jiménez et al. [4] measured the air temperature distribution in FBs to identify three well-mixed zones (i.e., a wetting, an isothermal and a heat transfer zone). The boundary of the wetting zone was supposed to correspond to the isotherm that is $2°C$ lower than the average bed temperature in the isothermal zone. Similar zones were distinguished based on the distribution of temperature and humidity in the Euler-Lagrange (EL) simulations performed by Duangkhamchan et al. [5].

Following the work of Jiménez et al. [4], Turchiuli et al. [6] identified two well-mixed zones via temperature measurements in an FBG. Specifically, i) a cool wetting zone under the nozzle (the size of this zone depends on the droplet diameter and penetration depth of the spray into the bed of particles); and ii) an isothermal/heat transfer zone (i.e. a non-active zone) were identified. They observed that the temperature distribution is symmetric in the former, and increases from the center sideways. In contrast, the temperature variation does not exceed $1°C$ in the isothermal heat transfer zone. Therefore, a high-temperature gradient zone next to the wetting zone must exist. This was also reported by Smith and Nienow [7]. Turchiuli et al. [6] reported that the size of the wetting zone was tremendously influenced by the FB's operating parameters. To put it in more detail, an increase in the spray pressure brings about a smaller wetting zone (due to the resulting smaller spray angle, higher droplet velocity and smaller droplet size). The wetting zone grows with spray rate as the spray's momentum influences the flow behavior. This is in accordance with the experimental study of Börner et al. [8] discussed below. According to the measurement performed by Turchiuli et al. [6], the size of the wetting zone is mainly governed by the

penetration length of droplets and their diameter. The experimental results of Turchiuli et al. [6] also revealed that the shape of the wetting zone is dependent of the atomization pressure: i) a funnel shape at low pressure and small particle load. In this case, particle move upward in the central region of the bed and downward close to the wall after wetted by droplets; ii) a bell shape at high pressure with downward movement of particle in the central region of the bed and upward close to the wall. The latter is more desirable since only the dry particles move upward and then enter the wetting zone.

In another study, Maronga and Wnukowsk [9, 10] measured temperature and humdity in an FBC (Fluid Bed Coater), and observed that the wetting zone can be divived into two sub-zones: i) an active-spraying zone situated next to the nozzle (the size depends on the penetration length of the droplets.); and ii) an active-drying zone located between the acitve-spraying zone and a non-active zone with a size larger than the active-spraying zone. expnading the active-drying zone seems to be advantagous for coating purposes since this zone acts as a safeguard against wet quenching and droplet loss due to wall spraying [9, 10]. Maronga and Wnukowsk [9, 10] claimed that the size of the active-spraying zone is a few percent of the bed volume.

Börner et al. [11] suggested another approach to divide the wetting region into three sub-regions based on the particle-wetting mechanism. Specifically, their suggestion reads as follows: i) a single-particle wetting zone in the freeboard characterized by high velocities (resulting in perfect wetting); ii) a bed surface wetting zone on the surface of the bed with high solid volume fraction (resulting in one-sided wetting); and iii) a sporadic and selective particle wetting zone at the bottom region of the spray zone. Börner et al. [8] tried to identify the spray zone in a fluidized bed using a conductivity probe. They quantified the demarcation into a wetting and drying zone based on the spatial distribution of the droplets in the FB. As presented by Börner et al. [8], the droplet penetration length is limited by the upward gas speed. As a result, a higher fluidization velocity reduces the volume of the wetting zone. According to Börner et al. [8], the size of the wetting zone, as well as the shape of this zone, is also influenced by nozzle position. They claimed that in case of placing the nozzle at a lower position (i) a more compact wetting zone will be formed, and that – most important – (ii) the wetting

zone's volume is then independent of the operating conditions. In other words, a lower nozzle position and a higher spray rate results in the formation of a more distinct wetting zone with a fixed size.

1.1.2 Exchange rates between zones

The flow behavior of particles plays a key role in the bed performance since it determines particle exchange rates between the zones described in the previous chapter. We next review findings from literature related to these exchange rates.

According to Jiménez et al. [4], a higher spray rate induces faster particle circulation and consequently reduces the drying time. Experimental observations of Börner et al. [8] confirm this dependency. We note in passing that Börner et al. [8] concluded that in the range of u_{mf} and $4u_{mf}$ for the fluidization velocity, similar hydrodynamic behavior is observed for both rectangular and cylindrical beds. Thus, the shape of the FB is not essential, motivating studies in rectangular beds that are easier to analyze both with experiments and simulations.

Vanderroost et al. [12] proposed a mathematical model for particle motion in an FBC based on a superposition of bubble-induced particle motion and a particle random walk model. They claimed that their model can predict the solid flow behavior reliably in the absence of atomization air injection. As it will be shown in our study, atomization air significantly influences the solid flow, and clearly needs to be considered.
Experimental results of Börner et al. [8] revealed that particles in the freeboard are pushed downward to the spray zone due to the momentum of atomization air and the injected droplets. The particle wetting in the spray zone is assumed perfect in their study. Particles in the lower circulation loop in the dense bed enter the spray zone from bottom. They claimed that wetting of the particle entering the spray zone from the bottom is selective and imperfect.

1.1.3 Particle residence time distribution in each zone

Another important parameter influencing the coating performance of the FBC is the particle residence time and its distribution. These distributions were in the focus of previous studies [13, 14], however, mainly focused on agitated or drum coaters. Next, we review the literature that considered residence times in FBs.

While Börner et al. [11] employed CFD-DEM to compute the residence time of the particles in the spray zone and drying zone, as well as their crossing length in each zone. Additionally, considering particle-droplet interaction, they obtained a characteristic life time of the droplets. They investigated the effect of the fluidization velocity on the size of the spray zone, and claimed that increasing the fluidization velocity enlarges the crossing length of particle in the spray zone. Furthermore, the particle residence time in the spray zone and the particle circulation time are reduced, consequently decreases the solid volume fraction in the spray zone. This trend was also observed in their earlier experimental study [15]: their experiment showed that a higher spray rate shortens the particle residence time in the spray zone due to lower particle volume fraction in this zone. This importance of the spray in FBCs will be addressed in great detail in our present study

1.2. Simulation approaches

Fluidized beds are characterized by spatio-temporal fluctuations of the flow quantities (e.g., the local particle concentration, the fluid and particle velocity, as well the concentration of vapor or temperature). Since these phenomena are coupled, the overall behavior of a fluidized bed granulator is complex. A variety of approaches was adopted to analyses the bed performance, of which i) detailed models based on computational fluid dynamics (CFD) (Euler-Euler and Euler-Lagrange approaches), and ii) compartment models are the most important ones.

For the simulation of gas-particle flows, typically two approaches are adopted. In Euler-Lagrange approach, the gas phase is simulated as a continuum phase by solving the Navier-Stokes equation, and the particles are considered as discrete entities and Newton's second law is solved for individual particles. In Euler-Euler (EE) approach, both gas and particles are simulated as interpenetrating continua. In the EE approach, the rheology of solid phase needs to be considered, e.g., through kinetic theory of granular flow (KTGF).

We note in passing that simulations of FBs (and hence also FBCs) suffer from the difficulty to resolve clustering and bubbling phenomena. We here only refer to the study of Wang et al. [16] that proposed one approach to overcome this difficulty. In our

present study we assume that clustering and bubbling phenomena can be resolved, and hence there is no need to account for this phenomena with a dedicated model.

1.2.1. The Euler-Euler approach

Duangkhamchan et al. [17] used the EE approach for the simulation of solid particles flow in an FBC with air-blast nozzle. Droplets were simulated as discrete entities. Due to the limitation of the software package they used, interactions between the particles and the droplet were not accounted for. They identified a low-temperature zone below the nozzle which is associated with droplet evaporation. Later, Duangkhamchan et al. [18] investigated the effect of atomization air pressure (i.e., the variation of the inlet velocity through the nozzle; droplets were not considered) on the voidage distribution in an FBC using CFD. Their study was followed by Ronsse et al. [19], who examined the flow behaviour of gas and particle and droplets in a fluid bed coater using CFD. In their study, droplets were modelled as discrete entities. Nevertheless, droplet deposition and particle drying were not considered in their simulation (i.e. no droplet-particle interaction model was used). The predicted outlet temperature deviated from the experiment in their study, which can be attributed to neglecting particle drying phenomena.

Szafran and Kmiec [20] used the EE approach to study heat transfer in a spouted bed dryer having a draft tube. The particles' LoD was simulated as a scalar transport equation in the "FLUENT" software package; droplet motion was not considered in their simulations. The rate of drying includes both constant-rate and falling rate periods. Their simulation results showed almost the same temperature for the particles and the gas, i.e., heat transfer rates between these phases were fast. A weak point of their study is that only half of the domain was simulated. However, the symmetric assumption cannot be adopted to FBs due to influencing solid particle flow across the center line of the bed as reported by Reuge et al. [21] .

1.2.2. The Euler-Lagrange approach

Heine et al. [22] used CFD-DEM approach to describe the spray zone of a two-fluid nozzle in an Fluid Bed Granulator (FBG). In their study, droplets were considered as discrete phase. Particle wetting was considered through an analogy to dust deposition:

the deposition efficiency was taken as the product of impingement and adhesion probability. Their simulation results proved that the spray zone can be seen as a conical region, which is in qualitative agreement with experimental observations. Nonetheless, they reported that simulation cannot predict the droplet deposition quantitatively with their model. They attributed the observed deviation to insufficient grid resolution, since the trajectories of the droplet close to the particles could not be resolved, leading to higher rates of collision and deposition.

Duangkhamchan et al. [5] used the Euler–Lagrange approach (droplets as discrete phase and particle as Eulerian phase) for simulation of an FBC. To identify well-mixed zones, air temperature and humidity were tracked in the bed. Particle-droplet interaction and particle drying were neglected in their study.

Börner et al. [11] employed the CFD-DEM approach to simulate an FBC. In order to simulate particle-droplet interactions, every collision was considered as a wetting event. To conserve the mass of droplets in the system, a sink term for the droplet concentration was considered. To reduce computational effort, a scaling approach proposed by Link et al. [23] was utilized for coarse-graining the particles, thereby limiting the number of (computational) particles that need to be simulated. The application of such scaling laws for DEM simulation is still a controversial issue, and only comparably small coarse-graining factor can be used when hoping for reliable predictions [24, 25].

Sutkar et al. [26] performed CFD-DEM simulations and considered droplets as discrete entities. This previous work used a wet restitution coefficient to account for droplet-particle interactions. Unfortunately, the evaporation from the spray droplets, and droplets deposited on the particle surface were disregarded in their study. In addition, the non-uniformity of the droplet distribution on the particle surface was not considered in their study, as well as in the most other studies.

Askarishahi et al. [27] extended a CFD-DEM code for simulation of particle-droplet-fluid interaction in a wet fluidized bed and verified their implementation against analytical solutions [28]. Their contribution is one of the first studies attempting a full-physics simulation of wet fluidized beds including droplet evaporation and deposition, as well as particle drying. They also revealed the importance of considering incomplete

surface coverage by droplets when estimating the drying rate. However, due to the constrain imposed by computational time, the simulated domain was very small.

1.2.3. 0D approaches: compartmental models

A pioneer in the description of FBCs via compartment models is Sherony [29], who developed a two-compartment model based on the stochastic model for surface renewal initially presented by Hulburt and Katz [30].

Maronga and Wnukowsk [9, 10] investiaged a top-spray FB using the population balance equations for a three-compartment method. The size of spray zone was fixed to 10% without further justification. They varied the size of active-drying zone as well as the rate of paticle exchange between the zones to study coating performance of the bed. They studied the uniformity of coating distrbution in the bed and concluded that existence of stagnant regions within the bed will widen the coating distribution.

In another study, Ronsse et al. [31] divided the fluid bed into horizontal compartments having a constant volume and mass of particle. As stated in their article, the trend of the temperature along the bed cannot be captured. In fact, their experiments showed a uniform temperature distribution followed by gradual reduction in the temperature. In contrast, the temperature predicted by their model continuously decreases along the bed with almost constant slope. They associated this deviation to the non-uniformity of the temperature uniformity in the lateral direction. Their sensitivity study revealed that the spray rate and the fluidization velocity have highest impact on the uniformity of coating layer growth. Besides the spray rate and fluidization velocity, atomization air pressure, as well as the position of the spraying nozzle relative to the bed have the most considerable influence on particle temperature. Finally, they claimed that increasing the distance between the nozzle and the fluidized bed deceases the size of the spray zone [31]. Therefore, the less number of particles have the chance to enter the spray zone, so a wider distribution of the particle temperature and LoD can be expected.

Hussain et al. [32] simulated a top-spray fluid bed granulator using population balance method. Specifically, the bed was divided into the following two well-mixed zones: i) a spray zone; and ii) a drying zone with constant size and mass of particle. They varied

the circulation time and compartment size, aiming at investigating their influence on the agglomeration process. This emphasizes the necessity of using detailed flow modelling (such as CFD) for a more reliable prediction of parameters when following a compartment approach.

1.3. Gaps in Literature

From our literature review it can be concluded that the studies on wet fluidized beds suffer from several deficiencies. Specifically, according to the best of authors' knowledge, the following phenomena have been neglected in the open literature:

- droplet-particle interaction was often neglected when identifying the spray zone [5].
- when calculating the rate of drying, surface coverage (with droplets) of the particle was disregarded. This simplification can greatly over-predicts the rate of drying as reported in our previous work [27] .
- the rate of droplet evaporation was marginalized in most previous studies, e.g., [26].
- compartment models are often not compared against comprehensive flow models (e.g., CFD or CFD-DEM), and the zone size and exchange rate of particles between these zones (or the residence time in these zones) are often only estimated [9, 10]. A notable exception is the work of Freireich et al. [14], which combined a DEM flow model with a compartment model that considered the residence time distribution in two compartments and a number of sub-compartments.
- As reported in the open literature [4, 6, 9, 10], the zones used in compartment models are often demarcated based on the gas temperature and humidity. However, these zones should be related to regions having similar heat & mass exchange characteristics. As a matter of fact, the obtained temperature and humidity are only a consequence of the contribution of these exchange phenomena. Therefore, detailed flow models can be applied to identify the well-mixed zones, based on exchange rate characteristics. Such a detailed study could be of high benefit to quantify the flow and thermal behavior of the bed in these regions.

- the degree of mixing in each zone is rarely quantified, e.g., via an analysis of the temperature and moisture variance in each zone.
- particle residence times are often considered to be fixed [11], despite it is well known that they are correlated with bed configuration and operating parameters.

1.4. Goals

By considering the gaps in literature addressed in the previous section, we distilled the following main goals of our present study:

1. Employ the EE approach to identify well-mixed compartments in a wet fluidized bed by examining the spatial distribution of the involved exchange phenomena (e.g., the distribution of the particles' drying rate). This is done in addition to considering classical gas and particle quantities in the wet fluidized bed (e.g., the temperature);
2. Quantify the degree of uniformity of particle LoD and gas temperature in the bed. This is to assess the "well-mixed" condition for individual zones in the studied fluidized bed;
3. Evaluate and improve the validity of a simple 0D model to predict wet fluidized bed performance (i.e., the temporal evolution of the evaporation rate, temperature, and LoD) via a comparison of the gas and solid phases quantities predicted by 0D model with domain-averaged values predicted by the EE approach. This evaluation should be performed for different spray properties (injection rate and droplet velocity), bed configurations (bed size, and static bed aspect ratio) and initial bed temperatures.
4. Propose criteria for the validity of the investigated 0D model against data from the EE approach. These criteria should be based on the degree of uniformity, the solid flow behavior, and the droplet penetration length.

To achieve these goal, the open-source code MFiX (Multiphase Flow with Interphase eXchange) [33] was extended to consider all relevant exchange phenomena in a wet fluidized bed (see Chapter 2 for details). It should be noted that the rheology of the granular phase is not affected by the liquid content in the present contribution.

Likewise, we consider the situations in which liquid bridges are too weak to affect granular flow. In summary, MFiX was utilized to follow the EE approach to perform simulations of a so-called “Two Fluid Model” (TFM) using a classical rheological model for a non-cohesive powder that is wetted by a liquid spray.

After successful verification of the newly implemented models, a set of simulations was performed to investigate the bed performance at various operating conditions. Afterwards, a 0D model was developed and validated against TFM to obtain the range of reliability of this compartmental model. In the following section, the description of the governing and constitutive equations for the hydrodynamics as well as the heat and mass transfer will be presented.

As mentioned above, one may argue against the application of a TFM for wet fluidized bed systems since a rigorous rheological model for wet cohesive powders is not available yet. However, various research studies [34-37] were devoted to developing such rheological models of wet granular material in the recent past. For instance, Roy et al. [34] used DEM simulation to obtain the better insight into local rheology of bulk flow in partially wetted granular shear flows. They proposed that the conventional rheology needs to be modified to consider other factors such as cohesion, contact softness, etc. Also, the study of Liu et al. [37] has as the future goal the prediction of cohesive powder flow in the context of a kinetic theory-based continuum model. Hence, it was not a goal of our present study to account for cohesive effects in our powder flow model.

2. Mathematical model

2.1. Hydrodynamics

Eulerian-Eulerian approach was applied to simulate the gas-solid flow in the present study. In this approach, different phases are treated mathematically as interpenetrating continua. Conservation equations were derived for each phase and linked by interphase momentum transfer coefficient and pressure. For the calculation of solid phase rheological properties, the kinetic theory of granular flow (KTGF) was

used. A complete list of governing and constitutive equations is available in literature [38], and summarized in Tables 1.1-1.5.

For Table 1.1 – 1.5 see pages 133 – 137

2.2. Mass and heat transfer

Due to the exchange of heat, vapor, and liquid between gas and solid phases, it is required to solve the heat and mass balance equation as presented in Table 1. The deposited liquid and evaporated vapor from the particle surface were considered as sink/source terms in the corresponding phases. In addition, the change in enthalpy due to phase change was also taken into account in the heat balance equation. Our modifications to the MFiX code [33] are described in following paragraphs in greater detail.

2.2.1. Closure for the rates of droplet evaporation and particle drying

In this study, the rate of droplet evaporation on the particle surface was calculated based on the driving force to transfer water vapor between the particle and the gas phase. This rate was computed based the saturation density of water vapor at the particle temperature, i.e., $\rho_{w,sat}$ as

$$\dot{S}_{dry} = \left|\rho_{w,sat} - \rho_g \mu_{vap}\right| a_{dp} \beta \qquad (1)$$

This rate was added as a source and sink term for water vapor and solid liquid content respectively as reported in Table 1. In Eqn. 1, β is the mass transfer coefficient which can be calculated based on the Sherwood number defined as $Sh = \left(\beta d_p\right)/D_{vap}$. This coefficient has been calculated in analogy to the heat transfer coefficient correlation developed by Deen et al. [39] as reported in Eqns. T1.4.11-12 in Table 1.4. In case of zero gas-particle slip velocity, this correlation approaches to the correct limit (i.e., $Nu = Sh = 2$). This assumption is realistic for the computation of the free-flowing droplets evaporation rate due to low droplet volumetric concentration in the spray region.

In Eqn. 1, $\rho_{w,Sat}$ can be estimated based on ideal gas law and the equilibrium vapor pressure of water; a_{dp} is the surface area of the particle available for liquid evaporation

and computed based on the correlation developed by Kariuki et al. [40], in which the surface coverage is calculated as

$$\psi_{liq} = 1 - [1 - f]^{\Phi_p / f} \tag{2}$$

Where the parameter f is the fraction of the particle surface coated by a single droplet (defined as $\frac{A_{d,projected}}{A_p}$), and Φ_p is the particle coating number given by $N_d f$ where N_d is the number of the droplets deposited on the particle surface and is given by $LoD\left(d_p / d_d\right)^3$.

The rate evaporation of freely-flowing droplets is computed based on the same methodology as for the evaporation from the particle surface. Specifically, we use

$$\dot{S}_{evap} = \left|\rho_{w,Sat} - \rho_g \mu_{vap}\right| \varphi_{liq} a_d \beta \tag{3}$$

Where $\rho_{w,Sat}$is the saturation density of water vapor in the gas phase at the gas temperature; φ_{liq} is the volume fraction of liquid water in the gas phase; and a_d is the specific surface area of a single droplet given by $a_d = \frac{6}{d_d}$. It should be noted that droplets are not simulated as a separate phase. Instead, droplets are considered as one of the component of the gas phase, i.e., they share the same speed as the gas. Besides, it was assumed that droplet mass loading is not so high that it can change the density of the gas phase since the spray rate is much smaller than the fluidization gas flow rate.

2.2.2. Closure for the droplet deposition rate

In order to simulate the deposition of droplets on the particle surface, a clean-bed filter model was utilized as suggested in the work of Kolakaluri [41]. In his model, the droplet deposition rate can be calculated from

$$\dot{S_d} = -\lambda \left|\boldsymbol{u}_d - \boldsymbol{u}_p\right| \mu_{liq} \varphi_f \rho_f \tag{4}$$

Where $\left|\boldsymbol{u}_d - \boldsymbol{u}_p\right|$ is the slip velocity between the fluid phase and the particle. As reported in Table 2, the filtration coefficient is a function of Reynolds Number and Stokes Number. It should be noted that the droplet Stokes Number in Eqn. T2.5 is computed based on the true slip velocity, while Re_m in Eqn. T2.6 is calculated using the superficial velocity.

For Table 2 see page 138

After successful implementation and verification of the above-mentioned models (see Appendix A for details), a set of simulations were performed in order to examine the effect of operation conditions on uniformity of the LoD and temperature distributions in the bed.

2.3. Compartment model

The mass and heat balance equations were derived and numerically solved to track the temporal evolution of gas and particle properties (e.g. temperature, moisture and vapor content) in the well-mixed bed based on the assumptions and the parameters adopted from the results of TFM simulations based on *uniform distribution of temperature and water vapor in the bed*. Specifically, the continuity equation for water vapor, derived based on mass loading, μ_{wv}, is given by

$$\frac{\partial}{\partial t}\left(\rho_g V_g \mu_{wv}\right) = \left[\dot{m}_{air}\mu_{wv}\right]_{in} - \left[\dot{m}_{air}\mu_{wv}\right]_{out} + \dot{m}_{evap} + \dot{m}_{dry} \tag{5}$$

Where V_g denotes the volume of the gas in the dese bed and is calculated based on the mean voidage of the dense bed computed by TFM simulation

In Eqn. 5, the rates of evaporation, $\dot{m}_{evap}$, and drying, $\dot{m}_{dry}$, are computed based on the driving force available for evaporation and given by

$$\dot{m}_{exchange} = \left|\rho_{w,sat} - \rho_g \mu_{vap}\right| \beta a_m V_{m_{tot}} \tag{6}$$

Where $a_m V_{m_{tot}}$denoted the total surface area of medium m (e.g. particle and droplet) available for evaporation. It should be noted that the surface coverage of particle has been considered in the calculation of drying rate.

As it was assumed that the mass of droplet is conserved, the mass balance equation for the particle liquid content can be derived as

$$m_{p_{tot}} \frac{\partial}{\partial t}\left(\mu_{lp}\right) = \dot{m}_{spray}\mu_{wl} - \left(\dot{m}_{dry} + \dot{m}_{evap}\right) \tag{7}$$

Where μ_{wl} represents the mass loading of the liquid in the solid phase and can be related to the LoD by considering the density ratio of particle and liquid water.

The energy balance equation of the gas phase and the solid phase can be respectively derived as

$$\frac{\partial}{\partial t}\left(\rho_g V_g \Delta H_g\right) = \Delta H_{in} + \dot{m}_{spray}\Delta H_{spray} - \dot{m}_{out}\Delta H_{out} - hV_{p_{tot}} a_p (T_g - T_p) \quad (8)$$

$$\frac{\partial}{\partial t}\left(m_{p_{tot}}\Delta H_{P_{tot}}\right) = hV_{p_{tot}} a_p \left(T_g - T_p\right) - \dot{m}_{dry}\Delta H_{latent} \quad (9)$$

Where ΔH represents the enthalpy of the stream compared to the reference condition and given by

$$\Delta H = C_{p_{mix}}\left[T - T_{ref}\right] + x_{wv}\Delta H_{latent} \quad (10)$$

The first term on the left-hand side of Eqn. 8 shows the accumulation of the thermal energy in the FB. The first and second terms on the right-hand side of the Eqn. 8 denote the energy input by fluidization gas and the injected spray respectively. The third and fourth term represents the energy of the outlet gas, and the energy consumed by the heat exchange between gas and solid phases, respectively. The schematic illustration of the developed 0D model has been presented in Figure 1b.

3. Results and discussion

Since wet fluidized beds have a dynamic and complex behavior, the qualitative distribution of particle and gas quantities will be investigated first for a typical operating point. In our present work, the main focus is given to examining the validity of 0D model, hence, TFM approach is employed to compute the temporal evolution of (i) selected sample-averaged quantities (e.g. LoD, temperature, and gas vapor content), as well as (ii) the variance of LoD and temperature. Afterwards, the validity of the 0D model will be assessed through a comparison of sample-averaged quantities against the corresponding values predicted by the 0D model. Finally, the effect of operating parameters will be investigated to comprehensively evaluate the reliability of the developed 0D model.

3.1. TFM Results and qualitative analysis

3.1.1. Setup and Parameter Ranges

The fluidized bed set-up used for simulation is schematically represented in Figure 1. The MFiX code [33] was modified to consider a conical zone for the spray injection so that the droplets can be sprayed over the particles from the top. It should be noted that the droplet velocity was fixed in the spray region based on the available measurement data. The total flow rate of the injected droplets to the conical zone is equal to the injection (spray) rate from the nozzle. The fluidization gas was assumed to be uniformly distributed over the distributor. The initial temperature of gas and particle is identical in the studied cases and summarized in Table 3.

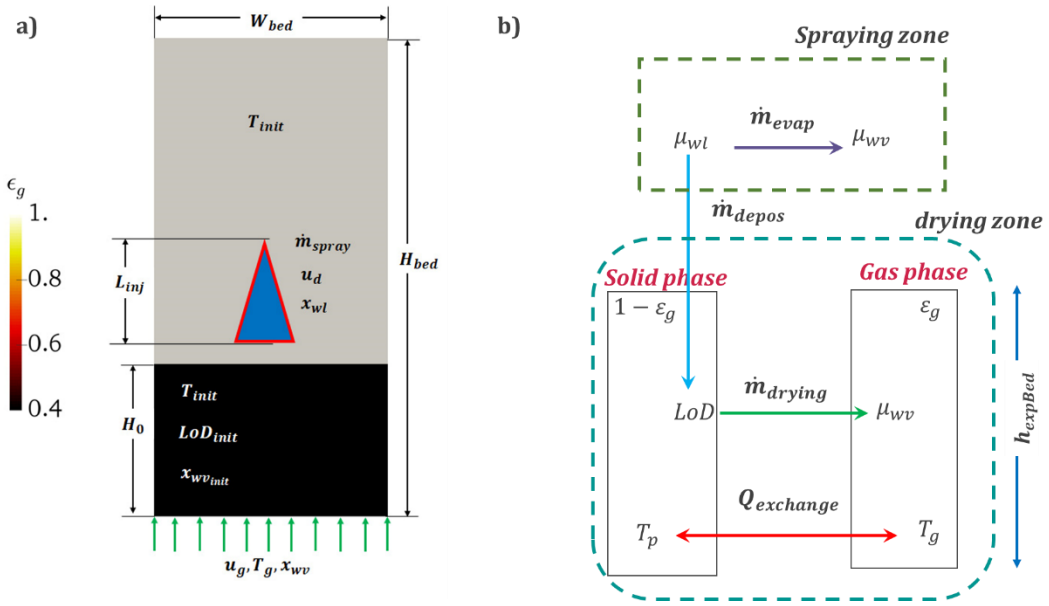

Figure 1 – Schematic illustration of wet fluidized bed used for a) TFM simulation (black indicates the particle bed), and b) 0D (compartment) model.

To thoroughly evaluate the 0D model developed in this study, the wide range of operating condition were simulated in our current work. The summary of the studied range of various quantities can be found in Table 3. It should be noted that the spray rate has been normalized base on the drying capacity of the system as

$$\dot{m}_{spray}^{norm} = \frac{\dot{m}_{spray}}{\dot{m}_{spray}^{max}} \tag{11}$$

Where $\dot{m}_{spray}^{max}$ corresponds with the spray rate at which the outlet gas is fully saturated, (i.e. $RH = 100\%$). For more information on the procedure for calculation of $\dot{m}_{spray}^{max}$ please refer to Appendix B. It should be mentioned that the summary of the studied operating conditions and bed configurations can be found in Table 4.

For Table 3 see page 139

For Table 4 see page 140

To gain an insight into the temporal behavior of the bed, exemplary contour-plots for the gas and particle quantities are shown in Figure 2 for $t = 30s$. The instantaneous distribution of the voidage demonstrates the bubbles formation in the bed. The motion of these bubbles plays the most significant role in the overall rate of heat and mass transfer in the FB. As a result, a rather uniform distribution of temperature and particle LoD is expected in the dense bed, as also discernible in Figures 2b-c. However, a lower temperature is predicted in the spray zone due to the injection of relatively cold air and droplets, which induces a high rate of evaporation in this region. A slightly higher LoD was predicted in this region due to the particles' liquid uptake. Therefore, the injected droplet is totally consumed in the spray zone due to the evaporation or deposition on the particle as also easily discerned from the water mass fraction distribution shown in Figure 2d.

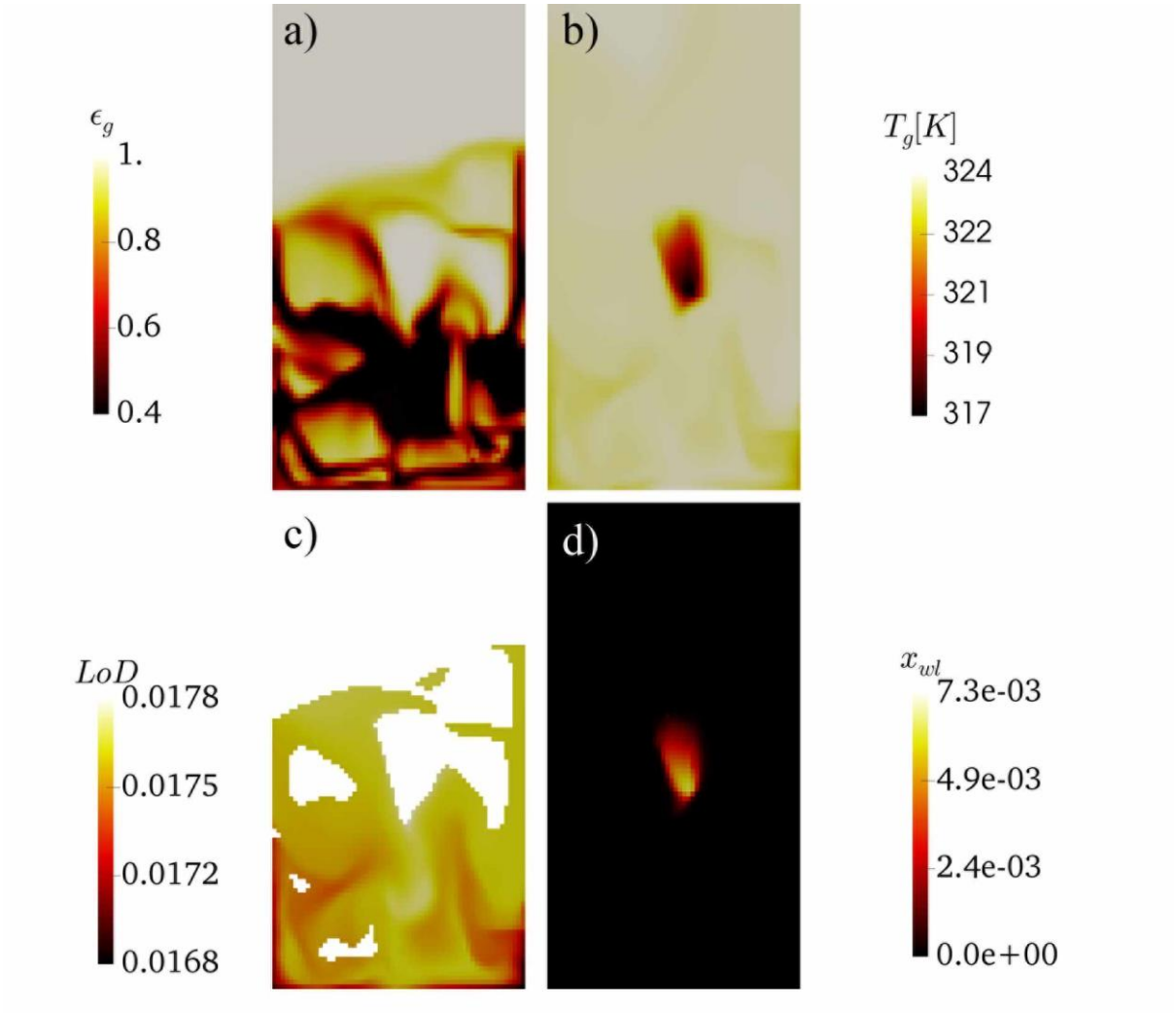

Figure 2 – instantaneous distribution of a) voidage, b) gas temperature, c) particle LoD, and d) water liquid mass fraction in the gas phase at $t = 30\,s$ for $\dot{m}_{spray}^{norm} = 0.33$ and $T_{init} = 330$ (instantaneous data)

3.1.2. Exchange rate distribution

Aimed at assessing the "well-mixed" condition with respect to the key exchange rates, corresponding time-averaged values of these exchange rates were computed over $300s$ of flow time. Averaging was started after a pseudo-steady state rate of the exchange quantities was reached. Figure 3 shows the predicted distribution for a typical case.

As shown in Figures 3b-c, free droplet evaporation and deposition happen only in the spray zone. Therefore, the evaporation of the freely-flowing droplets can be limited to

the spray zone. This finding will be used for computing the rates of evaporation and drying in 0D model. As shown in Figure 3a, close to the distributor surface, a higher rate of drying (with a sharp gradient) is predicted due to the higher driving force. In contrast, the rate of drying is almost uniform in the particle bed, which proves the reliability of well-mixed assumption for the studied fluidized bed.

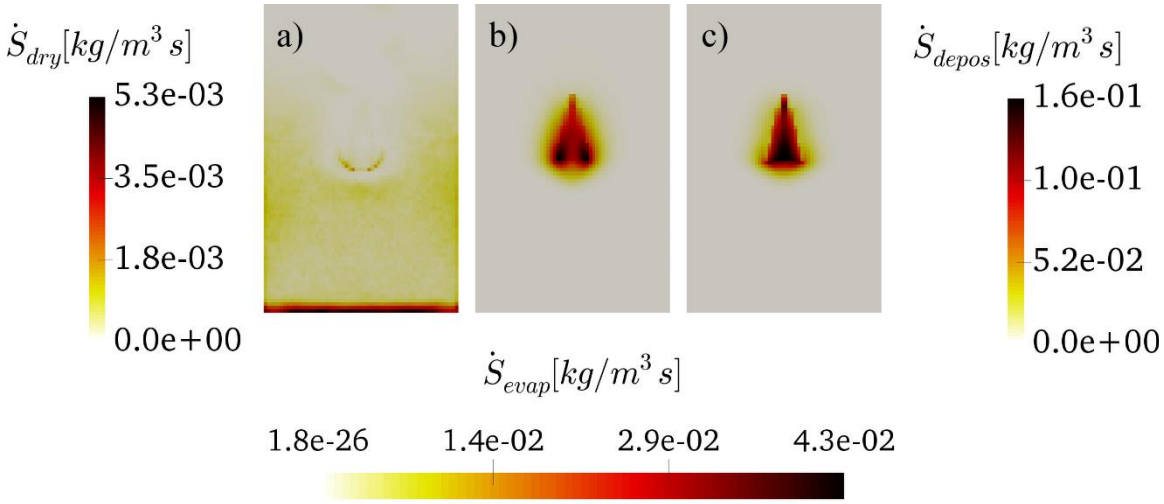

Figure 3 – Distribution of key exchange rates in the wet fluidized bed: a) drying rate; b) evaporation rate; and c) deposition rate for $\dot{m}_{spray}^{norm} = 0.66$ and $T_{init} = 333$ (time-averaged data).

3.1.3. Particle and gas properties

As expected, the contribution of the involved exchange phenomena influences the distribution of relevant gas and particle quantities. As depicted in Figure 4a, due to the high rate of evaporation and deposition in the spray region, droplets are totally consumed in the spray zone. Hence, there is no droplet loss in case of the process parameters used to produce Figure 4. This finding will be used to simplify the mass balance for the particle LoD in our 0D model. This high rate of evaporation results in the generation of a large amount of water vapor in the spray region as observable in Figure 4b. As easily seen in Figures 4a-b, the rate of droplet evaporation in the spray region is more significant compared with the rate of drying in the dense bed,

disregarding the zone size. Therefore, a higher mass fraction of water vapor is predicted in the spray zone.

Figure 4c revealed that the injection of droplets highly influences the distribution of the voidage in the top-center of the dense bed. This is associated with the solid flow pattern being affected by the droplets' momentum that is acting on the particle bed: As depicted in Figure 4d, droplets push the particles downward in the central region of the bed, subsequently to the side due to high downward velocity of the droplets.

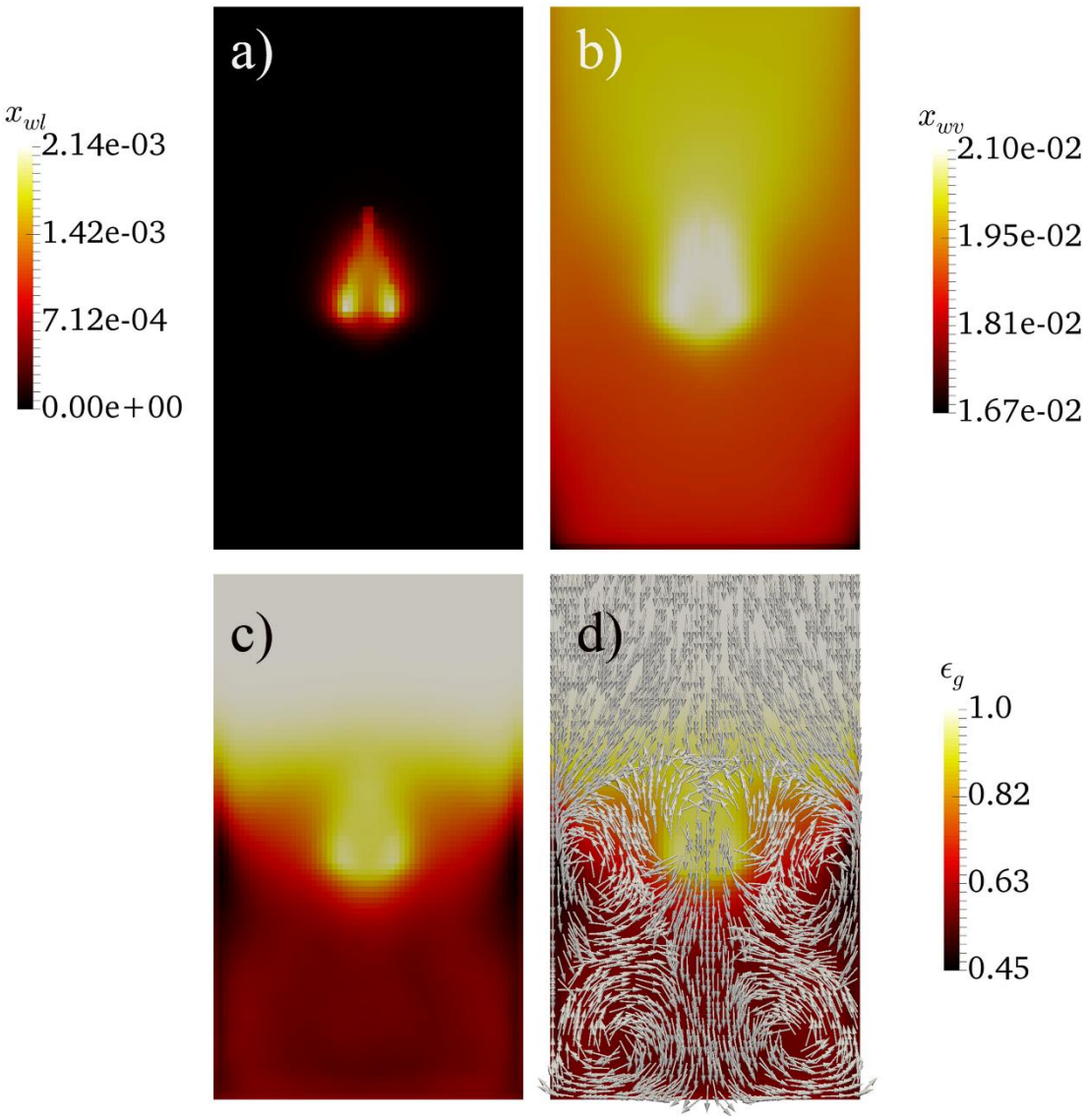

Figure 4 – Distribution of a) water liquid mass fraction; b) water vapour mass farction; c) voidage; and d) solid flow map in the wet fluidized bed for $\dot{m}_{spray}^{norm} = 0.66$ and $T_{init} = 330$ (time-averaged data).

According to Figure 2c, the distribution of the particles' LoD is almost uniform in the dense bed. This is due to the efficient mixing of particles and consequently a uniform rate of drying (see Figure 3b). It should be noted that the maximum LoD was obtained in the spray zone because of rapid droplet deposition on the particle surface, and the low driving force for drying (as noted above, the temperature is small in this region, and the air almost saturated with vapor).

3.2. Quantification of the degree of mixing in the bed

In order to quantify the uniformity of LoD distribution in the bed, the following sampling procedure was developed:

1. The computational domain is divided into sample regions consisting of an identical number of cells in each direction.
2. Since the mass of particle in each sample must be identical, a fixed mass of solid particles is considered in each sample as follows: the solid mass is summed up by looping over the cells in each sample region. This loop continues until the desired mass of solid particles in the sample is reached. This means that in a sample region whose voidage is higher, a larger number of cells will contribute to the sample as shown in Figure 5. It can also happen that the voidage in the sample is so high that the total mass of particles in all cells of that specific sample region cannot reach the desired value. Consequently, such a sample region must be skipped as indicated in Figure 5.
3. The average LoD in each sample must be weighted by the solid volume fraction in the cell to get a meaningful value for the amount of liquid in each sample. Thus, we use

$$LoD_{sample}(i) = \frac{\sum_{j=1}^{N_{cell}} \varepsilon_{s_{cell}}(j,i)\ LoD_{cell}(j,i)}{\sum_{j=1}^{N_{cell}} \varepsilon_{s_{cell}}(j,i)} \tag{12}$$

4. The sample averaged LoD is then calculated as (note, since all samples have the same solid mass, no weighting is necessary here)

$$\overline{LoD}_{sample} = \frac{1}{N_{sample}} \sum_{i=1}^{N_{sample}} LoD_{sample}(i) \tag{13}$$

5. The variance of LoD can be given by

$$\sigma_{LoD}^2 = \frac{1}{N_{sample}-1} \sum_{i=1}^{N_{sample}} \left[LoD_{sample}(i) - \overline{LoD}_{sample}\right]^2 \tag{14}$$

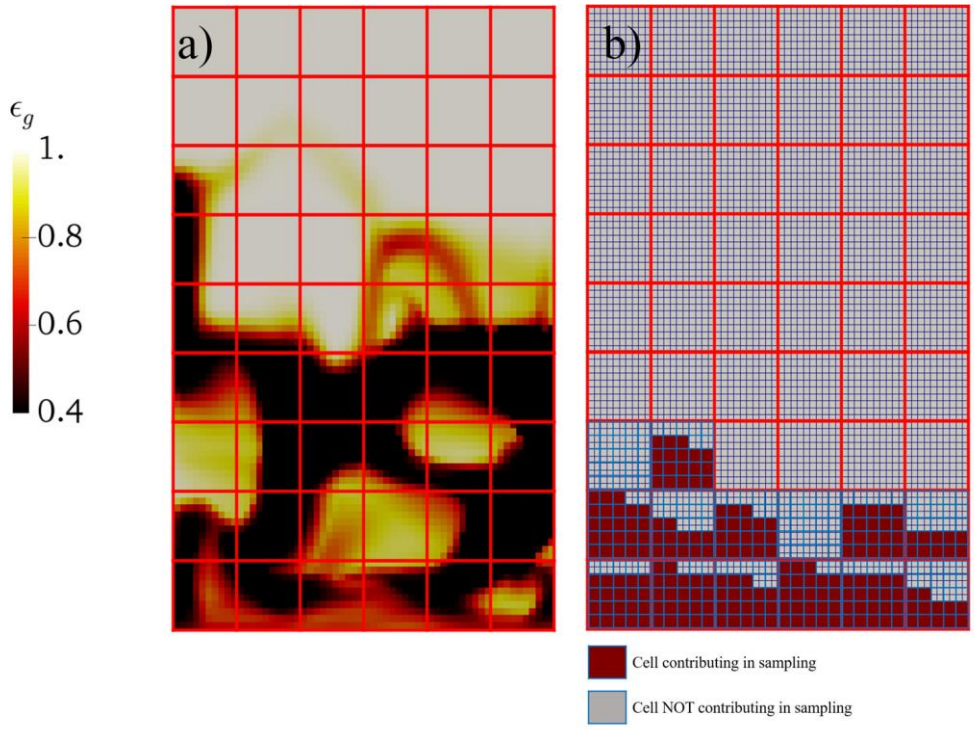

Figure 5- Illustration of sampling procedure for computation of sample-averaged LoD and its variance based on a) dividing the bed to the samples voidage distribution, and b) the example of the cells contributing in sampling

The same procedure was used to compute the temperature variance in the bed. This procedure was successfully implemented and tested in MFiX. To test the implementation, the computational domain was divided to the limited number of samples with different *LoD*s and particle volume fractions, and the computed values form the TFM simulation were compared with one obtained analytically.

3.2.1. Effect of spray rate and initial bed temperature

After implementing the automatic computation of LoD and temperature variance in the MFiX code [33], the effect of various operating parameters on the sample-averaged LoD and degree of uniformity (based on the variance of ley quantities) were investigated. Specifically, Figure 6 presents the effect of initial bed temperature and spray rate. As easily discerned from this Figure, the initial bed temperature has a tremendous impact on the temporal evolution of LoD. Specifically, a higher bed temperature results in a fast drop of the LoD due to the higher driving force for drying. Consequently, a fast drop of the gas temperature can be observed in Figure 6b, however, the temperature stays above that for the lower initial bed temperature. This defers particle liquid uptake (due to faster evaporation), followed by prolonging the drying process time which requires more energy (for heating particles to compensate for the latent heat necessary for evaporation) and cost (for running the process until a certain LoD is obtained).

The way that spray rate influences the temporal evolution of the particles' LoD is coupled with the initial bed temperature. Specifically, as shown in Figure 6a, at the higher initial temperature, the lower spray rate induces faster liquid loss since the rate at which liquid added to the particles via deposition cannot compensate the rate of liquid loss stemming from particle drying. However, at the higher initial bed temperature, a rise in spray rate leads particle LoD to hitting a minimum, which shows the equilibrium condition in the bed. It should be added that reducing the spray rate increases the time when the local minimum is achieved.

On the other hand, at the lower initial bed temperature, an increase in the spray rate results in a faster particle liquid uptake. It is worth noting that at the lower initial bed temperature the particle LoD increases continuously as the deposition rate outweighs the drying rate. This is due to the lower driving force for drying.

Considering the temporal evolution of temperature, according to Figure 6b, at the lower initial temperature and spray rate, due to very low rate of drying the bed temperature increases over the time slowly, while in other cases the bed temperature decreases sharply especially for the higher initial bed temperature due to high rate of drying. It should be added that in Figure 6b the temperature computed in TFM

simulation has been compared with one predicted by the 0D model. This will be explained in greater detail in Section 3.3.

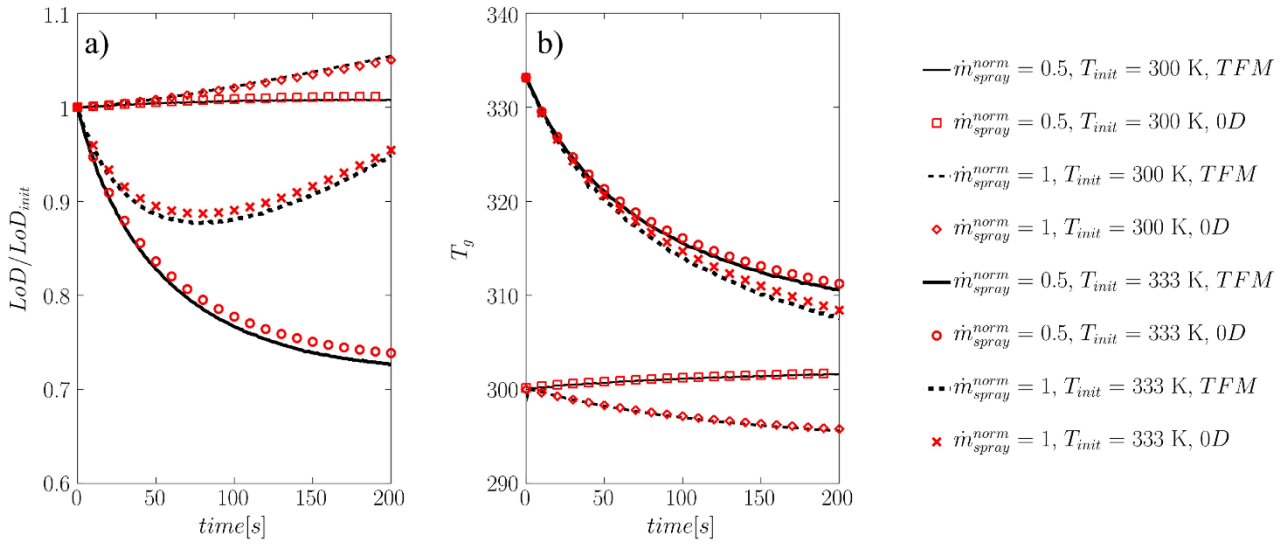

Figure 6 – The influence of the initial bed temperature and spary rate on the temporal evolution sample-averaged LoD

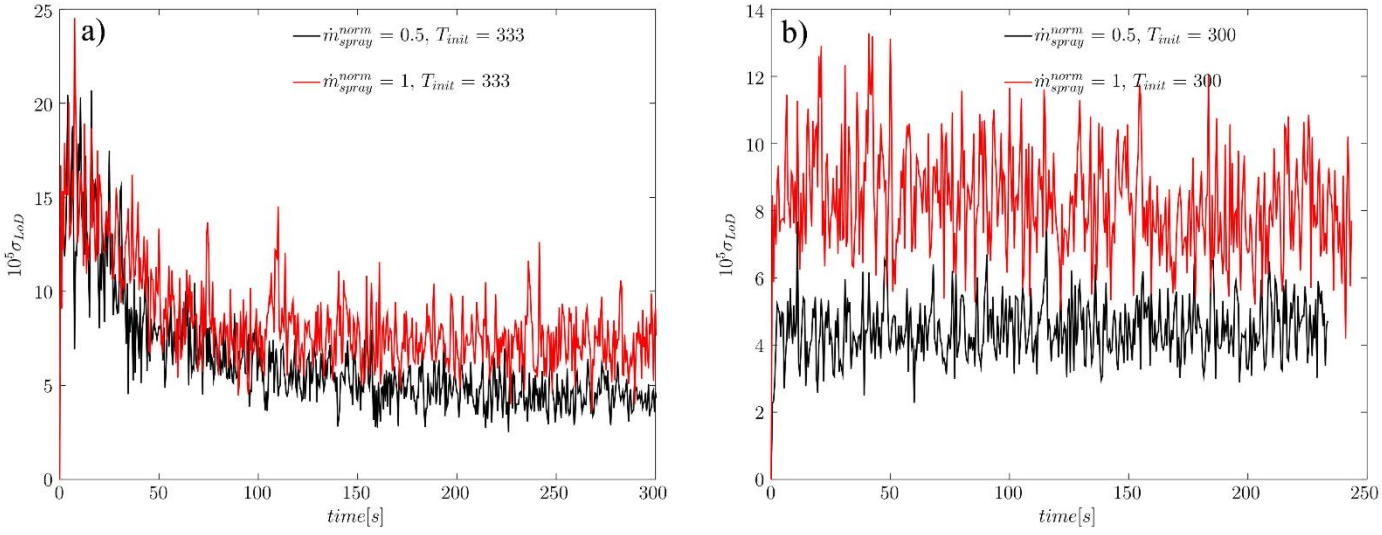

Figure 7 – Temporal evolution of the LoD standard deviation in the fluidized bed for various spray rates for an initial bed temperature of a) 333 K and b) 300 K.

In order to evaluate the degree of uniformity with respect to LoD, the variance of LoD for these cases is computed and shown in Figure 7. As seen in this Figure, a significant difference was predicted in the temporal evolution of LoD variance for different initial temperatures. Particularly, higher T_{init} induces a higher LoD variance. This is due to particle liquid uptake in the spray region, and particle liquid loss (i.e., drying) near the distributor. To put it in more detail, as seen in Figure 7a, at higher T_{init}, δ_{LoD} increases drastically at early times, followed by a gradual decrease, and finally reaches a plateau when the rate of drying reaches its pseudo steady state value. In contrast to T_{init}, the spray rate does not influence the temporal evolution of LoD variance significantly. Only the final value of the variance is affected by the spray rate, and to a less degree by the initial solids temperature. It is worth mentioning that running the simulation at various inlet gas flow rates (i.e. $1.5u_{mf} - 4u_{mf}$) reveals that as long as the bed falls into bubbling regime, the effect of the fluidization velocity on the LoD variance is not significant. This is due to the efficient particle mixing in the bubbling regime in the range of investigated fluidization speeds.

The distribution of exchange rates, as well as the gas and particle quantities in the bed and quantification of degree of mixing confirms the formation of two compartments in the studied wet fluidized bed:

1. A wetting/spraying zone where
    i) the droplets impact on particles;
    ii) free-flowing droplet evaporation happens quickly
    iii) droplets are completely consumed.
    iv) the rate of particle drying is negligible compared to the rate of deposition, and drying can be considered to occur only outside of this zone.

2. A drying zone where
    i) particle drying takes place uniformly in the bed.
    ii) no droplet enters, and consequently the rate of droplet evaporation and deposition is negligible;
    iii) the distribution of the particles' LoD is highly uniform

iv) the dense bed can be assumed as well-mixed

The communication between the two zones is established by the motion of individual particle as implied by the predicted solid flow pattern. As easily understood from the contour plot of exchange rates in Figure 3, the size of spraying zone is relatively small compared to the drying zone (i.e. dense bed). Therefore, having considered the above outlined characteristics of the zones, a 0D model can be employed to predict the behavior of a wet fluidized bed as follows:

1. a wetting/spraying compartment (called spray zone hereinafter) in which droplets are consumed in two ways
    a. by evaporation: the rate is calculated based on the driving force for saturation; and uniform distribution of the water vapor in the bed
    b. by deposition: the rate is calculated based on the mass balance for droplets (i.e., their total consumption); and the rate will be added as a source to the mass balance equation for particle LoD.
2. a drying/mixing compartment in which particles receive the deposited droplets from the wetting compartment and the mass and heat balance equations are derived for two phases:
    a. the solid phase with the domain-averaged volume fraction and expanded bed height extracted from TFM simulation
    b. the gas phase with voidage calculated based on the expanded bed height

as depicted in Figure 1b, the spraying zone is used for calculation of the rate of droplet evaporation based on the travel time of the droplet in this region and vapor content of the gas, i.e. x_{wv}. According to the TFM Simulation results, the predicted standard deviation of x_{wv} is less than 3%, so uniform distribution of the water vapor can be assumed in the bed. The comparison of the bed performance using TFM and 0D model supports the validity of this assumption as described in next section.

3.3. Comparison of TFM results with 0D model predictions

The 0D model was developed based on these two compartments explained in previous section. In order to evaluate the reliability of the compartment model, the results of our TFM simulations will be compared with the ones obtained with the 0D model for

various operating parameters including i) spray rate, ii) initial bed temperature, iii) bed dimension, iv) bed aspect ratio (fill level) defined as ratio of h_{init} (static be height) to bed width, v) droplet penetration length, vi) atomization air flow rate, and vii) droplet-atomization air mass ratio.

3.3.1. Effect of spray rate and initial bed temperature

The assumption of validity of the well-mixed condition was presented and confirmed in Chapter 3.2 model for various spray rates and initial bed temperature. In this section, this reliability will be demonstrated by comparison of the gas and particle quantities predicted by our TFM simulation and the 0D model as reported in Figures 6 and 8. As can be easily seen in these Figures, the value of LoD, water vapor mass fraction and gas temperature predicted by the 0D model are in a very good agreement with the sample-averaged data values predicted by the TFM. As a result, it can be concluded that as long as (i) the standard deviation of LoD is small compared to the total change of LoD, and (ii) there is no droplet loss, the bed can be assumed well-mixed and the bed performance can be predicted well by the 0D model. In other words, if solid circulation is so fast that liquid uptake is almost uniform in the bed, the particle bed can be assumed well-mixed with respect to LoD.

It is worth noting that a maximum droplet loss of 0.3% and 0.05% was predicted for $\dot{m}_{spray}^{norm}$ of 0.5 and 1 respectively, which shows that the droplet loss is negligible and the simplification made in the droplet mass balance is valid for the 0D model.

At very high spray rate, e.g. $\dot{m}_{spray}^{norm} = 3.5$, a fast drop of averaged bed temperature was predicted by TFM (data not shown here). This can be associated with the high rate of evaporation stemming from the injection of a significant amount of liquid at the top of the bed, and the driving force available for evaporation. The thermal energy needed for evaporation cannot be immediately supplied from the hot gas flowing to the bed from distributors. In fact, depending on the residence time of the gas in the particle bed, it can take a few seconds for the gas to reach the spray zone, which causes the temperature drop in that region. As soon as the gas reaches the spray zone, the heat loss will be compensated and the average bed temperature raises, as also predicted by the TFM. This shows the deviation of the bed from well-mixed condition in the first few seconds of the process time. Since the bed temperature is lower, the driving force for

drying and evaporation is lower, therefore, a lower amount of water vapor is predicted by TFM in this case.

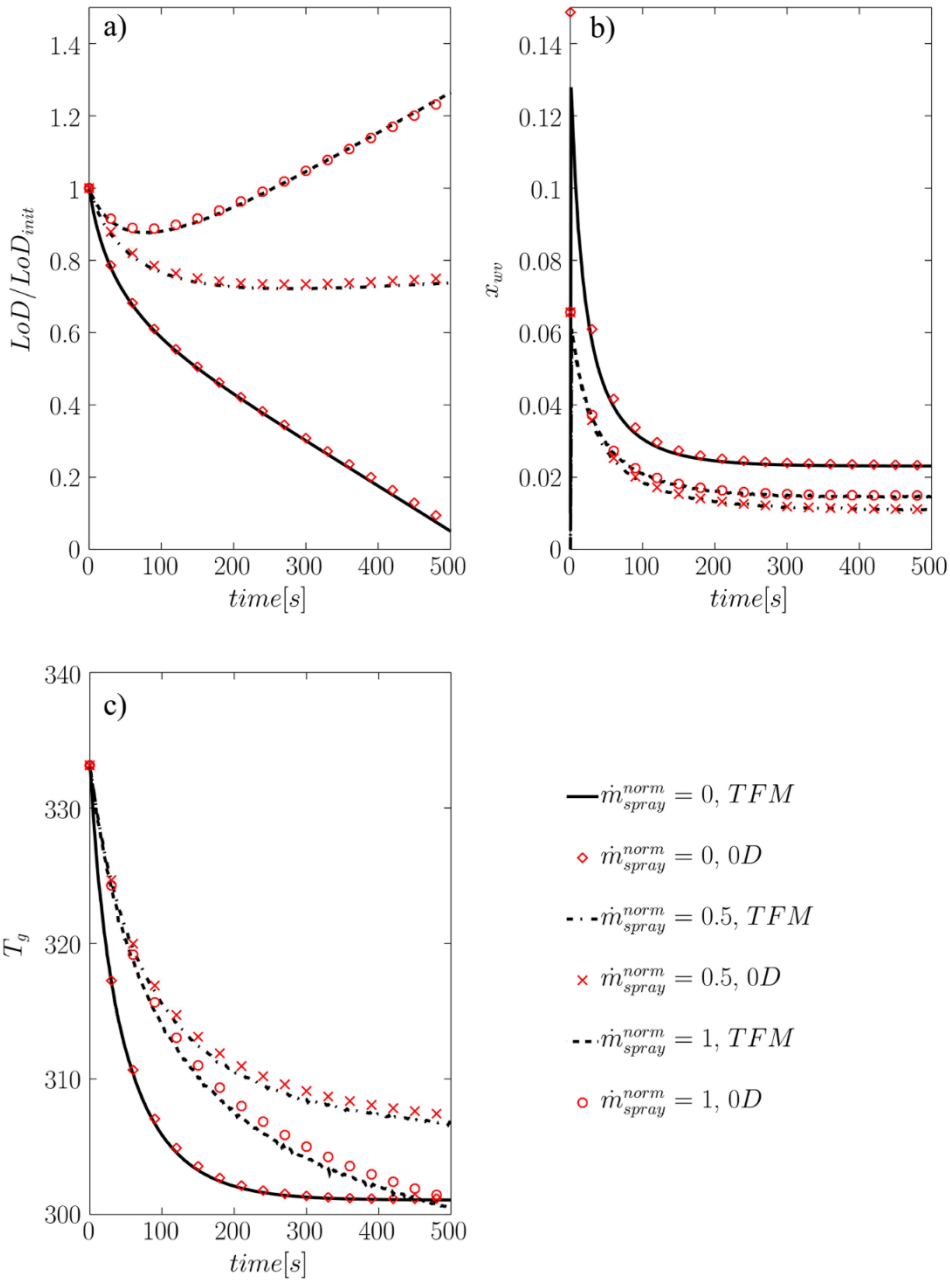

Figure 8 - comparison between TFM and 0D model for a) particle LoD, b) water vapor mass fraction in gas phase, and c) gas temperature at different spray rates, $\dot{m}_{spray}^{norm} = 0$ denotes pure particle drying

3.3.2. Larger FB with different aspect ratio

In order to examine the reliability of developed 0D model in a larger scale, several simulations were performed for the bed three times larger in each direction, and for an aspect ratio of 0.15 and 0.65 as shown in Table 4. The comparison of the results predicted by the two approaches is presented in Figure 9. As seen in this Figure, at the beginning of the process (i.e. for $t < 10\ s$), the values of T_g and x_{wv} predicted by 0D model deviate from the TFM one. This can be justified by higher residence time of the gas in the particle bed in the larger bed. In other word, as the height of the bed increases, a longer time (in this case, ${H_0}/{u} = 0.75s$) is needed to reach the well-mixed condition. Besides, it takes time for the hot air to flow over all particles in the bed. Therefore, the bed deviates from the well-mixed condition, and a lower amount of water vapour will be generated in the bed due to the lower rate of drying as predicted by the TFM simulation.

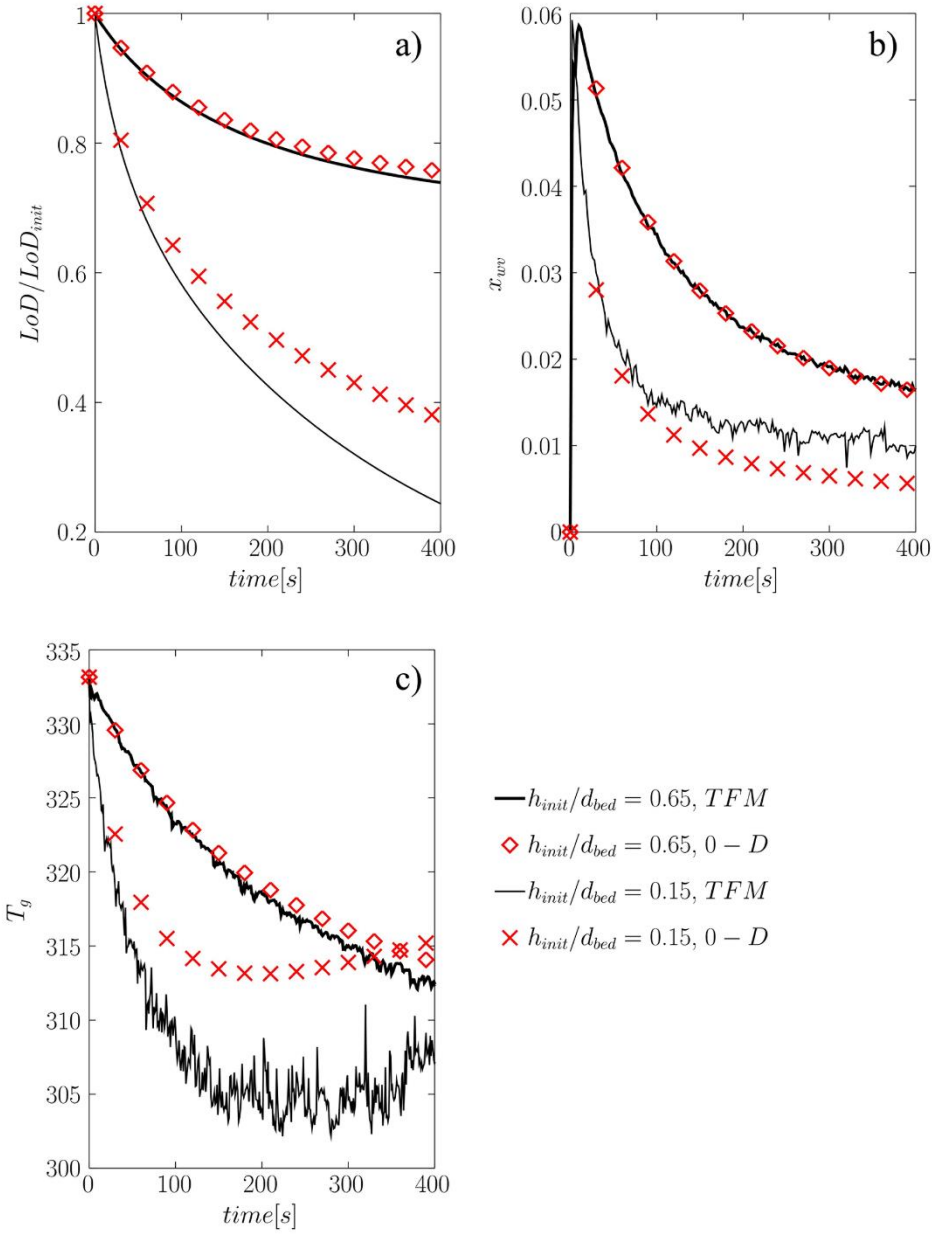

Figure 9 - comparison between TFM and 0D approaches for a) particle LoD, b) water vapor mass fraction fraction in gas phase, and c) gas temperature at different bed aspect ratios.

In case of lower static bed height, i.e., considering a bed aspect ratio of 0.15, the 0D model fails to predict the wet fluid bed performance. In fact, the highest deviations were observed for the gas temperature and the particle LoD due to the following reasons:

i) some of the particles cannot enter the spray zone for the liquid take-up due to deficient mixing, so the droplets will be consumed for droplet evaporation, as predicted by the simulation, such a high rate of evaporation results in the saturation of the gas in the spray region, as the flow in top of the spray zone is close to the plug flow. Consequently, a number of droplets will leave the bed neither evaporating nor depositing, as a droplet loss of 9.6% was predicted by TFM. Besides, the rate of evaporation at top of the bed in the TFM simulation is significant, which results in a lower particle liquid take-up predicted by the TFM (i.e., a lower LoD was predicted for TFM);

ii) Due to the lack of efficient mixing of particles, and the high rate of evaporation in top of the bed, the heat distribution cannot be assumed uniform in the bed. Specifically, two zones with comparable size and different temperatures will be formed in the bed. However, in the developed model it was assumed that the size of spray zone is relatively small compared to drying zone to assumed uniform distribution of water vapor and temperature in the bed. In order to quantify this non-uniformity of temperature, the variance of this quantity was computed in TFM simulation and is depicted in Figure 10. The standard deviation of $5K$ compared to total temperature change of $30K$ proves a high degree of non-uniformity of bed temperature with relative standard deviation of 16.6%

iii) having considered the solid velocity vector field, in case of low bed aspect ratio, the axial mixing of solid is less intense than the lateral one (see Figure 11), which hinders the efficient mixing on the bed surface. Hence, the particles cannot pass the spray zone and the injected droplets will be consumed via evaporation. In addition, the predicted solid flow pattern in Figure 12 reveals that the lateral flow of particle is more intense in case of a lower bed aspect ratio. According to this Figure, in the bed with the aspect ratio of 0.15 (see Figure 12c), the particles move upward in the central region of the bed, while for the higher aspect ratio (see Figure 12a), due to the deep penetration of the droplet in the dense bed, the particle are pushed downward by droplets. Hence, such a downward velocity field in the central region of the bed can be an indicator for deep droplet penetration.

To compare the axial and lateral velocities more quantitatively, the mean velocity is calculated in the half of the bed at various heights from the distributor surface. As reported in Table 5, the ratio of the lateral to axial velocity is higher for an aspect ratio of 0.15. This dominance of the lateral solids velocity leads the particles to having a lower chance to meet the droplets and take up liquid. Therefore, the droplets may either leave the bed (note a non-zero water mass fraction in the outlet was predicted) or evaporate near the top of the bed. such a droplet loss results in a higher water vapor mass fraction as well as a lower LoD and temperature compared to the one predicted by TFM as also seen in Figure 9.

For Table 5 see page 141

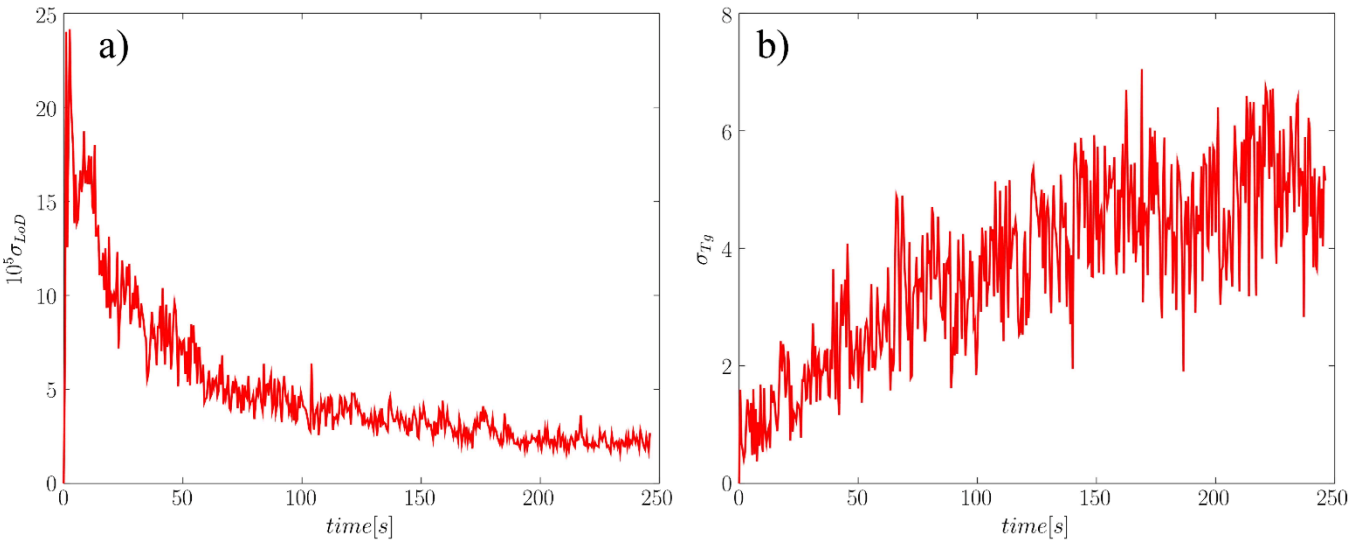

Figure 10 – temporal evolution of a) LoD variance and b) gas temperature variance for aspect ratio of 0.15 ($\dot{m}_{spray}^{norm} = 1.5, T_{init} = 333K$)

As discussed above, it can be concluded that 0D model fails if the following criteria are not met: i) no droplet loss; ii) negligible variance of LoD and temperature compared to the total change of the corresponding values during the process time (e.g. $LoD_{end} - LoD_{init}$) ; and iii) deep penetration of the droplets to the dense bed indicated by downward velocity field in the central region of the bed.

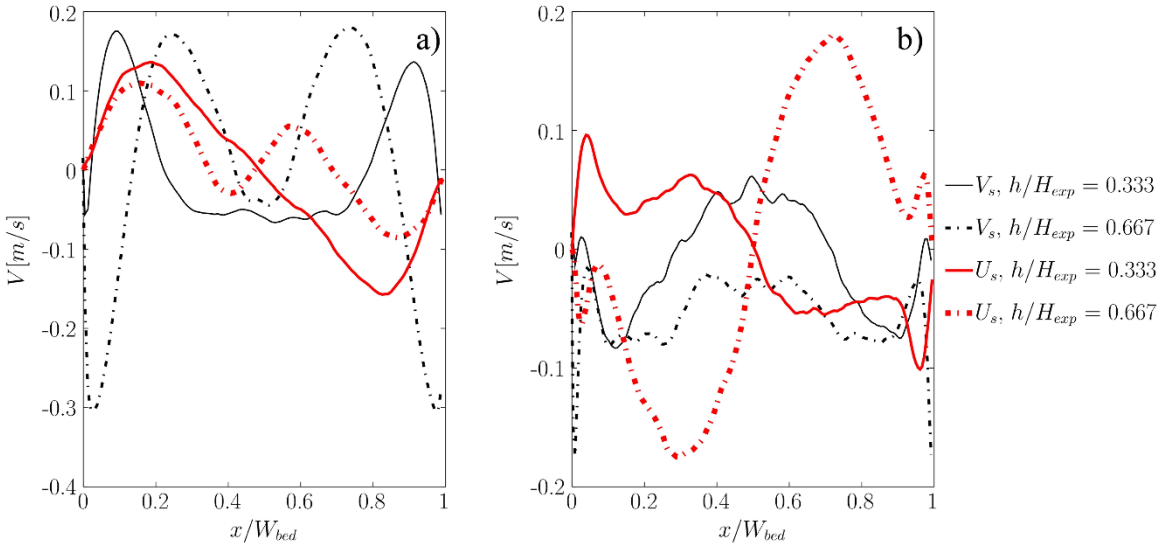

Figure 11 – comparison of time-averaged lateral and axial solid velocities at two different heights for bed aspect ratios of a) 0.65 and b) 0.15

Having considered the axial and lateral velocities of solid phase in Figure 11, the injection of droplets significantly influences the motion of particles in the bed. As depicted in Figure 12a, in case of droplet injection, the particle motion is downward in the central region of the bed in both top and bottom vortices in the dense bed. What is more, the volume fraction of particle is higher close to the wall at top of the bed because droplets push particles towards the walls, while in case of pure drying as depicted in Figure 12b, the particles in two top vortices move upward at the position far from the walls and downward close to the wall. The same pattern was observed for the bed with aspect ratio of 0.15, as shown in Figure 12c, due to the lack of droplet penetration into the dense bed.

According to the voidage distribution in Figure 12a, the volume fraction of solid particles is very low in the top-central region of the dense bed which is immediately below the spray zone. This corresponds the inflection point observed by Börner et al. [8] in the spray region. In fact, the region top of this inflection point is in the freeboard, while the region below is located in the dense bed. At this point the spray zone starts to shrink due to the collisions of the droplet with the particle bed.

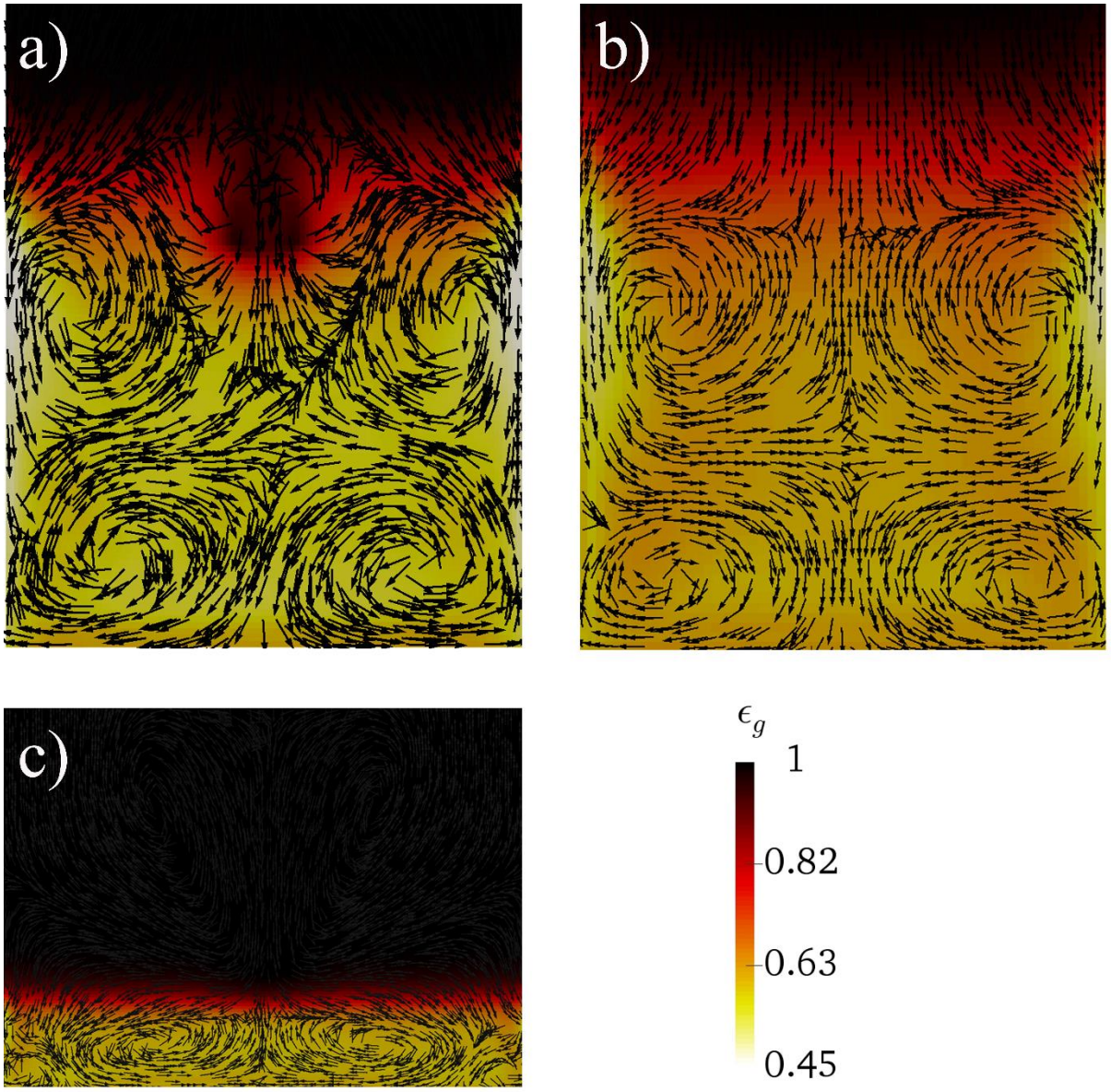

Figure 12 – predicted time-averaged voidage distribution and solid flow for case acpect ratio of a) 0.65, $\dot{m}_{spray}^{norm} = 1.5$; b) 0.65, $\dot{m}_{spray}^{norm} = 0, u_d = 0$ (pure drying); and c) 0.15 , $\dot{m}_{spray}^{norm} = 1.5$

3.3.3. Penetration length of the droplets

Another important parameter influencing the assumption of "well-mixed" condition in the bed is penetration of droplets into the dense bed, governed by: i) spray position and its configuration, ii) droplet velocity and iii) the distance between spray and bed surface. In this section, the effect of droplet velocity and the nozzle position on validity of 0D model is investigated

3.3.3.1. Effect of the droplet velocity

At an identical droplet injection rate of $\dot{m}_{spray}^{norm} = 1.5$, as stated in Table 4, the effect of droplet velocity on the bed performance was investigated. Specifically, the simulations were performed at different droplet velocities (i.e. 0.1 m/s and 7 m/s) and compared with the 0D model. As depicted in Figure 13, in case of a very low penetration length of droplet, the 0Dmodel deviates from the TFM model due to a deficient interaction of the particles with the spray zone. This is since the bed deviates from the well-mixed condition. Particularly, in case that the droplet velocity is comparable with the fluidization velocity (in accordance with a low penetration length of droplet) an accurate computation of the droplet travel time is challenging due to the influence of upward-flowing gas on droplet motion. Hence, the fraction of the liquid at the top outlet must be simulated in 0D model. In other words, significant droplet loss causes the 0D model failing to predict the bed performance for all measured quantities. In this case, due to the deviation of the bed from well-mixed condition, the evaporation rate and consequently water vapor mass fraction are considerably over-predicted at the very beginning of the process, and consequently a lower LoD and temperature is predicted by 0D model.

In case of low droplet velocity case, the droplets will be entrained at the top of the bed, so the gas will be almost saturated due to the high rate of evaporation and the (almost) plug flow of the gas: evaporation happens in the freeboard, and the flow is far from well-mixed condition. Consequently, the gas can be saturated when leaving the bed, as also predicted by TFM simulation in the present study. In contrast, in the 0D model the bed is assumed well-mixed, and the gas is far from the saturation condition.

In summary, this results in a higher LoD value predicted by the TFM simulation compared to the 0D model with a travel time calculated based on the droplet velocity. To support this conclusion, gas and particle quantities were computed in our 0D model for various values of droplet travel time. A shown in Figure 13, upon using different values of t_{trav}, it is not possible to match all quantities with identical correction factor for droplet travel time. The main reason for such a mismatch is the droplet loss in the TFM simulation that is not accounted for in our 0D model. This highlights the

importance of the accurate calculation of droplet travel time as well as the droplet loss fraction, which is significant in case of low droplet penetration.

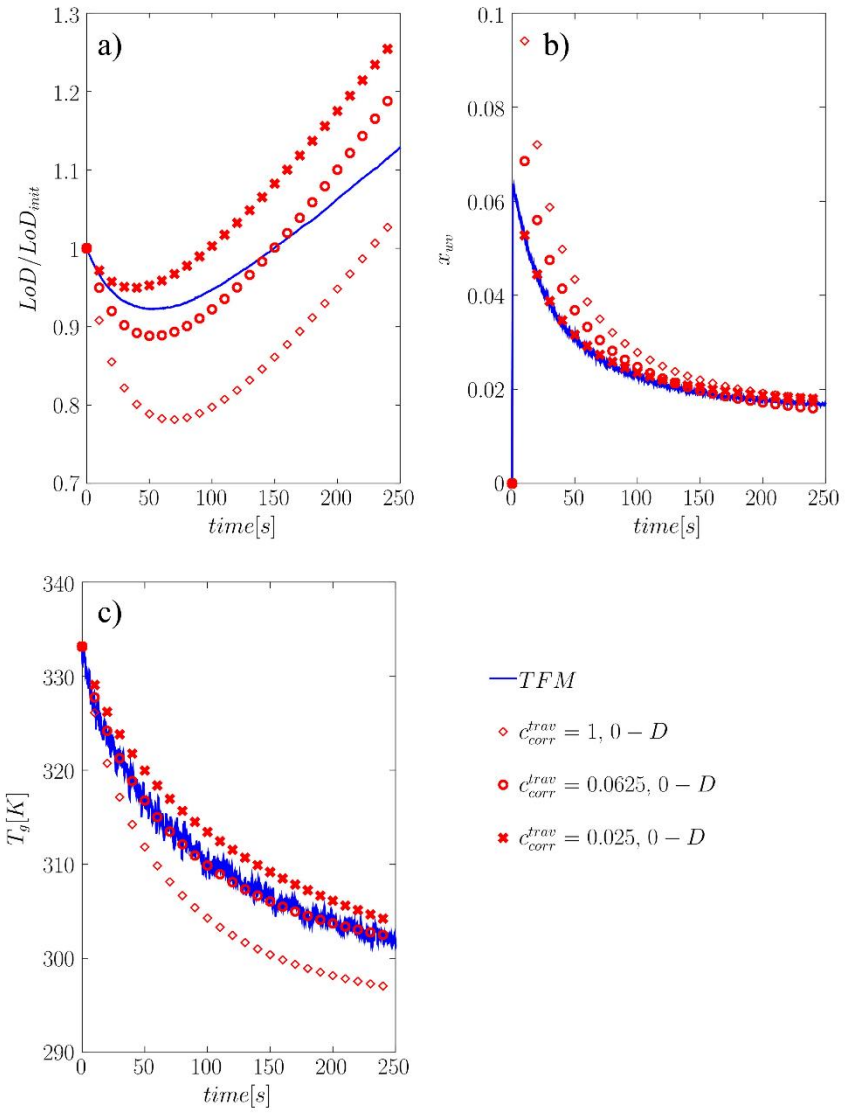

Figure13 - comparison between TFM and 0D approaches for a) particle LoD, b) water vapor mass fraction, and c) gas temperature for different correction factors of the droplet travel time.

Aiming on investigating the effect of droplet velocity on the involved phenomena, the rates of evaporation, drying, and deposition were obtained at different distances from the nozzle positions.

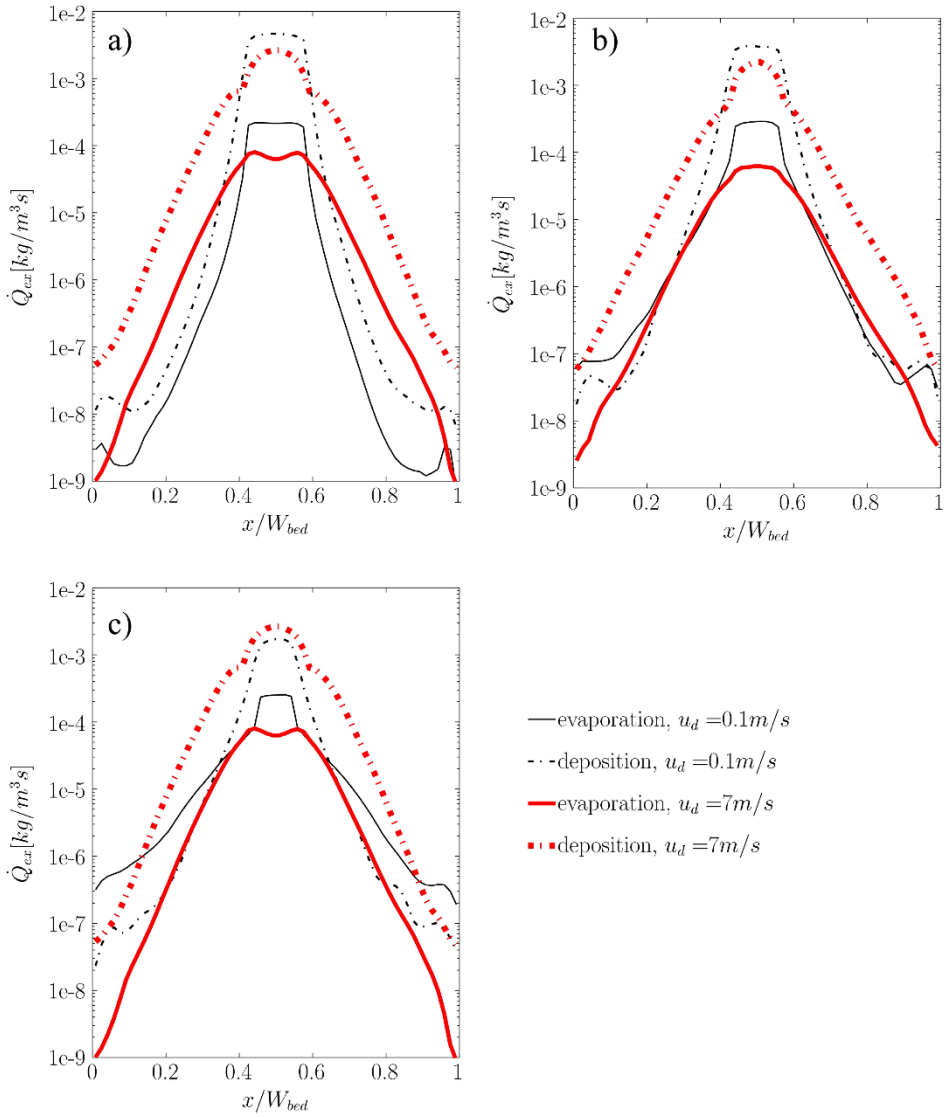

Figure 14 - comparison of the exchange rate for drying, evaporation, and deposition at different droplet velocies and at a dimensioless distance (based on spray zone length) of a) 0.75, b) 0.5, and c) 0.25 from the nozzle .

As depicted in Figure 14, a higher rate of evaporation was predicted for $u_d = 0.1\ m/s$ at the central region due to longer residence time of the droplets. What is more, at $u_d = 0.1\ m/s$, due to the lower probability of droplet-particle collision at a higher distances from the bed surface, the rate of evaporation outweighs the rate of deposition significantly at these distances. Additionally, the evaporation zone is broadened at

small distances from the nozzle (black solid lines in Figure 14c). This can be justified by the competition between the deposition and evaporation phenomena for the droplet consumption. In fact, a higher droplet velocity gives a rise to the expanded bed height. Hence, particles have more chance to enter the spray zone and take up liquid (see the solid flow pattern versus water liquid mass fraction contour plot in Figure 15). Therefore, a lower number of droplets will be available for evaporation. On the other hand, at $u_d = 0.1\ m/s$, since the particle volume fraction is very low close to the nozzle position, droplets have very low chance to collide with particles. Thus, they either evaporate or leave the bed with the gas flow.

At larger distances from the nozzle, i.e. closer to the bed surface (see solid lines in Figure 14a), the higher rate of evaporation was predicted for $u_d = 7\ m/s$ compared the one at $u_d = 0.1\ m/s$ because a larger fraction of droplets can travel downward to more distant regions from the nozzle. In other words, as droplets move away from the nozzle at lower u_d, the evaporation rate decreases and become smaller than the one at $u_d = 7\ m/s$.

Another point discerned from 14 is that at lower u_d and $h/L_{spray} = 0.25$ (see the dash lines in figure 14c), the rate of deposition is smaller compared to the value at higher u_d. This is since the longer penetration length of droplet induces particles close to the wall to move upward faster (for the sake of continuity). Consequently, these particles have a greater chance to enter the spray zone and collide with the droplets (see the solid lines in Figure 14c).

This probability for particles to enter the spray zone highly depends on the flow behavior of particle in the bed. As depicted in Figure 15b, particles in the freeboard are pushed downward to the spray zone due to downward velocity of droplets and leave the bed from sideways. This behavior is consistent with the observation of Börner et al. [8] and Maronga and Wnukowski [10]. Despite the agreement in solid flow in the freeboard (i.e. upper circulation loop), Börner et al. [8] observed different flow behavior for the particles in the lower circulation loop of the dense bed as the particles enter the spray zone from the bottom This is in contrast to the pattern predicted in our present contribution. Particularly, based on our TFM results, the particles meet the droplet at the boundary of the spray zone due to their downward velocity. This

inconsistency stems from the discrepancy in the solid flow pattern observed by Börner et al. [8] and the one predicted in our present study. In fact, since the particle size used in their study falls into Geldart D classification, two vortices are observed in the dense bed. In contrast, in our present work the particles belong to Geldart B classification, and four vortices were predicted in the bed. More information regarding the effect of particle size on solid flow map can be found somewhere else [42, 43], and supports this conclusion.

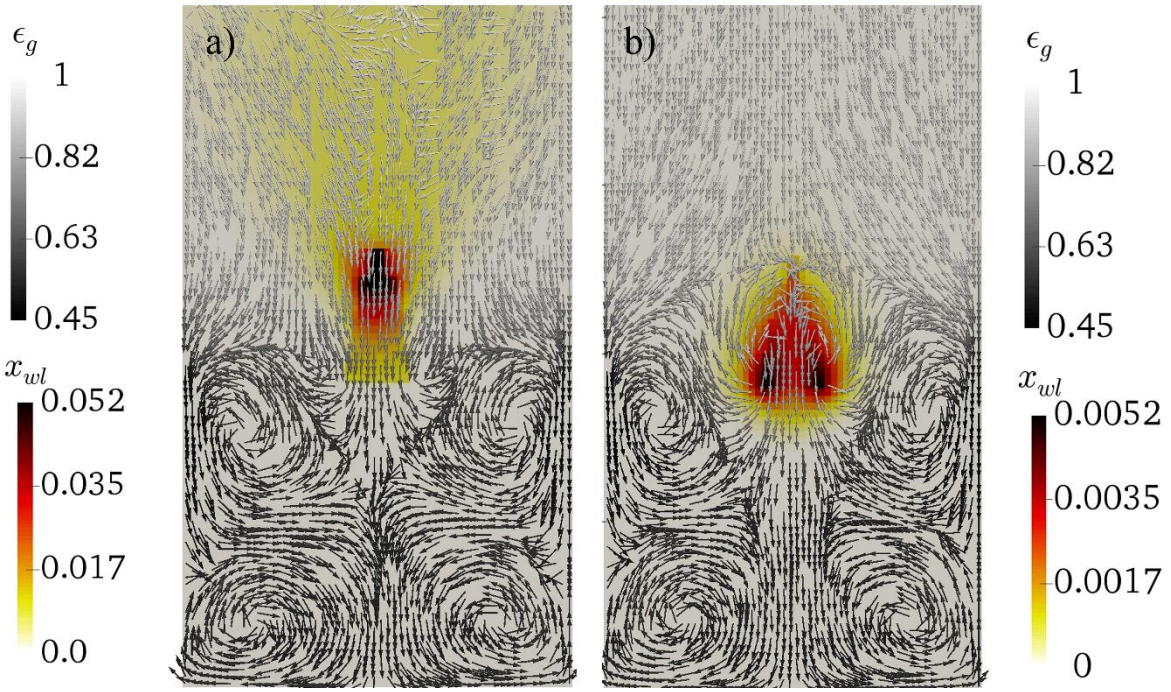

Figure 15 – Comparison of solid flow pattern (colored by gas volume fraction) and water liquid mass fraction in the gas phase for droplet velocity of a) $0.1 m/s$ and b) $7 m/s$

3.3.3.2. Effect of the nozzle position

It is essential to evaluate the reliability of developed 0D model in case that the WFB have the higher degree of non-uniformity, and may not fulfill the “well-mixed” condition. To do so, the nozzle position was changed in the simulation in such a way that $L_{trav} = 3L_{trav_{base}}$. It should be added that increasing the nozzle-to-bed-distance can depreciate the performance of the bed, and may be far from the optimal condition

for operating the WFB. Nevertheless, for examination of the validity of the developed model, such an extreme condition, which is out of interest for industry, were simulated. As depicted in Figure 16 and quantified in Figure 17, in case of $L_{trav}/L_{trav_{base}} = 3$, the predicted values of LoD and gas and particle temperature deviate $-27.9\%, -15.7\%,$ and -2.3% respectively from the predicted value in TFM. This deviation can be associated with the high degree of non-uniformity of the temperature distribution in the bed. According to the variance of temperature presented in Figure 17b. to this Figure, the standard deviation of the temperature is around 10% of the total change of gas temperature over flow time. Clearly, this non-uniformity is caused by a lack of deep penetration of droplets into the dense bed. To express in more detail, in case of long travel distance of the droplets, the droplet kinetic energy will be dissipated and droplets cannot penetrate to the bed and push the solid particles downward. In such a case, the droplet will be entrained and will be consumed by the evaporation instead of depositing on the particle surface. For more detail, please see previous section.

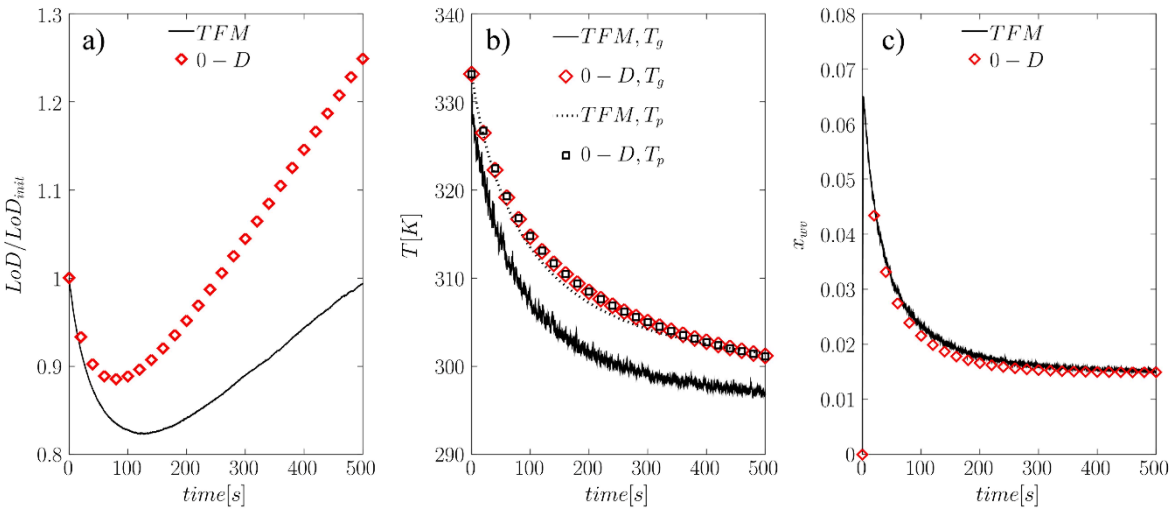

Figure 16 - comparion of a) LoD, b) particle and gas temperatures, and c) wate vapour mass fraction predicted by 0D model and TFM approach for $\frac{L_{trav}}{L_{trav_{base}}} = 3$ ($\dot{m}_{spray}^{norm} = 1.5, T_{init} = 333K$)

It should be noted that such a configuration that impairs the efficiency of the injected droplets is not of interest for industrial application, and hence a deeper discussion is skipped.

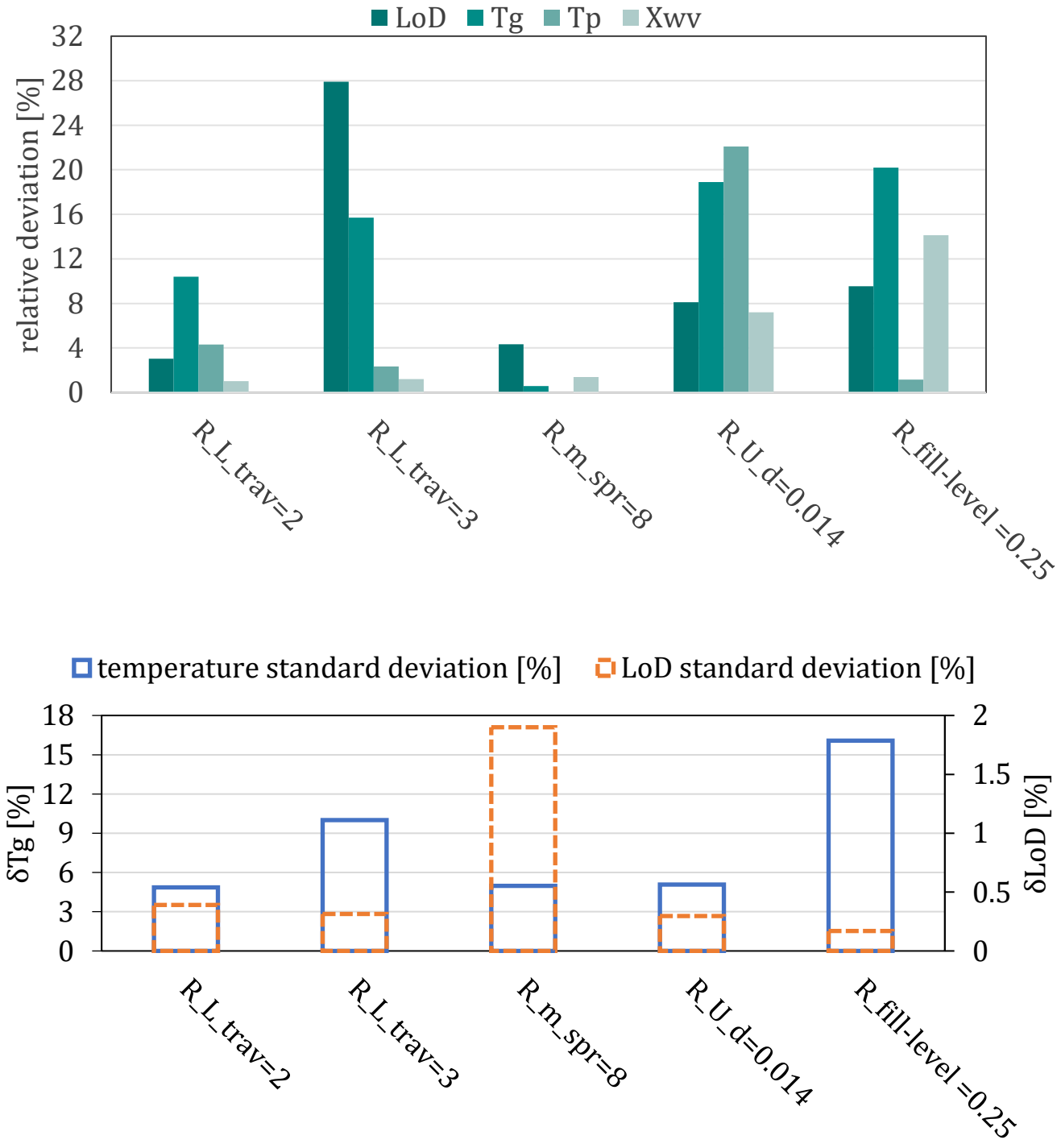

Figure 17 – Relative deviation of 0D model prediction from TFM results (top panel) and relative standard deviation of temperature and LoD (bottom panel) for various operating parameters and bed characteristics ($R\_L\_trav = \frac{L_{trav}}{L_{trav_{base}}}$, $R\_m\_spr = \dot{m}_{spray}^{norm}$, $R\_U\_d = \frac{u_d}{u_{d_{base}}}$, $R\_fill\_level = (H_0/L_{bed})/(H_0/L_{bed})_{base}$

3.3.4. Effect of the atomization air flow rate

To induce a higher level of non-uniformity in the temperature distribution in the bed, both the atomization air flow rate and spray rate were extremely increased. Consequently, a high amount of gas with low enthalpy was injected into the system at $\dot{m}_{spray}^{norm} = 8, x_{wl} = 0.1$. As seen in Figures 18 and 17, the comparison between 0D model and TFM approach reveals a relative deviation of 4.3% for particle LoD, of less than 1% for temperatures, and of 2% for x_{wv}. This demonstrates the reliability of the developed 0D model for the case of high atomization air.

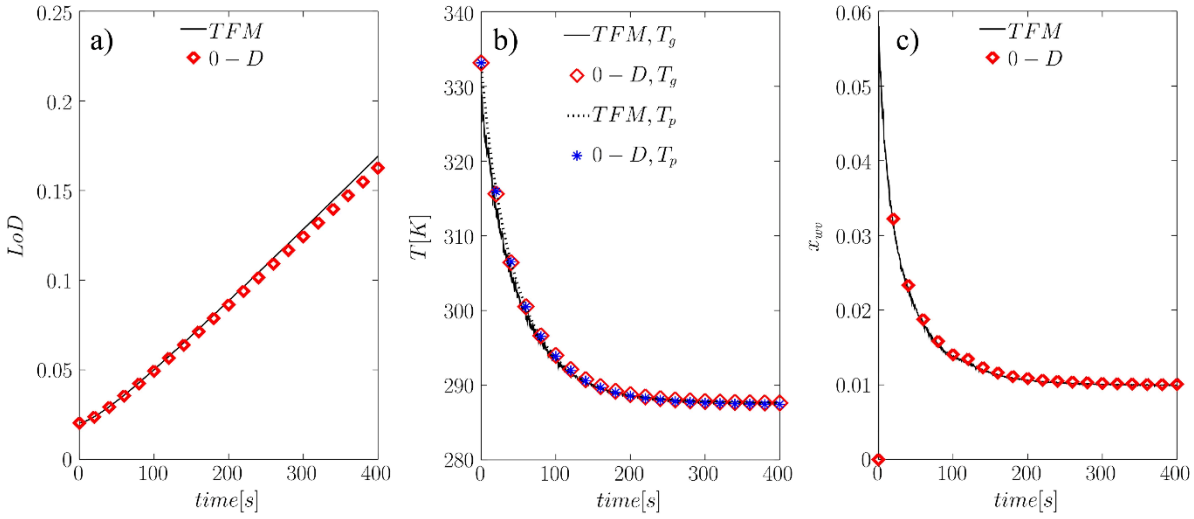

Figure 18 - comparion of a) LoD, b) particle and gas temperatures, and c) wate vapour mass fraction predicted by 0D model and TFM approach ($\dot{m}_{spray}^{norm} = 8, T_{init} = 333K$).

3.4. Discussion of the reliability of the proposed 0D model

Now that the dependency of bed uniformity was quantified for various operating parameters through LoD and temperature variance, as well as a comparison between results from the 0D model and the TFM, the validity of 0D model can be summarized as follows:

1. The higher the variance of LoD and temperature, the higher the degree of deviation of the 0D model from the TFM results when predicting gas and solid quantities (i.e., LoD, vapor content, and temperature). This finding can be also supported by Figure 17. As reported in this figure, in case of low bed aspect ratio

and long travel time of droplet, the standard deviation of temperature exceeds 10%. This induces the deviation of LoD and temperature predicted by the 0D model from the one in TFM.

2. Hydrodynamics of the bed greatly affects the uniformity of the bed. To put in detail, downward flow of solid particles in the central region of the bed is an indication of sufficient droplet penetration. Consequently, this indicates efficient mixing of particles and droplets, i.e., complete deposition of the injected droplets. If this condition is fulfilled, no droplet loss happens in the bed, and the variance of LoD and temperature will be low enough to assume the bed is well-mixed. An example for an extremely insufficiently mixed bed are the cases with a low bed aspect ratio, and a low droplet velocity. In the latter, the solid movement is upward in the top central region, and a remarkable deviation between 0D and TFM, for LoD and temperature can be observed as reported in Figure 17.
3. At extremely high atomization air flow rates, the 0D model manages to predict the bed performance with the largest deviation being 4.3% for the particles' LoD. This appears still acceptable. This deviation can be associated with the approximations made for the rate of droplet evaporation and drying in the spray zone.

In summary, to examine the validity of the developed 0D model, it is important to consider the degree of uniformity along with the droplet penetration and droplet loss. A good example is the case with low droplet velocity, as reported in Figure 17, the relative standard deviation of LoD and temperature for low droplet velocity do not exceed 6%. Nonetheless, due to insufficient penetration of droplet, as indicated by solid flow pattern in Figure 15, the 0D model fails to predict the bed performance due to the droplet loss. Consequently, to use the model presented in the present work, it is essential to fulfill all proposed criteria. It should be emphasized that the extreme cases showing the high deviation are usually out of interest for industry due to depreciation of the WFB performance.

4. Conclusion

In this work, TFM simulations of wet fluidized beds were performed to study the bed performance in terms of mixing quality and particle drying rate. The open-source code MFiX [33] was extended to simulate the involved exchange phenomena including i) droplet evaporation; ii) droplet deposition; and iii) particle drying in the bed. In order to examine the formation of well-mixed zones in the bed, the degree of uniformity of was computed in the bed based on TFM simulation results. It was demonstrated that the degrees of uniformity of LoD and gas temperature can be a useful indicator for the validity of the well-mixed condition in a wet fluidized bed, and consequently the validity of a 0D model. Another essential indicator to examine the "well-mixed" condition is attributed to the solid flow pattern predicted by the TFM. Specifically, if the droplets can penetrate through the dense bed and influence the flow of the particles, the bed is close to the well-mixed condition. This finding reveals the importance of considering the droplet velocity (and the spray) on solid flow behavior and bed performance for Geldart B particles. This bed-spray interaction has been ignored in most of the previous studies in which i) the spray zone was considered as a point (and droplet trajectories as straight, massless ray [2, 44]; or ii) the hydrodynamics of the spray is simulated separately from the gas-solid flow in the fluidized bed to identify the spray zone for simulation of heat and mass transfer in the bed [17, 18].

Based on our comparison of bed performance predicted by TFM and 0D model, it was demonstrated that the wet fluidized bed can be assumed as "well-mixed" by maximum deviation of 3% for gas and particle properties if:

a. The degrees of non-uniformity of LoD and temperature are small in comparison to the total temporal change of the corresponding quantity during the process; to express it in a quantitative way, standard deviations of smaller than 2 % for LoD and 5% for temperature (the basis for the relative temperature change is the temporal change over the process time, i.e. $|T_{end} - T_{init}|$) and gas vapor content, x_{wv}, indicate that the bed can be assumed to be well-mixed. It is worth mentioning that both criteria for the standard deviations must be fulfilled. For

instance, in case the bed aspect ratio was chosen to be 0.25, the standard deviation of LoD was 0.16%, while the standard deviation of the temperature exceeded 16%. Consequently, the values of LoD, temperature, and gas vapor content predicted by the 0D model deviated 10% , 20%, and 14% respectively, which appears unacceptable.

b. The solid flow pattern is a good indicator for sufficient droplet penetration into the bed.
c. No or only very little (i.e., less than 1%) droplet loss should occur.

In case the “well-mixed" condition is valid and the 0D model utilizes the macroscopic bed characteristics computed from the TFM data, the 0D model can predict the bed performance accurately with a maximum deviation of 3%. In case of excessive droplet loss (e.g., as observed for a low bed aspect ratio) and low droplet penetration length (e.g., caused by a low droplet velocity), the bed deviates from the well-mixed condition and the 0D model fails to predict TFM data.

Furthermore, the results of TFM simulation proved that the initial bed temperature significantly influence the temporal evolution of LoD variance, though its effect on the pseudo-steady state value is negligible. In contrast, spray rate has a significant impact on the pseudo-steady state value of LoD variance. What is more, the initial bed temperature plays a key role in temporal evolution of LoD. In case of high initial bed temperature, and due to the high rate of particle drying, the LoD profile first hits a minimum, and then gradually increases. Consequently, the initial bed temperature can be optimized to reduce the process time if the goal is to increase the LoD of the particles.

Symbols

a_d	specific mass transfer surface area of droplet, $6/d_d$;$1/m$
a_{dp}	specific mass transfer surface area of particle, $\left(1-\varepsilon_g\right) 6/d_p$
C_d	Drag coefficient
C_{Ps}	Specific heat of the fluid phase; $^{J}/_{kg.K}$
C_{Pg}	Specific heat of the solid phase; $^{J}/_{kg.K}$
d_d	Diameter of the droplets; m
d_p	Diameter of the particles; m
D_{gij}	Rate of strain tensor, fluid phase; s^{-1}
D_{sij}	Rate of strain tensor, solid phase; s^{-1}
D_{gn}	Diffusion coefficient of n^{th} gas-phase species; $kg/m \cdot s$
D_{vap}	molecular diffusivity of vapour in air; m^2/s
e	Coefficient of restitution for the collisions in solid phases
e_w	Coefficient of restitution for the collisions between solid particles and wall
f	fraction of particle surface coated by droplet; m^2/m^2
g_i	Acceleration due to gravity; m/s^2
g_0	Radial distribution function at contact
ΔH	Enthalpy; $^{J}/_{m^3.s}$
ΔH_{latent}	latent heat of vaporization; $^{J}/_{m^3.s}$
H_0	Static bed height; m
H_{bed}	bed height; m
i, j	Indices to identify vector and tensor components; summation convention is used only for these indices
I_{gsi}	Interphase momentum exchange force; N/m^3
J_s	Granular energy transfer; m^2/s^3
k_g	Fluid-phase conductivity; $^{J}/_{m.K.s}$
k_s	solid phase conductivity; $^{J}/_{m.K.s}$
L_{bed}	bed length; m
L_{inij}	spray zone length; m
LoD	Loss on drying, defined as mass fraction of liquid in the particle;
$\dot{m}_{spray}$	rate of droplet injection; kg/s
n	Constant in the friction model
N_{cell}	number of cells in each sample
N_{sample}	numbers of sample in the computational domain
Nu_m	Nusselt number
P_g	Pressure in the fluid phase; Pa
$P_{s,f}$	Frictional pressure in the solid phase; Pa
P_s	Solid pressure; Pa
Pr	Prandtl number; $C_p \nu_f \rho_f / k_g$
$\boldsymbol{q}_g$	Fluid-phase conductive heat flux; $^{J}/_{m^2.s}$
$\boldsymbol{q}_s$	solid phase conductive heat flux; $^{J}/_{m^2.s}$
Re_p	Solids phase particle Reynolds Number;
Re_m	mean particle Reynolds Number;
RH	relative humidity;
S_{gij}	Gas phase shear rate; s^{-1}
S_{sij}	Solid phase shear rate; s^{-1}
Sh_m	Sherwood Number, $\beta d_p / D_{vap}$
$\dot{S}_{depos}$	Rate of droplet deposition on particle; $kg/s/m^3$
$\dot{S}_{dry}$	Rate of particle drying; $kg/s/m^3$

$\dot{S}_{evap}$	Rate of droplet evaporation; $kg/s/m^3$
St	Droplet Stokes Number
St^*_{eff}	Effective droplet Stokes Number
t	Time; s
T_g	Thermodynamic temperature of the fluid phase; K
T_s	Thermodynamic temperature of the solids phase; K
$\boldsymbol{u}_d$	droplet velocity; m/s
u_{mf}	Minimum fluidization velocity; m/s
U_{gi}	Fluid-phase velocity vector; m/s
$\boldsymbol{u}_g$	Superficial gas velocity; m/s
U_{si}	Solid-phase velocity vector; m/s
W_{bed}	bed width; m
x_n	Mass fraction of the chemical species n

Greek Letters

α	A constant with value of 1.6; dimensionless
γ_{gm}	Fluid-solids heat transfer coefficient corrected for interphase mass transfer; $J/m^3.K.s$
β	mass transfer coefficient; m/s
β_{gs}	Coefficient for the interphase force between the fluid phase and the solid phase; $kg/m^3 \cdot s$
δ_{ij}	Kronecker Delta function
ΔH_s	enthalpy of phase change(evaporation) in gas phase; j/kg
ΔH_s	enthalpy of phase change (evaporation) in solid phase; j/kg
ε_g	Volume fraction of the fluid phase (void fraction)
ε^*_g	Volume fraction of the fluid phase in minimum fluidization condition
$\varepsilon_{s,max}$	Packed-bed (maximum) solids volume fraction
ε_s	Volume fraction of solids phase
η	Function of restitution coefficient
Θ	Granular temperature of solid phase; m^2/s^2
κ_s	Granular energy diffusion coefficient; $kg/m.s$
λ	filtration coefficient; $1/m$
λ_{rm}	Solid conductivity function
μ_g	Molecular viscosity of the fluid phase; $kg/m \cdot s$
μ_{sf}	Frictional shear viscosity of the solid phase; $kg/m \cdot s$
μ_{liq}	mass loading of liquid in gas phase; kg/kg
μ_{vap}	mass loading of vapour in gas phase; kg/kg
Π_s	Exchange force in granular energy equation; $kg/m \cdot s^3$
ρ_g	Microscopic (material) density of the fluid phase; kg/m^3
ρ_s	Microscopic (material) density of the m^{th} solids phase; kg/m^3
$\rho_{w,Sat}$	saturation density of water vapour; kg/m^3
σ_{LoD}	standard deviation of LoD
σ_T	standard deviation of temperature
τ_{gij}	Fluid-phase stress tensor; Pa
τ_{sij}	Solids phase m stress tensor; Pa
$\bar{\bar{\tau}}_{s,f}$	Solid phase frictional stress tensor; Pa
φ	Angle of internal friction, also used as general scalar
φ_s	Specularity coefficient
ψ_{liq}	particle surface coverage

subscripts

d	droplet
g	gas phase
in	inlet
$init$	at time of zero

max	maximum
mix	mixture
out	outlet
p	particle
s	solid phase
wl	water liquid
wv	water vapor

superscripts

norm	normalized
sat	saturation condition

Abbreviation

0D	Zero-Dimensional
CFD	Computational Fluid Dynamics
DEM	Discrete Element Method
DNS	Direct Numerical Simulation
EE	Euler-Euler (method)
EL	Euler-Lagrange (method)
FB	Fluidized Bed
FBC	Fluid Bed Coater
FBG	Fluid Bed Granulator
KTGF	Kinetic Theory of Granular Flow
LoD	Loss on Drying
MFiX	Multiphase Flow with Interphase eXchange
MFM	Multi-Fluid Model
PBE	Population Balance Equation
TFM	Two-Fluid Method
WFB	Wet Fluidized Bed

References

[1] I. Jacobs, N. Mason, Polymer delivery systems concepts, ACS Publications1993.

[2] D. Suzzi, G. Toschkoff, S. Radl, D. Machold, S.D. Fraser, B.J. Glasser, J.G. Khinast, DEM simulation of continuous tablet coating: Effects of tablet shape and fill level on inter-tablet coating variability, Chemical engineering science, 69 (2012) 107-121.

[3] L. Fries, S. Antonyuk, S. Heinrich, S. Palzer, DEM–CFD modeling of a fluidized bed spray granulator, Chemical Engineering Science, 66 (2011) 2340-2355.

[4] T. Jiménez, C. Turchiuli, E. Dumoulin, Particles agglomeration in a conical fluidized bed in relation with air temperature profiles, Chemical Engineering Science, 61 (2006) 5954-5961.

[5] W. Duangkhamchan, F. Ronsse, S. Siriamornpun, J. Pieters, Numerical study of air humidity and temperature distribution in a top-spray fluidised bed coating process, Journal of Food Engineering, 146 (2015) 81-91.

[6] C. Turchiuli, T. Jimenèz, E. Dumoulin, Identification of thermal zones and population balance modelling of fluidized bed spray granulation, Powder technology, 208 (2011) 542-552.

[7] P. Smith, A. Nienow, Particle growth mechanisms in fluidised bed granulation—I: the effect of process variables, Chemical Engineering Science, 38 (1983) 1223-1231.

[8] M. Börner, T. Hagemeier, G. Ganzer, M. Peglow, E. Tsotsas, Experimental spray zone characterization in top-spray fluidized bed granulation, Chemical Engineering Science, 116 (2014) 317-330.

[9] S. Maronga, P. Wnukowski, Modelling of the three-domain fluidized-bed particulate coating process, Chemical Engineering Science, 52 (1997) 2915-2925.

[10] S. Maronga, P. Wnukowski, The use of humidity and temperature profiles in optimizing the size of fluidized bed in a coating process, Chemical Engineering and Processing: Process Intensification, 37 (1998) 423-432.

[11] M. Börner, A. Bück, E. Tsotsas, DEM-CFD investigation of particle residence time distribution in top-spray fluidised bed granulation, Chemical Engineering Science, 161 (2017) 187-197.

[12] M. Vanderroost, F. Ronsse, K. Dewettinck, J.G. Pieters, Modelling overall particle motion in fluidised beds for top-spray coating processes, Particuology, 11 (2013) 490-505.

[13] G. Toschkoff, J.G. Khinast, Mathematical modeling of the coating process, International journal of pharmaceutics, 457 (2013) 407-422.

[14] B. Freireich, J. Li, J. Litster, C. Wassgren, Incorporating particle flow information from discrete element simulations in population balance models of mixer-coaters, Chemical Engineering Science, 66 (2011) 3592-3604.

[15] M. Börner, M. Peglow, E. Tsotsas, Particle residence times in fluidized bed granulation equipments, Chemical Engineering & Technology, 34 (2011) 1116-1122.

[16] H. Wang, W. Yang, P. Senior, R. Raghavan, S. Duncan, Investigation of batch fluidized-bed drying by mathematical modeling, CFD simulation and ECT measurement, AIChE Journal, 54 (2008) 427-444.

[17] W. Duangkhamchan, F. Ronsse, F. Depypere, K. Dewettinck, J. Pieters, CFD study of droplet atomisation using a binary nozzle in fluidised bed coating, Chemical Engineering Science, 68 (2012) 555-566.

[18] W. Duangkhamchan, F. Ronsse, K. Dewettinck, J. Pieters, CFD study of solids concentration in a fluidised-bed coater with variation of atomisation air pressure, Powder technology, 212 (2011) 103-114.

[19] F. Ronsse, W. Duangkhamchana, K. Dewettinckb, J.G. Pietersa, Computational Fluid Dynamics (CFD) modelling of the fluidised bed coating process, 7th International conference on Simulation and Modeling in the Food and Bio-industry (Foodsim'2012), Eurosis-ETI, 2012, pp. 34-41.

[20] R.G. Szafran, A. Kmiec, CFD modeling of heat and mass transfer in a spouted bed dryer, Industrial & engineering chemistry research, 43 (2004) 1113-1124.

[21] N. Reuge, L. Cadoret, C. Coufort-Saudejaud, S. Pannala, M. Syamlal, B. Caussat, Multifluid Eulerian modeling of dense gas–solids fluidized bed hydrodynamics: influence of the dissipation parameters, Chemical Engineering Science, 63 (2008) 5540-5551.

[22] M. Heine, S. Antonyuk, L. Fries, G. Niederreiter, S. Heinrich, S. Palzer, Modeling of the spray zone for particle wetting in a fluidized bed, Chemie Ingenieur Technik, 85 (2013) 280-289.

[23] J. Link, W. Godlieb, P. Tripp, N. Deen, S. Heinrich, J. Kuipers, M. Schönherr, M. Peglow, Comparison of fibre optical measurements and discrete element simulations for the study of granulation in a spout fluidized bed, Powder technology, 189 (2009) 202-217.

[24] A. Ozel, J. Kolehmainen, S. Radl, S. Sundaresan, Fluid and particle coarsening of drag force for discrete-parcel approach, Chemical Engineering Science, 155 (2016) 258-267.

[25] S. Radl, S. Sundaresan, A drag model for filtered Euler–Lagrange simulations of clustered gas–particle suspensions, Chemical Engineering Science, 117 (2014) 416-425.

[26] V.S. Sutkar, N.G. Deen, A.V. Patil, V. Salikov, S. Antonyuk, S. Heinrich, J. Kuipers, CFD–DEM model for coupled heat and mass transfer in a spout fluidized bed with liquid injection, Chemical Engineering Journal, 288 (2016) 185-197.

[27] M. Askarishahi, M.S. Salehi, S. Radl, Full-physics simulations of spray-particle interaction in a bubbling fluidized bed, AIChE Journal, 63 (2017) 2569-2587.

[28] M.-S. Salehi, M. Askarishahi, S. Radl, Analytical solution for thermal transport in packed beds with volumetric heat source, Chemical Engineering Journal, 316 (2017) 131-136.

[29] D.F. Sherony, A model of surface renewal with application to fluid bed coating of particles, Chemical engineering science, 36 (1981) 845-848.

[30] H.M. Hulburt, S. Katz, Some problems in particle technology: A statistical mechanical formulation, Chemical Engineering Science, 19 (1964) 555-574.

[31] F. Ronsse, J. Pieters, K. Dewettinck, Modelling heat and mass transfer in batch, top-spray fluidised bed coating processes, Powder Technology, 190 (2009) 170-175.

[32] M. Hussain, J. Kumar, M. Peglow, E. Tsotsas, On two-compartment population balance modeling of spray fluidized bed agglomeration, Computers & Chemical Engineering, 61 (2014) 185-202.

[33] M. Syamlal, W. Rogers, T.J. OBrien, MFIX documentation theory guide, USDOE Morgantown Energy Technology Center, WV (United States), 1993.

[34] S. Roy, S. Luding, T. Weinhart, Towards a general (ized) shear thickening rheology of wet granular materials under small pressure, arXiv preprint arXiv:1609.03098, (2016).

[35] S. Roy, S. Luding, T. Weinhart, Towards hydrodynamic simulations of wet particle systems, Procedia Engineering, 102 (2015) 1531-1538.

[36] S. Roy, A. Singh, S. Luding, T. Weinhart, Micro–macro transition and simplified contact models for wet granular materials, Computational particle mechanics, 3 (2016) 449-462.

[37] P. Liu, K.M. Kellogg, C.Q. LaMarche, C.M. Hrenya, Dynamics of singlet-doublet collisions of cohesive particles, Chemical Engineering Journal, 324 (2017) 380-391.

[38] M.-S. Salehi, M. Askarishahi, H.R. Godini, R. Schomäcker, G.n. Wozny, CFD Simulation of Oxidative Coupling of Methane in Fluidized-Bed Reactors: A Detailed Analysis of Flow-Reaction Characteristics and Operating Conditions, Industrial & Engineering Chemistry Research, 55 (2016) 1149-1163.

[39] N.G. Deen, S.H. Kriebitzsch, M.A. van der Hoef, J. Kuipers, Direct numerical simulation of flow and heat transfer in dense fluid–particle systems, Chemical Engineering Science, 81 (2012) 329-344.

[40] W.I. Kariuki, B. Freireich, R.M. Smith, M. Rhodes, K.P. Hapgood, Distribution nucleation: quantifying liquid distribution on the particle surface using the dimensionless particle coating number, Chemical Engineering Science, 92 (2013) 134-145.

[41] R. Kolakaluri, Direct Numerical Simulations and Analytical Modeling of Granular Filtration, Iowa State University 2013.

[42] M. Askarishahi, M.-S. Salehi, A.M. Dehkordi, Numerical investigation on the solid flow pattern in bubbling gas–solid fluidized beds: Effects of particle size and time averaging, Powder Technology, 264 (2014) 466-476.

[43] M. Askarishahi, M.-S. Salehi, H.R. Godini, G. Wozny, CFD study on solids flow pattern and solids mixing characteristics in bubbling fluidized bed: Effect of fluidization velocity and bed aspect ratio, Powder Technology, 274 (2015) 379-392.

[44] G. Toschkoff, S. Just, A. Funke, D. Djuric, K. Knop, P. Kleinebudde, G. Scharrer, J.G. Khinast, Spray models for discrete element simulations of particle coating processes, Chemical Engineering Science, 101 (2013) 603-614.

List of tables

Table 1.1- momentum equation used in TFM simulation

Momentum Conservation Equations	
$\frac{\partial(\varepsilon_g \rho_g \boldsymbol{U_g})}{\partial t} + \nabla.(\varepsilon_g \rho_g \boldsymbol{U_g U_g}) = -\varepsilon_g \nabla P_g + \nabla \cdot \bar{\bar{\boldsymbol{\tau}}}_{\boldsymbol{g}} - \boldsymbol{I_{gs}} + \varepsilon_g \rho_g \boldsymbol{g}$	(T1.1.1)
$\frac{\partial(\varepsilon_s \rho_s \boldsymbol{U_s})}{\partial t} + \nabla.(\varepsilon_s \rho_s \boldsymbol{U_s U_s}) = -\varepsilon_s \nabla P_g + \nabla \cdot \bar{\bar{\boldsymbol{\tau}}}_{\boldsymbol{s}} + \boldsymbol{I_{gs}} + \varepsilon_s \rho_s \boldsymbol{g} - \nabla P_s$	(T1.1.2)
Interphase Momentum Transfer	
$\boldsymbol{I_{gs}} = \beta_{gs}(\boldsymbol{u_g} - \boldsymbol{u_s})$	(T1.1.3)
$\beta_{gs} = 18\rho_g \lvert \boldsymbol{u_g} - \boldsymbol{u_s} \rvert \varepsilon_g (1-\varepsilon_g) \frac{F(\varphi_f, Re)}{d_s^2}$	(T1.1.4)
$F(\varphi_f, Re) = 10\frac{1-\varepsilon_g}{\varepsilon_g^2} + \varepsilon_g^2\left(1 + 1.5\sqrt{1-\varepsilon_g}\right) + \frac{0.413\,Re}{24\varepsilon_g^2}\frac{\left(\frac{1}{\varepsilon_g} + 3\varepsilon_g(1-\varepsilon_g) + 8.4Re^{-0.343}\right)}{\left(1 + 10^{3(1-\varepsilon_g)}Re^{\frac{-1}{2}\left(1+4(1-\varepsilon_g)\right)}\right)}$	(T1.1.5)
$Re_p = \frac{\rho_g \lvert \boldsymbol{u_g} - \boldsymbol{u_s} \rvert d_p}{\mu_g}$	(T1.1.6)
$Solid - phase\ stress\ tensor$	
$\bar{\bar{\tau}}_s = -\varepsilon_s\left[\left(\xi_s - \frac{2}{3}\mu_s\right)(\nabla \cdot u_s)\bar{\bar{I}} + \mu_s(\nabla u_s + (\nabla u_s)^T)\right]$	(T1.1.7)
$\mu_s = \mu_{s,KTFG} + \mu_{s,f}$	(T1.1.8)
$P_s = P_{s,KTFG} + P_{s,f}$	(T1.1.9)
Gas-phase stress tensor	
$\bar{\bar{\tau}}_g = -\varepsilon_g\left[\left(\xi_g - \frac{2}{3}\mu_g\right)(\nabla \cdot u_g)\bar{\bar{I}} + \mu_g\left(\nabla u_g + (\nabla u_g)^T\right)\right]$	(T1.1.10)

Table 1.2. transport equation for granular energy

$$\frac{3}{2}\left(\frac{\partial(\varepsilon_s\rho_s\Theta)}{\partial \mathrm{t}}+\nabla\cdot(\varepsilon_s\rho_s u_s\Theta)\right)=\left(-P_s\bar{\bar{I}}+\bar{\bar{\tau}}_s\right):\nabla u_s-\nabla\cdot q-\Pi_s+J_s \tag{T1.2.1}$$

$$\kappa_s=\left(\frac{\kappa_s^*}{g_0}\right)\left[\left(1+\frac{12}{5}\eta\varepsilon_s g_0\right)\left(1+\frac{12}{5}\eta^2(4\eta-3)\varepsilon_s g_0\right)+\frac{64}{25\pi}(41-33\eta)\eta^2(\varepsilon_s g_0)^2\right] \tag{T1.2.2}$$

$$\kappa_s^*=\frac{\varepsilon_s\rho_s g_0\Theta\kappa}{\varepsilon_s\rho_s g_0\Theta+\frac{6\beta\kappa}{5\varepsilon_s\rho_s}} \tag{T1.2.3}$$

$$\kappa=\frac{75\rho_s d_p\sqrt{\pi\Theta}}{48\eta(41-33\eta)} \tag{T1.2.4}$$

$$\Pi_s=-3\beta\Theta+\frac{81\varepsilon_s\mu_g^2\left|u_g-u_s\right|^2}{g_0\rho_s d_p^3\sqrt{\pi\Theta}} \tag{T1.2.5}$$

$$J_s=\frac{48}{\sqrt{\pi}}\eta(1-\eta)\frac{\varepsilon_s g_0}{d_p}\Theta^{3/2} \tag{T1.2.6}$$

Table 1.3. Constitutive equations for calculation of solid stress tensor

Solid Viscosity	
$\mu_{s,KTGF} = \left(\frac{2+\alpha}{3}\right)\left[\frac{\mu_s^*}{g_0\eta(2-\eta)}\left(1+\frac{8}{5}g_0\eta\varepsilon_s\right)\left(1+\frac{8}{5}\eta(3\eta-2)g_0\varepsilon_s\right)+\frac{3}{5}\eta\mu_b\right]$	(T1.3.1)
$\mu_s^* = \frac{\varepsilon_s\rho_s\Theta g_0\mu}{\varepsilon_s\rho_s\Theta g_0 + \frac{2\beta\mu}{\varepsilon_s\rho_s}}$	(T1.3.2)
$\mu = \frac{5}{96}\rho_s d_p\sqrt{\pi\Theta}$	(T1.3.3)
$\mu_b = \frac{256}{5\pi}\mu\varepsilon_s\varepsilon_s g_0$	(T1.3.4)
$\xi_s = \frac{4}{3}\varepsilon_s\rho_s d_p g_0(1+e)\sqrt{\frac{\Theta}{\pi}}$	(T1.3.5)
Solid Pressure	
$P_s = \varepsilon_s\rho_s\Theta[1+4\eta\varepsilon_s g_0]$	(T1.3.6)
$\eta = \frac{1+e}{2}$	(T1.3.7)
Frictional Stress	
$\bar{\bar{\tau}}_{s,f} = P_{s,f}\bar{\bar{I}} + +\mu_{s,f}[\nabla u_s + (\nabla u_s)^T]$	(T1.3.8)
$\mu_{s,f} = \begin{cases} min\left(\frac{P_s\sin(\varphi)}{2\sqrt{\bar{\bar{I}}_{2D}}}, \mu_m^{max}\right), & for\ \ \varepsilon_g < \varepsilon_g^* \\ 0, & for\ \ \varepsilon_g \geq \varepsilon_g^* \end{cases}$	(T1.3.9)
$\mu_m^{max} = 1000\ Poise$ and $\varepsilon_g^* = 0.5\ in\ the\ present\ study$	
$\bar{\bar{I}}_{2D} = \frac{1}{6}\left[\left(\frac{\partial u_{s,x}}{\partial x}-\frac{\partial u_{s,y}}{\partial y}\right)^2+\left(\frac{\partial u_{s,y}}{\partial y}-\frac{\partial u_{s,z}}{\partial z}\right)^2+\left(\frac{\partial u_{s,z}}{zx}-\frac{\partial u_{s,x}}{\partial x}\right)^2\right] + \frac{1}{4}\left[\left(\frac{\partial u_{s,x}}{\partial y}+\frac{\partial u_{s,y}}{\partial x}\right)^2+\left(\frac{\partial u_{s,y}}{\partial z}+\frac{\partial u_{s,z}}{\partial y}\right)^2 + \left(\frac{\partial u_{s,z}}{\partial x}+\frac{\partial u_{s,x}}{\partial z}\right)^2\right]$	(T1.3.10)

$$P_{s,f} = Fr\frac{(\varepsilon_s - \varepsilon_{s,min})^n}{(\varepsilon_{s,max} - \varepsilon_s)^p} \quad \text{(T1.3.11)}$$

$Fr = 0.05, n = 2, \text{and } p = 5$

Table 1.4. thermal energy equations and constitutive equations

$$\varepsilon_g \rho_g C_{Pg} \left(\frac{\partial T_g}{\partial t} + \boldsymbol{u}_g . \nabla T_g \right) = -\nabla . \boldsymbol{q}_g + h a_p (T_s - T_g) - \Delta H_g \quad \text{(T1.4.1)}$$

$$\varepsilon_s \rho_s C_{Ps} \left(\frac{\partial T_s}{\partial t} + \boldsymbol{u}_s . \nabla T_s \right) = -\nabla . \boldsymbol{q}_s - h a_p (T_s - T_g) - \Delta H_s \quad \text{(T1.4.2)}$$

$$\boldsymbol{q}_g = -\varepsilon_g \, k_g \, \nabla T_g \quad \text{(T1.4.3)}$$

$$\boldsymbol{q}_s = -\varepsilon_s \, k_s \, \nabla T_s \quad \text{(T1.4.4)}$$

Heat Transfer Coefficient

$$h = \frac{k_g Nu}{d_p} \quad \text{(T1.4.5)}$$

$$Nu = \left(7 - 10\varepsilon_g + 5\varepsilon_g^2\right).\left(1 + 0.7 Re_p^{0.2} Pr^{1/3}\right) + \left(1.33 - 2.4\varepsilon_g + 1.2\varepsilon_g^2\right) Re_p^{0.7} Pr^{1/3} \quad \text{(T1.4.6)}$$

Species transport Equations

$$\frac{\partial}{\partial t}\left(\varepsilon_g \rho_g x_{wl}\right) + \nabla . \left(\varepsilon_g \rho_g x_{wl} \boldsymbol{u_g}\right) = \nabla . D_{gn} \nabla x_{wl} + \dot{S}_{spray} - \dot{S}_{evap} - \dot{S}_{depos} \quad \text{(T1.4.7)}$$

$$\frac{\partial}{\partial t}\left(\varepsilon_g \rho_g x_{wv}\right) + \nabla . \left(\varepsilon_g \rho_g x_{wv} \boldsymbol{u_g}\right) = \nabla . D_{gn} \nabla x_{wv} + \dot{S}_{dry} + \dot{S}_{evap} \quad \text{(T1.4.8)}$$

$$\frac{\partial}{\partial t}(\varepsilon_s \rho_s x_{ls}) + \nabla . (\varepsilon_s \rho_s x_{ls} \boldsymbol{u_s}) = \nabla . D_{sn} \nabla x_{ls} + \dot{S}_{depos} - \dot{S}_{dry} \quad \text{(T1.4.9)}$$

Mass Transfer Rate and Coefficient

$$\dot{S}_{dry} = \left|\rho_{w,sat} - \rho_g \mu_{vap}\right| a_{dp} \beta \quad \text{(T1.4.10)}$$

$$\beta = \frac{D_{wv} Sh_m}{d_p} \quad \text{(T1.4.11)}$$

$$Sh_m = \left(7 - 10\varepsilon_g + 5\varepsilon_g^2\right).\left(1 + 0.7 Re_p^{0.2} Sc^{1/3}\right) + \left(1.33 - 2.4\varepsilon_g + 1.2\varepsilon_g^2\right) Re_p^{0.7} Sc^{1/3} \quad \text{(T1.4.12)}$$

Table 2- Equations for Calculation of Filter Coefficient

$$\lambda = \eta_s \frac{3}{2} \frac{\varepsilon_s}{d_s} \tag{T2.1}$$

$$\eta_s = \frac{{St^*_{eff}}^{3.2}}{4.3 + {St^*_{eff}}^{3.2}} \tag{T2.2}$$

$$St^*_{eff} = \left[A(\varepsilon_s) + 1.14 Re_m^{\frac{1}{5}} (1 - \varepsilon_s)^{-3/2} \right] \frac{St}{2} \tag{T2.3}$$

$$A(\varphi_p) = \frac{6 - 6{\varepsilon_s}^{\frac{5}{3}}}{6 - 9{\varepsilon_s}^{\frac{1}{3}} + 9{\varepsilon_s}^{\frac{5}{3}} - 6{\varepsilon_s}^2} \tag{T2.4}$$

$$St = \frac{|u_g - u_s| {d_d}^2 \rho_d}{18 d_p \nu_g \varepsilon_g} \tag{T2.5}$$

$$Re_m = \frac{|u_g - u_s|(1 - \varepsilon_g)\rho_g d_p}{\nu_f \varepsilon_g} \tag{T2.6}$$

Table 3- simulation conditions and parameters used in the TFM approach

Parameter	Base Case	Studied range
Bed geometry		
H_{bed} $[m]$	0.75	$0.75 - 2.25$
L_{bed} $[m]$	0.23	$0.23 - 0.69$
H_{inj} $[m]$	0.26	–
H_0/L_{bed} $[-]$	0.65	$0.15 - 0.65$
$\theta_{half,inj}$ [°]	15	–
Particle properties		
ρ_s $[kg/m^3]$	2600	–
d_p $[\mu m]$	400	–
$e_{w,p}$ $[-]$	1	–
$e_{pp}[-]$	1	–
$\phi_{p,w}$ $[-]$	0.5	–
$T_{p_{init}}$ $[K]$	333	$300-333$
LoD_{init} $[-]$	0.0204	$0.0204 - 0.0309$
Spray properties		
ρ_d [kg/m^3]	1000	–
d_d [μm]	20	–
μ_g $[Pa.\,s]$	1.79×10^{-5}	–
u_d $[m/s]$	7	$0.1-7$
$\dot{m}_{spray}[kg/s]$	$2/3\dot{m}_{spray}^{max}$	$0 - \dot{m}_{spray}^{max}$
Gas phase properties		
ρ_g[kg/m^3]	1.188	–
μ_g $[Pa.\,s]$	1.79×10^{-5}	–
$T_{g_{init}}$ $[K]$	333	$300-333$
T_{g_i} $[K]$	333	–
u [m/s]	$3.5u_{mf}$	–
Wall boundary condition		
gas	$no - slip$	–
$solid$	$partial - slip$	–

Table 4- summary of the operating conditions and bed configurations of the cases investigated in the present work. Please note that only the unspecified values are identical to the base case, as reported in the first raw

sections	Studied effect	$\dot{m}_{spray}^{norm}$	u_d	H_0/L_{bed}	H_{bed}	L_{bed}	T_{init}	x_{wv}	$L_{trav}/L_{trav_{base}}$
3.1	*base case*	0.66	7	0.65	0.75	0.23	333	0.5	1
3.2.1 3.3.1	1. *spray rate* 2. *initial bed temperature*	0							
		0.5							
		1							
		0.5					300		
		1					300		
3.3.2	1. *bed aspect ratio*	1.5		0.65	2.25	0.69			
	2. *bed dimension*	1.5		0.15	0.75	0.69			
3.3.3	1. *droplet velocity* 2. *droplet travel distance*	1.5							
		1.5	0.1						
		1.5							2
		1.5							3
3.3.4	*atomization air*	8						0.1	

Table 5- Comparison of averaged upward axial to lateral solid velocity at different heights in the bed with various bed aspect ratios

$Bed\ aspect\ ratio$	h/H_{exp}	$\bar{U}_s[m/s]$	$\bar{V}_s[m/s]$	$\bar{U}_s/\bar{V}_s$
0.15	0.33	0.047	0.036	1.31
0.15	0.66	0.1	0.056	1.79
0.65	0.33	0.076	0.071	1.07
0.65	0.66	0.045	0.12	0.38

Appendix A: Model verification

Verification studies were performed in the packed bed to examine the accuracy of the models implemented in MFiX open-source code.

A.1. droplet evaporation

It was assumed that the liquid mass loading is so high and evaporation rate is so small that droplet surface area available for evaporation cannot change over the time. Besides, the droplets are assumed to flow with the gas velocity

$$\frac{\partial \mu_{vap}\epsilon_g\rho_g}{\partial t} + \nabla \cdot \left(u_f \mu_{vap}\epsilon_g\rho_g\right) = \dot{S}_{evap} \tag{A.1}$$

$$\dot{S}_{evap} = \left|\rho_{w,sat} - \rho_g\mu_{vap}\right| a_d\beta \tag{A.2}$$

As shown in Figure A.1, the predicted vapour mass loading along the packed bed is in correspond with the value obtained through analytical approach. It should be noted that x represents the distance from the distributor and L_{bed} denotes the packed bed length.

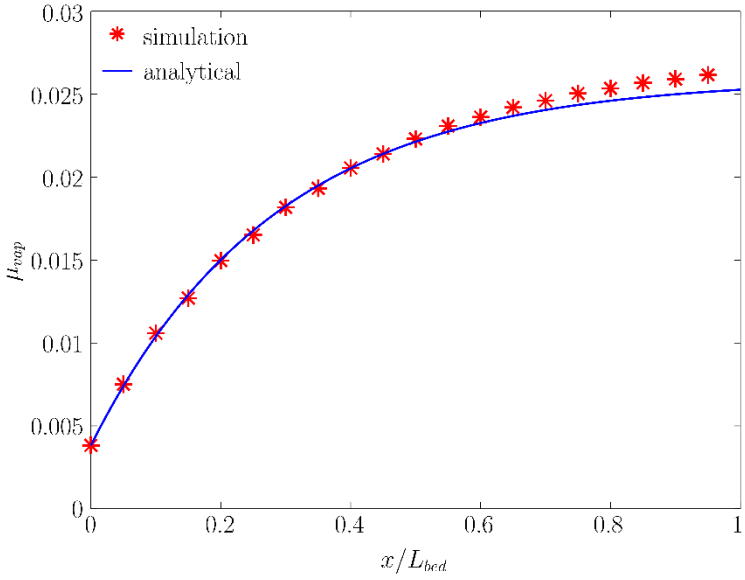

Figure A.1 – comparison of water vapour mass loading in the gas phase along the bed due to freely-flowing droplet evaporation

A.2. particle drying

To verify the implemented model for drying rate, the mass balance equation for water vapour was derived as

$$\frac{\partial \mu_{vap} \epsilon_g \rho_g}{\partial t} + \nabla \cdot \left(u_f \mu_{vap} \epsilon_g \rho_g \right) = \dot{S}_{dry} \tag{A.3}$$

$$\dot{S}_{dry} = \left| \rho_w^{sat} - \rho_g \mu_{vap} \right| a_{dp} \beta \tag{A.4}$$

It was assumed that the saturation pressure of vapour remains constant. The distribution of water vapour along the bed is analytically obtained at steady state condition. As shown in Figure A.2, the predicted vapour mass loading along the packed bed is in correspond with the value obtained through analytical approach

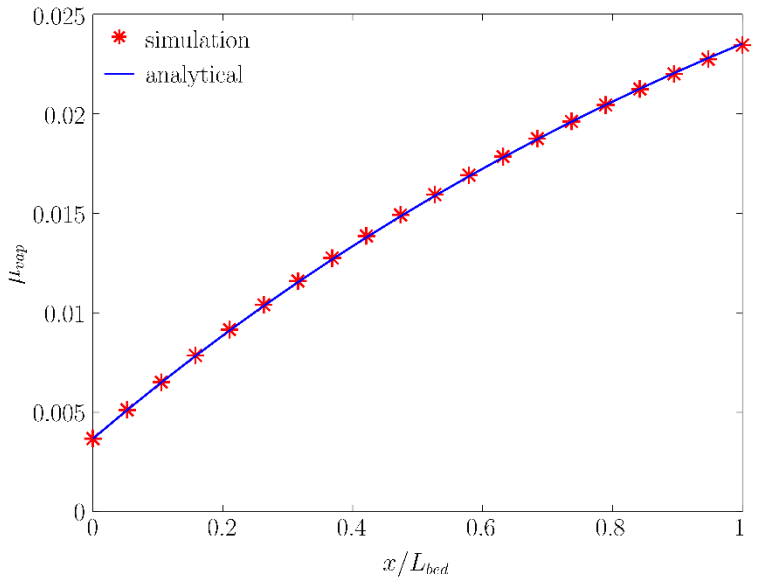

Figure A.2 – comparison of water vapour mass loading in the gas phase along the bed due to particle drying

A.3. Droplet deposition

To verify the implemented model for droplet deposition, an analytical solution was obtained for a packed bed with a clean-bed filter (filtration coefficient is assumed to be constant along the bed)

$$\frac{\partial(\mu_{liq}\epsilon_g\rho_g)}{\partial t} + \nabla\cdot(u_g\mu_{liq}\epsilon_g\rho_g) = \dot{S_d} \tag{A.5}$$

$$\dot{s}_{depos} = -\lambda|\boldsymbol{u}_d - \boldsymbol{u}_p|\mu_{liq}\epsilon_g\rho_g \tag{A.6}$$

$$ln\left(\frac{\mu_{liq}}{\mu_{liq,in}}\right) = -\lambda x \tag{A.7}$$

Where μ_{liq} denotes the liquid mass loading. As shown in Figure A.3, the predicted liquid mass loading along the packed bed is in good agreement with the value obtained through analytical approach

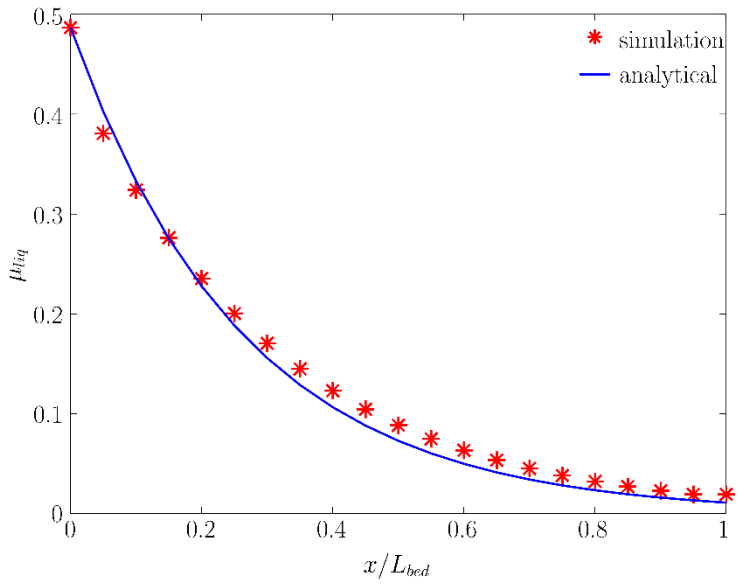

Figure A.3– comparison of water liquid mass loading in the gas phase along the bed due to droplet deposition on the particle surface

Appendix B: maximum spray rate calculation

The maximum rate of the spray rate corresponds to the spray rate at which the steady state relative humidity of outlet gas is 100% while not over-wetting the particles. This corresponds to the evaporation of the entire droplets injected to the system. Therefore, the partial pressure of the outlet gas should be equal to the saturation pressure at T_{out} given by

$$P_{wv} = P_{tot}\left(\frac{x_{vw_{out}} MW_{mix}}{MW_{wl}}\right) = P^{sat}(T_{out}) \tag{B.1}$$

$$\ln\left(P^{sat}(T_{out})\right) = A - \frac{B}{T + C} \tag{B.2}$$

Where mass fraction of water vapour in the outlet can be given by

$$x_{wv_{out}} = \frac{\dot{m}_{spray} x_{wl}}{m_{in} + \dot{m}_{spray}(1 - x_{wv})} \tag{B.3}$$

In Eqn. B.2, the parameters A, B, and C are the component-specific constants of Antoine equation (in this study water vapor).

In order to close the set of equations, the heat balance equation at steady state condition should be introduced as

$$\dot{m}_{in}\Delta H_{in} + \dot{m}_{spray}\Delta H_{spray} = \dot{m}_{out}\Delta H_{out} \tag{B.4}$$

In which ΔH denotes the enthalpy of the stream and is a function of temperature and heat capacity of the flow. It should be noted that the latent heat of water should be considered for calculation of ΔH_{spray}. Now that the set of equations is closed, $\dot{m}_{spray}$, as the maximum spray rate, and T_{out}, outlet temperature can be easily calculated.

$$\left[\rho_{mix}\dot{Q}C_{p_{mix}}(T-T_{ref})\right]_{in}+\left[\dot{m}\left\{C_{p_{mix}}(T-T_{ref})+\Delta H_{latent}\right\}\right]_{spray} = \left[\rho_{mix}\dot{Q}C_{p_{mix}}(T-T_{ref})\right]_{out} \tag{B.5}$$

Where ΔH_{latent} donates the latent heat of evaporation for water, $\dot{Q}$ represents the inlet volumetric flow rate.

5

Conclusion and Outlook

Conclusions are summarized based on the key findings of the research studies carried out in the present thesis. These results are structured based on the goals defined in Section 1. Afterwards, several ideas are proposed in the continuation of the present study to improve the fidelity of the present work for real industrial applications.

5.1 Conclusion

In the present thesis, the primary focus was given to the full-physics simulation of the wet fluidized bed (WFB). This was realized by extending CFD-based approaches to take the involved phenomena into account while keeping the computational effort manageable. To do so, first, using Euler-Lagrange (EL) and Euler-Euler (EE) approaches, CFD-based platforms, i.e. CFD-DEM and CFD-TFM (goals I and II) were developed with a focus on the reduction of the computational cost. To put in more detail, it was tried to decrease the computational time by improving the reliability of the coarse-grid simulations in the CFD-DEM approach (goal III). Since this approach is computationally very expensive for simulation of fluidized bed on a pilot and industrial scale, an extended CFD-TFM approach was employed to develop a compartment model. The latter is an affordable tool which can be readily used by industry for the simulation of fluid bed coaters and dryers (goal IV). Next, the results of the studies carried out to achieve the goals, as outlined in Chapter 1 of the present thesis, will be briefly reflected to draw general conclusions.

5.1.1 Goal I: full-physics simulation of droplet-particle-fluid in wet fluid bed

Aimed at obtaining the profound understanding of the phenomena occurring in the WFB, we developed two numerical approaches, i.e. i) Euler-Lagrange (EL), and ii) Euler-Euler (EE). Particularly, CFDEM® and MFiX platforms were extended to account for the exchange phenomena involved in a WFB, i.e., i) droplet deposition on the particle surface, ii) free-flowing droplet evaporation, and iii) drying of the deposited droplet on the particle surface. The implemented models were successfully verified after deriving the analytical solution of each individual phenomenon in a packed bed.

The simulation of WFB through the extended platforms demonstrated the importance of considering all phenomena involved in the performance of the WFB. Specifically, it was proved that the contribution of the droplet evaporation cannot be neglected as done in most of the studies in the open literature [1-3]. This is due to the fact that this phenomenon competes against particle drying and droplet deposition in the vapour generation and the droplet consumption respectively. Therefore, it is essential to account for all interactions between the particles, droplets, and the fluidization gas in

a WFB. The developed platform was used for comprehensive investigation of the dependency of the WFB performance on the operating condition. For more details please see Chapters 2 and 4.

5.1.2 Goal II: verified CFD-based full-physic simulation platform

After successful development of the required platforms for the simulation of WFBs, the performance of the bed was comprehensively investigated. For instance, it was shown that

- a high initial particle LoD suppresses the evaporation rate of the freely-flowing droplet, while
- a higher nozzle-to-bed-surface distance induces stronger droplet evaporation due to the longer travel time for the droplets, and the less effective penetration of the droplets into the dense bed.

It is worth noting that the predicted relative contributions of various exchange phenomena were also supported by analyzing and comparing the characteristic time scale for the individual phenomena and "droplet-in-suspension" time. (For more details please see chapter 2).

Furthermore, the analysis of the solid flow pattern revealed that the effect of the droplet velocity on the motion of the particles cannot be disregarded. Specifically, the droplet injection plays a key role in the particle circulation rate. Hence, a higher droplet velocity can improve particle mixing, and increase the frequency at which the particles can meet the droplets in the spray zone. Nonetheless, the droplet velocity cannot be increased to the extent that the particles are completely pushed towards the walls and the efficient mixing of the particle is hindered. Such a dominant effect of the droplet velocity on the particles motion highlights the potential weaknesses of some previous studies which considered the spray zone using a simplified approach [4] (these previous studies investigated much larger particles, and hence they are not 1:1 comparable with the FBs studied in the present work). The simulation results of the present thesis also demonstrated the direct effect of the droplet velocity on the expanded bed height.

5.1.3 Goal III: a voidage correction algorithm to improve coarse-grid CFD-DEM simulation

As the EL approach allows to acquire information on the particle level, the third goal of the present thesis was set to the reduction of computational effort associated with CFD-DEM simulations. To achieve this goal, the effect of the grid (fluid)-coarsening on the prediction of the hydrodynamics and the heat transfer in dense gas-particle flows was investigated. It was numerically and analytically proven that the application of coarse grids can result in the reduction of the total drag force acting on a packed bed. This is in contrast with the artificial drag increase observed in comparably dilute flows of clusters [5]. In other words, upon fluid-coarsening, in contradiction to the chaotically-oriented particles (e.g. dilute flow), distinctly-oriented particle cluster necessitates a positive drag correction. Therefore, application of the filtered models developed for dilute flow worsens the prediction of the exchange rates in case of simulating dense flows. The detailed analysis of the simulation results proved that the main reason for the deviation of the predicted drag force is related to the misprediction of the voidage and the heterogeneity distribution in case of fluid coarsening. Specifically, when coarsening the grid, blurring the voidage gradients results in the misprediction of the exchange coefficients (e.g. momentum exchange coefficient and heat transfer coefficient, which are a strong function of voidage). An easy-to-implement algorithm was proposed in the present work to correct the voidage distribution in these situations. The proposed algorithm was successfully implemented in CFDEM® code [6]. The simulation results showed a remarkable improvement of the predicted total drag force for the wide range of grid sizes (i.e., a grid-particle-size ratio of up to 12). However, the improvement for the total heat exchange rate was less significant due to the less strong dependency of the applied heat transfer coefficient on the voidage.

5.1.4 Goal IV: an improved, verified compartment model

Since the CFD-DEM approach is computationally much more expensive than the TFM approach, in the present work, the TFM approach was employed to develop a compartment model. To put in more detail, the results of the TFM simulations were analyzed to examine the applicability of the compartment model for WFBs. To do so, the degree of non-uniformity of LoD and temperature distribution were quantified by

computing the standard deviation of the relevant quantities in the bed. Such a quantification proved that the mixing of the particle in the dense bed is efficient enough to achieve the “well-mixed” condition.

What is more, based on the TFM simulation results, two well-mixed compartments were identified in the fluidized bed if certain criteria are fulfilled. This was supported via a comparison of the distribution of time-averaged exchange rates and key flow quantities in the WFBs. This led us to developing a compartment model, whose underlaying assumption is based on the “well-mixed” condition suggested by the results of the TFM simulations.

The comparison of the results of the developed TFM approach and compartment model proved that the 0D model can successfully predict the bed performance given that the following criteria are met:

i) no droplet loss occurs, i.e. the droplets are consumed by evaporation and deposition in the spray zone. Hence, droplets cannot be entrained, or evaporate at the top of the freeboard;
ii) Droplets should deeply penetrate the dense bed, which is indicated by the dominance of the solid downward velocity over the lateral one in the central region of the dense bed; and
iii) The relative standard deviation of particle LoD, temperature, and vapor content of gas is small enough (i.e., less than 5%) in reference to total temporal change over the process time in the bed.

Based on these criteria, the validity of the developed compartment model was examined for a wide range of operating conditions and spray characteristics. It was proven that in the case of long travel distances of the droplets (originating from low droplet velocities or the low fill levels) a high deviation of the developed compartment model from the TFM data should be expected. It is worth mentioning that these extreme cases are not of interest for industry since the spraying efficiency would be very low. Therefore, such conditions are avoided in real applications anyhow.

In conclusion, a CFD-based approach should be combined with 0D models to design and optimize WFB performance based on a deep understanding of the droplet and particle flow in these devices.

5.2 Outlook

In the present thesis, it was attempted to develop a reliable platform for full-physics simulation of WFBs using CFD-based approaches, as well as a compartment model. Since WFBs are associated with complex phenomena, still there is a lot of room available for future research and development, which is summarized below.

- To make the CFD-DEM approach more affordable, a voidage correction algorithm developed in the present thesis needs to be extended to account for the effect of the angle between the flow field and voidage gradient. In fact, such a modification could follow the idea of Li et al. [7].
- In future, the rheology of wet particles needs to be considered since the flow behavior of cohesive particles differs from the dry particles' one. In several studies in the open literature [8-11], an attention was paid to the development of a rheological model for (wet) cohesive powders. Therefore, such a model needs to be implemented and used in the presence of other phenomena involved in a WFB.
- Another important phenomenon, and essential to consider, is the agglomeration of wet particles. In fact, if the kinetic energy of the colliding particles is not enough to overcome viscous energy dissipation associated with the liquid on the particle, the particles cannot rebound and agglomeration occurs. Such an agglomeration event can be considered through adding the liquid bridge forces in the CFD-DEM simulation. This has been done previously for idealized conditions (i.e., uniform liquid coating [12]), and needs to be refined in future work.
- In order to examine the fidelity of the developed model for real-world industrial applications, experimental studies of WFBs are still required. In this case, the

validity of the developed compartment model should be assessed for a wide range of operating conditions and the spray characteristics.

5.3 Abbreviations

CFD	Computational Fluid Dynamics
CFD-DEM	Computational Fluid Dynamics- Discrete Element Method
CFDEM®	A software tool that implements CFD-DEM
DEM	Discrete Element Method
EE	Euler-Euler (Model)
EL	Euler-Lagrange (Model)
MFiX	Multiphase Flow with Interphase eXchanges (software)
TFM	Two Fluid Model
WFB	Wet Fluidized Bed

5.4 References

[1] V.S. Sutkar, N.G. Deen, A.V. Patil, V. Salikov, S. Antonyuk, S. Heinrich, J. Kuipers, CFD–DEM model for coupled heat and mass transfer in a spout fluidized bed with liquid injection, Chemical Engineering Journal, 288 (2016) 185-197.

[2] W. Duangkhamchan, F. Ronsse, K. Dewettinck, J. Pieters, CFD study of solids concentration in a fluidised-bed coater with variation of atomisation air pressure, Powder technology, 212 (2011) 103-114.

[3] F. Ronsse, W. Duangkhamchana, K. Dewettinckb, J.G. Pietersa, Computational Fluid Dynamics (CFD) modelling of the fluidised bed coating process, 7th International conference on Simulation and Modeling in the Food and Bio-industry (Foodsim'2012), Eurosis-ETI, 2012, pp. 34-41.

[4] G. Toschkoff, S. Just, A. Funke, D. Djuric, K. Knop, P. Kleinebudde, G. Scharrer, J.G. Khinast, Spray models for discrete element simulations of particle coating processes, Chemical Engineering Science, 101 (2013) 603-614.

[5] S. Radl, S. Sundaresan, A drag model for filtered Euler–Lagrange simulations of clustered gas–particle suspensions, Chemical Engineering Science, 117 (2014) 416-425.

[6] C. Kloss, C. Goniva, A. Hager, S. Amberger, S. Pirker, Models, algorithms and validation for opensource DEM and CFD–DEM, Progress in Computational Fluid Dynamics, an International Journal, 12 (2012) 140-152.

[7] T. Li, L. Wang, W. Rogers, G. Zhou, W. Ge, An approach for drag correction based on the local heterogeneity for gas–solid flows, AIChE Journal, 63 (2017) 1203-1212.

[8] S. Roy, S. Luding, T. Weinhart, Towards a general (ized) shear thickening rheology of wet granular materials under small pressure, arXiv preprint arXiv:1609.03098, (2016).

[9] S. Roy, S. Luding, T. Weinhart, Towards hydrodynamic simulations of wet particle systems, Procedia Engineering, 102 (2015) 1531-1538.

[10] S. Roy, A. Singh, S. Luding, T. Weinhart, Micro–macro transition and simplified contact models for wet granular materials, Computational particle mechanics, 3 (2016) 449-462.

[11] P. Liu, K.M. Kellogg, C.Q. LaMarche, C.M. Hrenya, Dynamics of singlet-doublet collisions of cohesive particles, Chemical Engineering Journal, 324 (2017) 380-391.

[12] M. Wu, J.G. Khinast, S. Radl, Liquid transport rates during binary collisions of unequally-sized particles, Powder technology, 309 (2017) 95-109.